

Multimodal image integration to better explain human ventricular tachyarrhythmias

Citation for published version (APA):

Stoks, J. (2024). *Multimodal image integration to better explain human ventricular tachyarrhythmias*. [Doctoral Thesis, Maastricht University, University of Hasselt]. Maastricht University. <https://doi.org/10.26481/dis.20240222js>

Document status and date:

Published: 01/01/2024

DOI:

[10.26481/dis.20240222js](https://doi.org/10.26481/dis.20240222js)

Document Version:

Publisher's PDF, also known as Version of record

Please check the document version of this publication:

- A submitted manuscript is the version of the article upon submission and before peer-review. There can be important differences between the submitted version and the official published version of record. People interested in the research are advised to contact the author for the final version of the publication, or visit the DOI to the publisher's website.
- The final author version and the galley proof are versions of the publication after peer review.
- The final published version features the final layout of the paper including the volume, issue and page numbers.

[Link to publication](#)

General rights

Copyright and moral rights for the publications made accessible in the public portal are retained by the authors and/or other copyright owners and it is a condition of accessing publications that users recognise and abide by the legal requirements associated with these rights.

- Users may download and print one copy of any publication from the public portal for the purpose of private study or research.
- You may not further distribute the material or use it for any profit-making activity or commercial gain
- You may freely distribute the URL identifying the publication in the public portal.

If the publication is distributed under the terms of Article 25fa of the Dutch Copyright Act, indicated by the "Taverne" license above, please follow below link for the End User Agreement:

www.umlib.nl/taverne-license

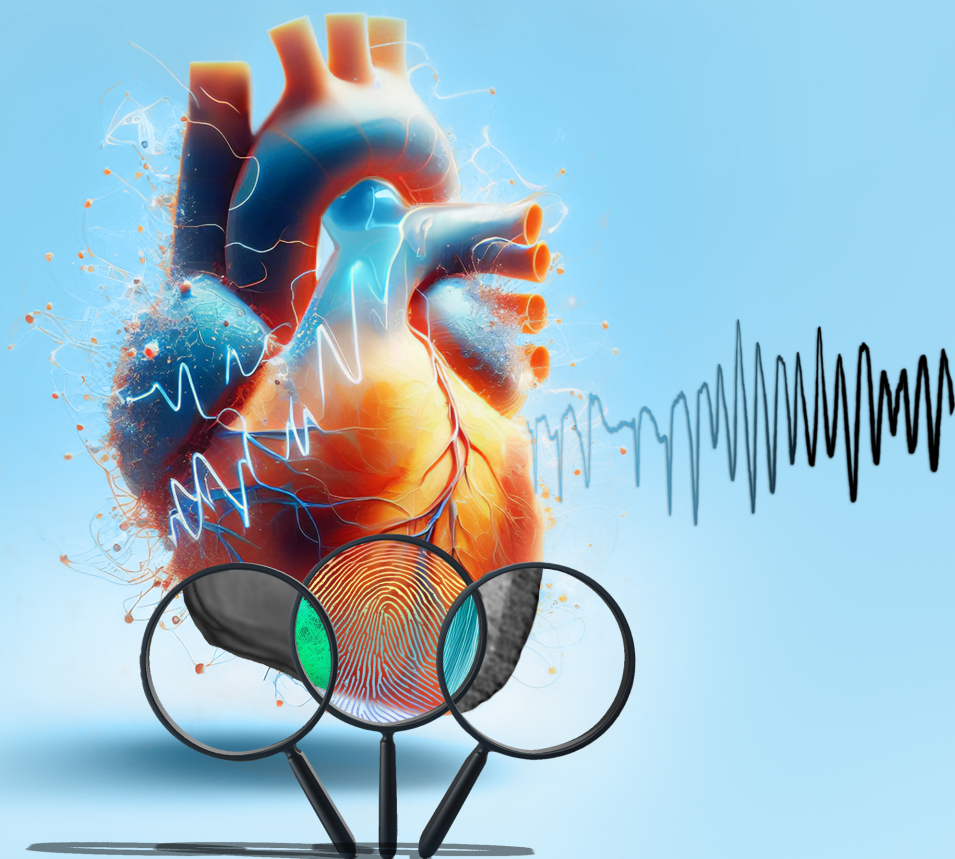
Take down policy

If you believe that this document breaches copyright please contact us at:

repository@maastrichtuniversity.nl

providing details and we will investigate your claim.

Multimodal Image Integration to Better Explain Human Ventricular Tachyarrhythmias



Job Stoks

Multimodal Image Integration to Better Explain Human Ventricular Tachyarrhythmias

Job Stoks

Multimodal Image Integration to Better Explain Human Ventricular Tachyarrhythmias

PROEFSCHRIFT

ter verkrijging van de graad van doctor aan de Universiteit Maastricht,
op gezag van de Rector Magnificus, Prof.dr. Pamela Habibović

en de graad van doctor in de Medische wetenschappen
aan de Universiteit Hasselt,
op gezag van de Rector, Prof.dr. Bernard Vanheusden
volgens het besluit van het College van Decanen,

in het openbaar te verdedigen
op donderdag 22 februari 2024 om 13.00 uur

door

Job Stoks

Promotores

Prof.dr. P.G.A. Volders (Universiteit Maastricht)
Prof.dr.ir. R.L.M. Peeters (Universiteit Maastricht)
Prof.dr. P. Dendale (Universiteit Hasselt)

Copromotor

Dr. M.J.M. Cluitmans (Universiteit Maastricht)

Beoordelingscommissie

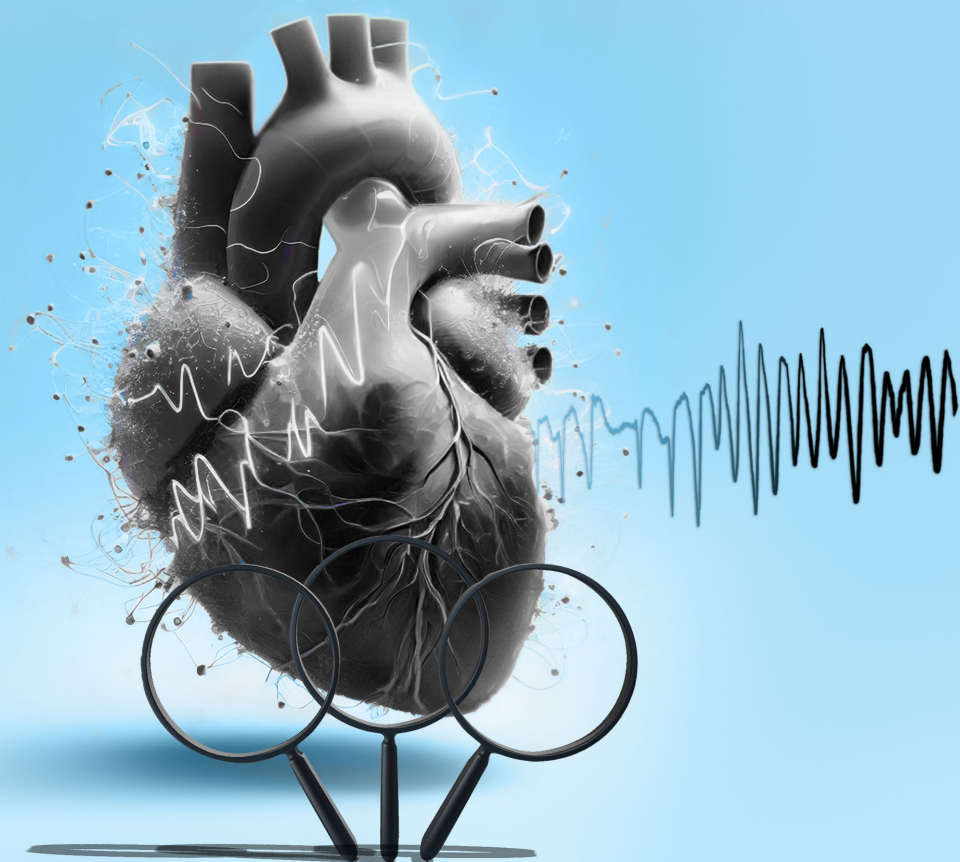
Prof.dr. T. Delhaas (voorzitter, Universiteit Maastricht)
Dr. V. Bito (Universiteit Hasselt)
Prof.dr. M.E. Kooi (Universiteit Maastricht)
Prof.dr. P.D. Lambiase (University College London, UK)
Prof.dr. D. Linz (Universiteit Maastricht)
Prof.dr. Y. Rudy (Washington University, USA)

Het verschijnen van dit proefschrift werd mede mogelijk gemaakt door de steun van de Nederlandse Hartstichting.

Het onderzoek dat aan dit proefschrift ten grondslag ligt is mogelijk gemaakt door een subsidie van de Nederlandse Hartstichting (CVON2017-13 VIGILANCE).

CONTENTS

CHAPTER 1	Introduction and outline	9
CHAPTER 2	Electrocardiographic Imaging: History, Applications, and Future Perspectives.....	25
CHAPTER 3	Novel insights into Electrocardiographic Imaging to Advance Interpretation and Standardization ...	41
CHAPTER 4	Understanding Repolarization in the Intracardiac Unipolar Electrogram: A Long-Lasting Controversy Revisited	61
CHAPTER 5	Variant Electrical Activation and Recovery in Normal Human Hearts Revealed by Noninvasive Electrocardiographic Imaging.....	85
CHAPTER 6	Dipeptidyl-Aminopeptidase-Like Protein 6 Regulates the I_{Na} - I_{to} Balance: Implications for Arrhythmogenesis and Clinical Phenotyping.....	115
CHAPTER 7	High-Resolution Structural-Functional Substrate-Trigger Characterization: Future Roadmap for Catheter Ablation of Ventricular Tachycardia ..	151
CHAPTER 8	General Discussion	175
APPENDIX A	Summary/Samenvatting.....	205
APPENDIX B	Impact.....	215
APPENDIX C	References.....	221
APPENDIX D	Acknowledgements.....	255
APPENDIX E	Curriculum Vitae	265



CHAPTER 1

Introduction and Outline

1.1 Cardiac arrhythmogenesis

The heart is the key component in the circulation of blood throughout the body, and its mechanical pumping action is controlled by a complex electrical system that regulates rhythm and rate. Under normal physiological conditions, the sinus node dictates the rhythm of the heart (**Figure 1.1A**) to ensure synchronous contraction and normal cardiac output. However, an arrhythmia disrupts this normal rhythm. Particularly, ventricular tachyarrhythmias disrupt the electrical behavior of the ventricles and can be life-threatening. These arrhythmias include ventricular tachycardia (VT, **Figure 1.1B**) and ventricular fibrillation (VF, **Figure 1.1C**). VT usually occurs at a rapid rate ($>100/\text{min}$) and can result in the loss of effective pumping function and adequate cardiac output. Some patients tolerate VT if, and as long as, the hemodynamic consequences of their arrhythmia are relatively minor. VF is disorganized and always leads to the loss of pumping function. VT and VF are the leading causes of sudden cardiac arrest (SCA) and sudden cardiac death (SCD), and the latter accounts for 15-20% of all deaths (1). Preventive medicinal treatment and acute cardioversion or defibrillation of VT/VF are important measures to maintain/restore sinus rhythm (or a stable alternative) and provide many saved years of acceptable quality of life to the victim (2).

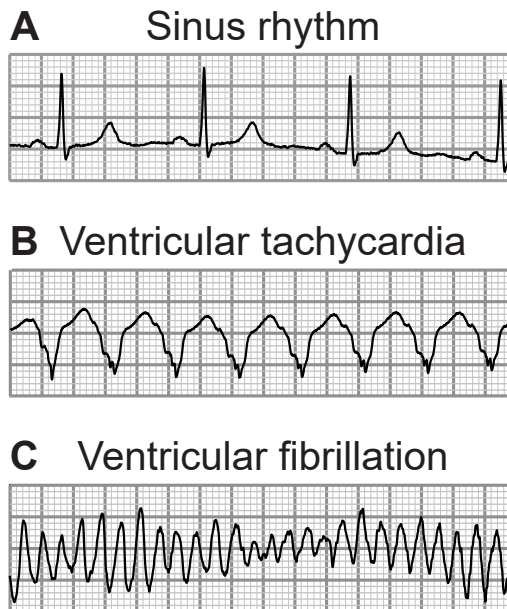


Figure 1.1: Electrocardiograms of sinus rhythm (A), ventricular tachycardia (B) and ventricular fibrillation (C).

Identifying individuals at risk for VT/VF and providing them with the right (prophylactic) therapy, such as medications, catheter ablation and/or

implantable cardioverter defibrillators (ICDs) can significantly reduce SCA/SCD rates (3). However, in many cases risk assessment is challenging. Current decision support tools are derived from population-based clinical parameters (4) and lack accuracy to tailor the right therapy for the right patient (e.g., only 5% of implanted ICDs deliver appropriate therapy per year (5)). Furthermore, current VT treatment options are often associated with high rates of recurrence (40-50% in <2 years (6)) and complications (e.g., >4% major adverse events and 1-2% in-hospital mortality for catheter ablation (7,8) and 9% for ICDs (9)).

Better mechanistic understanding of cardiac electrophysiology and arrhythmogenesis under different conditions is key to improve VT/VF risk stratification in individual patients and to prevent SCA/SCD (3,10). Such understanding of arrhythmias requires advancing insights at multiple scales, i.e., at the patient, organ, tissue, cellular and genetic level, with dedicated clinical and experimental methodologies. It also requires the *integration* of findings across scales, which poses own scientific challenges and is central to the content of this doctorate thesis. This multimodal integration of information enables to translate basic-science findings to the clinical setting.

In this doctorate thesis, I investigate cardiac ventricular electrophysiology under various *physiological* and *pathological* conditions by using multimodal image integration in order to better explain human ventricular tachyarrhythmias. I aim at providing comprehensive frameworks of arrhythmia mechanisms, which will help to identify potential diagnostic and therapeutic targets and improve risk stratification in clinical settings.

1.2 Multimodal research of cardiac arrhythmology

In this section, I discuss specific technologies to study arrhythmia mechanisms and improve management at different scales. I will discuss different molecular and electrophysiological recording techniques, imaging of cardiac anatomical variations and structural characteristics that can influence electrical function, and computational modeling techniques for the integration of information. These can be used to study arrhythmia mechanisms on larger scales. I also discuss their respective advantages and disadvantages. An overview of technologies (many used in this thesis) is given in **Table 1.1**. These are further compared in **Table 1.2**.

At the molecular level lies the question of whether there is a genetic predisposition of cardiac disease. For this reason, DNA diagnostics is of importance in many patients. DNA diagnostics is the analysis of an individual's DNA to identify genetic variations associated with diseases or traits. Although DNA diagnostics does not directly measure the electrical function of the heart, it can provide important information about the mechanisms of (genetic) arrhythmias. It involves collecting a tissue or blood sample from an individual, extracting DNA from the sample, and sequencing it to determine the order of nucleotides. By

comparing the obtained results to genetic databases, this form of testing can aid in diagnosing genetic disorders, predicting disease risk, and personalizing treatment. For example, in the field of cardiac electrophysiology, genetic testing can be used to estimate an individual's predisposition to VT/VF, e.g., in the context of an inherited arrhythmia syndrome. However, the relationship between genotype and disease manifestation is often complex. Whereas some diseases can be directly linked to a single genetic mutation, in other cases multiple variants (often as part of genetic background) or additional factors such as age, sex, environment, or comorbidities play a role in the expression of the disease (11).

1.2.1 In vitro

In vitro experiments are performed outside of the living organism in a controlled environment, e.g., a test tube, culture dish or the chamber of a microscope. They allow the study of isolated, small-scale processes without other factors that are present in vivo. However, they may not accurately reflect the complexity of in-vivo conditions and may miss important interactions between different components of the living organism. An example of in-vitro experimentation in this doctorate thesis is the measurement of ion currents that contribute to cardiac action potentials in single cells, by patch clamp (**Chapter 6**).

1.2.1.1 Patch clamp

The patch-clamp technique is a precise method for measuring membrane potential or ion currents of isolated cells at the single-cell or channel level. This involves creating a seal between a glass pipette with a tip of several micrometers and the cell membrane (12). Subsequent negative pressure to the pipette interior ensures a seal between the pipette tip and the cell membrane, resulting in a high seal resistance and low background noise (13). Once the membrane in the pipette opening is removed, voltage or current across the cell membrane can be controlled, and detailed information on cellular electrics can be obtained. However, the technique is not ideal for multicellular preparations as the seal may be lost during contraction. Therefore, the technique does not account for intercellular electrotonic effects.

1.2.1.2 High-resistance microelectrode

The high-resistance microelectrode technique with a high intra-pipette potassium concentration is used to measure cellular membrane voltage, in single cells or tissues such as ventricular wedge preparations. While the technique can be used to study electrical activity in contracting multicellular preparations, it is less suitable for maintaining a stable impalement over extended periods of time (14).

Experiment	Scale	Examples of investigative modalities of cardiac electrical function
In vitro	Molecular to tissue level, e.g., single channels (channel subunits), transfected heterologous cell systems, human induced pluripotent stem cell cardiomyocytes (hiPSC-CMs), native myocytes	<ul style="list-style-type: none"> • Patch clamping • High-resistance microelectrode recordings
Ex vivo	Tissue to organ level, e.g., ventricular wedge preparation or explanted heart	<ul style="list-style-type: none"> • Electrographic recordings* • Monophasic action potential recordings* • Optical mapping of voltage and calcium* • Panoramic electrographic contact mapping by an epicardial multielectrode sock/cage*
In vivo	Organism level	<ul style="list-style-type: none"> • Standard 12-lead electrocardiogram • Body-surface potential mapping • Electrocardiographic imaging • Electrographic contact mapping • Electroanatomical mapping
In silico	Any level from subcellular to organism	<p>Computational integration and simulation of electrophysiological data based on inputs, e.g.,</p> <ul style="list-style-type: none"> • Molecular dynamics at ion-channel level • Simulation of cardiac action potentials based on patch-clamp data • Finite-element tissue model for activation and recovery characteristics • Simulation of VT based on personalized heart geometry and location of structural scar from cardiac magnetic resonance imaging

Table 1.1: Investigative modalities relevant for arrhythmia research across scales.

*: also applicable in vivo.

1.2.2 Ex vivo

Ex-vivo experiments are performed outside of the living organism, but with an intact tissue architecture, e.g., in explanted hearts. This allows for more realistic studies of the interactions between different types of tissues, and the effects of interventions. However, the absence of other organs and systems, such as the nervous system or hormones, limits the generalization of the findings to the level of the organism. In this doctorate thesis, an example of ex-vivo experimentation is the panoramic measurement of unipolar contact electrograms by an epicardial electrode sock in explanted hearts in **Chapter 4**.

1.2.2.1 Monophasic action potential catheter

In contrast to transmembrane voltage measurements, monophasic action potentials (MAPs) are extracellular recordings of action potentials. They are obtained by recording the potential difference between an "active" contact electrode and a nearby "inactivating" contact electrode. The latter inactivates the local tissue by applying either suction or pressure. MAP catheters allow for the long-term measurement of action potentials in ex-vivo or in-vivo hearts (15,16). However, MAPs capture *extracellular* information from *multiple* cells because the electrodes are larger than individual cells. Therefore, MAPs are not reliable for determining the absolute upstroke velocity or amplitude of the action potential of single cells, but they enable the recording of local repolarization characteristics quite accurately (15).

1.2.2.2 Optical mapping

Optical mapping involves loading the myocytes in the heart with a voltage- or calcium-sensitive fluorescent dye that emits optical signals in response to changes in cellular transmembrane voltage or intracellular calcium. These signals are recorded by rapidly scanning the heart with a laser beam at multiple locations (17). While optical mapping was historically limited to two-dimensional (2D) mapping, advancements in imaging have enabled panoramic three-dimensional (3D) mapping (18). Historically, the use of excitation-contraction uncouplers was required to avoid interference caused by cardiac contraction during optical mapping. However, these uncouplers can affect the electrophysiological characteristics under study (19). Recent developments in mathematical techniques enable to correct for motion due to contraction, eliminating the need for uncouplers (20). Optical mapping provides high spatial and temporal resolution, but it requires optical access to the heart with homogeneous illumination.

1.2.2.3 Electrographic contact mapping

This technique enables to directly record extracellular electrical activity using electrodes positioned on the inner or outer surface of the heart. Unipolar and bipolar electrograms can be measured, as discussed in **Chapter 4**. This allows to study the arrhythmia itself, or to identify sites that are important for arrhythmia formation and/or maintenance. Such information is clinically used to guide the treatment of VT by catheter ablation. The spatial resolution (i.e., the regional

accuracy) is determined by the diameter of the electrodes, which is typically less than 1 mm in modern systems (21). Contact mapping requires operational skills and is a time-consuming technique; to gain high-precision substrate information electrograms should be recorded and analyzed at multiple points.

1.2.3 In vivo

In-vivo experiments are performed on, or inside, the living organism, providing a comprehensive understanding of biological processes and responses to interventions. However, they are often more difficult to control than experiments on other levels due to integrative complexities that cannot be (easily) disentangled. Examples include autonomic influences to the heart or circulating hormones or paracrine factors that have systemic or local effects. In-vivo experiments are subject to ethical constraints and practical limitations. In this doctorate thesis, examples of in-vivo measurements include electrocardiograms (**Chapters 5 - 7**), electrocardiographic imaging (**Chapters 2 - 7**), electroanatomical mapping (**Chapter 7**), and imaging of heart structure, such as computed tomography (CT, **Chapter 7**) and cardiac magnetic resonance imaging (CMR, **Chapter 7**).

1.2.3.1 The standard 12-lead electrocardiogram

The recording of an electrocardiogram (ECG) requires the placement of 10 electrodes on the body surface to record the net vector of electrical activity of the heart in multiple directions. The ECG is widely used in clinical electrocardiology for the diagnosis of many cardiac pathologies. It is a patient-friendly and cost-effective method that provides convenient insights into cardiac electrophysiology. However, the spatial resolution of the ECG is limited to macroscopic regions of the heart. This makes it challenging to identify and precisely locate regional gradients or electrical abnormalities in specific regions of the heart.

1.2.3.2 Electrocardiographic imaging

Electrocardiographic imaging (ECGI) is described in detail in **Chapter 2**. It is a noninvasive imaging technique that combines the recording of numerous electrograms on the body surface with a CT or CMR to provide anatomical reference for subsequent reconstructions of localized electrograms. Using mathematical algorithms, ECGI reconstructs the electrical activity at the level of the heart. It offers higher spatial resolution compared to the conventional ECG and is well suited for studying cardiac electrophysiology at the heart level without the invasiveness of contact mapping with catheters. ECGI is much more time consuming and costly than the recording of a standard ECG and has lower accuracy and spatial resolution compared to contact catheter mapping.

1.2.3.3 Electroanatomical mapping

Electroanatomical mapping (EAM) combines 3D navigation with contact mapping using an electrode catheter equipped with a location sensor. A mapping system detects the location of the catheter using electrical impedance or magnetic fields. During the mapping procedure, invasive electrograms and their corresponding 3D locations are stored, creating a high-resolution electrophysiological map with

anatomical reference (22). For endocardial mapping, the catheter is inserted into the endocardial cavity via vascular access, whereas for epicardial mapping, it is placed in the pericardium via percutaneous subxiphoid access. EAM can be integrated with anatomical imaging such as CT to provide a more extensive 3D anatomical context. EAM is the current standard when performing catheter ablation of VTs, and its spatial and temporal resolution are high. However, EAM is also time-consuming, invasive, costly and requires expert operational skills.

1.2.3.4 Cardiac magnetic resonance imaging

Magnetic resonance imaging (MRI) is a noninvasive imaging technique that uses magnetic fields and radio waves to create detailed cross-sectional images of the body. Cardiac magnetic resonance imaging (CMR) is the application of MRI to the heart and its associated blood vessels. Although CMR does not directly measure the electrical functions of the heart, it does provide important information about the cardiac structures that can affect electrical functions. CMR can also be used to quantify blood flow or characterize myocardial tissue such as scar or inflammation. This includes the quantification and delineation of scar areas critical for VT formation, as discussed in **Chapter 7**. Recent advancements in CMR technology (in particular 3D dark-blood late gadolinium enhancement (23,24)) have further improved its spatial resolution and its ability to delineate such areas. CMR has a high contrast resolution, but is more time-consuming and costly than CT and, in general, has a poorer spatial resolution (25).

1.2.3.5 Computed tomography

Computed tomography (CT) is a noninvasive medical imaging technique that uses X-rays to produce detailed, cross-sectional images of the body. In the heart, it is currently most often used to image coronary artery calcifications or plaques, but it also enables assessment of the structure and contractile function of the heart. Although CT does not directly measure the electrical function of the heart, it does provide important information about the cardiac structures that can affect its electrical functions. The use of contrast agents such as iodine can improve the ability of CT to delineate certain myocardial structures or vessels of interest. Recent developments in CT technology have enabled the identification of structural sites critical for VT formation (26). CT is relatively fast, inexpensive, and provides high spatial resolution, but its ability to characterize myocardial tissue is not as advanced as CMR due to its lower contrast resolution (25). Additionally, the use of CT involves exposure to radiation.

1.2.4 In-silico modeling

In-silico experiments are computer simulations of biological processes or systems. They provide the advantage of testing hypotheses and performing experiments under perfect control and observability, that may not be feasible in vivo or in vitro. In addition, they allow large numbers of different scenarios or parameters to be tested quickly and efficiently. Importantly, computer models are ideally suited to integrate findings across scales to achieve a translational understanding. However, the accuracy of in-silico experiments is determined

by the underlying models and assumptions, as any model is a simplification of reality. Therefore, these experiments may not fully reflect the complexity of real biological systems. An example of in-silico experiments in this doctorate thesis is the simulation of electrical activation and recovery at the cellular and tissue levels caused by missense variants in the dipeptidyl-aminopeptidase-like protein 6 (*DPP6*) gene, as described in **Chapter 6**.

Modality	Scale	Functional information	Structural information	Spatial resolution	Temporal resolution	Personalized 3D heart geometry	Beat-to-beat 3D heart mapping
Patch clamp	Channel/cell	Yes	No	Very high	Very high	No	No
High-resistance Microelectrode	Cell/tissue	Yes	No	Very high	Very high	No	No
MAP catheter	Tissue/organ	Yes	No	High*	High	No	No
Optical mapping	Tissue/organ	Yes	No	High	High	No	Yes
Electrographic contact mapping	Tissue/organ	Yes	No	High*	High	No	No
ECG	Organ	Yes	No	Low	High	No	Macroscopic regions
ECGI	Organ	Yes	No	Intermediate	High	Yes	Yes
EAM	Organ	Yes	No	High*	High	Yes	No
CT	Organ	No	Yes	High	Low	Yes	Yes
CMR	Organ	No	Yes	High	Low	Yes	No

Table 1.2: Functional and structural properties of modalities to (directly or indirectly) investigate cardiac electrophysiology and arrhythmogenesis. Spatial resolution refers to the regional accuracy of a modality. MAP: monophasic action potential. ECG: electrocardiogram. ECGI: electrocardiographic imaging. EAM: Electroanatomical mapping. CT: computed tomography. CMR: cardiac magnetic resonance imaging. *: exact spatial resolution depends on electrode size.

1.3 Open science and standardization

The FAIR principles (27) are a set of guiding principles for making data findable, accessible, interoperable, and reusable. These principles have been developed to promote good data management practices and to enable effective data sharing and reuse in the context of open science. Good data management can lead to knowledge discovery and innovation, as well as knowledge integration (27).

Standardization of research methodologies is essential to ensure consistent, reproducible, and comparable results and to minimize variability and bias. Yet, the constant technological advancement of multimodal imaging modalities and protocols poses a challenge to standardization. New standardization benchmarks are needed for novel imaging modalities (e.g., ECGI) and protocols (e.g., advanced CMR protocols to delineate scar with higher resolution).

To promote reproducibility and adhere to the FAIR principles, transparency of used methodologies and results is critical. This can be achieved through standardized reporting (e.g., according to the standards proposed in the Minimum Information about a Cardiac Electrophysiology Experiment (MICEE) paper (28)), specifically designed for cardiac electrophysiology research.

1.4 Aims and structure of this thesis

In this doctorate thesis, I apply multimodal image integration to better explain human ventricular tachyarrhythmias. This approach aims to overcome individual limitations of each modality and provides a more comprehensive understanding of cardiac electrophysiology and arrhythmogenesis. I acquired data from multiple electrophysiological and imaging modalities depending on the specific goals for each Chapter, see **Figure 1.2**. Each modality provides its own unique information, after which the mechanistic, computational and visual integration of these modalities leads to enhanced understanding of electrophysiology and pathology.

This thesis has the following objectives:

1. Provide a contemporary overview of the challenges, applications, and future directions of ECGI.
2. Understand and assess repolarization in the unipolar contact electrogram and ECGI.
3. Advance and standardize ECGI by providing a standardized visualization of results, and by investigating the effects of leadset configuration and diastolic heart geometry on the inverse solution.
4. Characterize the normal ventricular electrophysiology in human subjects by studying beat-to-beat stability within and among subjects of different ages, and comparing females and males.
5. Unravel arrhythmia mechanisms of unexplained SCA in subjects with a novel DPP6 missense mutation by a translational approach.
6. Unravel mechanisms of VT formation by performing high-resolution in vivo structural-functional trigger-substrate characterization.

This introductory **Chapter 1** provides a general outline of ventricular arrhythmogenesis, and the modalities used to study it. Since ECGI is used to investigate ventricular electrophysiology throughout this thesis, **Chapter 2** provides a contemporary literature review of the challenges and applications of ECGI. I then apply translational multimodal image integration to better explain human ventricular tachyarrhythmias. Electrical recovery plays an important role in VT/VF initiation and maintenance (29). In **Chapter 3**, I provide insights into the interpretation of the potential-based formulation of ECGI used in this thesis. I provide an algorithm for standardized visualization of results from ECGI, and I investigate the effect of lead set selection and use of a static diastolic geometry on the inverse solution. In **Chapter 4**, I investigate the

genesis of the electrographic recovery and the correct method to determine local recovery time by contact mapping and ECGI, as this has been historically controversial (30). This Chapter sets the stage for the understanding of cardiac electrical recovery by these modalities for the rest of the thesis. **Chapter 5** provides an overview of normal ventricular electrophysiology by ECGI and compares it to illustrative examples of pathology. In **Chapter 6**, translational multimodality image integration is used to investigate the mechanisms of action of the protein DPP6 and several missense variants in its gene to shed a new light on previously unexplained sudden cardiac arrest. **Chapter 7** discusses the image integration of ECGI with other structural and functional imaging modalities in a clinical setting to improve mechanistic understanding of infarct-related VT. Such an advanced, mechanistic approach to VT ablation may increase procedural efficiency and success. General Discussion **Chapter 8** puts the acquired results of this doctorate thesis into a broader perspective.

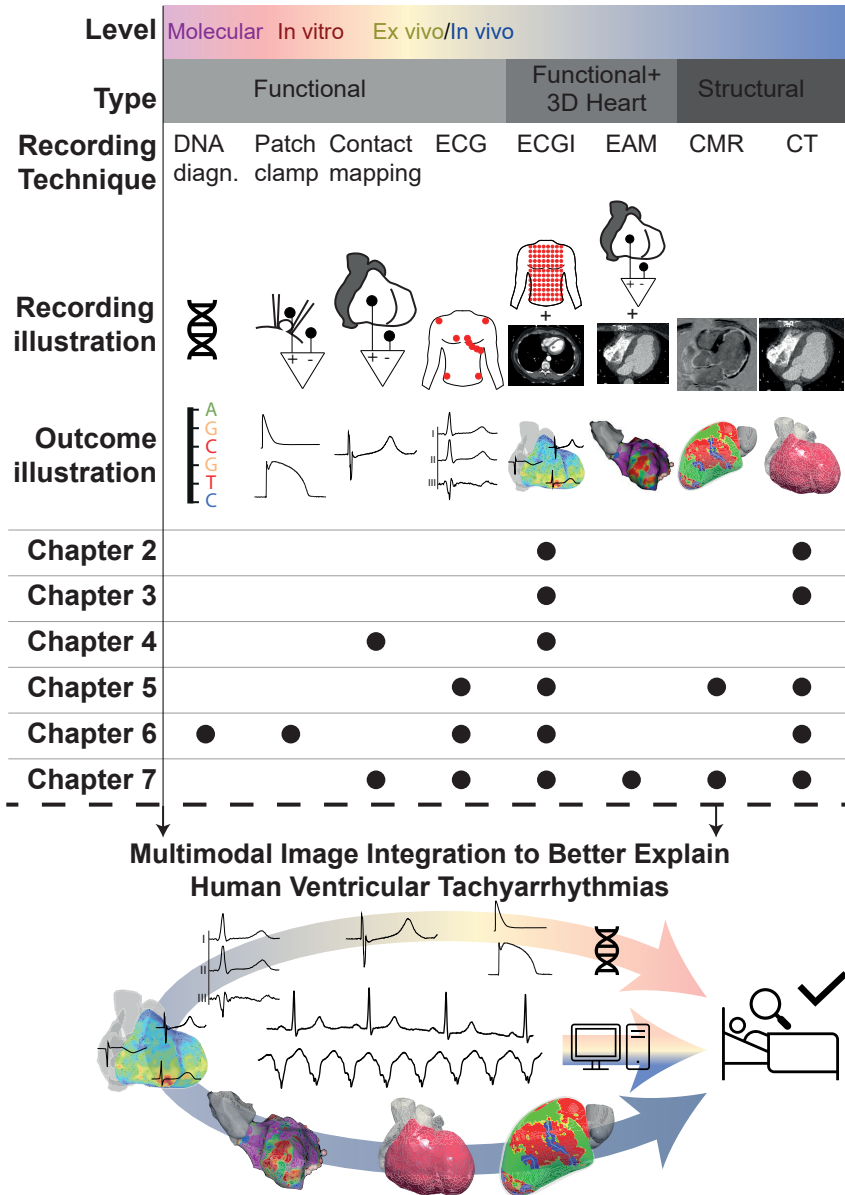
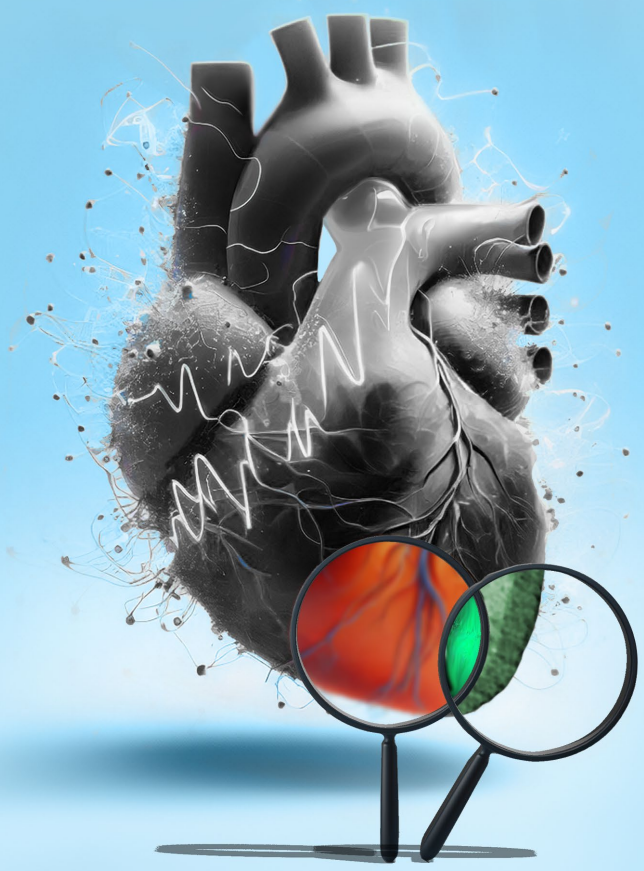


Figure 1.2: Overview of the modalities used in each Chapter of this doctorate thesis. Improved mechanistic understanding of ventricular tachyarrhythmias is a crucial step towards better diagnostic and therapeutic management. DNA diagn.: DNA diagnostics. ECG: electrocardiogram. ECGI: electrocardiographic imaging. EAM: Electroanatomical mapping. CMR: cardiac magnetic resonance imaging. CT: computed tomography.



CHAPTER 2

Electrocardiographic Imaging: History, Applications, and Future Perspectives

J. Stoks and M.J.M. Cluitmans

In: IEEE Milestone Award 'String Galvanometer': The Heritage and the Promise of Electrocardiography and Electrophysiology, edited by W. van Etten, C.A. Swenne, and E.T. van der Velde, p. 65-84. Leiden, NL: Boerhaave Continuing Medical Education, 2022. ISBN 978 90 67677 82 0.

Abstract

Electrocardiographic imaging (ECGI) is a noninvasive modality that reconstructs electrical activity at the heart level from a patient-specific body-surface potential map and heart geometry obtained by medical imaging. Here, we describe its history, advantages and challenges, validation studies, state-of-the-art applications, and future directions. Briefly, ECGI provides a trade-off between the noninvasive low-resolution electrocardiogram (ECG) and invasive high-density contact catheter mapping. Even though ECGI comes with its intrinsic challenges, most validation studies show a moderate-to-good accuracy and ECGI yields anatomy-based insights that the ECG cannot provide. Most ECGI applications currently bring value in a research setting. This includes investigating disease mechanisms, optimizing cardiac resynchronization therapy, identifying arrhythmogenic substrate, and multi-modality imaging. For clinical adoption, further maturation is still required in terms of standardization, ease of use, and external validation of study results. Its ultimate potential may lie not only in investigating disease mechanisms and providing risk stratification for future arrhythmic events but most likely also in obtaining personalized insights through the integration of ECGI with other clinical modalities.

2.1 Introduction

Electrocardiographic imaging (ECGI) is a noninvasive modality that reconstructs electrical activity at the heart from a body-surface potential map (BSPM) and patient-specific heart geometry, see **Figure 2.1**. This allows to study the heart's electrophysiological properties noninvasively, including its activation and recovery sequence. Typically, the heart geometry is imaged through a computed tomography (CT) scan or magnetic resonance imaging (MRI). The BSPM is acquired through a dense array of electrodes attached to the torso, typically detected through MRI, CT, or a three-dimensional camera. Combined, this yields the three-dimensional relationship between the electrodes and the heart geometry. This then allows calculating the electrical activity of the heart by solving the "inverse problem of electrocardiography" (31). Many implementations of ECGI exist, amongst which methods to directly estimate activation times or transmural voltages (32). However, the most widely used implementation of ECGI is the so-called potential-based formulation of ECGI. This approach estimates potentials on the ventricular or atrial surface and will be the focus of this article. First, we address the history of ECGI. Thereafter, we address the mathematical, physiological, and experimental challenges in ECGI. Furthermore, we discuss the current state-of-the-art and future applications of ECGI.

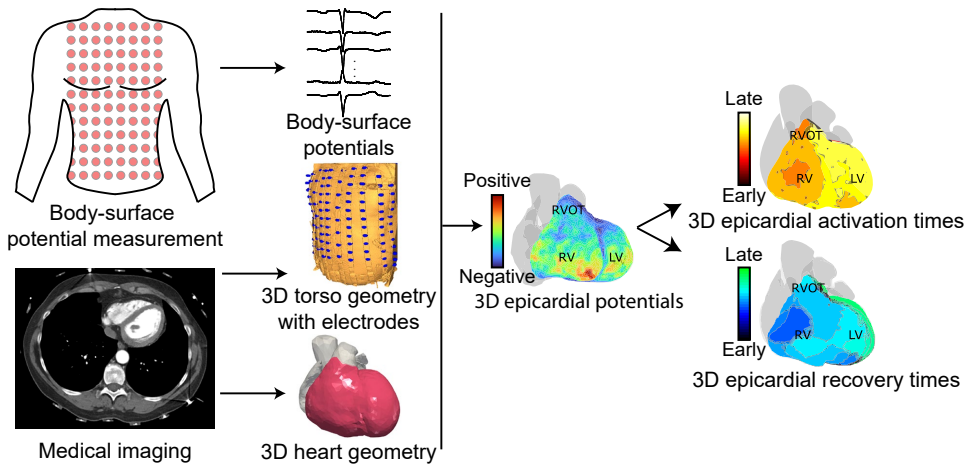


Figure 2.1: Electrocardiographic imaging (ECGI). Body-surface potential recordings and a medical imaging scan are combined in a torso-heart geometry. Epicardial potentials are reconstructed from the body-surface ECGs and yield local electrograms, activation isochrones, and recovery isochrones.

2.2 Background and history of ECGI

Since the late 1700s, many scientists have tried to study the heart's electrical activity in great detail. After the development of the three-lead electrocardiogram (ECG) by Dr. Willem Einthoven, Drs. Wilson and Goldberger added more leads to the ECG, eventually giving rise to the clinical 12-lead ECG (31). The 12-lead ECG is still in widespread use and remains the cornerstone of clinical electrocardiology. However, even though the 12-lead ECG is easy to use and can identify many kinds of cardiac pathologies with either electrical causes or consequences, it has limited spatial resolution: i.e., it is difficult to localize abnormalities in detailed regions of the heart. For this reason, from the late 1960s onwards, researchers started using tens to hundreds of electrodes to investigate BSPMs (see Figure 2.2) (31). Even though these BSPMs provide more detail about the heart's electrical activity than the 12-lead ECG, they are less easy to use and require specific equipment, knowledge, and time. Moreover, analyses that are confined to the body surface only allow to study the heart from a distance, through signals that are attenuated and dispersed by the conducting torso volume. At the other end of the spectrum, contact catheter mapping with an electrode catheter applied to the heart's inner or outer surface allows to directly measure the heart's electrical activity. Contact catheter mapping is highly accurate and could count as a golden standard for electrical signals. Moreover, it allows direct catheter-based intervention, e.g. by applying ablation to terminate arrhythmias.

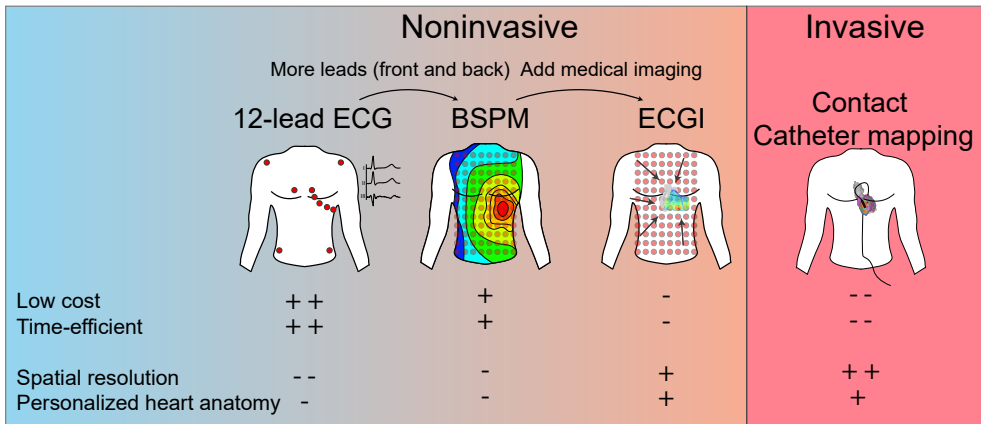


Figure 2.2: Comparison of the clinical 12-lead electrocardiogram (ECG), body-surface potential measurement (BSPM), electrocardiographic imaging (ECGI), and invasive contact catheter mapping. The first three modalities are noninvasive, and the latter is invasive. A BSPM can be obtained by adding additional leads to the 12-lead ECG, and ECGI can be performed by further adding medical imaging and calculating the inverse reconstruction. Each method comes with its own advantages and disadvantages, listed below. + indicates positive properties (cheap, time-efficient, etc.) while - indicates negative properties (expensive, time-consuming etc.)

However, these measurements are invasive, come with risks of dangerous complications, and are time-consuming and costly (**Figure 2.2**). Lastly, contact mapping requires the point-by-point measurement of individual electrograms, meaning that typically only a small portion of the heart can be measured in one beat, rendering beat-to-beat variability complex to investigate.

In search of an optimal trade-off between the detailed information that contact mapping provides and the noninvasive character of body-surface measurements, ECGI was developed (**Figure 2.1** and **Figure 2.2**). Through a BSPM and a known torso-to-heart geometrical relationship, cardiac electrical activity can be reconstructed by solving the so-called “ill-posed inverse problem of electrocardiography” (31). ECGI was first investigated through mathematical models, focusing on a spherical surface, investigating the basic mathematical requirements such as constraining the solution (33), and whether the technical estimation of cardiac potentials would be feasible with respect to noise (33). Later on, more realistic and complex scenarios were investigated and tested in dogs (34,35). Moreover, animal validation studies using clinically interesting outcomes (36,37) eventually led to the first real-life application in humans (38). Initial studies were limited to the ventricles, but later, the atria also became an active field of research. Nowadays, ECGI is still actively being improved (39), but is also widely applied in both the research and clinical domains.

2.3 Challenges in ECGI

ECGI’s main disadvantage in comparison to invasive contact catheter mapping (see **Figure 2.2**) is its accuracy, estimated to be around 10mm (see **Table 2.1**). Increasing ECGI’s accuracy is still an active field of research and comes with its own challenges. These can be divided into mathematical, physiological, validation, and standardization challenges, which we will now address. See **Figure 2.3** for an overview.

2.3.1 Mathematical

Mathematically, the forward problem of electrocardiography is formulated as

$$\Phi_B(t) = A \cdot \Phi_H(t) \text{ (Eq. 1)}$$

where $\Phi_H(t)$ represents the potentials on the heart as a function of time, $\Phi_B(t)$ the potentials on the body surface as a function of time, and A the transfer matrix which captures the geometrical and electrical relationship between the heart and body surface. The inverse problem of electrocardiography is intrinsically ill-posed, meaning that even if the transfer matrix A is invertible, the mathematical solution for potentials on the heart $\Phi_H(t)$ is sensitive to noise, and a small perturbation of body-surface signals $\Phi_B(t)$ can lead to a disproportionately large change in the solution (31). For this reason, the solution needs to be constrained, based on knowledge of the physiology and physics of the heart’s electrical activity. This leads to a mathematical frame in which the solution

should be found and is termed ‘regularization’. Commonly, a zeroth-, first-, or second-order Tikhonov regularization (40) is used,

$$\hat{\Phi}_H(t) = \min_{\Phi_H(t)} \{ \|A \cdot \Phi_H(t) - \Phi_B(t)\|_2^2 + \lambda(t) \cdot \|L \cdot \Phi_H(t)\|_2^2 \} \text{ (Eq. 2)}$$

In which λ is the regularization parameter which controls the trade-off between the residual norm ($\|A \cdot \Phi_H - \Phi_B\|_2^2$) and the constraint norm $\|L \cdot \Phi_H\|_2^2$, and L is a regularization matrix, which is equal to the identity matrix in zero-th order Tikhonov regularization. For example, zeroth-order Tikhonov regularization provides a trade-off between a small amplitude and a small absolute error. (Eq. 2) is solved for $\Phi_H(t)$ after determining an optimal λ .

Challenges in ECGI

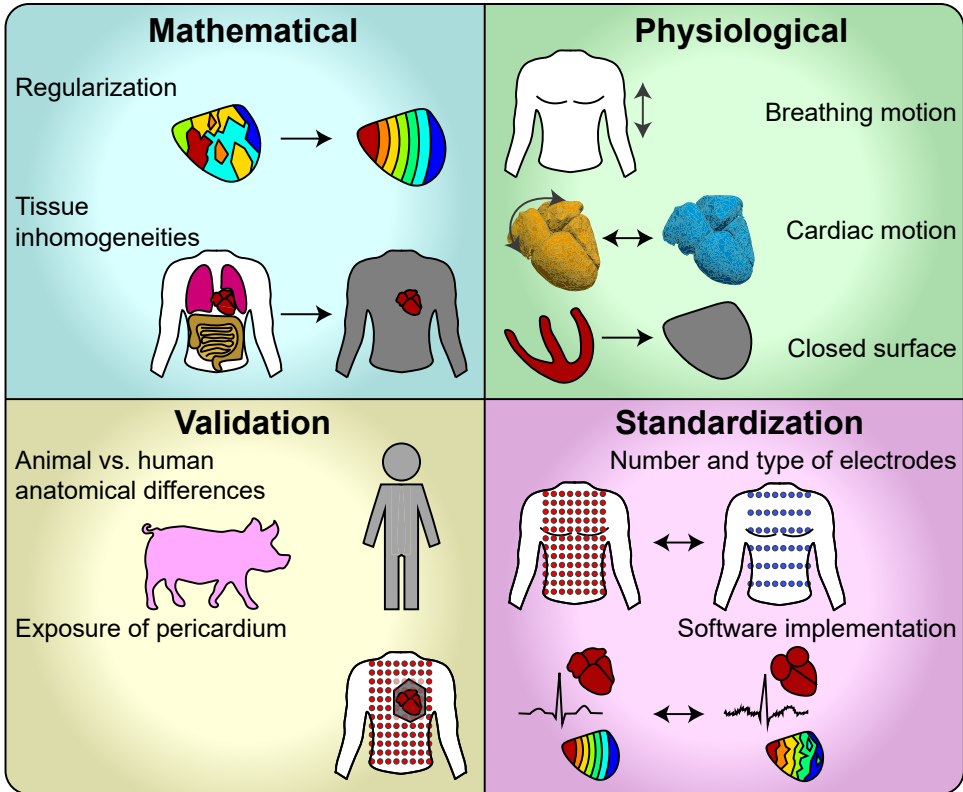


Figure 2.3: Challenges in ECGI. Challenges can be divided into mathematical, physiological, validation and standardization challenges. See text for further explanation.

Lastly, in ECGI, the torso as a volume conductor is often estimated to be homogeneous in terms of conductance. However, in real life, organs and tissues inside the torso lead to inhomogeneous conductivities. The estimation of the

torso to be a homogeneous volume conductor leads to problem which is less ill-posed and in practice does not yield results that are significantly worse than more complex piecewise homogeneous torso volumes (41).

2.3.2 Physiological

The transfer matrix A is commonly approximated to be static since the position of the heart and torso are typically captured with a CT or MRI scan during breath-hold and at the same timepoint within the cardiac phase. However, in reality, the geometry-conductivity relationship is dynamic. Firstly, the heart contracts, causing changes in its volume, position, and orientation. Secondly, variations in position and geometry of heart, lungs, and body surface are driven by inspiration and expiration. A preliminary study showed a small effect of the contractile motion of the heart on common outcome measures, see **Section 3.4**. A recent computational study showed that cardiac motion due to breathing is non-negligible, thereby also proposing a geometrical correction method (42). Secondly, the potential-based formulation of ECGI typically does not take the contribution of the septum and endocardial layers into account. Septal and endocardial information can be extracted from the body-surface ECG to a certain extent (43). The most common implementation of ECGI uses potentials measured on the body surface to estimate epicardial potentials only, and the physiological origin of enclosed underlying (i.e., transmural and/or septal) components is not separately considered in **Eq. 2**. Even though this effect has never been actively studied to the best of the authors' knowledge, this could contribute to the inaccuracy of ECGI. Until then, the "epicardial-only"-reconstructed signals should probably be considered to be a mainly epicardial representation of the total transmural cardiac electrical activity.

2.3.3 Standardization

Lastly, since ECGI is currently being developed and being applied in different centers in parallel, methodologies in ECGI hardware and software can vary greatly. For example, the amount of electrodes used for ECGI can vary from 32 to 256, and electrodes can be either passive or active. Software-wise, researchers segment the heart differently (44) and use different source models (32). Even within one source model, such as the potential-based formulation of ECGI which is discussed in this chapter, different kinds of regularization, filtering, smoothing, and other parameters can be applied. Additionally, ECGI provides a large amount of multidimensional data, resulting in many possibilities for outcome measures that makes a comparison of studies or systems challenging. These differences in methodology also affect practical ease-of-use: e.g., a reduced number of electrodes is easier to apply but may be less accurate (45), and automated methods may be faster than ones requiring trained operator input, but may also negatively impact reliability. Exploring different methodologies is paramount for identifying ECGI's potential, but it remains essential to realize that there is a large variety in implementation choices, which is why different (validation) studies yield different results. To achieve further maturation or clinical implementation, ECGI could benefit from the standardization of hardware and software.

2.3.4 Validation

Validation of ECGI can either be performed computationally, in a bucket or torso-shaped tank filled with fluid containing an ex-vivo heart, or in-vivo in either animals or humans. These validation methods are increasingly accurate in resembling a real-life situation at the cost of experimental complexity. Even in-vivo experiments may not completely mimic human application in a clinical setting. For example, in animal validation studies, the position of the heart and composition and size of the thorax can be different from humans. In human validation studies, the pericardium needs to be exposed to perform an invasive measurement. This means that ECGI can only either be validated in a non-time-aligned manner, or with a limited number of electrodes. Validation studies are discussed in more detail in the next section.

2.4 Validation studies

Even though ECGI's technology comes with its intricacies, it still provides valuable information on cardiac electrical activity with a relatively high spatial accuracy. Since ECGI knows many implementations, we only describe ex-vivo and in-vivo experimental validation studies of the potential-based formulation of ECGI for the ventricles. Validation has been performed in many forms, through varying hardware setups, experimental setups and computational methods. For a more elaborate overview of different forms of validation, we refer to Cluitmans et al. (46). Here, we discuss some key findings from various validation papers. An overview can be found in **Table 2.1**.

As visible in **Table 2.1**, most studies have focused on the localization error of paced beats and on correlation coefficients (CCs) of the reconstructed epicardial electrograms. Fewer studies focused on activation or recovery times. Even though Bear et al. (47) reported no significant differences between torso tank and in vivo results for recovery, most in-vivo studies reported slightly lower accuracy than torso tank studies. Furthermore, results of most studies qualitatively agree, except for the study by Duchateau et al. (48), who found much poorer localization errors and activation time correlation than other studies. In this study, a commercial system was used. They reported that ECGI was much more accurate for paced rhythm than for sinus rhythm, and was prone to displaying artificial lines of slow conduction.

Even though this study did expose some of ECGI's important intricacies, other authors have warned that such a commercial implementation of ECGI without careful investigation of underlying electrograms and data should not be overgeneralized and requires further investigation (49,50). On the other hand, clinical applications should be based on commercially available systems and should be easy to use and accurate at the same time. Apart from the study by Duchateau et al. (48), other studies show a reasonable performance of ECGI. Median pacing site localization errors vary from 2 to 13mm, and median correlations with invasive electrograms (CCs) differ from 0.71 to 0.86. ECGI's

accuracy was reported to be lower on the left ventricular anterior side and during the QRS complex rather than during the T wave (51), the endocardial rather than the epicardial side (52), in scar rather than in viable tissue (53), outside rather than within the end-inspiratory phase (54), and during sinus rhythm rather than during paced rhythms (48) (even though a smaller study disagreed (52)).

Ref	Setup	Species (n)	Beats (n)	EGM CC	LE (mm)	AT R	RT R
(36)	Torso tank	D (1)		>0.9 for 72% of electrodes	<10		
(52)	In vivo (NTA)	H (3)	5	0.73	13		
(55)	Torso tank	D (1)	4	0.81	2		
(53)	In vivo	H (4)	79		13±9†		
(54)	In vivo	H (29)	456		9±6		
(54)	In vivo	H (5)	412		7±2		
(51)	In vivo	D (4)	93	0.71 [IQR 0.36-0.86]	10 [IQR 7-17]	0.82	0.73
(48)	In vivo (NTA)	H (55)	59		76±38	0.03 ±0.43	
(47)	Torso tank	P (8) and H (1)		0.85 [IQR 0.52-0.96]*			0.73 [IQR 0.63-0.83]
(47)	In vivo	P (5)		0.86 [IQR 0.52-0.96]*			0.76 [IQR 0.67-0.82]

Table 2.1: Quantitative results of validation studies. Only quantitative results with one or more of our selected validation metrics were included. ECGI study results are shown relative to invasive mapping, the gold standard. Some studies are shown twice, since separate experiments were performed and not pooled. EGM: electrogram. CC: correlation coefficient. LE: localization error. R: Pearson's R. NTA: no time-aligned validation. D: Dog. H: Human. P: Pig. IQR: interquartile range. †: results of only healthy myocardium are shown. *: CC of only the T-wave, not the QRS complex.

Of note, two studies showed that ECGI-reconstructed outcome measures may contain a spatial shift of 1-2 cm in relation to invasive electrograms (47,51), which could adversely affect validation outcomes that compare epicardial metrics node-by-node, while this spatial shift may not be important for most of ECGI's applications (e.g., detecting spatial gradients of activation or recovery isochrones or highlighting regions of interest).

Furthermore, several validation studies also assessed pacing site localization of endocardial origins, which can successfully be identified. Oster et al. (56) evaluated ECGI's performance in a torso tank containing a dog heart, by pacing from varying intramural depths. They reported epicardial breakthroughs occurring progressively later with deeper intramural pacing (56). High-pass filtering of electrograms further aids in identifying the transmural origin of PVCs (57).

2.5 Applications and future directions

ECGI is currently widely used in a research setting but also increasingly to evaluate its clinical applicability (46). ECGI has many applications, amongst which localizing the origin of premature ventricular contractions (PVCs), identification of accessory pathways from atria to ventricles, identification of atrial or ventricular fibrillation rotors, the optimization of cardiac resynchronization therapy (CRT), and arrhythmogenic substrate identification. Still, ECGI's clinical application is currently limited, considering that most applications would require more evidence of clinical benefits such as a better patient outcome or higher time-efficiency and cost-efficiency.

2.5.1 Premature ventricular contractions

Through activation time mapping or isopotential mapping, the origin of PVCs can be localized through ECGI with greater accuracy than a trained operator through clinical algorithms through the 12-lead ECG and to reduce procedural time in case of interventions (58).

2.5.2 Identification of fibrillation rotors

For atrial arrhythmias, ECGI is used to determine the mechanisms of the arrhythmia (59), though it remains challenging to correctly identify atrial fibrillation rotors (60). In a recent clinical study, ECGI was used to successfully guide the targeting of persistent atrial fibrillation drivers (61). ECGI is also used to identify mechanisms of ventricular fibrillation (46).

2.5.3 Optimizing cardiac resynchronization therapy

CRT is a therapy in which both ventricles are electrically paced to improve cardiac function in patients with heart failure and low ejection fraction. Due to the relative simple activation and recovery patterns that cardiac pacing produces compared to normal sinus rhythm, this is where ECGI's accuracy is highest (48). For this reason, cardiac pacing and CRT seem to be ECGI's most promising applications. ECGI has been used to predict CRT outcomes, optimize CRT therapy, evaluate electrical dyssynchrony between the ventricles, and to optimize CRT lead placement (62).

2.5.4 Arrhythmogenic substrate identification

Lastly, ECGI allows the investigation of arrhythmogenic substrates and disease mechanisms in a novel and time-efficient manner. ECGI outcomes are often in line with hypotheses regarding the mechanisms of these diseases, such as premature and abnormal ventricular activation in the presence of an atrioventricular accessory pathway (63), increased repolarization gradients in long QT syndrome (64), conduction slowing and altered repolarization in the right ventricular outflow tract in Brugada syndrome compared to controls and more outspoken in mutation carriers (65–67), multiple abnormal repolarization properties in early repolarization syndrome (68), prolonged activation and recovery in arrhythmogenic right ventricular cardiomyopathy and correlation between ECGI parameters and MRI images (69), and increased activation time dispersion in hypertrophic cardiomyopathy (70).

Identifying subjects at risk for sudden cardiac death (SCD) remains the very challenging holy grail of ventricular electrophysiology. Identifying subjects at intermediate risk for SCD is challenging (71), particularly when routine clinical tools fail to identify any abnormality. Assessment of SCD risk is also challenging in relatives of affected individuals, who may carry genetic abnormalities. Several studies hint toward a promising role for ECGI for SCD risk stratification. For example, (unexplained) SCD survivors displayed an abnormal repolarization response to exercise (72). A case in the Maastricht University Medical Center+ showed the same phenomenon, see **Figure 2.4A**. Furthermore, SCD survivors have shown to display increased activation time variability on ECGI after exercise, compared to non-SCD survivors (73). Lastly, survivors of idiopathic ventricular fibrillation (SCD in patients without any substrate detectable by clinical tools) displayed distinct repolarization abnormalities through ECGI, in line with mechanistic studies (74), see **Figure 2.4B**. Generally, external validation and further evidence in the shape of prospective studies regarding the role of ECGI in risk stratification for SCD (e.g., by performing ECGI in family members of SCD survivors) is still required, but initial results seem promising.

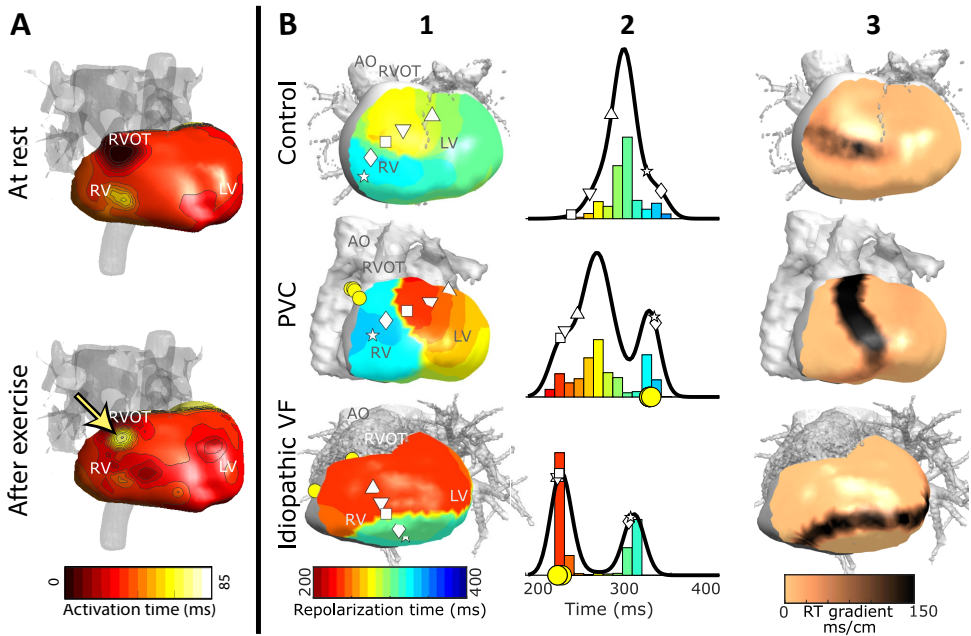


Figure 2.4: Arrhythmogenic substrate identification through ECGI. **A:** an SCD survivor showing an area of delayed activation after exercise which was not present during rest, analogous to (72). **B:** adapted from (74) with permission: ECGI-derived repolarization maps of a control individual, a patient with frequent PVCs but without cardiac arrest, and an idiopathic ventricular fibrillation survivor. The latter showed two distinct repolarization areas separated by an increased repolarization gradient, whilst PVCs originated from the early-repolarizing area.

2.5.5 Multimodal image integration

Several studies highlight ECGI's potential to be implemented in clinical care as a complementary modality. In complex patient cases, a singular modality cannot fully phenotype the arrhythmogenic substrate in a patient or guide therapy. ECGI's potential may lie in combining its electrical assessment with other (structural) modalities, potentially leading to improved electrostructural phenotyping of complex patients and personalized medicine, see **Figure 2.5**.

For example, in combination with CT and MRI scans, ECGI has been demonstrated to guide lead implantation in patients requiring CRT (75) and to guide catheter ablation in a case of ventricular tachycardia (76), see **Figure 2.5A**. In combination with functional and anatomical imaging, ECGI was used to guide catheter-free noninvasive radioablation for ventricular arrhythmias (see **Figure 2.5B**), after which arrhythmia burden was greatly reduced (77). Conventional imaging provides information on tissue viability and scar, which is very useful to guide ablations. ECGI provides complementary electrical information which is vital to the working mechanisms of the arrhythmia.

Lastly, the current progression of medical science is slowly shifting from a “one size fits most” towards personalized medicine: a “one size fits one” approach. Recent advances in computational modeling and machine learning have led to highly accurate predictions for future SCD or atrial fibrillation events using high-quality clinical data (78). ECGI may be complementary to these techniques, providing further noninvasive personalization (see **Figure 2.5C**).

2.6 Conclusion

Almost 120 years after Einthoven made the first clinical ECG (79), conventional electrocardiography has been supplemented by ECGI, that was developed during the past 50 years. ECGI is a noninvasive modality to investigate cardiac electrical activity. Although challenges in ECGI exist, most validation studies show that ECGI can reconstruct cardiac electrical activity with moderate to good accuracy. Currently, ECGI is mostly used in a research setting, but for clinical implementation, further maturation is still required in terms of standardization, ease of use, and external validation of study results. Its ultimate clinical potential may lie not only in investigating disease mechanisms and providing risk stratification for future arrhythmic events, but most likely also in integrating ECGI with other clinical modalities for optimized personalized diagnosis and therapy guidance.

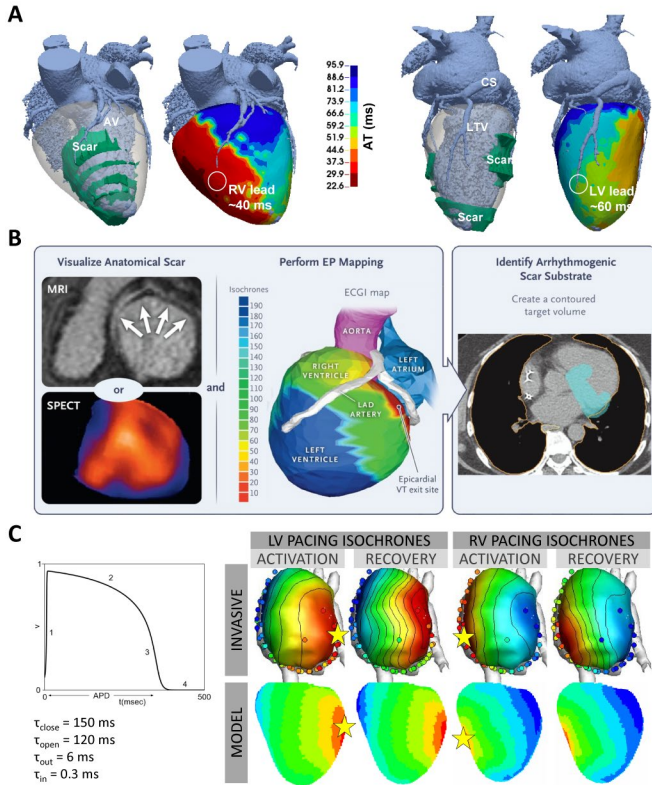


Figure 2.5: Image integration with ECGI. AV: anterior vein. RV: right ventricle. LV: left ventricle. CS: coronary sinus. LTV: lateral vein. LAD: left anterior descending. **A:** adapted from (75) with permission: optimizing lead placement in CRT by combining ECGI with MRI and CT scans. **B:** adapted from (77) with permission: Combining ECGI with anatomical imaging to guide catheter-free noninvasive cardiac radioablation for ventricular arrhythmias. **C:** use of ECGI to personalize computational models to further perform risk stratification for SCD.



CHAPTER 3

Novel Insights into Electrocardiographic Imaging to Advance Interpretation and Standardization

A collection of adapted versions of:

An Open-Source Algorithm for Standardized Bullseye Visualization of High-Resolution Cardiac Ventricular Data: UNISYS.

J. Stoks, U. C Nguyen, R. Peeters, P.G.A. Volders and M.J.M. Cluitmans.

Computing in Cardiology. 2020; 47.
DOI: 10.22489/CinC.2020.160

Variability of Electrocardiographic Imaging Within and Between Leadsets.

J. Stoks, B.D. van Rees, S.A. Groeneveld, D.J.M. Schipaanboord, L. Blom, R.J. Hassink, M.J.M. Cluitmans, R. Peeters and P.G.A. Volders.

Computing in Cardiology. 2020; 47.
DOI: 10.22489/CinC.2020.097

The Influence of Using a Static Diastolic Geometry in ECG Imaging.

J. Stoks, M.J.M. Cluitmans, R. Peeters and P.G.A. Volders.

Computing in Cardiology. 2019; 46.
DOI: 10.22489/CinC.2019.266

3.1 Introduction

As described in **Chapter 2**, ECGI provides anatomy-based insights into cardiac electrophysiology that the ECG cannot provide. Still, standardization of visualization and quantification of its technological uncertainties can provide a basis for further clinical adoption of ECGI.

In **Section 3.2**, we demonstrate our open-source algorithm Universal Ventricular Bullseye Visualization (UNISYS), which provides a standardized visualization of any kind of single-layer ventricular data. UNISYS ensures consistent bidirectionality and spatial conservation of points of interest, facilitating visual comparisons between patients and within patients, such as in **Chapter 5**. UNISYS can be applied to any type of single-layer ventricular data (e.g., epicardial electrophysiology by ECGI, left ventricle (LV)-only mechanics by cardiac magnetic resonance imaging (CMR), LV-only invasive mapping), aiding in interpretability and standardization of ECGI such as in the AHA 17-segment bullseye.

In **Section 3.3**, we describe variability in inverse reconstructions between and within different lead sets by assessing epicardial potential maps and isochrones. Differences between two lead sets are larger than beat-to-beat differences within a lead set, for all outcome measures except recovery times (RTs), which were more variable than activation times (ATs). This variability is primarily caused by noisy and low-amplitude signals, as well as regions of T-wave polarity switch. These findings increase our understanding of the consequences of electrode positioning on the inverse solution, as well as our understanding of the intricacies of recovery time estimation in ECGI.

In **Section 3.4**, we investigate the impact of using a static diastolic geometry on the inverse solution by comparing epicardial potential maps and isochrones on systolic and diastolic geometries. Although global correlation of ATs/RTs and correlation coefficients between both geometries are relatively high, clinical interpretation may differ because of regional differences in inverse solutions. Differences between inverse solutions are unrelated to linear or rotational movement of the heart, but often caused by low-amplitude epicardial T-waves.

3.2 Standardized bullseye visualization (UNISYS)

Adapted from: J. Stoks, U. C Nguyen, R. Peeters, P.G.A. Volders and M.J.M. Cluitmans. An Open-Source Algorithm for Standardized Bullseye Visualization of High-Resolution Cardiac Ventricular Data: UNISYS. Computing in Cardiology. 2020; 47. DOI: 10.22489/CinC.2020.160

3.2.1 Introduction

Visualizing electro- or mechano-anatomical results from cardiac ventricles for scientific purposes in a structured manner can be challenging. For example, displaying the full three-dimensional ECGI observation of a single subject typically requires three to four different views to cover all relevant cardiac structures. Moreover, comparing results of different subjects is difficult, due to inter-individual differences in anatomy. Providing a clear, unified graphical representation of data by standardization, whilst still considering inter-individual anatomical aspects, could aid researchers in gaining more insight from complex data. For these reasons, we developed UNISYS (Universal Ventricular Bullseye Visualization): an open-source algorithm to process the geometry of cardiac ventricular data and to display them uniformly in a 2D high-resolution circular representation (bullseye plot). The key steps to this pipeline are shown in **Figure 3.1**.

3.2.2 Bullseye projection

In short, the UNISYS algorithm is shown in **Figure 3.1**. After manual annotation of the interventricular septum and disregarding the values at the valvular plane, any three-dimensional data can be projected onto a UNISYS representation by a series of translations, rotations, transformations, and interpolation.

3.3.3 Bidirectionality

For four human hearts, one reconstructed AT pattern and one RT pattern from ECGI were transformed to a UNISYS representation, see **Figure 3.2**. Afterwards, these values were re-transformed back to the 3D heart, by selecting the values of the grid point closest to each original vertex. The differences between the original data and the re-transformed data were investigated to assess the bidirectionality of UNISYS. These are shown in **Figure 3.3**. Mean absolute deviation between original and re-transformed data was 0.07%. The 99th percentile of all absolute deviations was 0.9%. Maximum absolute deviation over all 8 patterns was 4.8%. Thus, our method shows a high degree of consistency in terms of bidirectionality. Some of these differences may arise from the fact that the 3D-to-UNISYS transformation was done by means of interpolation, while the UNISYS-to-3D transformation was done by means of nearest-neighbors.

3.2.4 User-defined septum and 24 segments

The original user-defined septum coordinates and the division of the heart into 24 segments are visualized on the UNISYS bullseye in **Figure 3.4**. The basal segments contain more vertices than apical segments. The originally denoted

user-defined septum coordinates (dashed line) show a high degree of agreement with the UNISYS-transformed septum coordinates (solid line dividing the left vs right side of the circle).

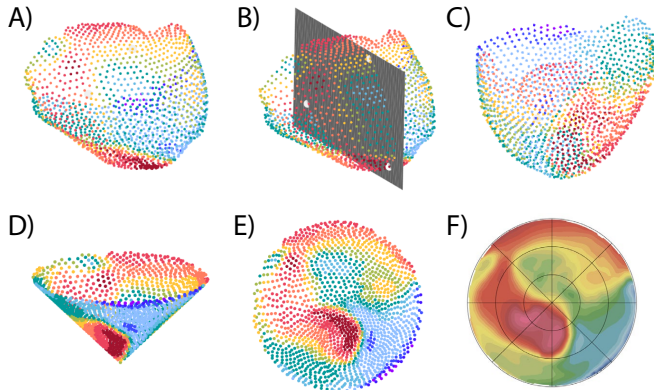


Figure 3.1: UNISYS pipeline. **A)** Input: vertices of heart, each with an associated value (color-coded here). **B)** The algorithm requires the user to denote three coordinates indicating the septum. **C)** After obtaining the user input, the heart is translated and rotated upright. **D)** The heart is transformed to a cone shape, with increasing radius from apex to base. **E)** The cone and its associated values are transformed onto a circular 2D disk. **F)** Associated values of remaining vertices are interpolated to render a continuous representation which is divided into 24 epicardial segments here.

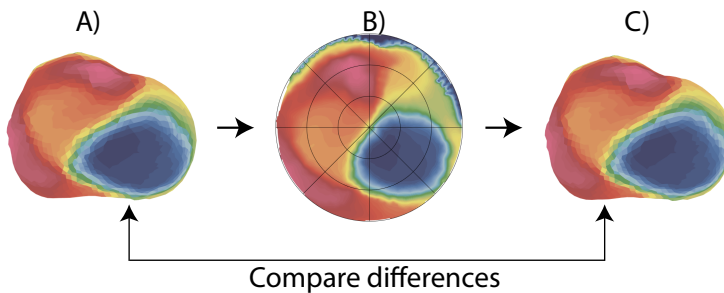


Figure 3.2: Analysis of re-transformed data. Original 3D data **(A)** were transformed to 2D UNISYS representation **(B)**, and back again **(C)**). Differences were quantified and are shown in Figure 3.3..Repolarization time data of subject 2 are shown here.

Still, data density may differ between subjects. The more equal both ventricles are in size, the more equal the density of data is for each of the 24 segments, which is most true in subject 1. Conversely, as visible in subject 3 in whom the septum was defined more laterally to the right, the percentage of vertices in the outer ring can vary from 1% (RV lateral wall) to 11% (LV lateral wall) in a single subject. Users interpreting this bullseye visualization should realize that data

density may differ. Furthermore, the location of certain anatomic structures (such as the outflow tracts and coronary arteries) on the bullseye may vary between subjects.

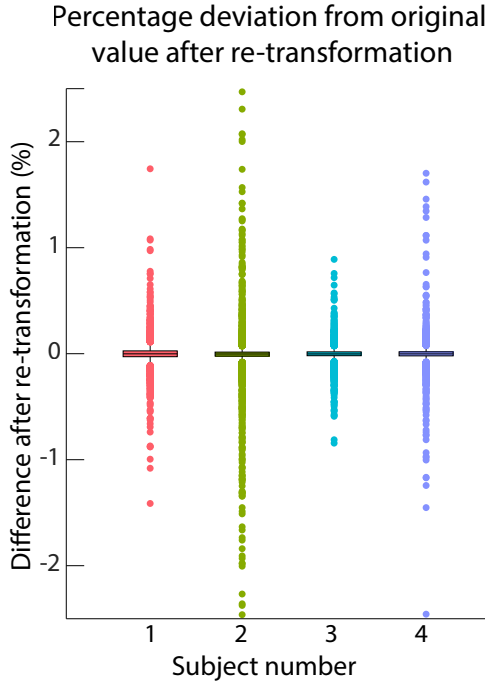


Figure 3.3: Boxplots of differences between original data on 3D heart and the re-transformed data. For each subject, one depolarization and one repolarization pattern from ECGI were used. Y-axis cropped at 2.5% for visualization purposes.

3.2.5 Other visualization techniques

Several other methods to transform 3D ventricular data to a standardized form are known. For example, the method by De Craene et al. (80) to visualize a standardized anatomy requires the calculation of a Laplacian to convert the LV into the AHA 17-segment representation. In contrast, our method can also be used to visualize both the LV and RV. The open-source method by Paun et al. (81) produces a patient-independent representation of the detailed cardiac anatomy onto a circular disk. Their method can also separate LV and RV. Conversely, our method focuses primarily on visualizing electro- or mechano-anatomical results. Lastly, the universal ventricular coordinate system (UVC) by Bayer et al. (82) also maps position within the ventricles of hearts to a generic frame of reference based on Laplacian solutions. Even though their method was not used to project ventricular data on a standardized circle, it could be suitable to do so.

Even though not shown here, UNISYS supports many optional visualization possibilities. For example, users can select their own (customized) colors of interest and bin width and color axis limits, as shown throughout this thesis.

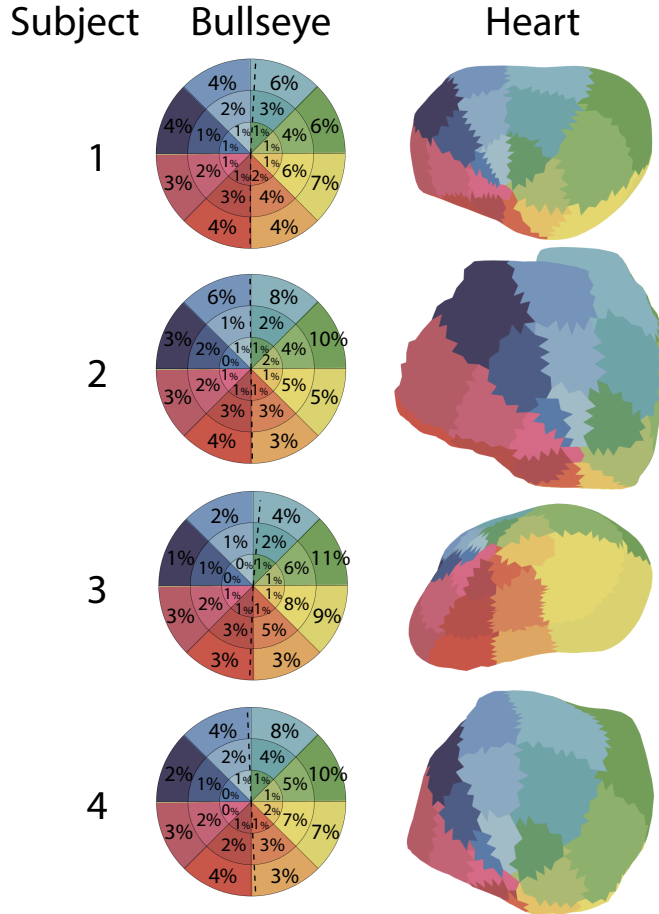


Figure 3.4: Hearts divided into 24 segments. Left: UNISYS bullseye representation. Original user-defined septum coordinates are shown by the dashed line. Each segment contains the percentage of vertices on the heart corresponding with that segment. Right: 3D heart.

3.2.6 Summary and interpretation

UNISYS allows for visualization of any kind of data, such as electrical, mechanical, anatomical or a combination of either of these. Data of a single ventricle can also be visualized with UNISYS in the same manner. This bullseye visualization allows for easy visual comparison of inter- and intra-patient observations. Even though the location of certain anatomic structures on the bullseye may vary mildly between subjects, the method is highly consistent in terms of bidirectionality and spatial conservation of points of interest. UNISYS is made freely available by the Consortium for ECG Imaging (CEI) through www.ecg-imaging.org.

3.3 Variability of the inverse solution within and between

lead sets

Adapted from: J. Stoks, B.D. van Rees, S.A. Groeneveld, D.J.M. Schipaanboord, L. Blom, R.J. Hassink, M.J.M. Cluitmans, R. Peeters and P.G.A. Volders. *Variability of Electrocardiographic Imaging Within and Between Leadsets. Computing in Cardiology. 2020; 47. DOI: 10.22489/CinC.2020.097*

3.3.1 Introduction

The stability of the inverse solution provided by ECGI remains largely unknown. For example, this holds true for inverse reconstruction when using reduced lead sets and when studying stable beat-to-beat characteristics. To improve assessment of this stability, we compared epicardial potential maps and isochrones for different beats and for two different lead sets. In-vivo recordings from four patients were used. Quantitative differences between inverse solutions and the reasons behind these differences are evaluated.

Methodology was similar to that of **Chapter 5**. For the exact methodology, see our full paper (83). Two separate body-surface potential maps (BSPMs) were simultaneously recorded using two independent lead sets at the same time: a 184-channel lead set and a 64-channel lead set (see **Figure 3.5**).

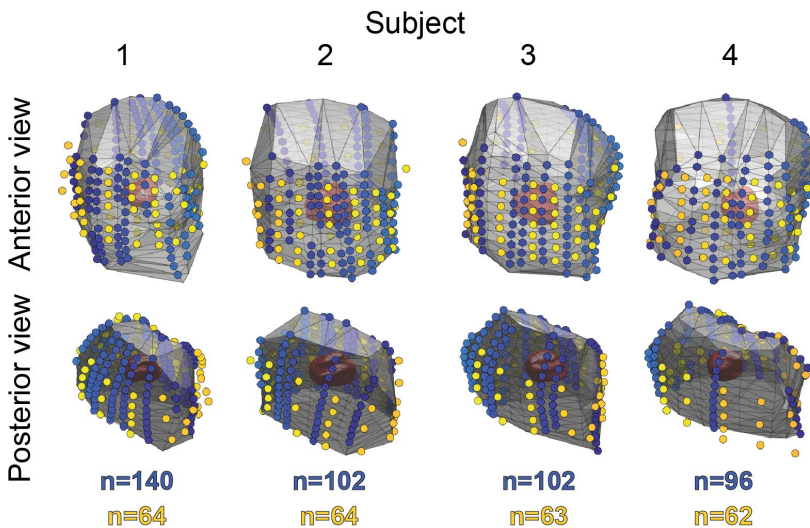


Figure 3.5: Distributions of electrodes for each patient and each lead set. 184-Lead set shown in purple, 64-lead set shown in yellow. Electrodes are shown only if they had sufficient signal quality for more than half of the beats, for each subject. The number of electrodes for each setup is noted as n.

The number of electrodes for each setup is noted as n.). Both were recorded with an acquisition system of the same manufacturer (BioSemi, Amsterdam, the Netherlands), with a 2048-Hz sampling rate.

3.3.2 Comparison of inverse solutions

Several comparisons of the inverse solution were made between and within the two lead sets: 1) consecutive beats with a similar RR interval were compared to each other within one lead set, and 2) single beats were compared between both lead sets. These comparisons were made for sinus beats, ventricular extrasystoles and sinus beats after ventricular extrasystoles. Comparisons were made quantitatively on a node-by-node basis on the epicardium. Results are expressed as absolute differences in AT, RT, and correlation coefficients of electrograms during the QRS complex and STT segment (CC_{QRS} and CC_{STT} , respectively). To calculate T-wave amplitude and noise level for each node, each electrogram was first normalized to the highest epicardial R-peak of the same beat. T-wave amplitude was subsequently calculated as the height of the peak with the largest absolute voltage within the STT segment. Noise level was calculated for each node, as the average squared amplitude of the signal between the end of the QRS complex and the start of the T-wave, divided by the absolute height of the corresponding R-peak.

3.3.3 Intra-lead set beat-to-beat variability

For both lead sets, beat-to-beat variability was addressed for consecutive sinus beats. The body-surface electrodes for each lead set and each patient are shown in **Figure 3.5**, showing the number of electrodes in the 184-setup was varied from 96 to 140 throughout the measurements, shifting from homogeneous coverage to a primary anterior coverage.

In total, 28 pairs of consecutive sinus beats were analyzed for each lead set. Beat-to-beat AT differences, RT differences, CC_{QRS} and CC_{STT} on a node-by-node basis on the epicardium are shown in **Table 3.1**. Results for the 64-lead set are averaged in this Table, since these were very similar between subjects. **Table 3.1** indicates that beat-to-beat inverse solutions were similar within subjects, with a median CC_{QRS} and CC_{STT} close to 1, and median beat-to-beat AT differences close to 1 ms. Beat-to-beat RT differences were much higher than those of AT. Distributions of CC_{STT} and RT differences were skewed. This indicates that most inverse solutions contained small beat-to-beat RT differences on average, but local differences may be higher.

	Absolute AT diff. (ms)	Absolute RT diff. (ms)	CC _{QRS}	CC _{STT}
Subject 1 184- Lead set	1.1 (0.5-1.9)	12.3 (5.1-26.7)	1 (0.99-1.00)	0.94 (0.79- 0.98)
Subject 2 184- Lead set	1.5 (0.6-3.4)	11.2 (4.5-22.7)	1.00 (0.99- 1.00)	0.96 (0.89- 0.98)
Subject 3 184- Lead set	1.9 (0.7-3.5)	10.9 (4.2-24.3)	0.99 (0.98- 1.00)	0.93 (0.62- 0.99)
Subject 4 184- Lead set	1.6 (0.6-4.2)	12.9 (5.4-27.4)	0.97 (0.71- 0.99)	0.88 (0.53- 0.97)
Avg. 64-Lead set	1.4 (0.5-2.5)	10.1 (4.2-21.7)	0.99 (0.97- 1.00)	0.94 (0.78- 0.98)

Table 3.1: Absolute beat-to-beat AT and RT differences, CC_{QRS} and CC_{STT} within a lead set, for each subject. Bottom row shows average results for the 64-lead set. Diff: difference. Values shown as median (Q1-Q3).

3.3.4 Inter-lead set variability

Qualitatively, BSPMs of both lead sets agreed well (data not shown). Inverse solutions were compared between both lead sets. In total, 83 beats were analyzed, of which 73 sinus beats, 6 ventricular extrasystoles and 4 sinus beats after ventricular extrasystoles. Statistics of differences between lead sets are shown in **Table 3.2**. Median differences between lead sets were relatively small, suggesting a high level of agreement overall. However, distributions were skewed, meaning that regional differences in the inverse solution between both lead sets can be considerably large, especially for repolarization. Consequently, clinical interpretation of the inverse solutions of two different lead sets could vary locally.

Differences between two lead sets were larger than beat-to-beat differences within a lead set, for all outcome measures except RT which always showed large variation. A direct comparison of intra-lead set beat-to-beat variability and inter-lead set variability for each heart rhythm is shown in **Figure 3.6**. Inter-lead set differences in the inverse solution were largest for VES, and smallest for SR.

RT differences as a function of T-wave amplitude and noise level are shown in **Figure 3.7B**, several other factors of influence on RT differences between lead sets are shown: 1) flat epicardial T-waves or high noise levels, 2) slight differences in upslope, or 3) areas of T-wave polarity switch.

184-Lead set vs. 64-Lead set	Absolute AT diff. (ms)	Absolute RT diff. (ms)	CC _{QRS}	CC _{STT}
Subject 1	3.6 (1.6-10.4)	16.9 (6.4-37.9)	0.87 (0.30-0.97)	0.84 (0.44-0.97)
Subject 2	5.2 (2.3-9.1)	10.3 (4.5-21.8)	0.93 (0.82-0.98)	0.96 (0.85-0.99)
Subject 3	4.5 (2.1-8.9)	14.2 (5.8-30.6)	0.91 (0.72-0.97)	0.87 (0.43-0.97)
Subject 4	2.1 (0.8-5.5)	9.3 (3.2-22.6)	0.97 (0.71-0.99)	0.91 (0.74-0.97)

Table 3.2: Absolute AT and RT differences, CC_{QRS} and CC_{STT} between different lead sets, for each subject. Diff: difference. Values shown as median (Q1-Q3).

Importantly, the amount and distribution of electrodes in the 184-lead set differed considerably and only four patients were analyzed. Consequently, this study does not provide a final answer to the comparison between the two lead sets, but rather is a first gross quantification of differences, while the factors that contribute to the observed differences between both lead sets need to be further elucidated.

As previously shown (51), the potential-based formulation of ECGI is subject to possible spatial displacement of electrograms on the cardiac surface. This spatial displacement is currently not predictable, and to the best of our knowledge it cannot be corrected for. It may also differ between beats and lead sets. In this study, comparisons were made on a node-by-node-basis, not taking a possible displacement into account. A more advanced analysis method, which takes the possible spatial displacement into account might be more suitable and may render more positive results. This may especially influence the inter-lead set or intra-lead set differences in RT caused by a high RT gradient or T-wave polarity switch. Such spatial displacement may not be critical for specific clinical applications (e.g., detection of the presence repolarization abnormalities may be more important than their exact localization).

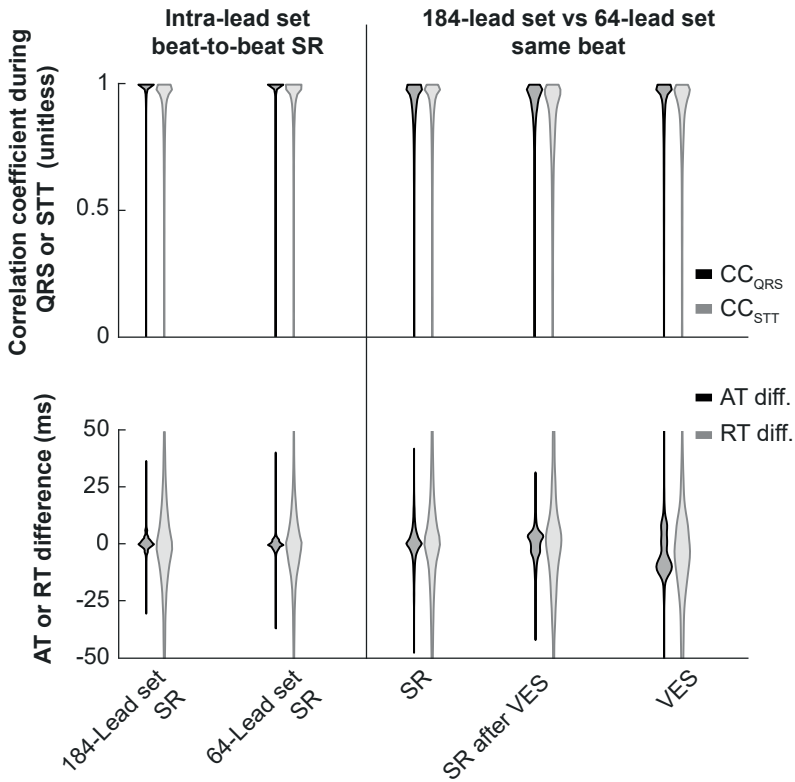


Figure 3.6: Violin plots of differences (diff.) in the inverse solution within and between lead sets. **Left:** intra-lead set beat-to-beat differences in the inverse solution during sinus rhythm (SR), **right:** inter-lead set differences (184-lead set vs 64-lead set) in the inverse solution of the same beat during SR, ventricular extrasystole (VES), or SR after VES. **Top:** correlation coefficient between epicardial electrograms during QRS complex or STT segment. **Bottom:** differences in activation times (ATs) or recovery times (RTs).

Our results are in accordance with an earlier study by Cluitmans et al. (84), in which the remaining 59 to 80 electrodes out of 169 produced similar median correlation coefficients to the ground truth as a full setup using 168 electrodes, although the first quartile of differences found in that study was considerably lower.

The goal of the current study was to investigate variability and to understand differences, which could ultimately benefit interpretation of inverse solutions and the development of reduced-lead sets. Some specific reduced-lead sets have previously proven to be of sufficient accuracy and quality, especially when the optimal electrode placement was produced by an iterative algorithm (45). In-vivo validation of such an optimal reduced-lead set, incorporating both activation and recovery, may significantly reduce procedural time and the potential of ECGI

to be incorporated in clinical practice.

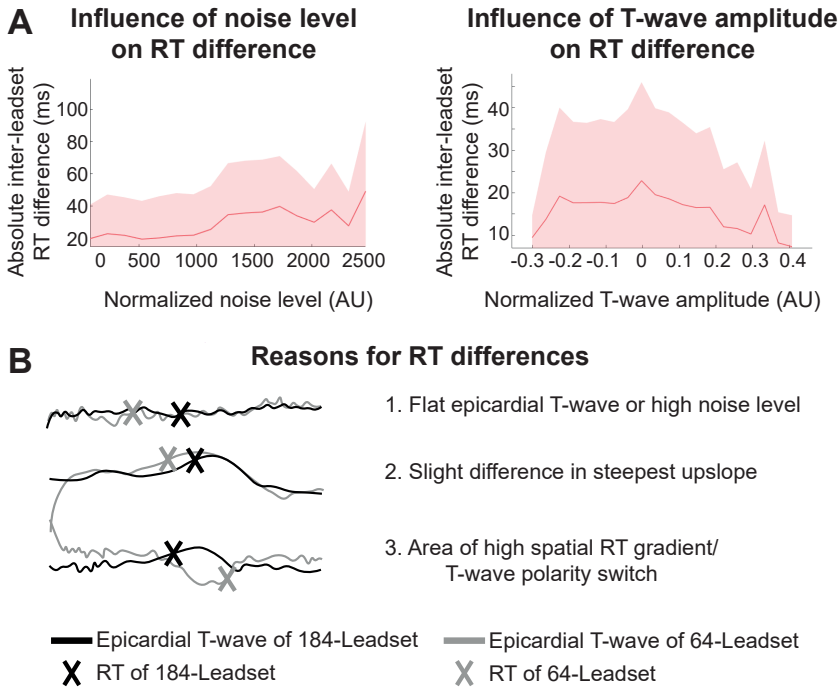


Figure 3.7: Reasons for RT differences between lead sets. **A:** effect of normalized noise level and T-wave amplitude (arbitrary units) on absolute RT difference between both lead sets. **B:** qualitative factors of influence for large RT differences: 1) flat epicardial T-waves or high noise levels, 2) slight differences in upslope, or 3) Areas of T-wave polarity switch.

3.3.5 Summary and interpretation

Inter-lead set differences in the inverse solution were generally low even though they exceeded beat-to-beat variations within one lead set, especially on a regional level. However, this does not hold for inter-lead set RTs differences that were comparable to beat-to-beat variations in RT. Differences in RTs between beats or lead sets could partially be explained through low T-wave amplitudes and high levels of noise, which suggests that RT determination may require more advanced methods in these cases. These findings increase our understanding of the consequences of electrode placement on the inverse solution, as well as our understanding of the intricacies of RT estimation in ECGI. We did not investigate spatial displacement of reconstructed electrograms, which may have limited consequences for clinical application but has large impact on our node-by-node comparisons. As such, this study has identified a lower bound on the quality of reconstruction between systems, and has determined that causes of that lower limit lie in noisy and low-amplitude signals.

3.4 The effect of using a systolic or diastolic geometry

Adapted from: J. Stoks, M.J.M. Cluitmans, R. Peeters and P.G.A. Volders. The Influence of Using a Static Diastolic Geometry in ECG Imaging. Computing in Cardiology. 2019; 46. DOI: 10.22489/CinC.2019.266

3.4.1 Introduction

The heart is a contracting and moving organ. The systolic and diastolic states are the two most extreme phases of the mechanically-moving heart. However, one of the common approximations when performing ECGI is that the cardiac geometry is in a mechanically static (non-moving) state, usually taken from the diastolic phase of the cardiac cycle, see **Section 2.3**. To investigate and quantify the influence of this approximation, we compared epicardial potential maps and isochrones on systolic and diastolic geometries for four subjects without structural heart disease. ECGI methodology was similar as described in **Chapter 5** of this thesis. For the exact methodology, see our full paper (85).

3.4.2 Systolic and diastolic geometries

The systolic and diastolic phases of the ventricular epicardium were segmented through automated software (Philips Intellispace version 10). Geometries were subsequently reduced to 2483 ± 26 nodes. The average node-to-node distance in one geometry was 3.8 ± 0.3 mm.

3.4.3 Differences in inverse solutions

We compared the inverse solutions of two sinus beats for each of the four subjects. Overall, there was a good correlation between activation times ($r_{AT}=0.78$ (interquartile range (IQR) 0.75-0.89)) and recovery times ($r_{RT}=0.74$ (0.62-0.91)) of systolic vs. diastolic geometries, see **Figure 3.8**. Correlation coefficients of epicardial UEG QRS complexes (CC_{QRS}) and STT segments (CC_{STT}) of systolic vs. diastolic geometries were 0.99 (0.95-1.00) for both. Differences in RT seemed to occur mostly at the inferior side, see **Figure 3.9**. Although global correlation of ATs/RTs and correlation coefficients between both geometries was relatively high, clinical interpretation could differ. For example, some pronounced areas of early or late repolarization in one geometry disappeared in the other. However, upon closer inspection, these differences appeared to be arising mostly in areas of flat T-waves, which rendered accurate RT determination in the local electrogram difficult. These T-waves were often close to high spatial RT gradients, indicating that a small shift in RT gradient may occur between systolic and diastolic geometry. The influence of using either a systolic or diastolic geometry on RT gradients should be further investigated in future work.

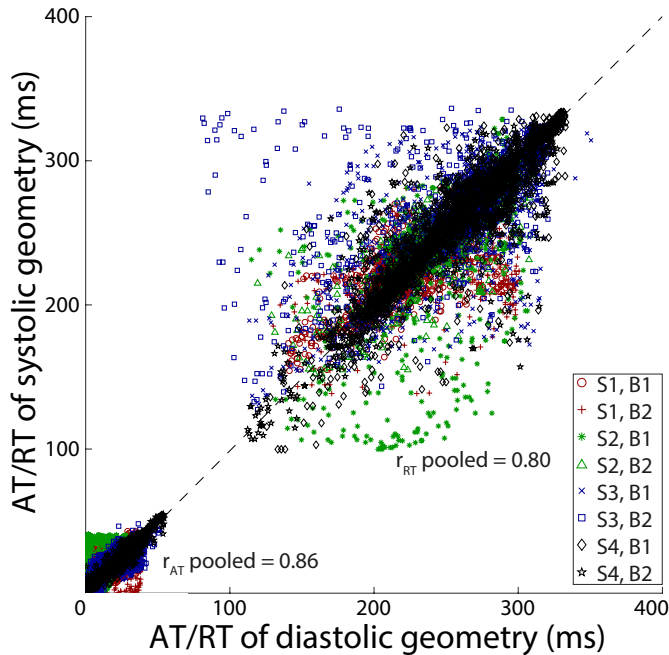


Figure 3.8: Comparison of ATs and RTs of diastolic vs. systolic geometries with ECGI. S: Subject. B: Beat.

3.4.4 Linear movement

Overall, the median linear movement from the systolic to diastolic state of the different nodes on the heart when averaged for all individuals was 4.0 (IQR 2.6-6.1) mm. The valvular plane was displaced the most during the systolic vs. diastolic phase: (5.9-9.5) mm, in contrast to 3.6 (2.4-5.1) mm for the non-valvular nodes. This can be related to qualitative observations from cardiac magnetic resonance imaging (CMR) and the echocardiogram: during systole, mostly the endocardial wall and the valvular plane move.

3.4.5 The influence of linear movement of the epicardium on the inverse solution

Correlations of absolute linear movement vs. AT and RT differences, CC_{QRS} and CC_{STT} were also addressed. Overall, these correlations were low ($r=0.08$ (0.06-0.13), 0.05 (0.03-0.08), 0.06 (0.01-0.17) and 0.09 (0.07-0.12), respectively), meaning that linear movement of nodes and differences in inverse solution appear uncorrelated. Furthermore, correlation of distance to the apex (as surrogate for rotational movement) vs. AT/RT differences and CC_{QRS} and CC_{STT} was addressed. Overall, these correlations were low ($r=0.14$ (0.11-0.31), 0.06 (0.01-0.14), 0.04 (0.03-0.11) and 0.12 (0.04-0.17), respectively), meaning that longitudinal distance to the apex of nodes (and thus rotational movement) and differences in epicardial potential maps and isochrones seem uncorrelated. This

means that neither linear nor rotational movement contribute substantially to differences in epicardial potential maps and isochrones.

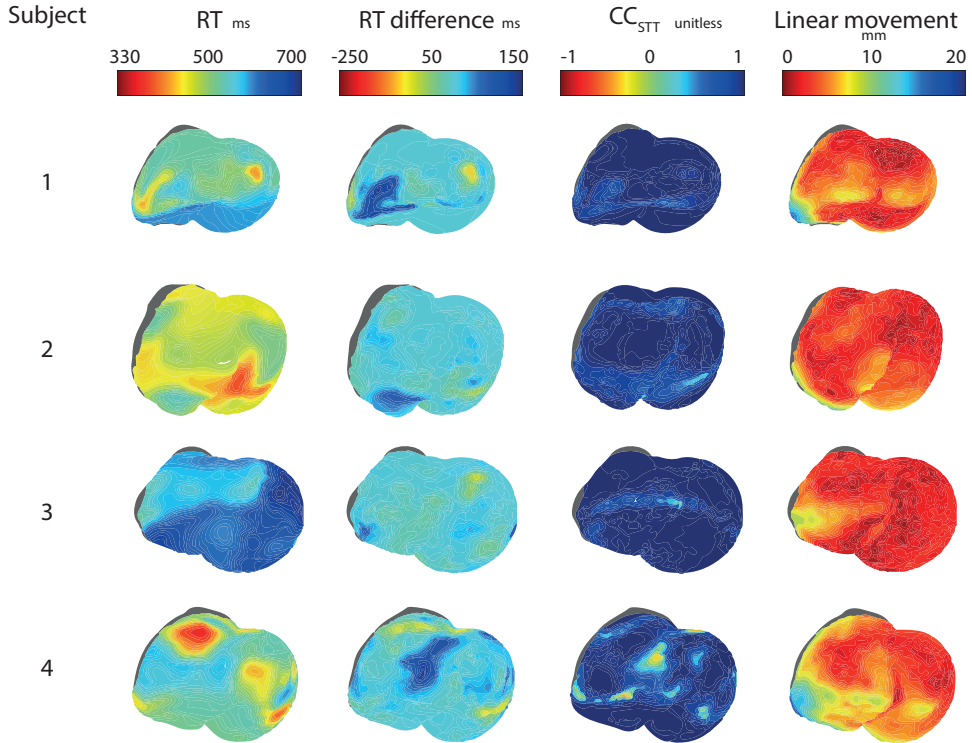


Figure 3.9: Diastolic geometries for the four individuals. Numbers denote subjects. **Column 1:** Recovery time (RT); **Column 2:** Difference between diastolic RT and the RT of the nearest neighbor on systolic geometries; **Column 3:** CC_{STT} : correlation coefficient during STT-segment; **Column 4:** linear distance of each diastolic node to its nearest neighbor on the systolic geometry. LV: left ventricle. RV: right ventricle. A: Apex.

3.4.6 Other studies investigating the effect of movement on the inverse solution

These results are in contrast with our previous experimental study where we compared the movement of implanted electrodes to the reconstruction quality (51). In that study, electrograms from epicardial electrodes which moved more, seemed to have lower correlation to inverse reconstruction at the corresponding ECGI node. However, that study was not designed to systematically study mechanical abnormalities and could analyze only one beat.

Tate et al. (44) quantitatively addressed the effect of segmentation differences in ECGI, and found that reconstruction differences on the epicardial surface mostly correlated with segmentation error, in contrast to our study, in which location differences between both geometries hardly correlated with reconstruction differences. The location of largest variance was also different: Tate et al.

found that this was highest on the anterior surface, while this was the inferior surface in our study (44). The difference in results might be due to the use of the spatiotemporal method in our study, the electrophysiological rhythm (RV and LV pacing produced the greatest effect in their study), the different outcome measures and the geometry of the heart itself.

The Tikhonov parameter used to regularize the inverse solution was not kept the same between systolic and diastolic geometries in this study. One might argue that the true differences in epicardial potential maps and isochrones would be reflected by fixing this parameter when calculating the inverse solution. Since the Tikhonov parameter is directly dependent on the used geometry, we did not fix it. Moreover, the ratio between the Tikhonov parameter between both geometries was 1.4 ± 0.3 on average, indicating that this was only of minor influence.

Even though we did assess the rotational movement of the heart, it was not measured directly. MRI may be more suitable to accurately track the different regions and nodes of the heart throughout the cardiac cycle. However, because of the very poor correlations between the distance from the apex and the inverse solution differences, we do not expect this to affect the corresponding results to a major extent.

Recommendations for future work include using MRI to track tissue movement more accurately on a point-to-point basis, including a larger and more heterogeneous patient cohort and studying the effects on ventricular extrasystoles and their mechanical correlates.

Importantly, although it may appear that ECGI's reconstruction accuracy is not much influenced by the approximation of a mechanically non-moving heart, mechanical movement and electromechanical feedback are key elements in understanding arrhythmogenesis.

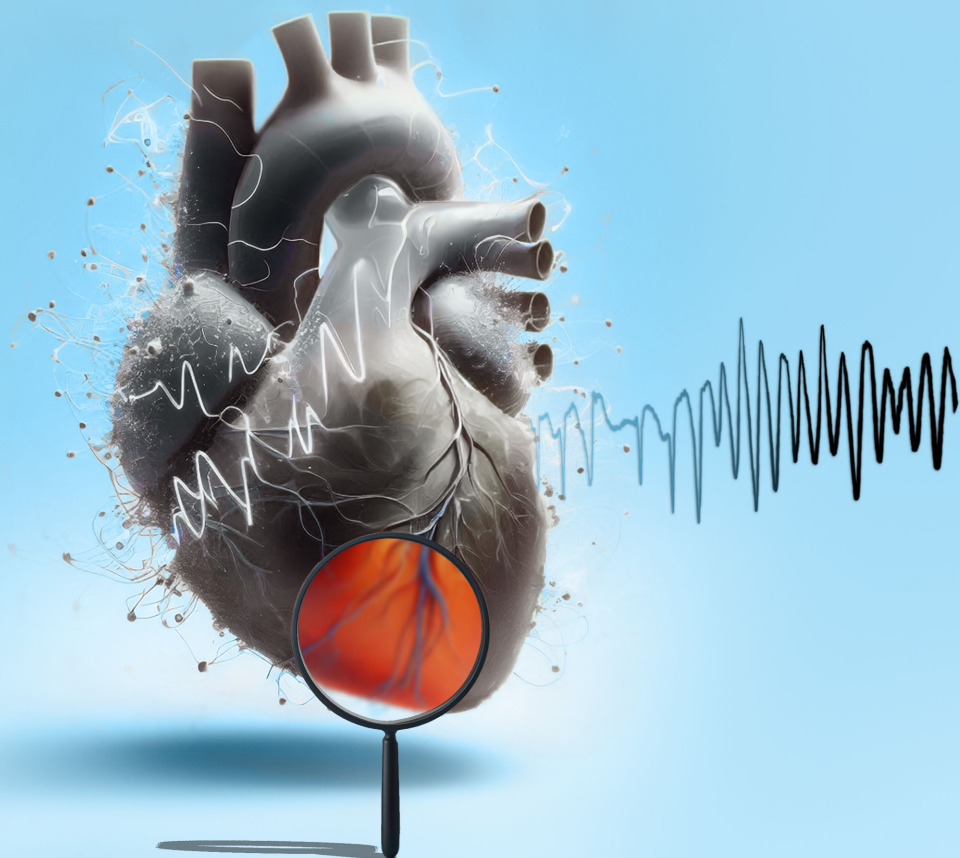
3.4.7 Summary and interpretation

These quantitative findings may further help in interpreting ECGI reconstructions in this thesis and in the literature, because of our new and more accurate quantification of possible errors caused by the approximation of a mechanically non-moving heart. For example, some pronounced areas of early or late repolarization in one geometry disappear in the other. However, these differences appeared to be arising mostly in areas of flat T-waves (as in **Section 3.3**), which makes it difficult to accurately determine RT of the local electrogram. Importantly, mechanical movement and electromechanical feedback are key elements in understanding arrhythmogenesis.

3.5 Conclusions

The findings of this Chapter provide insights into the interpretation of the potential-based formulation of ECGI in general and the specific findings of this thesis. **Section 3.3** and **Section 3.4** demonstrate that the results and interpretation of the inverse solution can vary depending on the specific implementation. Notably, the determination of recovery time (RT) presents challenges in certain areas, resulting in larger variations within or between implementations compared to activation time (AT). Consequently, results obtained from different implementations may not be comparable in an absolute sense. These findings reinforce the importance, as discussed in **Chapter 2**, of further standardizing ECGI in terms of software and hardware implementation.

As highlighted in multiple validation studies (see **Section 2.4**), ECGI generally offers a spatial localization error of approximately 1 cm. This spatial accuracy may extend to other outcome measures, such as a shift of 1-2 cm between ECGI-reconstructed electrograms and invasive electrograms (47,51), which affected our results but was not factored into our analyses. It is essential for end users to recognize that results obtained by ECGI should not be considered as a gold standard, much like other clinical modalities (e.g., activation wavefront direction affecting bipolar voltage in EAM, the accuracy of exercise stress testing for diagnosing myocardial ischemia, or the uncertainty of LVEF determination by echocardiogram). This requires careful consideration in clinical procedures. Different ECGI implementations may be better suited for specific objectives. Lastly, the integration of ECGI with other modalities can provide complementary information.



CHAPTER 4

Understanding Repolarization in the Intracardiac Unipolar Electrogram: A Long-Lasting Controversy Revisited

J. Stoks, L.R. Bear, J. Vijgen, P. Dendale, R. Peeters,
P.G.A. Volders[†] and M.J.M. Cluitmans[†]

[†] These authors have contributed equally to this work

Frontiers in Physiology. 2023; 14.
DOI: 10.3389/fphys.2023.1158003

Abstract

Background: The optimal way to determine repolarization time (RT) from the intracardiac unipolar electrogram (UEG) has been a topic of debate for decades. RT is typically determined by either the Wyatt method or the “alternative method,” which both consider UEG T-wave slope, but differently.

Objective: To determine the optimal method to measure RT on the UEG.

Methods: Seven pig hearts surrounded by an epicardial sock with 100 electrodes were Langendorff-perfused with selective cannulation of the left anterior descending (LAD) coronary artery and submersed in a torso-shaped tank containing 256 electrodes on the torso surface. Repolarization was prolonged in the non-LAD-regions by infusing dofetilide and shortened in the LAD-region using pinacidil. RT was determined by the Wyatt (t_{Wyatt}) and alternative (t_{Alt}) methods, in both invasive (recorded with epicardial electrodes) and in non-invasive UEGs (reconstructed with electrocardiographic imaging). t_{Wyatt} and t_{Alt} were compared to local effective refractory period (ERP).

Results: With contact mapping, mean absolute error (MAE) of t_{Wyatt} and t_{Alt} vs. ERP were 21 ms and 71 ms, respectively. Positive T-waves typically had an earlier ERP than negative T-waves, in line with theory. t_{Wyatt} – but not t_{Alt} – shortened by local infusion of pinacidil. Similar results were found for the non-invasive UEGs (MAE of t_{Wyatt} and t_{Alt} vs. ERP were 30 ms and 92 ms, respectively).

Conclusion: The Wyatt method is the most accurate to determine RT from (non) invasive UEGs, based on novel and historical analyses. Using it to determine RT could unify and facilitate repolarization assessment and amplify its role in cardiac electrophysiology.

4.1 Introduction

The intracardiac unipolar electrogram (UEG) is a powerful tool to assess cardiac electrophysiology. It reflects the potential difference between two electrodes in the extracellular space (86) (Figure 4.1), and in contrast to its bipolar counterpart, measures electrical activity irrespective of direction. The UEG is routinely employed in the clinical electrophysiology laboratory and basic science. There is good understanding of how electrical activation of cardiac tissue is reflected in the UEG. Conversely, a full appreciation of how repolarization manifests on the UEG remains elusive and has been a topic of debate for decades. This is mainly due to the inherently more complex process of repolarization and inconsistencies in experimental results. Repolarization abnormalities play an important role in arrhythmogenesis, e.g. in long-QT and Brugada syndromes, structural cardiomyopathies and idiopathic ventricular fibrillation (72,74,87). Repolarization heterogeneity can lead to unidirectional conduction block and reentry (74). A unified assessment of repolarization on the UEG could improve our basic and clinical understanding of repolarization in many aspects of electrophysiology, and may increase its role of (non)invasive arrhythmia substrate mapping. Here, we provide novel evidence – and a thorough analysis of previous data – that allows accurate assessment of repolarization from the UEG.

4.1.1 Importance of activation and repolarization assessment

Interest in the UEG focuses on the instants of local electrical activation and recovery, and different methods have been proposed to determine the corresponding activation time (AT) and recovery time (RT) from a UEG (30,86,88–99). It is widely accepted that the steepest downslope of the QRS-complex of the intracardiac UEG coincides with the moment of local activation, which was first validated in 1954 (97). Assessing AT from the UEG is well-established in arrhythmia studies and is routinely used to determine the origin of premature beats, regions with conduction slowing or low electrical amplitudes, or the exit of a ventricular tachycardia. For a more complete overview of the role of activation mapping in the intracardiac UEG, we refer the reader to (100).

The mechanistic role of repolarization in cardiac (patho)physiology is also well understood from experimental studies. Local repolarization heterogeneities (reflected by RT gradients or dispersion) can create a substrate for unidirectional block, a requirement for reentry (74). Understanding how to determine RTs from UEGs is crucial to fully comprehend arrhythmia substrates. However, the determination of RT from the UEG is more complex than that of AT, because repolarization is not a propagating wavefront, but a more localized phenomenon that is less dependent on the electrophysiological state of neighbouring myocardium.

4.1.2 Common methods to determine repolarization time

Investigators have predominantly used two distinct methods to determine RT: the Wyatt method and the “alternative” method. The Wyatt method, named after its inventor (88), defines the end of repolarization as the moment of steepest upslope of the T-wave in the UEG, irrespective of T-wave polarity (Figure 4.2A). Many investigators have accepted that from a theoretical point of view, the steepest upslope of the UEG T-wave coincides with local RT (86,93,99,101–103). However, some investigators are not convinced that the Wyatt method is optimal for RT determination, and others provide analyses based on both methods due to an apparent lack of consensus.

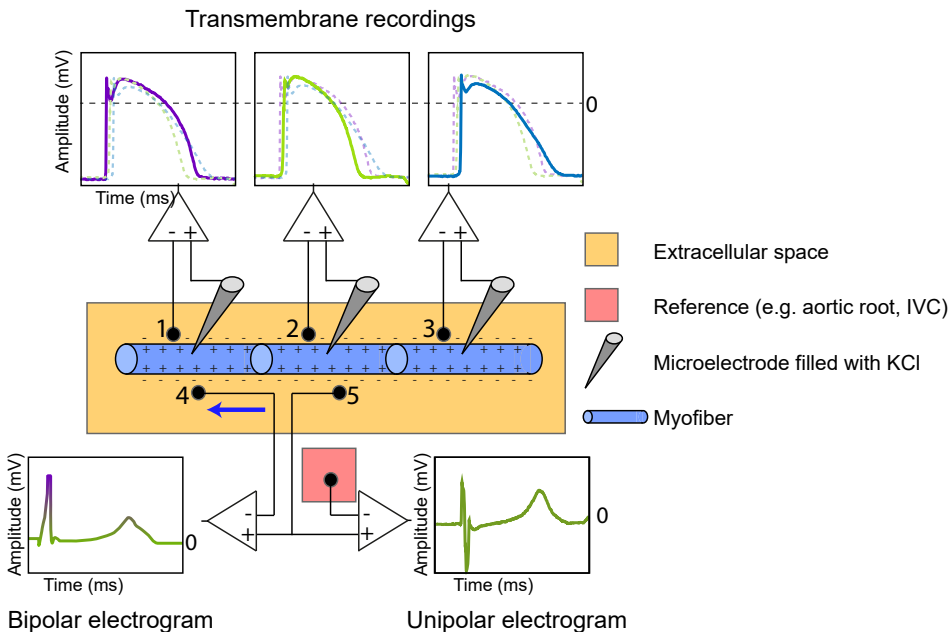


Figure 4.1: Measurement of the cardiac transmembrane action potential (TMP), bipolar electrogram and unipolar electrogram (UEG). The TMP is recorded by inserting an Ag/AgCl electrode filled with KCl in the intracellular space and using the extracellular potential as a reference. The number of myofibers is reduced for illustration purposes. The extracellular UEG is commonly referenced against electrically inactive tissue (e.g., aortic root, inferior vena cava (IVC)). The bipolar electrogram, measuring current in only one direction (from anode to cathode, see blue arrow), is equal to the subtraction of the UEG measured at location 4 from the UEG measured at location 5.

Here, we present novel experimental results comparing the Wyatt and alternative methods directly to the effective refractory period (ERP). ERP is an important measure for cardiac arrhythmogenesis as it directly relates to the potential occurrence of unidirectional block and reentry. We perform this comparison through contact mapping in the setting of repolarization-altering drugs, and we explain these results by addressing theoretical models.

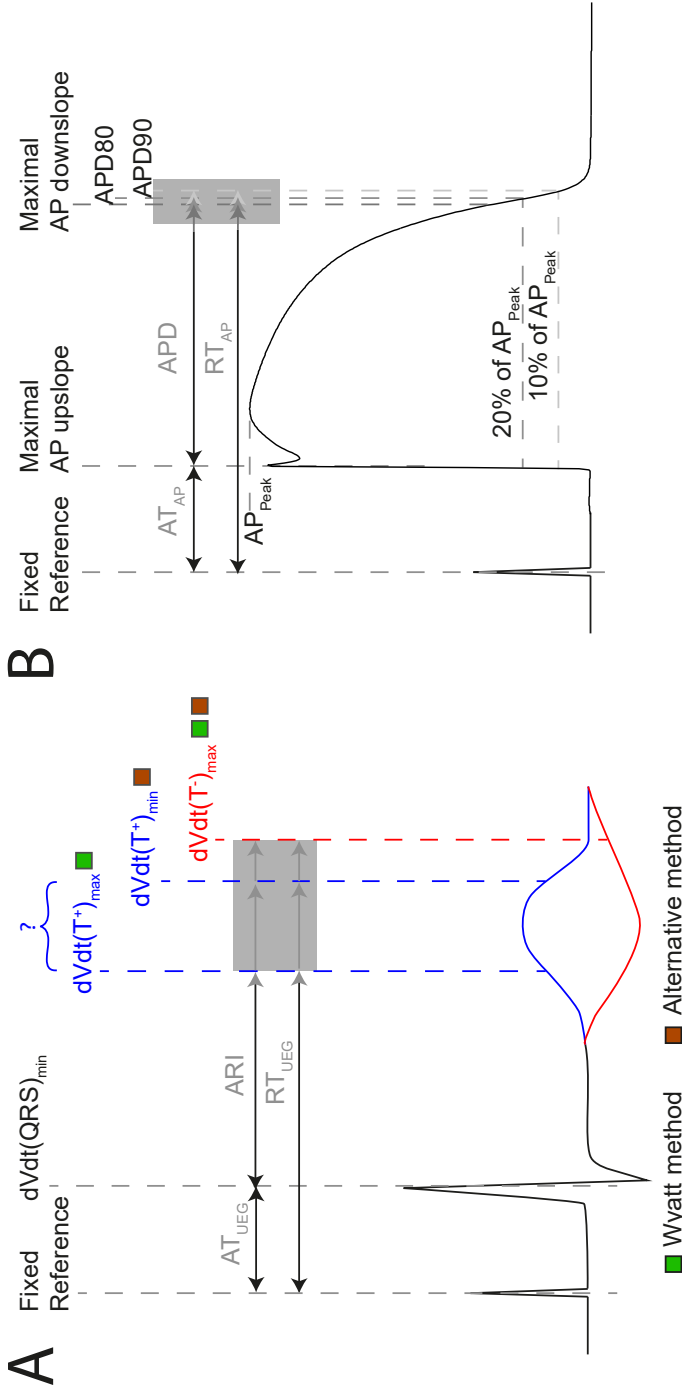


Figure 4.2: Definitions of terms related to the intracardiac UEG (A) and action potential (B). **A:** AT in the UEG is measured from a fixed reference point (e.g., a common pacing spike) until the steepest downslope of the local QRS complex. RT is measured from the same reference, but its end is defined differently throughout literature. The activation-recovery interval (ARI) is equal to the subtraction of AT from RT. The Wyatt method of determining RT and ARI uses the maximum upslope of the UEG T-wave, regardless of polarity. The alternative method uses the maximum downslope of the T-wave for positive T-waves, and the maximum upslope for negative T-waves. **B:** In the action potential, AT is defined uniformly: from fixed reference point until the steepest upslope of the action potential (AP). Action potential duration should reflect the same interval as the ARI, but is defined heterogeneously throughout literature (e.g., as the point in time where the cell has repolarized for 80% (APD_{80}), for 90% (APD_{90}), or the TMP reached its maximum downslope). RT in the action potential is measured from the same reference as AT, but its end has been defined differently (analogous to APD definition).

Moreover, because noninvasive mapping is increasingly being used (see **Chapter 2**) and some authors using noninvasive mapping are still in doubt about which method to use, we also investigated how to most accurately determine RT from UEGs from noninvasive electrocardiographic imaging (ECGI). We put our experimental results into historical context, by addressing historical theoretical models and experimental results. Finally, we propose consensus on the optimal approach to determine local RT from the UEG.

4.2 Methods

4.2.1 Experimental protocol and data analysis

Procurement was approved by the local ethics committee of Bordeaux CEEA50 and the National Biomedical Agency of France, in accordance with the Directive 2010/63/EU of the European Parliament. Seven male pig hearts were explanted and put on a Langendorff setup with retrograde perfusion of the aorta. A separate cannulation of the left anterior descending (LAD) artery was performed after its ligation, which allowed separate infusion of the LAD-perfused region and the remaining ('aorta-perfused') myocardium (**Figure 4.3A**). Hearts were perfused with a 1:9 mixture of blood and Tyrode's solution, oxygenated with 95%/5% O₂/CO₂ (pH 7.4, 37°C). A rigid electrode sock with 100 electrodes (1.8 mm diameter) was placed around the ventricles. The heart was then put in a torso tank as described previously(104), which provided 256 body-surface electrocardiograms, recorded simultaneously with the sock EGMs (both with a 2048Hz sampling frequency).

A drug-infusion protocol was used to create RT differences using dofetilide at 125 nmol/L and 250 nmol/L, typically in the aorta-perfused region (i.e., everywhere except LAD), and/or pinacidil at 17.5 μmol/L and 35 μmol/L, typically in the LAD. This resulted in regions with pronounced RT prolongation (non-LAD region) and RT shortening (LAD region). **Supplementary Table 4.1** shows which drugs were used for each experiment.

A pair of bipolar pacing electrodes on the atria was used to provide a baseline paced rhythm ("S1 pacing"). After a train of eight atrial S1 beats at 500/600/650ms, a single ventricular epicardial extrastimulus was provided ("decremental S2 pacing") at one of three available pairs of bipolar pacing electrodes: the left, right and inferior side of the heart. Near these pacing locations, electrograms were measured prior to measuring the so-called atrial-paced effective refractory period (A-pace ERP). First, the longest interval from atrial S1 to ventricular S2 was determined where the S2 stimulus was not captured. Under that condition, the A-pace ERP was defined as the interval from the body-surface R-peak to the ventricular S2 stimulus, reflecting the moment of local refractoriness at the S2 location with respect to a common, global reference. This was tested with 10-ms decremental intervals. When capture was detected, 1-ms intervals were used to determine the A-pace ERP with higher resolution. AV-conduction was maintained throughout the experiment. Compared to ERP metrics where both

S1 and S2 are given on the same (ventricular) location, our A-pace ERP metric captures a more 'natural' condition where a ventricular beat may interact with a preceding sinus beat.

Epicardial contact UEGs were filtered by removing 50Hz powerline noise, and by means of linear detrending. RT was determined by the Wyatt method (t_{Wyatt}) and alternative method (t_{Alt}) (Figure 4.2A). Electrograms containing too much noise or ST-segment elevation were disregarded. A-pace ERP was compared to both t_{Wyatt} and t_{Alt} at the electrodes nearest to the pacing electrodes. Metrics were determined relative to a common reference: the R-peak from the body-surface electrocardiogram.

For ECGI, the same experimental protocol was used. Additionally, a coronary angiography with contrast medium was used to obtain the heart geometry, using fluoroscopy. Body-surface electrograms were linearly detrended in combination with a 125Hz low-pass filter before ECGI was applied. Finally, a potential-based formulation of noninvasive ECGI was used to reconstruct local epicardial UEGs through previously-validated methods (51). t_{Wyatt} and t_{Alt} of noninvasive UEGs were also compared to A-pace ERP.

4.2.2 Statistics

Analyses were performed for both contact UEGs and ECGI. Linear regression was applied with A-pace ERP as the independent variable, and t_{Wyatt} or t_{Alt} as dependent variable. F-tests were used to analyze differences between linear regressions. Kolmogorov-Smirnov testing was used to test for normality. For remaining analyses, when comparing two groups, (non-normally distributed) data were compared using a two-tailed Mann-Whitney-U test. A Kruskal-Wallis test was used for comparing three groups. All tests, with exception of investigating the effect of repolarization-altering drugs vs. baseline, were unpaired and two-tailed. When both drugs were applied simultaneously, the LAD-region and non-LAD region were tested separately from each other. $P < 0.01$ was considered statistically significant.

4.3 Results

With contact mapping, most electrodes were positioned in the early repolarizing areas: 77% of T-waves were positive, 12% were biphasic and 12% were negative. Examples of RT isochrones as determined by both methods and corresponding electrograms before and after drug infusion are shown in Figure 4.3B-C. Clearly, t_{Wyatt} -but not t_{Alt} -shortened in the region infused with repolarization-shortening pinacidil. Supplementary Table 4.2 and Supplementary Table 4.3 summarize the effect of drugs on t_{Wyatt} and t_{Alt} over all experiments. t_{Wyatt} and t_{Alt} both prolonged when repolarization-prolonging dofetilide was infused locally, as mostly negative UEG T-waves were affected (Figure 4.4). When repolarization-shortening pinacidil was infused locally, t_{Alt} often incorrectly prolonged, while t_{Wyatt} shortened, as mostly positive UEG T-waves were affected. When pinacidil

was infused throughout the entire heart, both t_{Wyatt} and t_{Alt} shortened, due to a leftward shift of all UEG T-waves.

Mean absolute errors (MAE) of t_{Wyatt} and t_{Alt} relative to A-pace ERP were 21ms and 71ms, respectively ($P < 0.001$). For positive UEG T-waves only, MAE was 20ms for t_{Wyatt} and 78ms for t_{Alt} ($P < 0.001$). Linear regression using t_{Wyatt} rendered $RT_{\text{Wyatt}} = 0.79 \cdot \text{A-pace ERP} + 42$ ($r = 0.92$), while linear regression using t_{Alt} rendered $RT_{\text{Alt}} = 0.42 \cdot \text{A-pace ERP} + 168$ ($r = 0.64$) ($P < 0.001$ comparing linear regressions) (**Figure 4.3D**). Positive T-waves typically had an earlier A-pace ERP than negative ones, with biphasic T-waves in between ($P < 0.001$) (**Figure 4.3E**). Results of consecutive beats were generally consistent, although the pinpointing of RT from the UEG may be sensitive to slight changes in upslope (for an example, see **Supplementary Figure 4.2**).

Similar results were found for the noninvasive UEGs mapped with ECGI (**Figure 4.5**). Reconstructed UEG T-waves (closest to pacing electrodes) were compared to the A-pace ERP. MAE of t_{Wyatt} and t_{Alt} relative to A-pace ERP were 30ms and 92ms, respectively ($P < 0.001$). The shortening of t_{Wyatt} caused by pinacidil was much more in line with invasive measurements than the shortening of t_{Alt} (**Figure 4.3** and **Figure 4.5**). For positive T-waves only, MAE was 32ms for t_{Wyatt} and 98ms for t_{Alt} ($P < 0.001$). Linear regression for t_{Wyatt} rendered $RT_{\text{Wyatt}} = 0.82 \cdot \text{A-pace ERP} + 57$ ($r = 0.91$), linear regression with t_{Alt} rendered $RT_{\text{Alt}} = 0.49 \cdot \text{A-pace ERP} + 176$ ($r = 0.68$) ($P < 0.001$ comparing linear regressions) (**Figure 4.5D**). Compared to the mean measured A-pace ERP in the same experiment, local A-pace ERP was -6 ± 39 ms for positive ECGI T-waves, -7 ± 43 ms for biphasic T-waves and 32 ± 27 ms for negative T-waves ($P < 0.001$) (**Figure 4.5E**).

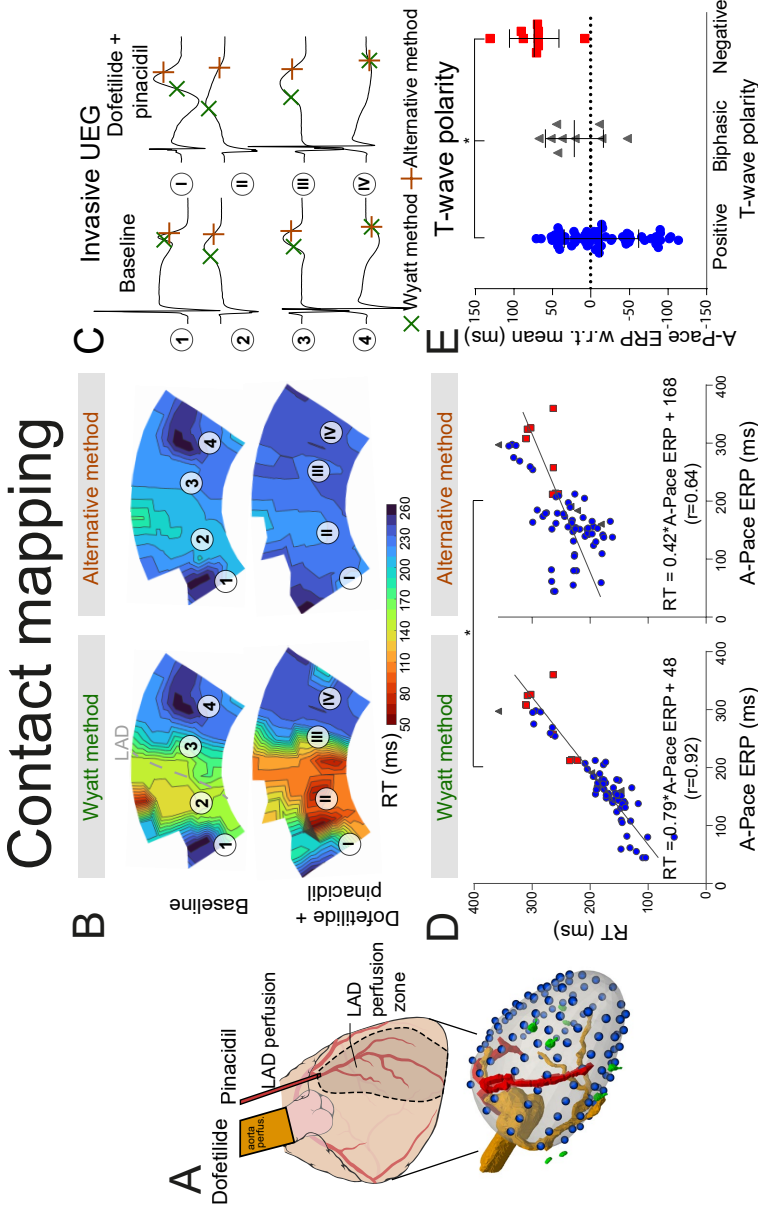


Figure 4.3: RT determined by the Wyatt and alternative method through contact mapping. **A:** experimental setup; the LAD was infused with pinacidil which shortens repolarization while the non-LAD region was infused with dofetilide, which prolongs repolarization. Unipolar electrograms were measured with an epicardial sock. **B:** RT as determined by the Wyatt versus alternative method before and during drug infusion. **C:** electrograms corresponding to different locations in **B**. **D:** linear regression when comparing A-pace ERP (see text) to RT determined by both the Wyatt and alternative method. Positive T-waves are shown in blue, biphasic T-waves in gray, and negative T-waves in red. **E:** A-pace ERP of positive, biphasic and negative UEG T-waves, with respect to the mean A-pace ERP of the same experiment. Figures **D** and **E** show pooled data of all our experiments with different drug settings.

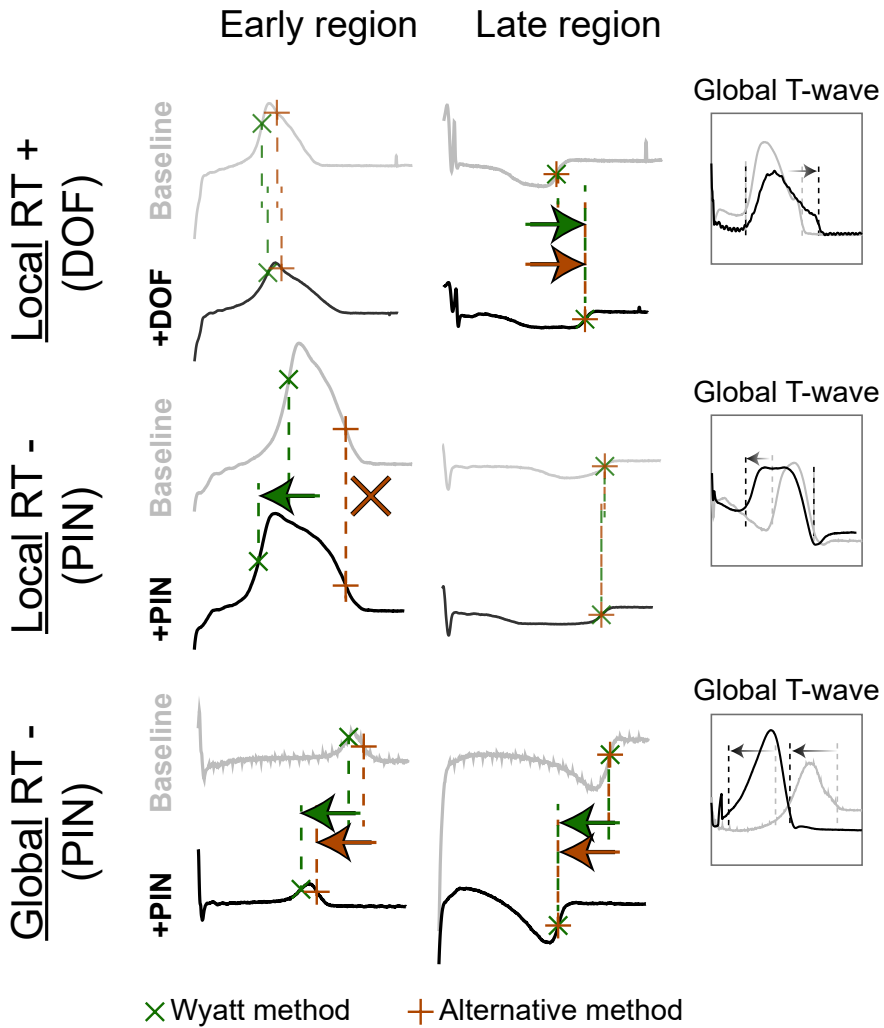


Figure 4.4: The effect of repolarization-altering drugs on T-wave morphology and RT. **Top:** repolarization-prolonging dofetilide (DOF) is infused in the late-repolarizing area, causing local RT-prolongation, as captured by both the Wyatt and alternative methods, and the “Global T-wave” (root-mean-square of all epicardial UEGs). **Middle:** repolarization-shortening pinacidil (PIN) is infused in the early-repolarizing area, causing local RT-shortening, captured by the Wyatt method, but not the alternative method. **Bottom:** global infusion of pinacidil in the entire heart causes a leftward shift of all T-waves (see global T-wave), which is captured by both methods.

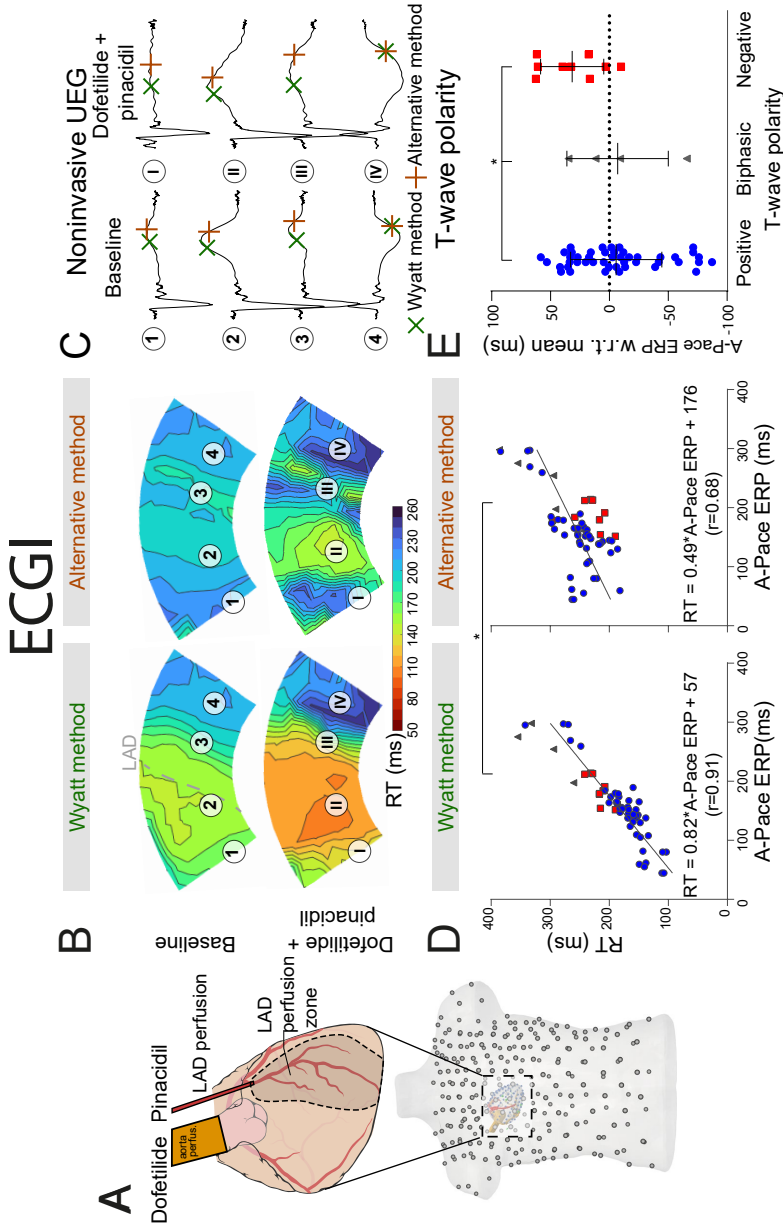


Figure 4.5: RT determined by the Wyatt and alternative method through noninvasive ECGI. **A:** experimental setup, similar to the setup in Figure 4.3. The explanted heart was placed in a torso-shaped tank filled with blood. **B:** RT as determined by the Wyatt and alternative methods before and after drug infusion. **C:** electrograms corresponding to different locations in **B**. **D:** linear regression when comparing A-pace ERP (see text) to RT determined by both the Wyatt and alternative method. Positive T-waves are shown in blue, biphasic T-waves in gray, and negative T-waves in red. **E:** A-pace ERP of positive, biphasic and negative ECGI T-waves, with respect to the mean A-pace ERP of the same experiment. Figures D and E show pooled data of all our experiments with different drug settings.

4.4 Discussion

Our novel experimental data show that the correlation between A-pace ERP (which we consider the most relevant ground truth for RT) and the Wyatt method is much higher than between A-pace ERP and the alternative method, and closer to the line of unity. Moreover, as in theoretical models, UEG T-wave polarity relates to RT, with UEG T-waves becoming increasingly negative as RT prolongs. Our new observations also show that local infusion of repolarization-shortening drugs was captured by the Wyatt method, while the alternative method often showed a prolongation of RT. Furthermore, our comparison of local vs. global infusion of repolarization-altering drugs provides additional mechanistic confirmation of theoretical models investigating RT in the UEG. The Wyatt method also performed consistently between consecutive beats.

For the first time, we show that the Wyatt method also reflects RT more accurately than the alternative method through ECGI. With ECGI, the relationship between T-wave polarity and RT was less evident, relating to earlier work showing that ECGI can reliably map RT and related gradients (47,51), but biphasic UEG T-waves can be challenging to reconstruct and may be rendered flat through ECGI (105).

4.4.1 Historical experimental and theoretical studies

Experimental studies validating either the Wyatt or alternative method by determining RT against ground truth-measurements are summarized in **Figure 4.6**. Generally, most studies agree that the Wyatt method outperforms the alternative method.

Studies validating the Wyatt method were performed in a variety of conditions: in Langendorff-perfused pig hearts (30,104), left-ventricular canine wedge preparations (95), in-vivo dogs (86,88,89) and humans (106,107). These experiments were done under a variety of conditions to alter repolarization: control, different pacing cycle lengths (88,89,95,106,107), coronary occlusion and reperfusion (88), epinephrine infusion (88,89), sympathetic nerve stimulation (86,89), local warming (30,86) and cooling (30), graded myocardial perfusion(86), during dl-sotalol infusion (106), in different locations on the heart.

Ref	Method	Measure	Species (n)	Experiment	Obs.	Wyatt method			Alternative method		
						α	β	r	α	β	r
Wyatt (1981)	TAP	APD ₉₀	D (8)	In vivo	88			0.85			
Millar (1985)	V-Pace ERP	-	D (11)	In vivo	2312	0.99	-7	0.96			
Haws (1990)	TAP	dVdt _{min}	D (12)	In vivo	349	0.97	6	0.98			
Chen (1991)	MAP	MAPD ₉₀	H (7)	In vivo	73	0.90	14	0.73			0.82
Gepstein (1997)	MAP	MAPD ₉₀	P (13)	In vivo	128						0.98
Chinushi (2001)	V-Pace ERP	-	H (19)	In vivo	133	1.06	-13	0.97		0.89	53
Yue (2004)	MAP	MAPD ₉₀	H (9)	In vivo	355	1.06	-33	0.83		1.04	-8
Coronel (2006)	MAP	dVdt _{min}	P (3)	Ex vivo	29	1.22	-52	0.89			
Franzone (2007)	Sim	dVdt _{min}	-	In silico	1872			1.00			
Potse (2007) [†]	Sim	dVdt _{min}	-	In silico	10,000	0.97	11	0.98		0.65	138
Boukens (2017)	OM	APD ₆₀	D (5)	Ex vivo	26	1.09	-18	0.91			
Wijers (2018)	MAP	MAPD ₈₀	D (10)	In vivo	17	1.12	-20	0.94			
Bear (2019) [‡]	OM	dVdt _{min}	P (3)	Ex vivo	53			0.83			
Orini (2019)	V-Pace ERP	-	H (11)	In vivo	41	0.75	55	0.63		0.66	115
This paper (2023) [*]	A-Pace ERP	-	P (7)	Ex vivo	71	0.78	48	0.92		0.42	169

ARI = $\alpha^* < \text{measure} > + \beta$



Figure 4.6: Literature results comparing the invasive unipolar electrogram (UEG) T-wave to different outcome measures (30,86,88-96,104,106,107). The Figure shows Pearson's r, the slope (α) and intercept (β) according to the equation $ARI = \alpha \cdot \text{local measure} + \beta$, i.e. for Orini (2019): $RT = \alpha \cdot V\text{-pace ERP} + \beta$ Figure 4.3 and Figure 4.5 for an example). [†]: Analysis only for positive T-waves. [‡]: RT instead of ARI (Figure 4.2A). If pooled data on r, α and/or β were not available, a weighted average was calculated for separate experiments. D: Dog. H: Human. MAP: monophasic action potential. Obs.: number of observations. OM: Optical mapping. P: Pig. Sim: Simulation. TMP: transmembrane action potential. V-pace ERP/A-pace ERP: ventricular/atrial-paced effective refractory period (see text).

The alternative method has been evaluated in fewer experimental studies than the Wyatt method. Experiments were performed in in-vivo pigs (91), humans with monomorphic ventricular tachycardia (92) and humans with right-ventricular hypertrophy (90) during normally-conducted sinus rhythm (90) and pacing with variable cycle lengths (91,92).

Two clinical studies (90,92) yielded results in support of the alternative method over the Wyatt method. In patients with right-ventricular hypertrophy, a better overall correlation between ARI and monophasic APD_{90} ($MAPD_{90}$) was found when using the alternative method, compared to the Wyatt method (0.82 vs. 0.73, respectively) (90). In patients with monomorphic ventricular tachycardia and a normal left-ventricular ejection fraction, use of the alternative method (compared to the Wyatt method) resulted in an increase of ARI- $MAPD_{90}$ correlation from 0.83 to 0.94 and decreased MAE (92). However, in that study, non-contact mapping was used, which was shown to correlate poorly with contact electrograms (108) and the method was not validated for intracardiac RT determination (109).

The theoretical underpinnings of the UEG have been extensively studied by comparing it with transmembrane potentials (TMPs) at the microstructural level. (86,99) Bidomain equations have been used to translate these one-dimensional models to a three-dimensional heart. Theoretical models (93,99,101) agree that the Wyatt method forms a solid theoretical basis for estimating the end of cellular repolarization from the UEG. However, these purely mathematical approaches are not intuitively straightforward to understand and only provide a physical, not physiological, explanation for the Wyatt method.

More recently, Potse et al. (94,101) developed a simpler model for UEG interpretation which agrees with the Wyatt method, validated with the more complex bidomain equations (110). In this model, the UEG is defined as the difference between the local TMP and the average TMP from the myocardial surface. For *relatively* early-repolarizing myocardium, the local TMP is less negative than the average TMP, leading to a positive T-wave in the UEG. Conversely, for *relatively* late-repolarizing tissue, the local TMP is more negative than the average TMP, leading to a negative T-wave (**Figure 4.7**). This model was later validated against in-vivo contact mapping (110). Our results are in agreement with these previous observations (**Figure 4.3E** and **Figure 4.5E**). Moreover, our experiments further confirmed the relationship between UEG T-wave upslope and repolarization pattern: *global* infusion of pinacidil caused a leftward shift of *all* T-waves and their upslopes, thereby maintaining the repolarization pattern (i.e. the relative relationship between early and late RT remained the same). In contrast, *local* infusion of repolarization-altering drugs caused only *local* changes in T-wave upslope, thereby altering the repolarization pattern (**Figure 4.4**).

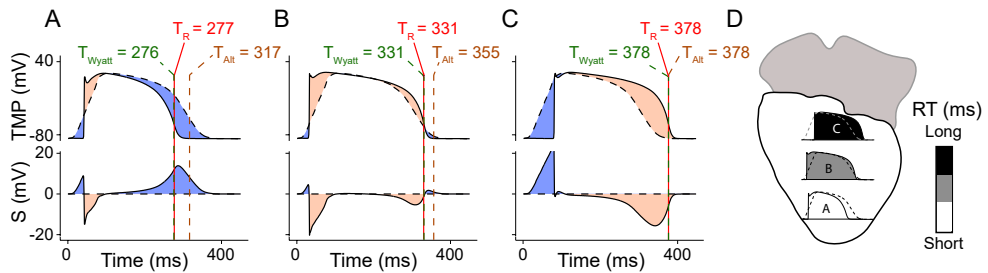


Figure 4.7: Model for improved interpretation of the UEG, as proposed by Potse et al (19), and slightly adapted from the original version. Panels A-C denote different locations (highlighted in panel D). The top frame of each panel shows simulated TMPs from 3 different locations in the model (solid line) and the location-independent mean action potential (dashed). The second frame shows S, i.e., the UEG itself (computed with the model), which is the subtraction of both. Each red vertical line indicates T_R , i.e., the instant of minimum dV/dt in the TMP. Each of these lines is half obscured by a dashed green line, which indicates t_{Wyatt} , leading to a green-red dashed line. Each dashed brown vertical line indicates t_{Alt} . **A:** Action potential and UEG for a short-RT-region, resulting in a positive UEG T-wave. **B:** Intermediate-RT-region, resulting in a biphasic T-wave. **C:** long-RT-region, resulting in a negative T-wave.

4.4.2 Experimental conventions and challenges

Multiple factors can influence the local unipolar T-wave and may explain the contradicting data from a small subset of the historical experiments.

First, larger electrode size and electrode-to-tissue distance may alter UEG T-wave morphology since both aspects increase the effective field-of-view of the electrode to a larger area, which could affect ARI-APD correlation in favor of the alternative method (103). Additionally, 2Hz high-pass electrogram filtering (often used for activation mapping) has been shown to flip T-wave polarity in some cases, which severely affects RT determination and could cause results to lean in favor of the alternative method (111). Consequently, high-pass filters should be used with great caution for repolarization mapping (i.e., use a low cut-off frequency) (111).

Secondly, heterogeneous definitions and measurement approaches have been used throughout the literature. For example, different gold standards have been used to compare UEG RT with, such as the local extracellular monophasic action potential (30,90–92,96), the more accurate TMP (88) (which can hardly be obtained in a beating heart) and optical mapping together with mechanical uncouplers (95,104). Some authors compared ARI to ERP, of which the latter is a robust measure in terms of arrhythmogenesis as it directly links to conduction block.

Additionally, even in ground-truth measurements, RT is not uniformly defined: e.g., as the maximum downslope of the action potential (30,86,99,101),(M)APD₉₀

(88,91,92), (M)APD₈₀ (95,96) and the end of the action potential (92)(Figure 4.2B). Moreover, species differences (dog/pig/human), recording site (endocardial/epicardial) and experimental model (in vivo/ex vivo/in silico) may play a role. However, the general conclusion of the Wyatt method outperforming the alternative method in historical literature still holds strong when isolating these factors (Supplementary Figure 4.1).

Moreover, the RT is typically measured from a global reference, e.g., a pacing spike, until the end of local repolarization (Figure 4.2A). However, most studies have compared APD to ARI, i.e., the subtraction of AT from RT. AT from the UEG and TMP can correlate poorly in certain conditions (112). Consequently, a comparison between APD and ARI may include measurement error in AT and could render different results than a comparison between RT (from UEG) and RT (from TMP).

Besides the Wyatt method and the alternative method to determine local RT from the UEG, other signal-analysis methods have been suggested, such as T-wave area-based methods (101) or spatiotemporal methods (112). These methods seem promising to determine RT in cases where slope-based methods are challenging, for example when noise levels are high or UEG T-wave amplitude is low. However, these methods have not been studied nearly as extensively as either slope-based method.

4.4.3 Study limitations

We selected the A-pace ERP as a gold standard for RT. This does differ from most of the historical literature where other gold standards were used. However, we believe ERP is the most robust measure for RT in terms of arrhythmogenesis, since it defines the ability of tissue to block conduction. Secondly, we did not investigate scenarios of postrepolarization refractoriness (PRR) which may affect the relationship between ERP and RT. However, as PRR occurs *beyond* termination of local repolarization (113), we do not expect it to be reflected in the UEG T-wave. Thirdly, the study was performed in pigs, not in humans. However, we believe that the physical and physiological mechanisms behind RT-determination do not differ between species, as also supported by Supplementary Figure 4.1. Furthermore, ERP was determined for a limited number of places in the heart because of the exhaustive experimental protocol. Lastly, we chose to investigate primarily the tissue with positive T-waves, because it causes a different RT by using either method. As such, this helped emphasize the differences between both methods in our analyses.

4.4.4 Application to basic and clinical arrhythmogenesis

In support of our novel experimental results, the collective results from previous experimental, clinical and computational studies show that the Wyatt method outperforms the alternative method in determining RT from the UEG (Figure 4.3, Figure 4.5, Figure 4.6, Figure 4.7), which is also supported by a theoretical understanding of the UEG T-wave (Figure 4.7): positive T-waves are found in

early-repolarizing tissue, while negative T-waves are found in late-repolarizing tissue. This aspect has been found widespread experimentally (30,89,102,110) even by authors who claim the alternative method should be used (91), except for Chen et al. (90)

Our novel findings and our historical overview support a unified repolarization assessment, thereby enhancing our understanding of mechanisms of repolarization. This augments our knowledge of repolarization in both structural and functional arrhythmias, since many arrhythmias are caused by local heterogeneities of repolarization - which can lead to unidirectional conduction block and reentry. A unified repolarization assessment may increase the role of invasive and noninvasive repolarization mapping.

4.5 Conclusion

We scrutinized our novel experimental results and historical experimental and theoretical studies to resolve the controversy between the Wyatt and alternative methods for determining RT from UEGs. The Wyatt method outperforms the alternative method not only on a theoretical basis but also in our data, and historical experimental data. Our results support that the Wyatt method provides a strong basis for RT determination from the invasive UEG and noninvasive (ECGI) UEG. Using it to determine RT could unify and facilitate repolarization assessment and amplify its role in basic and clinical electrophysiology.

Data availability statement

Upon reasonable request, the raw data supporting the conclusion of this article will be made available by the authors, without undue reservation.

Ethics statement

The animal study was reviewed and approved by the local ethics committee of Bordeaux CEEA50 and the National Biomedical Agency of France.

Author contributions

Study setup: LB, PV, and MC. Data acquisition: LB and MC. Data analysis: JS. Literature review: JS. Conceptualization: JS, LB, PV, and MC. Data interpretation: all authors. Manuscript draft: JS. Critical review of manuscript: all authors. All authors have read and approved the final manuscript.

Funding

This study was supported by the Special Research Fund (BOF) of Hasselt University (BOF17DOCMA15) and the Maastricht University Medical Center (MUMC+) to JS; the Netherlands CardioVascular Research Initiative (CVON 2017-13 VIGILANCE), Den Haag, the Netherlands, to JS and PV; the Hein Wellens Foundation, Health Foundation Limburg (Maastricht, the Netherlands), and a Veni grant from the Netherlands Organization for Scientific Research (TTW16772) to MC; and the Netherlands CardioVascular Research Initiative (CVON 2018B030 PREDICT2), Den Haag, Netherlands to PV. This work was furthermore supported by the French National Research Agency (ANR-10-IAHU04-LIRYC) and the Leducq foundation transatlantic network of excellence RHYTHM network (16CVD02).

Acknowledgements

The authors would like to thank Ruben Coronel, MD, PhD, Amsterdam UMC and IHU Liryc, Bordeaux, Bastiaan J. Boukens, PhD, CARIM, Maastricht University and Amsterdam UMC, and André G. Kléber, MD, PhD, BIDMC, Harvard Medical School, Boston, for their useful discussions on T-wave genesis and RT determination in the UEG, and Roel L.H.M.G. Spätjens, BSc, Maastricht University Medical Center+, for his suggestions on the figures. Moreover, the authors wish to thank Michele Orini, PhD, UC London and Barts Heart Centre, London, for providing data from a previous study (107) for additional analyses.

Conflict of interest

MC is part-time employed by Philips Research. The remaining authors declare that the research was conducted in the absence of any commercial or financial relationships that could be construed as a potential conflict of interest.

Supplementary Material

Supplementary Tables

Exp. ID	Baseline	Isolated DOF	Isolated PIN	DOF and PIN
1	Yes	Yes	No	Yes
2	Yes	Yes	No	No
3	Yes	No	Yes	No
4	Yes	Yes	No	Yes
5	Yes	Yes	No	No
6	Yes	Yes	No	Yes
7†	Yes	No	Yes	No

Supplementary Table 4.1: Drugs used in each experiment. Exp: experiment; DOF; dofetilide; PIN; pinacidil. “Yes” (in green) indicates that a drug setting was used, “No” (in red) indicates that a setting was not used. Dofetilide was typically infused in the aorta-perfused region (i.e., everywhere except LAD), pinacidil typically only in the LAD, with exception of experiment #7. †: global infusion of pinacidil, not only in LAD-region.

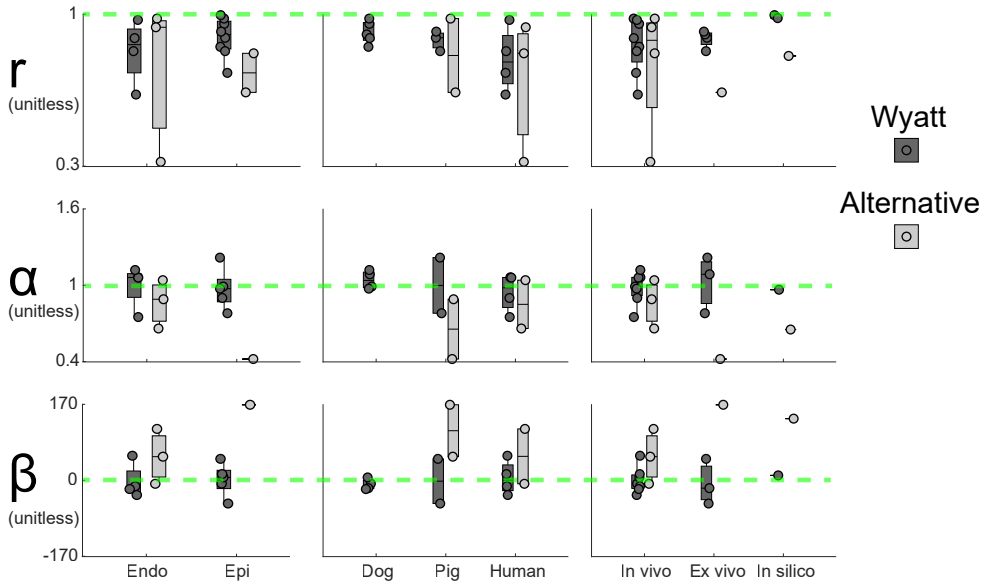
Delta-RT (ms)	Isolated DOF	Isolated PIN	DOF and PIN	
Exp. ID	Non-LAD region	LAD region	Non-LAD region (DOF)	LAD region (PIN)
1	37 [31 – 49]*	N/A	10 [7 – 16]*	-37 [-56 – -32]*
2	51 [46 – 56]*	N/A	N/A	N/A
3	N/A	-52 [-63 – -45]*	N/A	N/A
4	40 [36 – 44]*	N/A	26 [22 – 31]*	-77 [-88 – -71]*
5	49 [33 – 52]*	N/A	N/A	N/A
6	40 [27 – 53]*	N/A	14 [-8 – 26]*	-10 [-20 – -7]
7 [†]	N/A	-88 [-99 – -77]*	N/A	N/A

Supplementary Table 4.2: Differences between RT (delta-RT, in milliseconds) according to the Wyatt method after repolarization-altering infusion of drugs (repolarization-shortening pinacidil (PIN) and repolarization-prolonging dofetilide (DOF)), with respect to baseline situation without drugs. Values are noted as median [first quartile – third quartile]. A positive value indicates a prolongation of RT by the effect of drugs, with respect to baseline. Asterisks (*) denote significant differences ($P < 0.01$, one-tailed test). Colors denote whether the effect of the drug was correctly identified by delta-RT (green for yes, red for no). For experiment #7 ([†]), pinacidil was infused globally.

Delta-RT (ms)	Isolated DOF	Isolated PIN	DOF and PIN	
Exp. ID	Non-LAD region	LAD region	Non-LAD region (DOF)	LAD region (PIN)
1	38 [33 – 49]*	N/A	15 [10 – 17]*	16 [14 – 22]
2	54 [49 – 62]*	N/A	N/A	N/A
3	N/A	-8 [-10 – -3]*	N/A	N/A
4	40 [38 – 44]*	N/A	26 [24 – 29]*	22 [14 – 30]
5	51 [45 – 61]*	N/A	N/A	N/A
6	35 [22 – 40]*	N/A	37 [26 – 42]*	21 [13 – 32]
7	N/A	-93 [-113 – 82]*	N/A	N/A

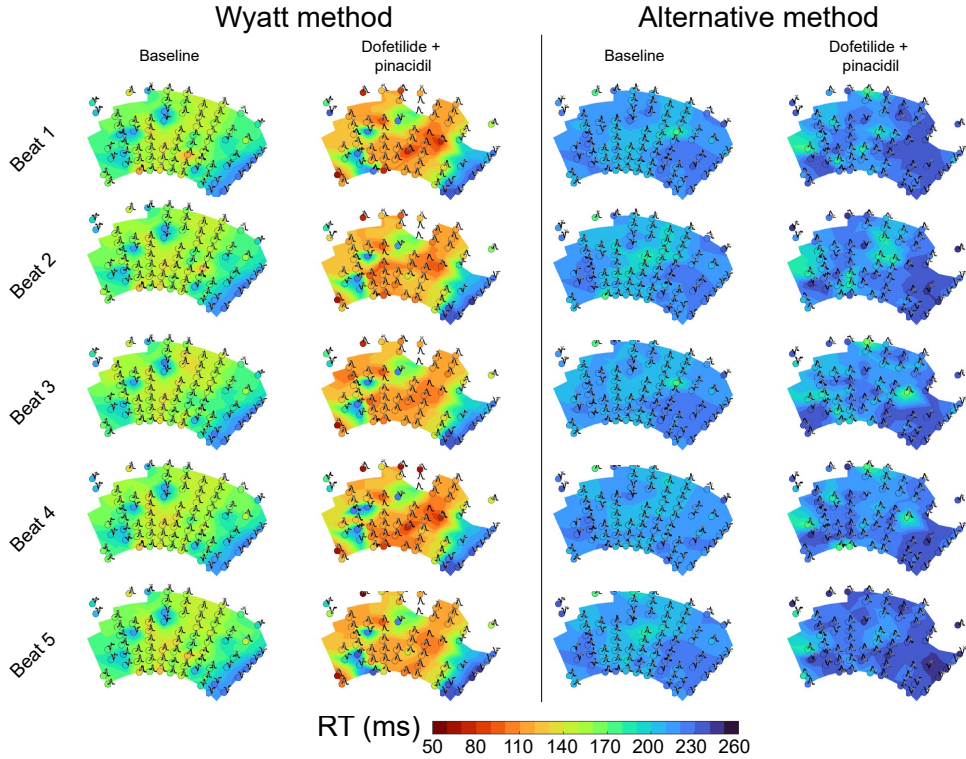
Supplementary Table 4.3: Differences between RT (delta-RT, in milliseconds) according to the alternative method after repolarization-altering infusion of drugs, with respect to baseline situation without drugs. Values are noted as median [first quartile – third quartile]. A positive value indicates a prolongation of RT by the effect of drugs, with respect to baseline. Asterisks (*) denote significant differences (P<0.01, one-tailed test). Colors denote whether the effect of the drug was correctly identified by delta-RT (green for yes, red for no). For experiment #7 (*), pinacidil was infused globally.

Supplementary Figures

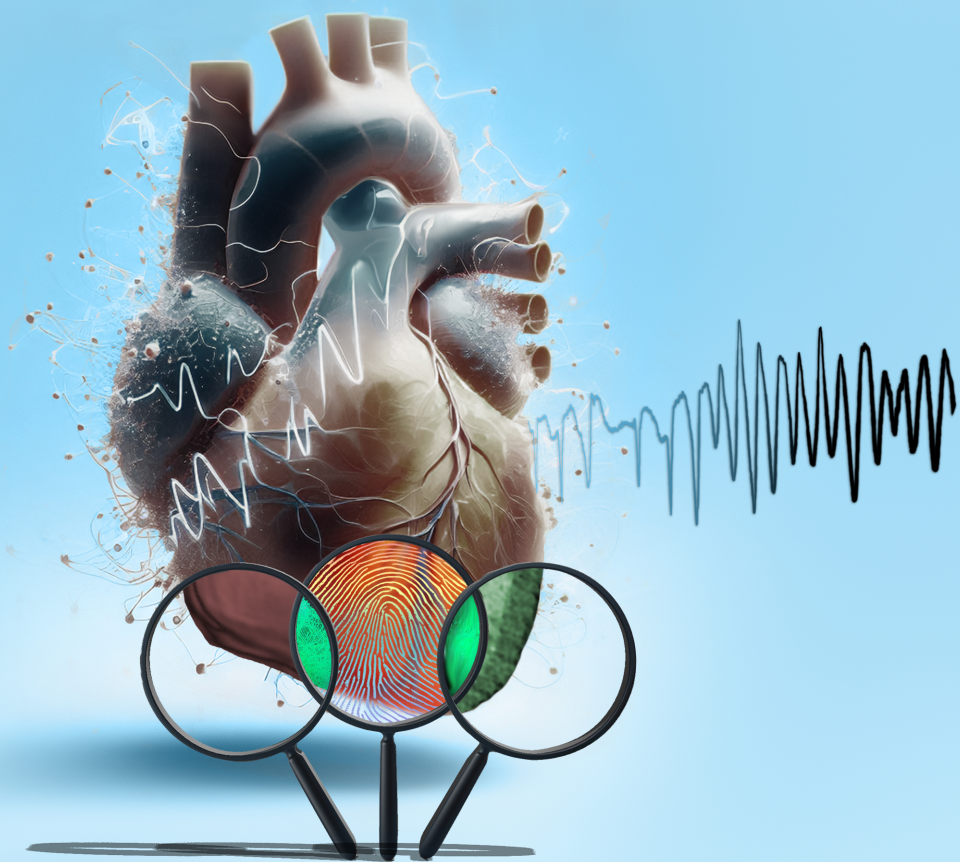


Supplementary Figure 4.1: Linear regression analyses for experimental results from previous studies in the literature (30,86,88–96,104,106,107). As in Figure 4.6, the accuracy of the Wyatt and alternative method were determined with respect to a local measure by addressing $ARI = \alpha \cdot \langle \text{local measure} \rangle + \beta$, e.g. $ARI = \alpha \cdot \text{MAPD}_{90} + \beta$. Results were separated based on endocardial/epicardial approach (left column), species (middle column) and ex vivo/in silico/in vivo studies (right column). As visible, the Wyatt method more accurately reflects RT (defined by local measure) than the alternative method, even if analyses were limited to certain experimental setups, meaning that this is a globally true conclusion, no matter the conditions (species, site of measurement, or type of experiment).

Contact mapping



Supplementary Figure 4.2: Beat-to-beat consistency of RT determination through the Wyatt method and alternative method. Isochronal RT maps for five consecutive beats are shown for one of our experiments (experiment 13, see **Figure 4.3**). Each row denotes a beat, while each column denotes a drug setting. Isochronal RT maps are consistent, although RT determination may locally be sensitive to slight changes in maximum T-wave upslope. However, standard deviations of beat-to-beat RTs were not significantly different between the Wyatt and alternative method ($p=0.84$ for baseline, $p=0.19$ for the drug-infused situation).



CHAPTER 5

Variant Electrical Activation and Recovery in Normal Human Hearts Revealed by Noninvasive Electrocardiographic Imaging

J. Stoks, K. Patel, B.D. van Rees, U.C. Nguyen, C. Muhl, R.M.A ter
Bekke, R. Peeters, J. Vijgen, P. De Suda, P. Ng, M.J.M. Cluitmans
and P.G.A. Volders

EMBARGOED

Submitted



CHAPTER 6

Dipeptidyl-Aminopeptidase-Like Protein 6 Regulates the I_{Na}^-/I_{to} Balance: Implications for Arrhythmogenesis and Clinical Phenotyping

A. Rossetti, J. Stoks, R.L.H.M.G. Spätiens, S. Kämmerer, J. Bayer, G. Kosmidis, R. Firneburg, S.R.M. Seelen, R.M. Ader Bekke, A.T.J.M. Helderma-van den Enden, J.P. van Antelen, A.A.M. Wilde, B. Loeys, J. Saene, J. Heijman and P.G.A. Volders

EMBARGOED

Submitted



CHAPTER 7

High-Resolution Structural-Functional Substrate-Trigger Characterization: Future Roadmap for Catheter Ablation of Ventricular Tachycardia

J. Stoks, B.J.M. Hermans, B.J.D. Boukens, R.J. Holtackers, S. Gommers, Y.S. Kaya, K. Vernooy, M.J.M. Cluitmans, P.G.A. Volders and R.M.A. ter Bekke.

Frontiers in Cardiovascular Medicine. 2023; 10.
DOI: 10.3389/fcvm.2023.1112980

Abstract

Introduction: Patients with ventricular tachyarrhythmias (VT) are at high risk of sudden cardiac death. When appropriate, catheter ablation is modestly effective, with relatively high VT recurrence and complication rates. Personalized models that incorporate imaging and computational approaches have advanced VT management. However, 3D patient-specific functional electrical information is typically not considered. We hypothesize that incorporating noninvasive 3D electrical and structural characterization in a patient-specific model improves VT-substrate recognition and ablation targeting.

Materials and methods: In a 53-year-old male with ischemic cardiomyopathy and recurrent monomorphic VT, we built a structural-functional model based on high-resolution 3D late-gadolinium enhancement (LGE) cardiac magnetic resonance imaging (3D-LGE CMR), multi-detector computed tomography (CT) and electrocardiographic imaging (ECGI). Invasive data from high-density contact and pace mapping obtained during endocardial VT-substrate modification were also incorporated. The integrated 3D electro-anatomic model was analyzed off-line.

Results: Merging the invasive voltage maps and 3D-LGE CMR endocardial geometry led to a mean Euclidean node-to-node distance of 5 ± 2 mm. Inferolateral and apical areas of low bipolar voltage (< 1.5 mV) were associated with high 3D-LGE CMR signal intensity (> 0.4) and with higher transmural fibrosis. Areas of functional conduction delay or block (evoked delayed potentials, EDPs) were in close proximity to 3D-LGE CMR-derived heterogeneous tissue corridors. ECGI pinpointed the epicardial VT exit at ~ 10 mm from the endocardial site of origin, both juxtaposed to the distal ends of two heterogeneous tissue corridors in the inferobasal left ventricle. Radiofrequency ablation at the entrances of these corridors, eliminating all EDPs, and at the VT site of origin rendered the patient noninducible and arrhythmia-free until the present day (20 months follow-up). Off-line analysis in our model uncovered dynamic electrical instability of the LV inferolateral heterogeneous scar region which set the stage for an evolving VT circuit.

Discussion and conclusion: We developed a personalized 3D model that integrates high-resolution structural and electrical information and allows the investigation of their dynamic interaction during arrhythmia formation. This model enhances our mechanistic understanding of scar-related VT and provides an advanced, noninvasive roadmap for catheter ablation.

7.1 Introduction

Catheter ablation of arrhythmogenic substrate and triggers of ventricular tachycardia (VT) reduces arrhythmia burden and implantable cardioverter-defibrillator (ICD) shocks (179,180) but recurrences (30-40% within 1-2 years (6,181)), costs and complication rates remain high (182,183). This limited procedural efficacy is attributed to the difficulty of identifying heterogeneous scar corridors related to the critical VT isthmus based on electrogram characteristics and pace mapping, especially during substrate-based ablation.

Recent advances in the field of catheter ablation for scar-related VT have primarily focused on defining target locations for ablation through pre-procedural characterization of the ventricular scar architecture by combining imaging techniques (such as computed tomography (CT) or cardiac magnetic resonance imaging (CMR)) with electrocardiogram (ECG)-VT algorithms. Image-guided or -aided substrate ablation may increase long-term success, decrease recurrence rates and reduce procedural duration (184,185). Imaging-based approaches mostly focus on structural myocardial targets, ignoring 3D functional information such as activation/propagation maps, repolarization maps, wavefront direction or arrhythmia triggers. Electrocardiographic imaging (ECGI) combines body-surface potential mapping and anatomical imaging to provide a noninvasive reconstruction of electrical activity. It enables a beat-to-beat noninvasive 3D assessment of epicardial activation, repolarization and propagation, besides the pinpointing of the VT exit site with relatively high spatial and temporal resolution (186,187).

In this study, we combined ECGI with high-resolution 3D dark-blood late gadolinium enhancement (3D-LGE) CMR and cardiac CT in a case with ischemic cardiomyopathy and recurrent monomorphic VT, providing a patient-specific structural-functional model to improve mechanistic understanding and to provide a road map for future personalized catheter ablation for VT. Additionally, we examined the accuracy of noninvasively-determined parameters compared to standard invasive VT-substrate characteristics.

7.2 Materials and methods

We constructed a personalized 3D cardiac model that integrates the individualized structural-functional characteristics of this case to identify mechanisms of arrhythmia formation and to develop an individualized framework for future VT ablation guidance.

The model incorporates 1) 3D dark-blood LGE CMR and cardiac CT delineating the myocardial anatomy and scar (structural aspects); and 2) functional-electrical aspects by noninvasive ECGI. Model outcomes were compared to data from invasive electro-anatomical mapping (EAM), and arrhythmia mechanisms were investigated.

7.2.1 Patient characteristics

A 53-year-old male was admitted to our hospital for electrical storm due to recurrent hemodynamically-tolerated, sustained monomorphic VTs with an inferobasal to mid, septal left-ventricular (LV) origin (**Figure 7.1A**) (188). He was previously known with anterior and inferolateral myocardial infarctions (LV ejection fraction 31%), also evident from the 12-lead electrocardiogram (**Figure 7.1B**), and coronary artery bypass grafting. The VT was managed with intravenous infusion of amiodarone. A 3D-LGE CMR and cardiac CT scan were performed to aid catheter ablation for VT. Additional electrical information was obtained by body-surface potential mapping before and during the VT ablation procedure.

7.2.2 3D dark-blood late gadolinium-enhancement CMR

The patient underwent a free-breathing 3D-LGE CMR with high isotropic resolution (acquired resolution 1.6 x 1.6 x 1.6 mm, reconstructed 0.8 x 0.8 x 0.8 mm) and dark-blood nulling (190) on a 1.5T MR system (Ingenia, Philips Healthcare, Best, the Netherlands). This allowed for more accurate scar demarcation and image quality with respect to conventional bright-blood nulled LGE CMR (191). Details of the dark-blood LGE mechanism without using additional magnetization preparation has been described earlier (24).

CMR-image processing was performed using a research software tool (ADAS3D Medical SL, Barcelona, Spain) (192). Pixel-signal intensity (PSI) maps were created from the 3D delayed enhancement acquisitions, and normalized for maximal PSI. A normalized PSI-based cut-off above 0.6 was defined as dense scar; border zone tissues were allocated in case of values between 0.4 and 0.6% (193). The LV myocardium was divided in nine three-dimensional transmural layers color-coded for scar architecture. Heterogeneous tissue corridors, defined as continuous corridors of border zone tissue connecting two regions of healthy tissue, bordered by dense scar and/or an anatomical barrier, were automatically calculated and visualized on the shells by the research tool (192). Subsequently, 3D-LGE CMR scar transmuralities were defined as the percentage of transmural layers having either dense scar (weight 1) or border zone (weight 0.5). Scar transmuralities were projected onto the endocardial shell.

7.2.3 CT and electrocardiographic imaging

Prior to the VT ablation procedure, an ECG-gated helical dual-source CT scan (Somatom Force, Siemens Healthineers, Forchheim, Germany) using intravenous iodine contrast medium was performed during breath-hold, to visualize cardiac geometry. Additionally, the patient underwent a low-dose thoracic CT scan to locate the body-surface electrodes, required for ECGI.

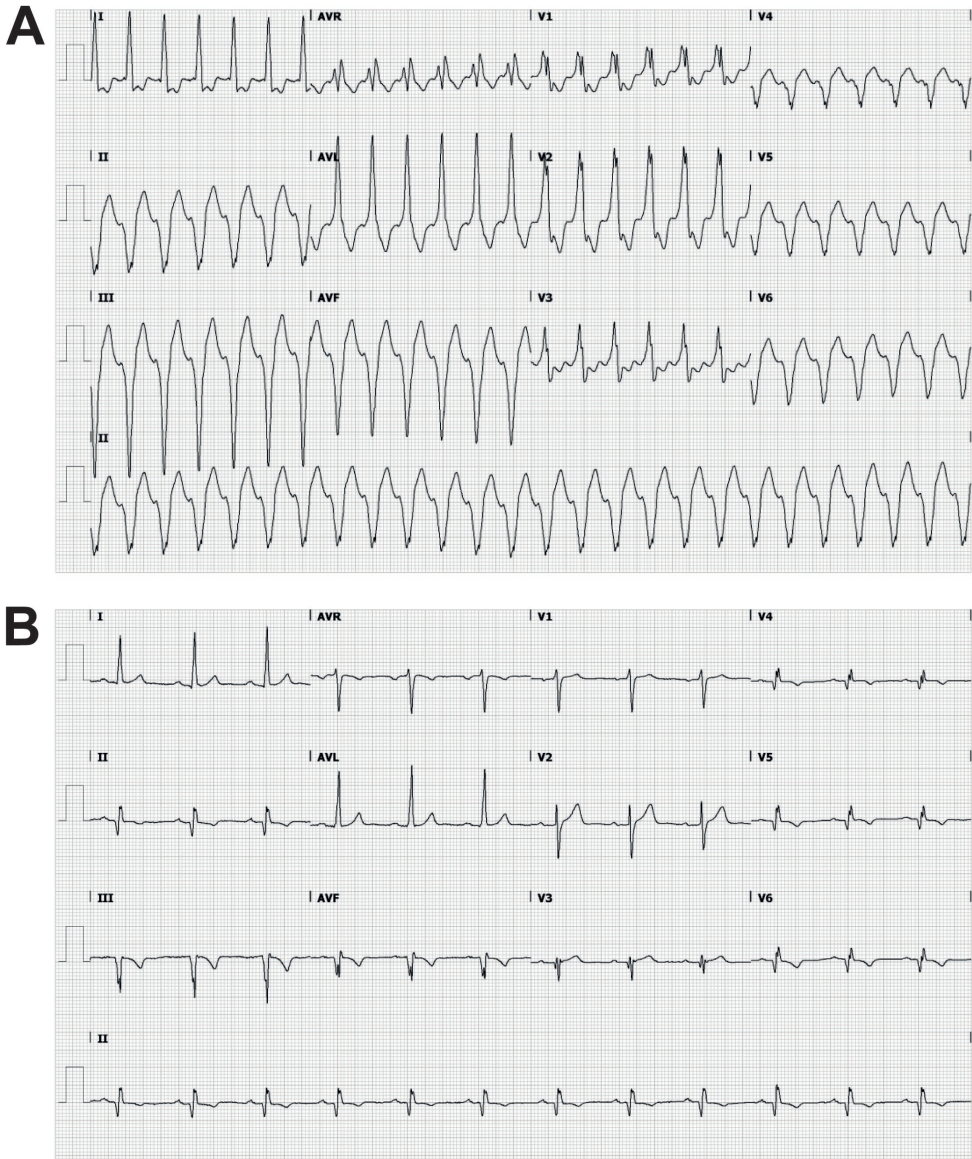


Figure 7.1: The patient's electrocardiogram during ventricular tachycardia (VT) (A) and sinus rhythm (B). **A:** Monomorphic VT demonstrating a wide QRS complex of 151 bpm with a right bundle branch block pattern (transition in V3) and a superior axis. The positive polarities in leads I and aVL suggest an inferomedial to inferobasal, septal origin (189). **B:** Sinus rhythm, 72 bpm, left axis deviation, a QRS width of 112 ms, pathological Q waves in inferior leads and V3-V6 and negative T waves in inferior leads and in V4-V6. Q waves are indicative of previous inferior/apical infarctions.

The ECGI was performed as previously described and validated (51,74). Briefly, 224 Ag-AgCl electrodes (BioSemi, Amsterdam, The Netherlands) were attached to the patient's torso to record body-surface potentials at a 2048Hz sampling rate starting 20 minutes prior to, and during, the electrophysiological study. From the thoracic CT scan, a 224-electrode torso was manually digitized. A ~2000-node diastolic cardiac geometry was semi-automatically segmented (194). Body-surface potential measurements were performed during sinus rhythm, atrial pacing, during programmed ventricular stimulation for VT induction and for evoked delayed potential (EDP) identification (195), and during VT.

Epicardial ventricular unipolar electrograms (UEGs) were reconstructed for selected beats through previously detailed methods (51). For each UEG, activation times (ATs) were determined from the steepest downslope (of the UEG QRS complex); this was done with a spatiotemporal approach that considers the spatial flow of current (112). ATs of each beat were calculated with respect to the average of the first 25 epicardial activations according to ECGI. UEGs were disregarded at the valvular base of the ventricles. VT dynamics were assessed by calculating the absolute activation time differences between consecutive VT beats.

7.2.4 Catheter ablation procedure for VT

The patient underwent continued body-surface potential mapping during the VT ablation procedure (**Supplementary Figure 7.1**). The procedure was performed under general anesthesia without preemptive hemodynamic support. The CARTO navigation system (Biosense Webster Inc., Diamond Bar, CA, USA) was used for guidance of the procedure. Both retrograde and anterograde access were obtained. The ADAS3D-derived anatomy and scar architecture were merged with the aortic root, main stem and pulmonary veins. After positioning of a quadripolar diagnostic catheter (6F, CRD-2™, Abbott, Chicago, IL, USA) in the right-ventricular (RV) apex, programmed RV stimulation was performed at 3 driving cycle lengths (600, 500, and 400 ms) with up to 3 ventricular extrastimuli (≥ 200 ms) to induce sustained VT (> 30 s or necessitating termination because of hemodynamic instability) and to determine the RV effective refractory period (ERP). During right-atrial (RA) pacing, a detailed electroanatomical voltage map was obtained using a high-density mapping (PentaRay, Biosense Webster Inc., Diamond Bar, CA, USA) and an irrigated contact-force sensing 3.5 mm-tip catheter (SmartTouch, Biosense Webster Inc., Diamond Bar, CA, USA). Near-field peak-to-peak bipolar voltage amplitude below 1.5 mV indicated scar, with dense scar < 0.5 mV and border zone 0.5 – 1.5 mV. EDPs, characterized by low-amplitude near-field potentials with 10-ms delay or block after RV extrastimulus (S2 50 ms above the ERP), were tagged in the 3D system, as previously described (196). The VT site-of-origin was identified using pace mapping aimed at a mean correlation coefficient between the VT-QRS morphology and the paced-QRS of $> 90\%$ (197). Substrate modification was performed aiming at complete EDP elimination and targeting the VT site-of-origin using radiofrequency energy delivery (power 50 W, temperature limit 43 °C, flow rate 20 – 30 mL/min). After the last lesion

set, the substrate was reassessed for the abolition of EDPs, and programmed ventricular stimulation was repeated to test for VT inducibility.

7.2.5 Postprocedural image integration and analysis

The geometries from 3D-LGE CMR, CT, ECGI and invasive EAM were manually aligned and registered digitally in 3D Slicer (198). The most important anatomic landmarks used for integration were: the LV and RV epicardium, LV apex and aorta from CT; LV apex, epicardium, endocardium and aorta from 3D-LGE CMR; and LV endocardium, apex and aorta from EAM. The accuracy of the image integration was based on Euclidean node-to-node distance calculation and visual evaluation. The EAM geometry was converted isotropic (i.e., equal node-to-node distances throughout the geometry) to ensure that all regions of the heart had equal weight in downstream analyses. Further analyses were performed in MATLAB R2020b (MathWorks, Natick, MA, USA).

Information from 3D-LGE CMR and ECGI was combined to examine triggers, substrate, and their interactions. 3D-LGE CMR scar delineation was compared to areas of low invasive bipolar voltage, by finding the corresponding nearest neighbours of the CMR anatomy and the invasive electroanatomic anatomy. Any neighbours with a corresponding distance of > 10 mm from each other were disregarded. The colocalization of endocardial EDPs with MRI-derived heterogeneous tissue corridors was also evaluated, disregarding EDPs that were tagged >10 mm from the endocardial 3D-LGE CMR shell.

7.3 Results

7.3.1 Ablation procedure and outcome

A sustained monomorphic VT arising from the inferobasal LV, closely resembling the documented arrhythmia, was repeatedly induced by programmed electrical stimulation (by minimally 2 ventricular premature beats) and led to hemodynamic compromise. The high-density LV-endocardial bipolar voltage map (5375 points) revealed two remote areas of scar in the lateral and apical regions of the LV, colocalizing with areas of increased endocardial PSI based on 3D-LGE CMR. 21 EDPs were tagged. Pace mapping at the inferobasal LV resulted in a 92% match with the induced VT. Radiofrequency delivery targeted at the inferolateral EDPs and the site of VT origin, eliminated the EDPs and rendered the patient non-inducible at the end of the procedure. Total procedural time was 330 minutes; fluoroscopy time 10 minutes. The procedure was without any complications. A single-chamber ICD was implanted afterwards. No VT had recurred at 20 months follow-up.

7.3.2 Contrast-enhanced CT and 3D dark-blood late gadolinium-enhancement CMR

Contrast-enhanced multidetector CT showed wall thinning in the inferolateral LV and apex (**Figure 7.2A**, **Supplementary Figure 7.2**). The CMR revealed a partly transmural infarcted area in the inferolateral and apical segments with aneurysm formation (**Figure 7.2B**, **Supplementary Videos**). Dense scar and border zone, as detected through CMR, consisted of non-uniform transmural patterns (**Figure 7.2C**). Heterogeneous tissue corridors, identified from CMR (**Figure 7.2D**) were localized in the basal to mid (infero)lateral, and apical aspects of the LV.

Manual image integration of invasive EAM and 3D-LGE CMR endocardial geometry led to a mean Euclidean node-to-node distance 5 ± 2 mm. Increased PSI (> 0.4) of the innermost endocardial layer of 3D dark-blood LGE CMR closely resembled reduced endocardial bipolar voltage (< 1.5 mV) using previously-defined cutoffs (192), while areas of non-agreement were near the scar-to-healthy border (**Figure 7.3A**). Both modalities agreed (both “scar” or both “healthy”) for 68% of tissue, and disagreed for the remaining 32%, mostly concerning the border zone. According to both modalities, the majority of scar consisted of border zone (76% according to EAM, 85% according to 3D-LGE CMR). Predicting bipolar scar through the CMR endocardial signal intensity rendered a receiver operating characteristic (ROC) area under the curve of 0.72. Further comparison of 3D-LGE CMR scar transmural to EAM bipolar voltage showed that low voltages were associated with higher scar transmural, and vice versa (**Figure 7.3B**).

17/21 EDPs were within 10 mm of the endocardial CMR-wall. 15/17 (88%) of these EDPs were located in an area of endocardial scar detected by 3D dark-blood LGE CMR (**Figure 7.4A-B**). EDPs were often identified within or close to (transmural) CMR-derived corridors. When projecting all EDPs and corridors onto the endocardial CMR layer, the average Euclidean distance from EDP to the nearest corridor was 3 (0 – 6) mm (median, (first and third quartiles)).

7.3.3 Structural-functional substrate characterization

Structural-functional overlay of the 3D-LGE CMR and ECGI data (body-surface potential mapping during the ablation procedure) allowed the investigation of the VT trajectory and mechanism. In **Figure 7.4C**, the endocardial (invasive EAM) and epicardial (ECGI) locations of the VT exit according to pace mapping are shown, together with transmural fibrosis and PSI-derived heterogeneous tissue corridors. ECGI pinpointed the VT exit in close proximity (spatial accuracy 10/14/13 mm) to the invasive endocardial site with the highest pace-mapping agreement (0.90/0.92/0.92, respectively). When projecting the ECGI-exit onto the endocardial geometry, i.e., omitting the endocardial-to-epicardial distance, the distance between invasive and noninvasive VT exit decreased to 5/12/12 mm, respectively.

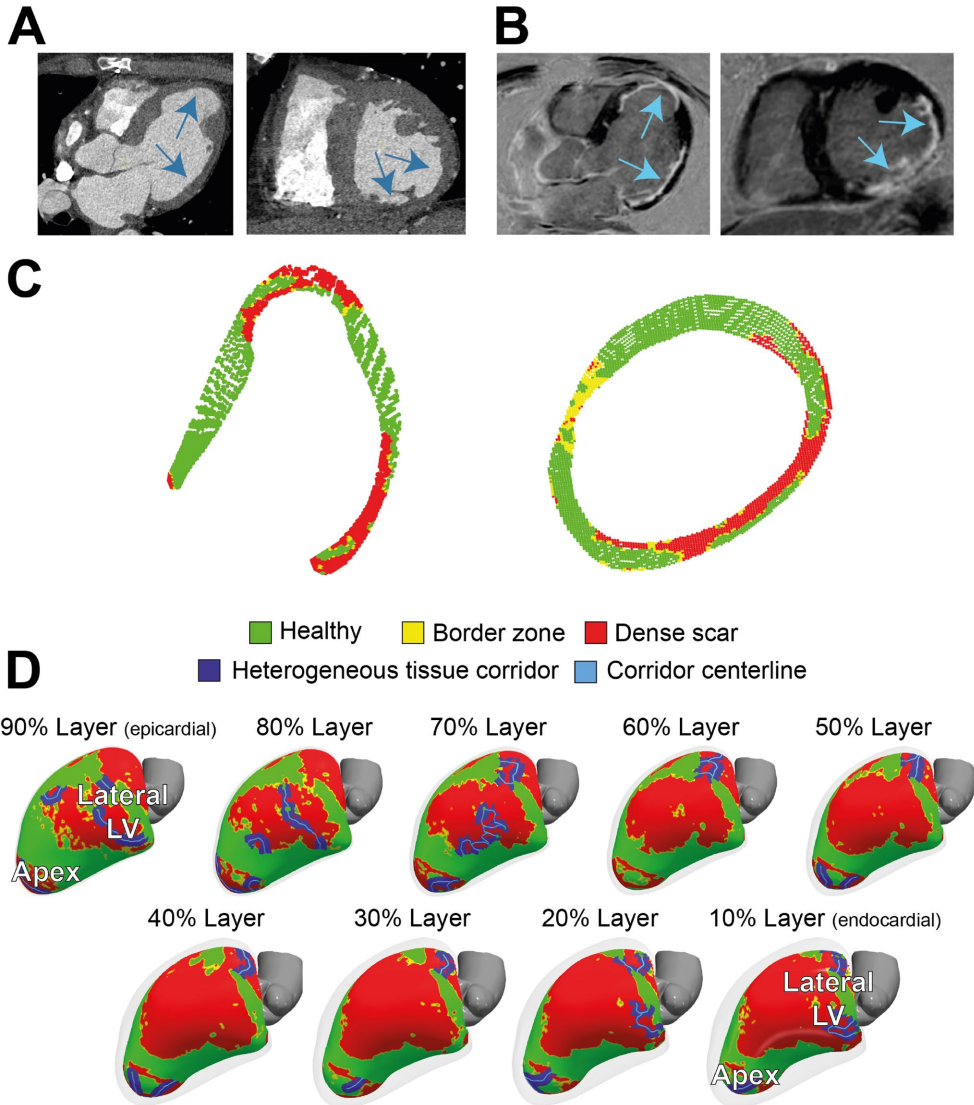


Figure 7.2: Cardiac imaging of the patient prior to the ablation procedure. A: Contrast-enhanced dual-source computed tomography (CT), performed for anatomical reference showing wall thinning in the apical aneurysm and laterobasal aspect of the left ventricle (LV). **B:** 3D dark-blood late gadolinium enhancement cardiac magnetic resonance imaging (LGE CMR) LGE CMR showing areas with hyperenhancement in the laterobasal and apical aspects of the LV. **C:** Two cross-sectional views of LV scar, detected by 3D dark-blood LGE CMR. **D:** CMR-derived healthy and scar tissue, including corridors and their centerlines, depicted in nine transmural layers (interlayer distance approximately 0.8 mm) of the ventricular myocardium. Colors correspond to colors in C).

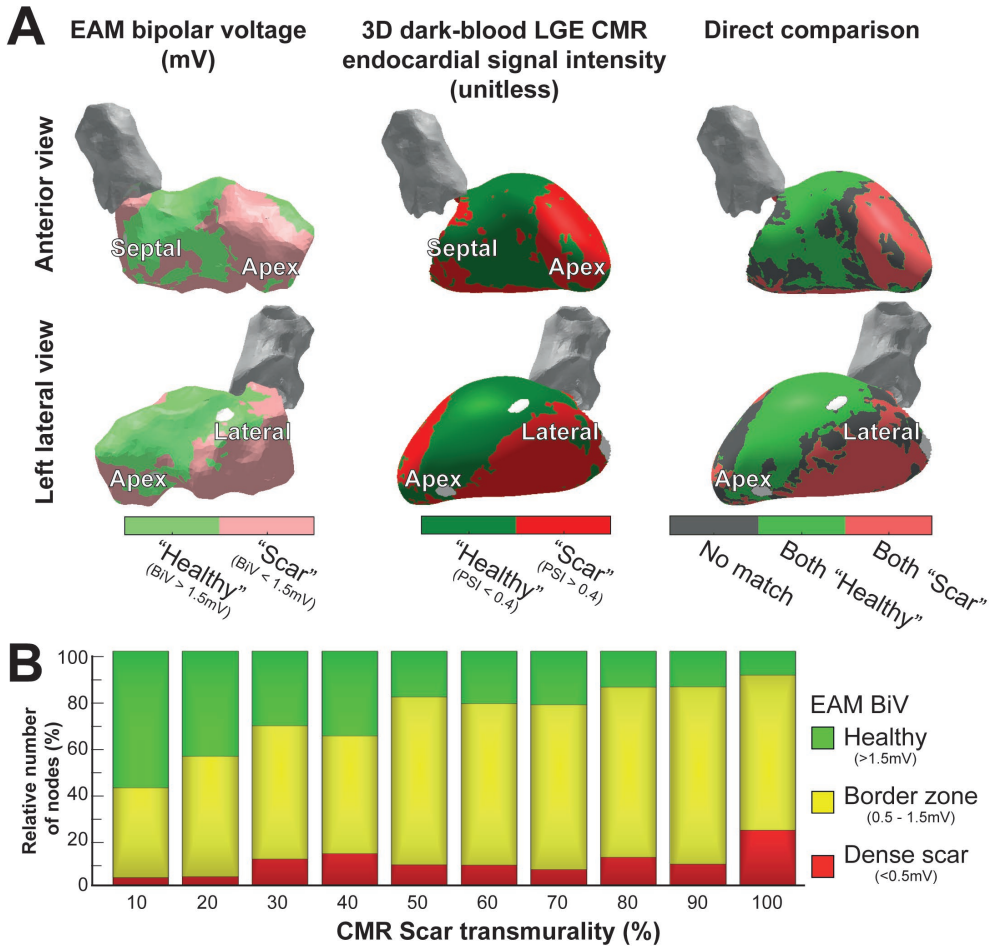


Figure 7.3: Comparison of 3D-late gadolinium enhancement cardiac magnetic resonance imaging (LGE CMR) to electroanatomical mapping (EAM). **A:** invasive EAM bipolar voltage map (left) and 3D dark-blood LGE CMR endocardial signal intensity (middle), and the comparison of both (right). Areas of agreement regarding healthy tissue are shown in green, agreement regarding scar tissue are shown in red, and differences between both maps are shown in gray. **B:** CMR scar transmuralty compared to EAM bipolar voltage. Higher transmuralty of scar (detected by 3D-LGE CMR) was associated with lower bipolar voltage in EAM.

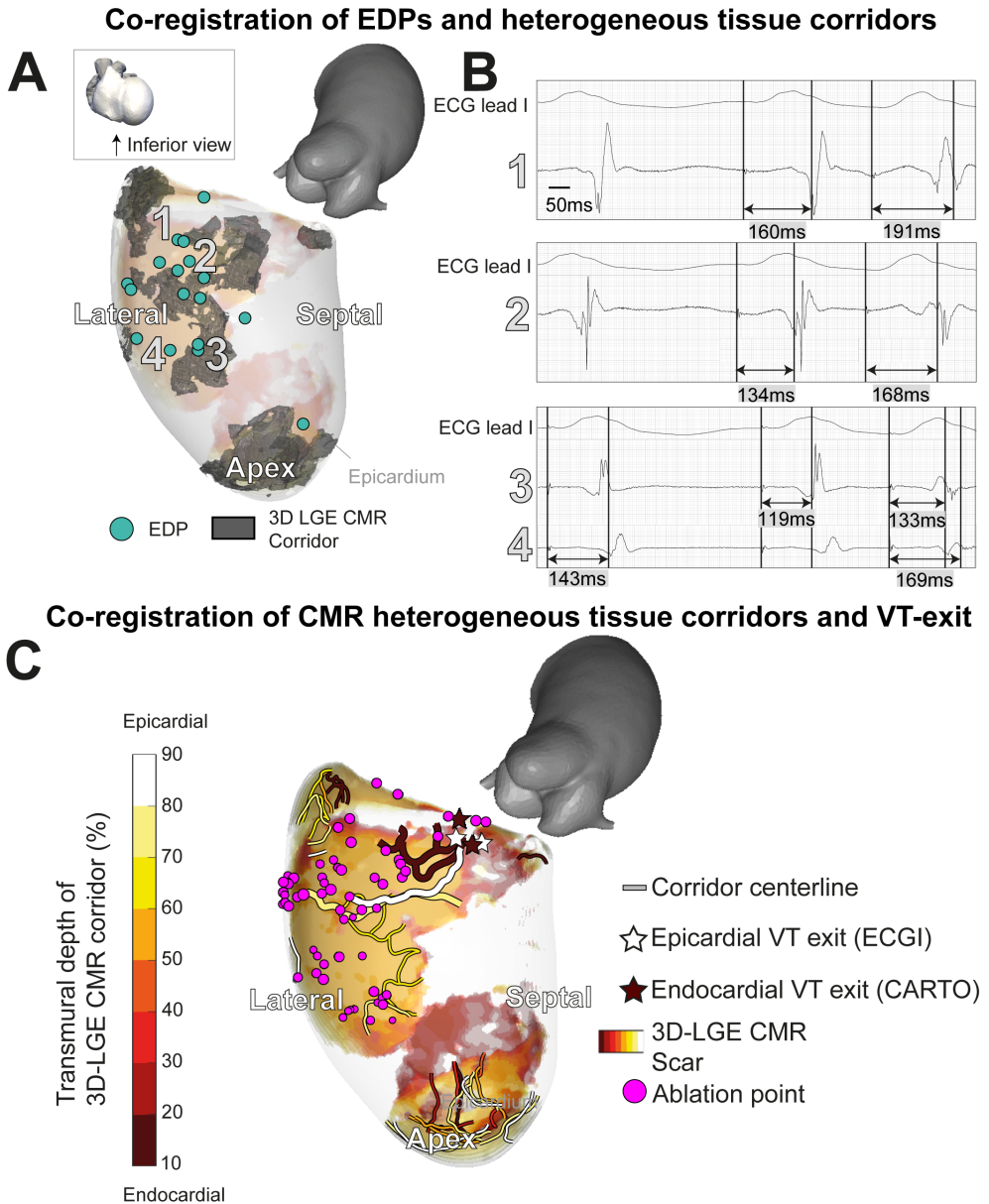


Figure 7.4: 3D-late gadolinium enhancement cardiac magnetic resonance imaging (LGE CMR) heterogeneous tissue corridors and evoked delayed potentials (EDPs). **A:** Annotation of EDPs during the electroanatomical mapping (EAM) procedure, compared to a superimposed anatomical view of transmural heterogeneous tissue corridors detected through 3D LGE CMR. All EDPs except one coincided with ventricular scar or border zone. EDPs qualitatively coincided well with corridors close to the endocardium. **B:** EDPs on locations 1-4 in panel A. **C:** Investigating of ventricular tachycardia (VT) working mechanisms through structural-functional image overlay. Transmural layers of scar and border zone with

centerlines of slow-conducting heterogeneous tissue corridors are superimposed and colored. VT exits were determined by pace mapping during the procedure. Invasively-determined endocardial (brown) and noninvasively-determined epicardial (white) exits coincide at the end of epicardial and endocardial corridors. Corridors of interest leading to the VT exit have an increased width. Ablation of the substrate (purple), including the identified corridors, rendered the patient arrhythmia-free.

Both epicardial and endocardial heterogeneous tissue corridors were adjacent to the VT exit, possibly serving as slow-conducting channels (isthmuses) for the VT. Radiofrequency ablation to, amongst other sites, the entrance of these corridors, rendered the patient arrhythmia-free (20 months follow-up).

Although the monomorphic VT (with exception of its first beat) appeared stable on the ECG (**Figure 7.5A**), ECGI revealed significant beat-to-beat differences in activation patterns during the onset of VT (**Figure 7.5B**). The VT stabilized over time, causing beat-to-beat differences in its activation pattern to decline. The anterolateral area of early activation migrated inferolaterally as the VT evolved. This area of shifting early activation correlated with CMR-detected corridors leading to the VT exit (**Figure 7.4B**). Beat-to-beat-differences in activation pattern were present during all inductions (episodes) of VT, higher than during sinus rhythm and ventricular pacing (**Figure 7.5C**).

Prior to the electrophysiological study, a premature ventricular complex (PVC) was recorded with ECGI (**Supplementary Figure 7.3A**). The PVC origin matched significantly, although not completely, with the VT exit. ECGI pinpointed the PVC to the lateral LV wall (**Supplementary Figure 7.3B**). The crowded activation isochrones superior to the first-activated area suggest a conduction block in the basolateral LV (blue arrow). CMR-detected heterogeneous tissue corridors (numbers 1-3, **Supplementary Figure 7.3C**) connected the PVC and VT origins and coincided with the area of shifting early activation during VT (**Supplementary Figure 7.3C**). Hence, we hypothesize the PVC could be involved in VT initiation.

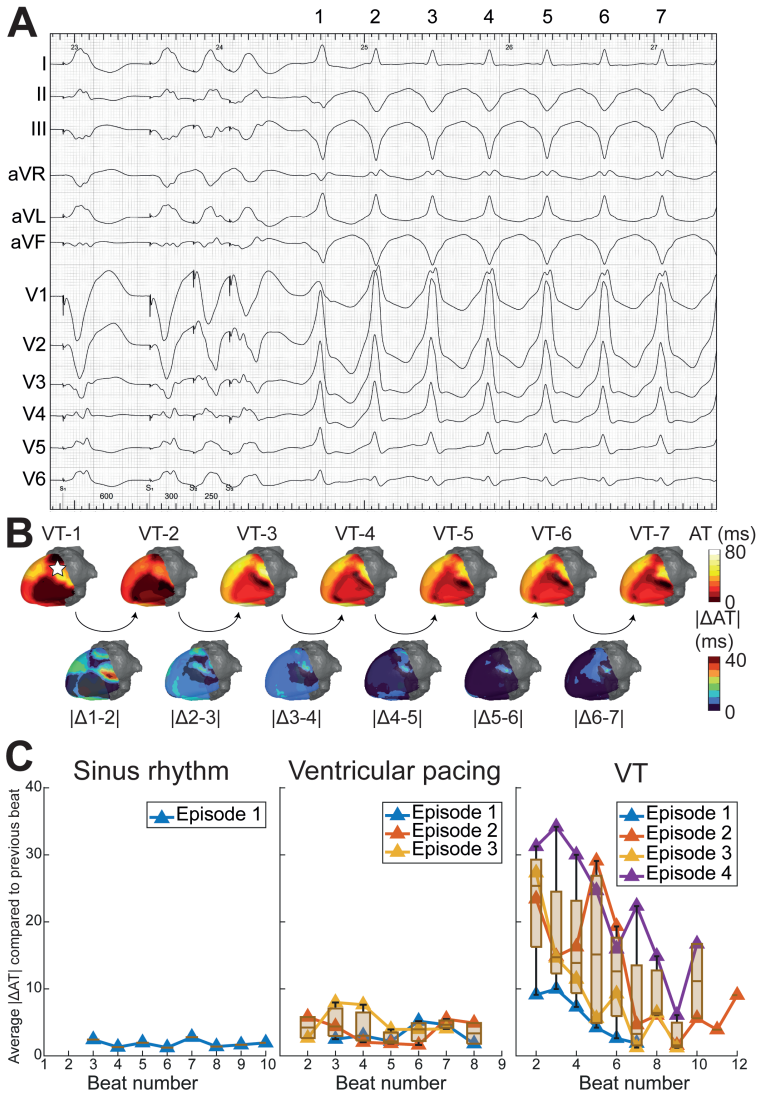


Figure 7.5: Dynamics of epicardial activation patterns through electrocardiographic imaging (ECGI). **A:** ventricular tachycardia (VT) during procedure in which beats 1 through 7 are depicted. **B:** Activation patterns of VT beats 1 through 7, with absolute difference in activation time (AT) of consecutive beats shown below. The pentagram in VT-1 illustrates the origin of the premature ventricular complex (PVC) (Supplementary Figure 7.3). For reference, dynamics of activation patterns in sinus rhythm (SR) and pacing are also shown. **C:** Average absolute difference in activation times of consecutive beats, over the entire epicardium. Dynamics in activation patterns decrease over time for several episodes (inductions) of VT, while SR and ventricular pacing show stable activation patterns.

7.4 Discussion

In this proof-of-concept study, we developed a 3D structural-functional model for scar-related VT by combining 3D dark-blood LGE CMR and ECGI (of PVC and VT) with high spatial and temporal resolution. This model was developed in an exemplary case with recurrent monomorphic VT in the setting of ischemic cardiomyopathy. Patient-specific VT substrates, triggers, and their interactions were detailed, in a noninvasive manner, serving as a roadmap for future individualized ablation strategies. Integrating high-density invasive EAM advanced the understanding of possible VT mechanisms.

In our integrated model, the (invasive and noninvasive) VT exit colocalized at the end of CMR-detected heterogeneous tissue corridors. Furthermore, the patient's spontaneous PVC originated in close proximity to the VT exit and CMR-detected corridors. This suggests that the PVC may be involved in patient's VT formation. Moreover, EDPs were found close to heterogeneous tissue corridors, suggesting a strong link between functional endocardial conduction slowing/block and structural border zone channels.

7.4.1 3D dark-blood LGE CMR

Acquiring 3D-LGE CMR with high isotropic resolution visualizes myocardial fibrosis from every desired direction compared to a fixed viewing angle when using (non-isotropic) 3D or standard 2D imaging (23). Subtle scar architectures, such as submillimeter tissue corridors, may be missed using these latter acquisition techniques. Additionally, the dark-blood nulling CMR, recently validated against histopathology in an experimental large-animal model (191), allows for improved detection and quantification of (sub)endocardial fibrosis, often encountered in ischemic etiologies, compared to conventional bright-blood LGE (24). We have shown that 3D dark-blood LGE CMR has a reasonable correlation, at least qualitatively, with the endocardial bipolar voltage. We found a 68% agreement between reduced (< 1.5 mV) endocardial bipolar voltage and increased (> 0.4) 3D-LGE CMR-signal intensity when applying a point-by-point comparison between both modalities. Areas of non-agreement were predominantly found at the healthy-to-scar-border zone. The ROC area under the curve to define areas of low voltage through 3D-LGE CMR was 0.72, which compared with the low range of values found in a recent study, although different methods of analysis may have affected the results (199). The observed electrostructural mismatch stems from the fundamentally different assessment of scar characteristics, with varying spatial resolution and dissimilar gating for cardiac phases and respiratory motion, besides the variable impact of modulators (e.g., contact force, fiber orientation, wavefront direction, sympathetic hyperinnervation). The scar border zone may be especially susceptible to these factors.

Additionally, we have shown a good correlation between the 3D dark-blood LGE CMR-derived myocardial heterogeneous tissue corridors and the invasively-measured areas of functional electrical conduction slowing or block (192). These

corridors may comprise slow-conducting pathways, or protected isthmuses, that may facilitate reentrant excitation (192) upon unidirectional conduction delay or block (22).

7.4.2 ECGI

ECGI has been validated in multiple studies. For a recent overview we refer to **Chapter 2**. Its strength lies in the reconstruction of (paced) rhythm of single origin (48). In a structurally normal heart, ECGI was more accurate than the 12-lead ECG to pinpoint the origin of VT or PVC (58). The 12-lead ECG was even less precise in the presence of myocardial scarring (30). We have shown that ECGI-based reconstructions localized the site of ventricular activation (adjacent to scar border zone) by pace mapping at ~10 mm from the endocardial location (if endocardial-to-epicardial distance was omitted). This was more accurate than in a recent study using a commercial system (200) but comparable to other reports (see **Section 2.4**).

Moreover, ECGI can generate a complete 3D-epicardial activation map in a single beat, while several VT cycle lengths are needed during invasive contact mapping EAM to construct an activation or propagation map (which is often not possible since VT is often polymorphic or hemodynamically not tolerated). This may be relevant for investigating the dynamic behavior of VT, especially in polymorphic VT but also during the onset of monomorphic VTs. In our case, ECGI uncovered marked initial activation dynamicity, only stabilizing after several beats. An area of electrical instability (shifting early activation) during VT was present close to the VT exit and structural-functional corridors (**Figure 7.4** and **Figure 7.5B**).

7.4.3 Structural-functional VT substrate characterization

(Non)invasive modalities identifying critical components of the VT circuit to guide catheter ablation have evolved considerably over the last decades. Historical milestones in the human heart are shown in **Figure 7.6**.

In 1972, Wellens et al. found that, in (mostly) post-infarction patients, VTs were based on reentrant excitation, that could be terminated through electrical stimulation (201). In 1981, Josephson et al. compared 12-lead ECG QRS morphologies of VTs to endocardial VT exit sites in 34 patients (202), demonstrating that the presence of myocardial scar diminishes the ECG accuracy to pinpoint the endocardial VT exit.

In 1999, Wittkamp et al. first validated an impedance-based 3D catheter navigation system in humans for EAM (203). In 2000, De Groot et al. introduced a 3D-catheter localization system using ultrasound transducers to guide VT ablation (204), that allowed real-time display of the catheter tip and repositioning to previously marked sites. In the same year, Marchlinski et al. introduced the magnetic mapping-based CARTO system to perform linear substrate ablation which proved effective to significantly reduce VT recurrence (205). These 3D-navigation systems could be considered the foundation of the modern-day

EAM.

In 2005, pioneering work on image integration was done by Dickfeld et al., who coregistered MRI acquisitions with the electromagnetic catheter positioning system to guide catheter navigation in the human right atrium and ventricle (206). In the same year, Ghanem et al. showed that near-simultaneous ECGI-derived (noninvasive) electrograms had a moderate correlation with invasive potentials recorded in sinus rhythm and during endocardial and epicardial pacing in patients (52). Five years later, Tian et al. (207) coregistered contrast-enhanced CT relying on distinct anatomic, dynamic and perfusion characteristics indicative of myocardial scar and border zone with electrogram voltage obtained during endocardial point-by-point mapping. A high segmental accuracy was reported. Though contrast-enhanced CMR still has superior contrast resolution compared to CT, the latter is more easily applicable for scar demarcation in patients with an ICD and allows for increased temporal and spatial resolution (207). Furthermore, wall thickness analysis with CT accurately predicted isthmuses in postinfarction VT (26).

In 2008, Codreanu et al. performed image integration of EAM and LGE CMR to conclude that transmural scar (by CMR) could be detected by spiky electrograms, reduced voltage amplitudes or prolonged bipolar electrogram durations (210). A year later, Desjardins et al. investigated the relationship between reduced bipolar voltage in EAM and automatically-segmented scar in LGE CMR, to find that sites critical to VT in humans are located within areas of delayed enhancement in CMR. In 2011, Wijnmaalen et al. performed a head-to-head comparison of LGE CMR with electroanatomical voltage mapping through image integration. They found that increased scar transmural thickness led to decreased endocardial bipolar voltage and that non-transmural and border zone scar was undetected by EAM (211). The combination of LGE CMR with multidetector CT is superior for structure-function relationship determination in scar-related VT (212). With the availability of 3D-LGE CMR acquisitions with high isotropic resolution, Andreu et al. (192) identified heterogeneous tissue corridors that colocalize in 79% with invasively recorded conduction channels (2015). VT ablation procedures guided by CMR led to increased procedure success, and decreased VT recurrence, inducibility and procedure time (184).

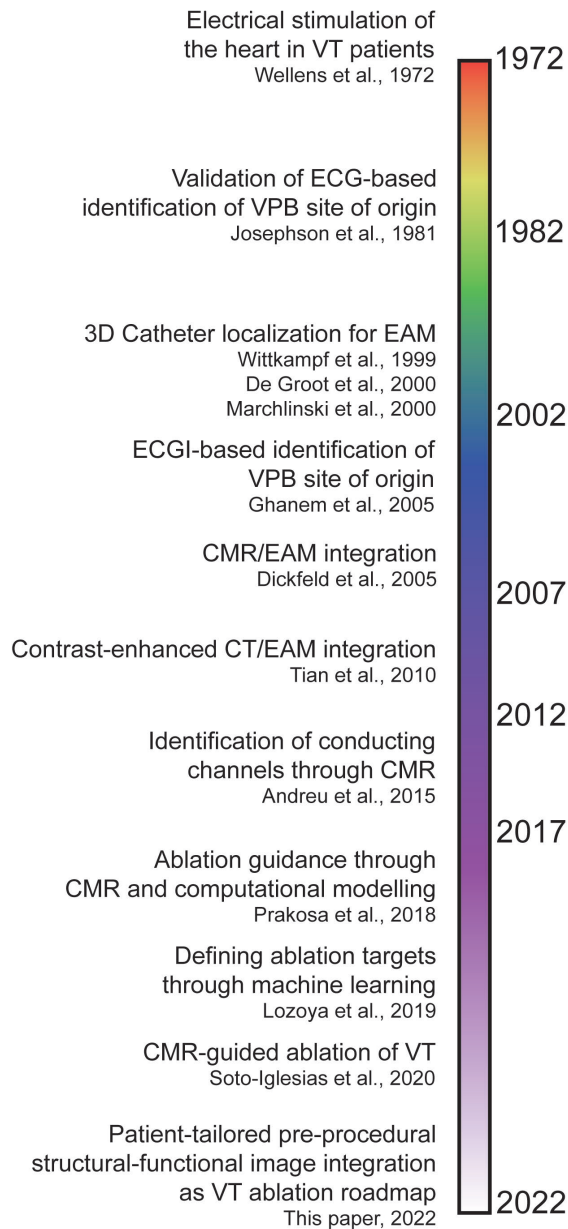


Figure 7.6: Timeline of invasive and noninvasive techniques to identify critical components of the ventricular tachycardia (VT) circuit and guide catheter ablation (52,184,192,201–203,205–209). Note that the time axis is not linear, which is reflected by the color gradients. ECG: electrocardiogram. PVC: premature ventricular complex. EAM: electroanatomical mapping. ECGI: electrocardiographic imaging. CMR: cardiac magnetic resonance imaging. CT: computed tomography.

In recent years, promising computational approaches have arisen. For example, Prakosa et al. performed CMR-based computational electrophysiological modelling, which allowed for prospective ablation guidance in a small cohort (208). Moreover, Lozova et al. used machine-learning algorithms to pinpoint ablation targets (209).

The aforementioned advances in the field of catheter-based ablation of scar-related VT have primarily focused on defining target locations for ablation through analysis of structural imaging modalities, typically CMR (208,209) and/or CT (212). Though such structural detailing holds promise and allows to noninvasively investigate the substrate and perform virtual stress tests, these strategies usually do not consider patient-specific 3D functional electrical parameters. Our current proof-of-concept patient-tailored model encompasses 3D-functional and structural information and their interactions. As an example, we have shown that invasively- and noninvasively-determined VT exits align colocalize with endings of heterogeneous tissue corridors, and are connected with the PVC site of origin. Moreover, we have demonstrated dynamic electrical instability of the heterogeneous scar region where the scar heterogeneity set the stage for an evolving VT circuit.

Combined, we argue that the integration (during spontaneous or induced PVCs and VT, including their spatiotemporal dynamics) of ECGI with high resolution 3D-LGE dark-blood CMR may be synergistic for the development of (noninvasive) individualized VT models to improve our understanding of VT mechanisms and treatment.

7.4.4 Future perspectives

Prospective studies are needed to investigate the procedural efficacy and cost-effectiveness of such personalized structural-functional models. This would require optimization of the modelling pipeline, including automated segmentation and merging of different modalities and automation of analyses, which is currently being developed.

Ideally, in future cases, ECGI recordings should be performed preprocedurally during spontaneous VT or noninvasive programmed stimulation (in the absence of deep sedation or general anesthesia) to allow preprocedural structural-functional analysis of the VT trajectory and its mechanism. This would guide targeted RF delivery to critical components of the VT circuit without the need for extensive intraprocedural voltage and pace mapping. For instance, CMR-derived heterogeneous tissue corridors (aligning to EDPs) connecting to ECGI-derived VT exit sites could be ablated. ECGI activation maps should be compared to invasively-acquired (endo- and epicardial) VT activation/propagation maps to investigate excitation accuracy, VT dynamicity and trajectories.

In absence of an ICD, CMR may replace CT for localization of ECGI electrodes and the heart geometry, thereby omitting radiation. Beyond ischemic

cardiomyopathies, this model could be extended to other cardiac diseases with increased susceptibility for VT/VF, including nonischemic and idiopathic etiologies. In the latter, ECGI uncovered previously undetected functional repolarization abnormalities, crucial for arrhythmia formation (74). Next, the model could be improved by the incorporation of static and dynamic ventricular repolarization. Furthermore, integration of our model with existing computational frameworks (digital twinning) may aid in identifying ablation targets and predict VT recurrences (risk stratification). Finally, structural-functional image modeling may be of value in novel emerging noninvasive ablation strategies, such as stereotactic cardiac radioablation (77,213).

7.4.5 Study limitations

This was a proof-of-concept study based on one exemplary case. We aimed to first develop the model before recruiting more patients, which is currently ongoing. Firstly, although the ECGI VT activation map and exit site were acquired during the procedure, the study data were merged and analyzed retrospectively. The VT ablation procedure was not guided by our model. Secondly, anatomies were merged based on visual inspection. Advanced merging methods may further improve results of invasive EAM vs. ECGI / 3D-LGE CMR comparisons (199). Thirdly, we used an epicardial-only formulation of ECGI (51) which does not actively consider *transmural* fibrosis, although this method is most widely applied and the most extensively validated, see **Chapter 2**. Lastly, we used bright-blood validated LGE CMR thresholds for scar delineation in the ADAS3D program. However, upon further analysis, in this patient, altering this threshold affected EAM vs. CMR scar comparisons by < 1%.

7.5 Conclusion

In this proof-of-concept study, we combined 3D-LGE CMR, CT and ECGI imaging modalities to develop a patient-tailored high-resolution noninvasive structural-functional model to investigate VT substrate and trigger in a case of recurrent VT in the setting of ischemic cardiomyopathy. The model accurately pinpointed the VT exit site, collocated areas of structural and functional corridors and provided insight into scar transmural and endocardial voltage characteristics. Beyond existing methods, our model encompasses beat-by-beat functional electrical information, such as dynamic 3D activation patterns of spontaneous ventricular ectopics and the VT circuit.

Data availability statement

Upon reasonable request, the raw data supporting the conclusions of this article will be made available by the authors.

Ethics statement

The studies involving human participants were reviewed and approved by the METC azM/UM. The patients/participants provided their written informed consent to participate in this study.

Author contributions

JS, MC, PV, and RTB: study setup. JS: ECGI data acquisition and processing, data integration and analysis, and manuscript draft. YK: CT wall thickness analysis. RH and SG: CMR data acquisition. RTB: EAM and clinical data acquisition. JS, MC, BH, BB, PV, and RTB: conceptualization. MC, BH, RH, SG, YK, KV, BB, PV, and RTB: critical review of manuscript. All authors have read and approved the final manuscript and data interpretation.

Funding

This study was supported by the Special Research Fund (BOF) of Hasselt University (BOF17DOCMA15) and the Maastricht University Medical Center (MUMC+), and the Netherlands CardioVascular Research Initiative (CVON2017-13 VIGILANCE) to JS; the Hein Wellens Foundation, Health Foundation Limburg (Maastricht, The Netherlands), and a Veni grant from the Netherlands Organization for Scientific Research (TTW16772) to MC; the Netherlands CardioVascular Research Initiative (CVON2017-13 VIGILANCE and CVON2018B030 PREDICT2), Den Haag, The Netherlands to PV; and a Veni grant from the Netherlands Organization for Scientific Research (NWO/ZonMw 0915016181013) to RTB.

Conflicts of interest

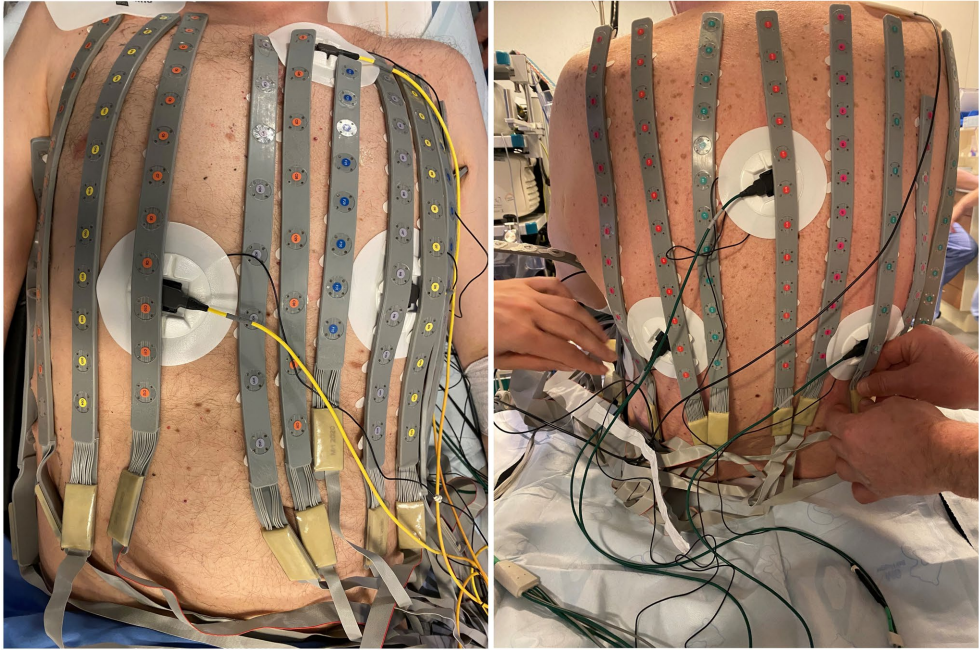
MC is part-time employed by Philips Research. The remaining authors declare that the research was conducted in the absence of any commercial or financial relationships that could be construed as a potential conflict of interest.

Supplementary Material

Supplementary Videos

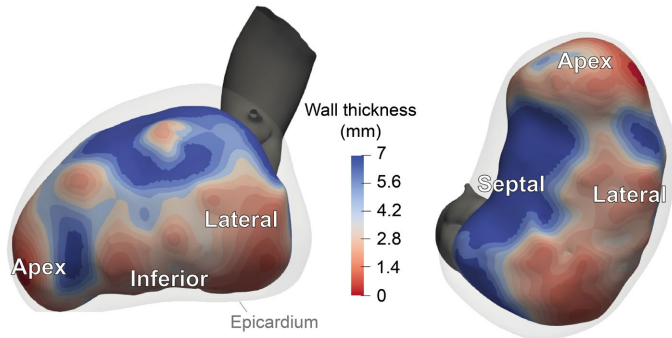
Supplementary Videos are available at <https://www.frontiersin.org/articles/10.3389/fcvm.2023.1112980/full#supplementary-material>

Supplementary Figures

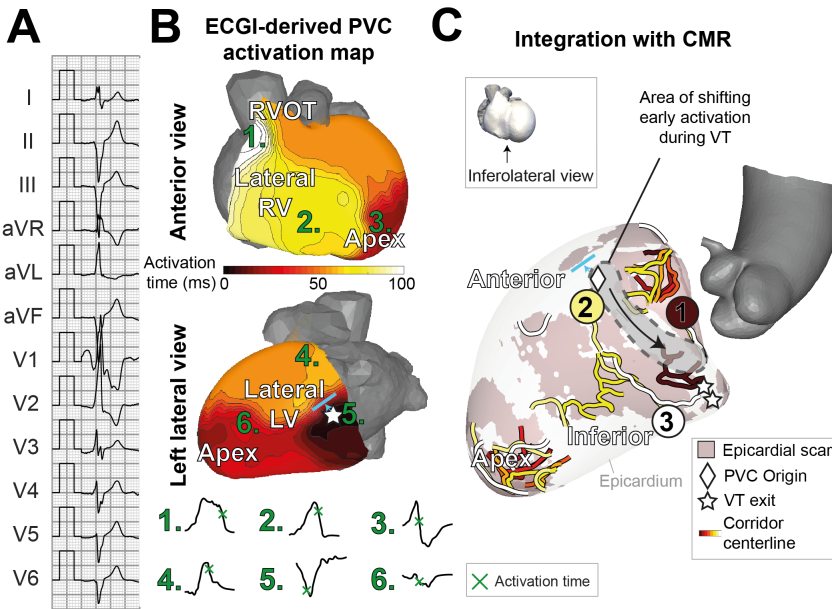


Supplementary Figure 7.1: Simultaneous body-surface potential mapping and electro-anatomical mapping during ventricular tachycardia (VT) ablation procedure.

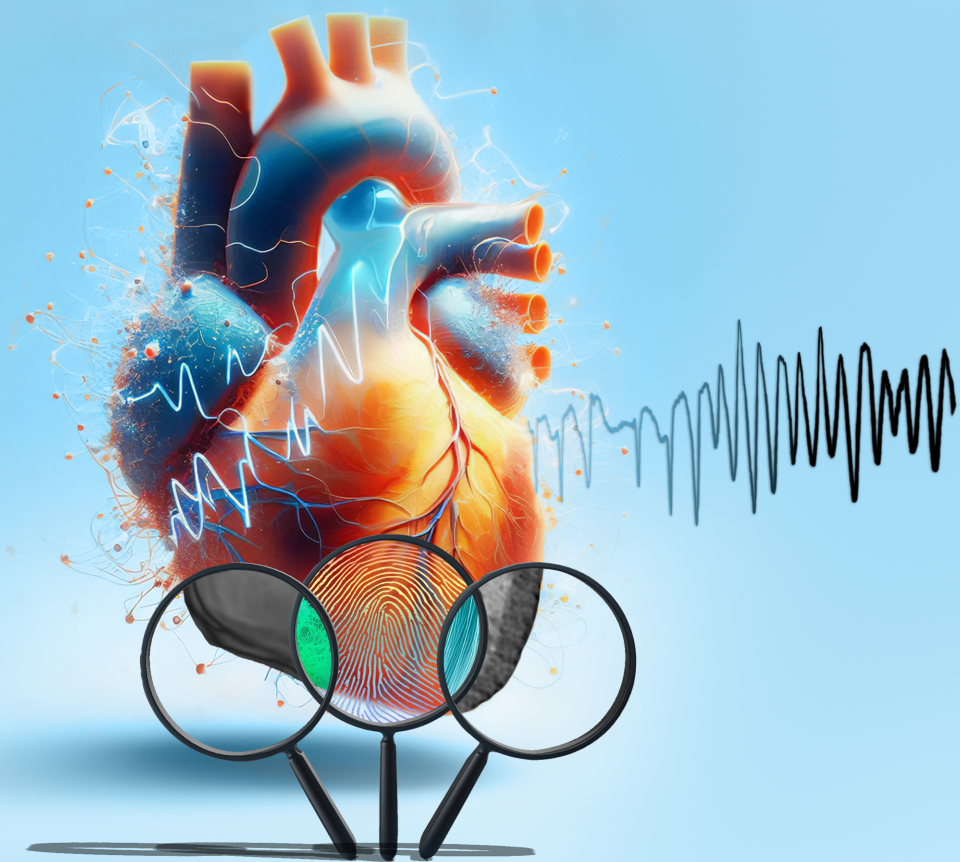
CT-derived left-ventricular wall thickness



Supplementary Figure 7.2: Left-ventricular (LV) wall thickness analysis through contrast-enhanced multidetector computed tomography (CT). The basal inferolateral and apical aspects of the LV show wall thinning.



Supplementary Figure 7.3: Hypothesis on trigger-substrate interaction. Electrocardiographic imaging (ECGI) and integration with 3D dark-blood late gadolinium enhancement cardiac magnetic resonance imaging (LGE CMR). **A:** 12-Lead electrocardiogram (ECG) of premature ventricular complex (PVC). **B:** Activation map of this PVC through ECGI. The crowded activation isochrones in the left lateral view, depicted in gray, suggest conduction block. **C:** Structural-functional image overlay of 3D dark-blood LGE CMR (**Figure 7.4**) and ECGI-derived activation map during PVC (B). 1, 2 and 3 indicate possible heterogeneous tissue corridors through which the ventricular tachycardia (VT) could have travelled to reach the exit site.



CHAPTER 8

General Discussion

Table of Contents of the General Discussion

8.1 Mechanistic understanding of ventricular arrhythmogenesis	178
8.1.1 Concepts of reentry.....	180
8.1.2 Coumel's triangle of arrhythmogenesis	182
8.1.3 The Circle of Reentry framework and the role of excitability	182
8.1.3.1 Substrate	183
1) <i>Local dispersion of excitability</i>	186
2) <i>Balance between regions of excitability and inexcitability</i>	190
8.1.3.2 Trigger	190
3) <i>The timing of the trigger relative to the excitability dispersion</i>	190
4) <i>Trigger origin relative to excitability dispersion</i>	192
8.1.4 The relevance of a personalized multimodal approach	192
8.2 Risk stratification for and treatment of individuals at risk for SCD	194
8.2.1 Current identification of individuals at risk for SCD	194
8.2.2 Current treatment of individuals at risk for SCD	196
8.2.3.1 The variability of arrhythmia propensity over time	197
8.2.3.2 Updating of risk stratification models	197
8.2.4 Future outlook: mechanism-based risk stratification and treatment for SCD.....	199
8.2.4.1 Personalized 3D computational heart models	199
8.2.4.2 The relevance of a personalized multimodal approach	199
8.2.4.3 Mechanism-based and noninvasive therapies	200
8.3 Conclusion	203

In this Chapter, I provide a broader perspective on the findings described in this PhD thesis. Overall, the aims of my doctoral work were to better explain human ventricular tachyarrhythmias through multimodal image integration. **Figure 8.1** summarizes the major results that collectively demonstrate that multimodal image integration enables a better characterization of VT/VF substrates, improves risk stratification of SCA/SCD and can improve the diagnostic and therapeutic management of VT.

The General Discussion consists of two sections:

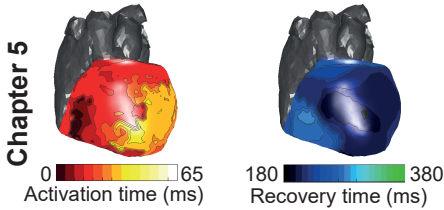
- **Section 8.1** focuses on the mechanistic understanding of VT, addressing concepts such as circular reentry, Coumel's triangle of arrhythmogenesis, and the novel framework "Circle of Reentry".
- In **Section 8.2**, I address risk stratification and treatment for SCA/SCD by VT/VF. I discuss current clinical decision-making tools and management, and the challenges associated with identifying individuals at risk for SCD. Based on the findings of this thesis, I provide a schematic for improved mechanism-based arrhythmia-risk prediction in a personalized manner.

Achieved in this thesis

Mechanistic understanding of pathophysiology

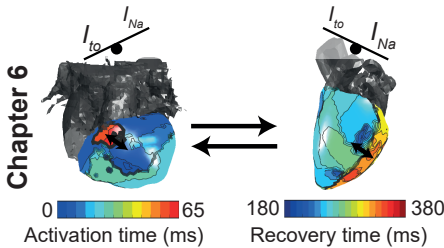
Physiology

Normal subjects



Pathology

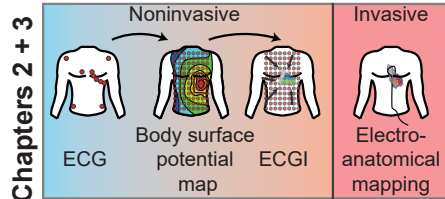
DPP6: $I_{to} \leftrightarrow I_{Na}$ balance



Advanced assessment of structure and function

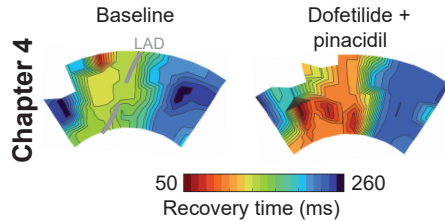
Function

State-of-the-art overview and improved interpretation of ECGI



Function

Recovery time determination in unipolar contact electrogram



Pathology

Structure + Function

Multimodal image integration in postinfarct VT

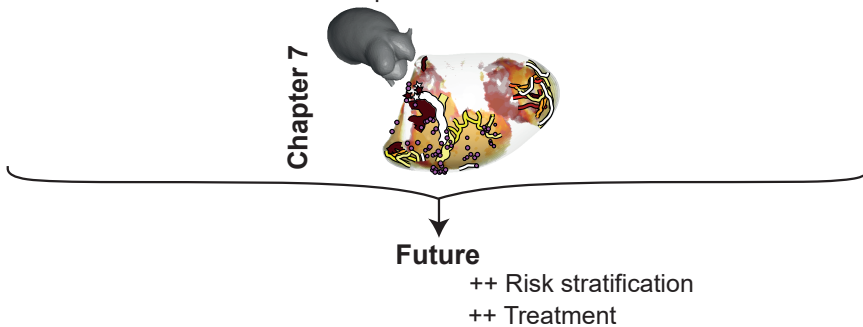


Figure 8.1: Summary of the major results of this thesis, achieved by multimodal image integration. Left: **Chapter 5** and **Chapter 6** have led to improved mechanistic understanding of ventricular pathophysiology. Right: **Chapter 2**, **Chapter 3** and **Chapter 4** have led to improved experimental and clinical application of tools used to investigate cardiac electrophysiology. Bottom: **Chapter 7** has led to improved mechanistic understanding and clinical application of tools that assess pathological cardiac function and structure.

8.1 Mechanistic understanding of ventricular arrhythmogenesis

8.1.1 Concepts of reentry

The concept of reentry as a mechanism of VT was established by Mayer (214), Mines (215) and Garrey (216) in the early 20th century. They performed experiments in which they mechanically or electrically stimulated circular structures, such as Scyphomedusae (jellyfish) or tissue rings excised from turtle or fish hearts (see **Figure 8.2A**, left). This caused two excitation wavefronts to travel in opposite directions: one clockwise, the other counterclockwise. Propagation ceased at the opposite side of the circle where both wavefronts collided, as they both encountered refractory tissue (**Figure 8.2A**, middle). By blocking one wavefront near the stimulus site and allowing the other to propagate, the remaining wavefront could circulate indefinitely, generating a reentry wave (**Figure 8.2A**, right).

In 1946, Wiener and Rosenblueth (217) mathematically formulated that the reentry wavelength is determined by multiplying the conduction velocity by the duration of the refractory period. For reentry to initiate and persist in circular tissue, the wavelength should not exceed the circumference of the circle to avoid encountering refractory tissue and "biting its own tail". This pioneering work revealed several key insights:

1. Unidirectional block is required for reentry-based arrhythmia formation and maintenance.
2. Shorter refractoriness increases the likelihood of reentry.
3. Slower conduction increases the likelihood of reentry.

In 1977, Allesie et al. demonstrated reentrant arrhythmias in rabbit atria without structural obstacles through microelectrode recordings (218,219) in either a circular fashion (**Figure 8.2B**) or a more complex figure-of-eight (**Figure 8.2C**). In the three-dimensional (3D) heart, the propagation of reentrant wavefronts is usually much more complex (see **Figure 8.2D**), and is influenced by anatomical, functional and structural tissue characteristics (220).

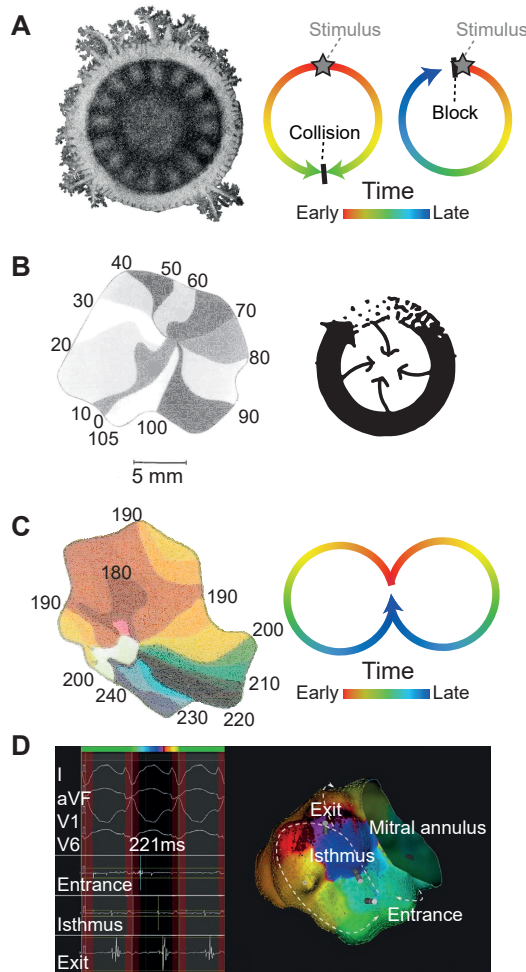


Figure 8.2: Concepts of reentry, from simple (A) to more complex (D). **A:** reentry in a Scyphomedusa (jellyfish) by Mayer (214). Left: anatomical image. Middle: a stimulus is given at the top of the circle, causing simultaneous propagation of a clockwise and a counterclockwise wavefront. These collide at the bottom of the circle, and cannot propagate further as they both encounter refractory tissue. Right: If one wavefront is blocked close to the stimulus site, the other can travel indefinitely, causing a reentrant wave. **B,** left: Activation isochrones during functional reentry without an anatomical substrate in the rabbit atrium, as shown by Alessie et al. (219). Right: schematic view of the reentry (219). The reentry wave exhibits a centripetal character, with activation spreading in a circular motion, from the outer ring to its center. **C:** Figure-of-eight reentry by Alessie et al. (218) in which two circular wavefronts occur simultaneously. **D:** Activation mapping of a more complex clinical VT, by Martin et al. (221), where the course of the wavefront is dependent on 3D anatomical, functional and structural characteristics of the tissue.

8.1.2 Coumel's triangle of arrhythmogenesis

In 1987, Coumel (Figure 8.3) summarized three essential elements for clinical arrhythmia development (222,223). These consist of:

1. The arrhythmogenic substrate. This refers to underlying conditions such as ischemic or nonischemic cardiomyopathy, or non-structural heart disease.
2. The trigger. This represents the abnormal electrical excitation that initiates arrhythmia.
3. The modulating factors. These can influence the trigger, substrate, or their interactions. Typically, the autonomic nervous system acts as the modulating factor (224).

The presence and severity of these elements can vary over time. However, when their combination reaches a critical point, they can create a "perfect storm" precipitating arrhythmia.

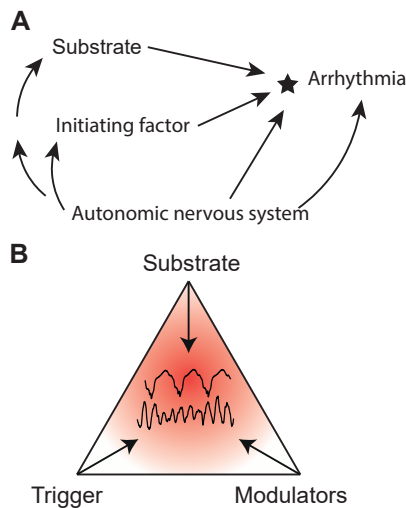


Figure 8.3: Coumel's theory of arrhythmogenesis. **A:** Coumel's original concept (223), showing that "the substrate and the initiating factor should combine (star) to produce the clinical arrhythmia. The autonomic nervous system may generate or modify the substrate and the initiating factor, allow their combination, and influence the arrhythmia itself". **B:** Adapted form of panel A, generally known as "Coumel's triangle of arrhythmogenesis". Any clinical arrhythmia is the result of the interaction of three ingredients: the substrate, trigger, and modulators.

8.1.3 The Circle of Reentry framework and the role of excitability

Recently, an advanced mechanistic framework for arrhythmia initiation was introduced by Cluitmans et al. (29), which integrates the concepts of reentry and Coumel's triangle to directly assess arrhythmia propensity based on spatiotemporal characteristics, see **Figure 8.4**. This framework, designated "the Circle of Reentry", consists of four elements (spatial vs. temporal, and substrate vs. trigger) influenced by modulators:

Substrate

1. Local dispersion of excitability.
For example, myocardial areas of (relatively) short refractoriness neighboring areas of (relatively) long refractoriness can cause unidirectional block.
2. The size balance between areas of excitable versus inexcitable myocardium.
A disbalance can cause a wavefront to die out at the threshold of inexcitability, as it lacks sufficient time to travel to the other region. This also depends on its conduction velocity.

Trigger

3. The timing of the trigger relative to the local dispersion of excitability.
Early triggers can cause unidirectional block, whereas late triggers can propagate without block. An example of an early trigger is represented by the "R on T" phenomenon on a 12-lead ECG, where (under pathological conditions) a (very) premature ventricular complex (PVC) during ventricular repolarization can result in VT/VF.
4. The origin of the trigger relative to the local dispersion of excitability.
Triggers from early-excitable regions lead to unidirectional block more likely than those from late-excitable regions.

The Circle of Reentry enables a comprehensive assessment of arrhythmia propensity by considering these interconnected elements and their modulation. The resulting reentry can be singular, caused by a "mother rotor" (potentially leading to VT or VF), or consist of multiple (chaotic) wavelets (predisposing to VF) (225).

8.1.3.1 Substrate

To assess substrate characteristics and arrhythmia propensity, catheter-based electro-anatomical mapping (EAM) and noninvasive ECG-imaging (ECGI) are particularly suitable as they record individual functional-structural characteristics of the heart (see **Chapter 2** and **Chapter 7**). However, the determination of local recovery time (RT) from the unipolar electrogram (UEG) in any of these techniques has been a topic of debate, hindering assessment of ventricular electrical recovery. In **Chapter 4**, we addressed the controversy surrounding local RT determination from the UEG, proposing a unified assessment of repolarization, which is used further throughout this thesis.

A thorough understanding of normal electrophysiology is crucial for comprehending arrhythmias. However, detailed analysis of ventricular electrophysiology in normal human subjects is sparse, particularly regarding the influence of sex and age. In **Chapter 5**, we used ECGI to expand our knowledge of localized electrical activation and recovery in normal individuals related to age, sex, and temporal dynamics. We found that despite normal ECGs, epicardial activation and recovery were profoundly different between individuals, but stable within an individual over time spans of seconds to minutes. Aberrant activation and recovery sequences were observed in subjects with bundle branch block or long-QT syndrome. These findings pave the way for further investigations of cardiac electrophysiology and VT/VF.

Importantly, in the context of tissue- or whole-heart arrhythmogenesis, excitability should be expressed with respect to a common reference in time. For example, the moment of end of local repolarization should be expressed in terms of *RT* (relative to a global common reference) rather than a local *ARI* or action-potential duration (APD; see also **Figure 4.2**) because relative changes in *RT* form dispersion of excitability. *RT* dispersion can be caused by heterogeneity in either *AT* (e.g., structural scar can cause zig-zag conduction through small conducting channels), *ARI* (e.g., macroscopic late-repolarizing areas can neighbor early-repolarizing areas in long-QT syndrome (64)), or both. These can result from structural or functional abnormalities (see **Figure 8.5**) and lead to unidirectional block.

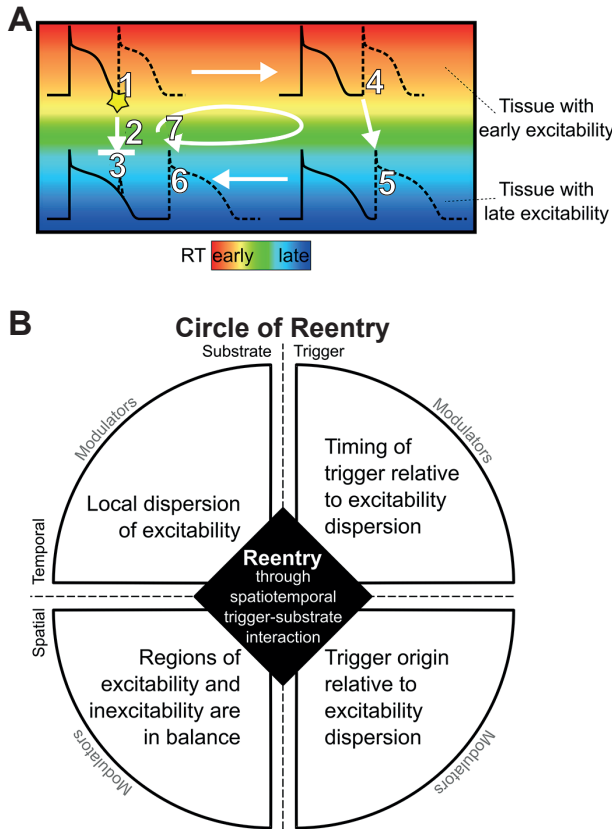


Figure 8.4, used from (29): The Circle of Reentry, by Cluitmans et al. A: Illustration of reentry in tissue. The tissue is color-coded for recovery time (RT, with the assumption that it resembles recovery from refractoriness). A premature beat from an early RT region (1) may be blocked by refractory tissue with a longer RT (2) and fail to activate the late RT region (3). If the early RT region is sufficiently large, the wavefront may propagate through it (4) while the late RT region recovers from refractoriness. When the wavefront arrives at the repolarized late RT region, this region can be reactivated (5). The wavefront can then travel back to the previously refractory region, now excitable (6), and restart the circuit (7). **B:** Original text: “The Circle of Reentry proposes four requirements for reentry arising from spatiotemporal interactions between trigger and substrate: (1) local dispersion of excitability (e.g., steep RT gradients), (2) a balance in size of the region of excitability and the region of inexcitability (e.g., sufficiently large region of early RT), (3) a trigger originating at a time when some tissue is excitable and other tissue is inexcitable (e.g., an early premature beat), and (4) which occurs from an excitable region (e.g., from early RT region). Each of the four elements can be affected by modulators.” (29)

1) Local dispersion of excitability

Increased spatial dispersion of excitability has been observed in dofetilide-infused (226) and sotalol-infused (227) dog hearts before arrhythmia, in patients with ischemic or nonischemic cardiomyopathy and VT (228), in survivors of idiopathic ventricular fibrillation (74), in critical sites for VT in humans (87) and pigs (229) with ischemic heart disease, and in the ischemic zone and structural border zone of pigs with prior myocardial infarction (230).

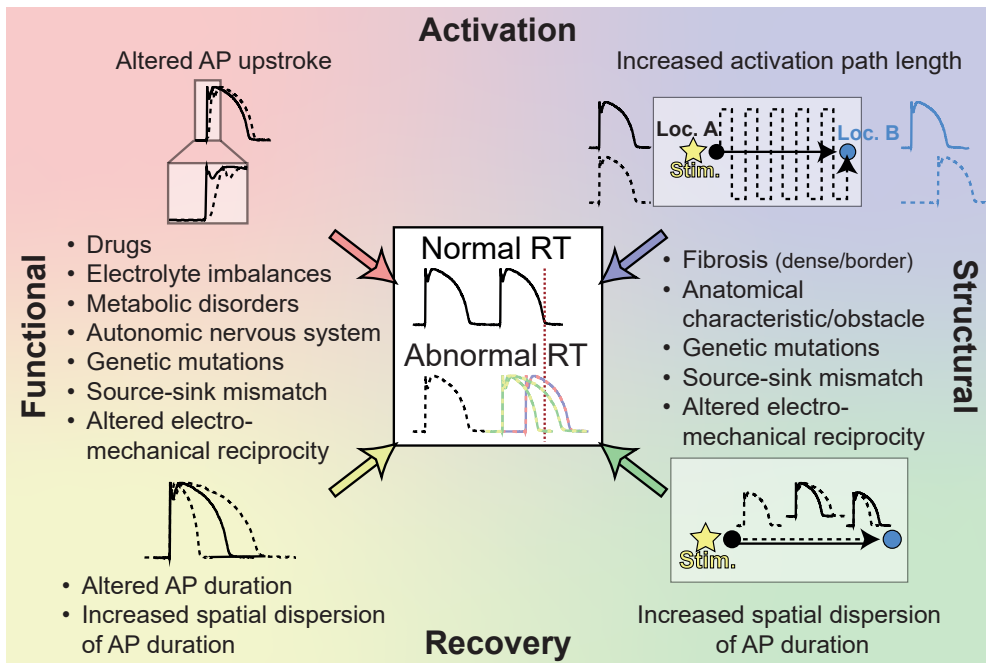


Figure 8.5: Abnormal excitability can be caused by pathologies in two axes: changes in activation (top) or recovery (bottom), which can be structural (left) or functional (right). Normal action potentials are shown in solid, abnormal action potentials in dashed lines. Functional changes in excitability can be caused by drugs, genetic mutations, electrolyte imbalances, metabolic disorders, or mechanics. These lead to altered action potential (AP) upstroke, or duration. Structural changes in excitability can be caused by fibrosis, anatomical obstacles, source-sink mismatches, or mechanics. These lead to heterogeneous activation or AP duration.

To illustrate the applicability of excitability dispersion to arrhythmia propensity, we applied ECGI in various cases with VT/VF: long-QT syndrome type 3 (LQT3, from **Chapter 5**), survivors of idiopathic ventricular fibrillation (IVF) and idiopathic VTs, ischemic cardiomyopathy (ICM, from **Chapter 7**) and twice in a subject with dilated cardiomyopathy and left bundle branch block (DCM; once the day of VT (DCM + VT), once a year later (DCM - VT)). See **Figure 8.6A** for their characteristics.

Spatial dispersion of electrical recovery (defined as “RT dispersion”; standard

deviation of RTs over the ventricular epicardium) of these subjects was compared to controls, see **Figure 8.6B-D**. As illustrated in **Figure 8.6B**, RT dispersion can be caused by dispersion in either AT or ARI. In most disease conditions (LQT3, IVF, ICM, DCM + VT), it was higher than in controls. In the DCM - VT subject, RT dispersion remained relatively high but decreased a year after the VT episode (Left panel of **Figure 8.6B**, orange vs. yellow). We speculate that the subject's substrate was affected by modulators in the (anti)arrhythmic setting, e.g., by medication and/or the decrease of concomitant myocardial ischemia or failure. Compared to controls, RT distribution curves were wider in LQT3 and IVF patients, and more binomial in ICM and DCM + VT subjects (**Figure 8.5D**). The patient with a *DPP6* p.(Arg274His) missense mutation from **Chapter 6** also exhibited increased RT dispersion with respect to controls, see **Figure 6.5**. Assuming that RT resembles excitability in these cases, we suggest that excitability dispersion was also increased in the subjects discussed above.

However, importantly, RT dispersion during sinus rhythm in a stable setting does not fully capture the complexity of excitability dispersion, as the latter is influenced by various modulating factors (231,232), activation pattern, coupling interval (227), and possibly, postrepolarization refractoriness (113). Finally, RT dispersion can be defined in different ways: e.g., localized late AT (e.g., in the right ventricular outflow tract, as in **Figure 2.4** and **Figure 6.5**) may lead to localized late RT, but not necessarily to an increased standard deviation of RTs across the entire heart.

The mechanisms of excitability dispersion in different cardiac diseases have been widely investigated. In ischemic VT, increased RT dispersion at critical sites for VT or border zones is attributed to the spatially heterogeneous expression of ion-channel subunits, leading to heterogeneous APDs (230). Gap-junction function and connexin-43 kinetics are also altered at these critical sites (233). Site-directed connexin-43 gene transfer in a pig model of myocardial infarction reduced VT susceptibility (234), indicating the causal role of these factors in VT and suggesting that disease-induced remodeling is amenable for repair. In other pathologies, abnormal intracellular calcium handling leading to spatially discordant APD alternans plays a role in increased RT dispersion (235), which is likely multifactorial.

In terms of specific localized vulnerability to reentry, early-repolarizing areas adjacent to late-activating areas are particularly vulnerable to reentry, see **Figure 8.7**. These areas exhibit a low "reentry vulnerability index" (RVI), which predisposes to unidirectional block (236–238). At least in some conditions, accurate mapping of RVI has the potential to make VT induction protocols obsolete, eliminating the risk of hemodynamic compromise. Prolongation of RT near infarct-border zones (which can be associated with low RVI (238) and VT exit) reduced the inducibility of VT in post-infarct pigs. These findings further validate RVI in identifying sites with increased susceptibility to VT (239,240).

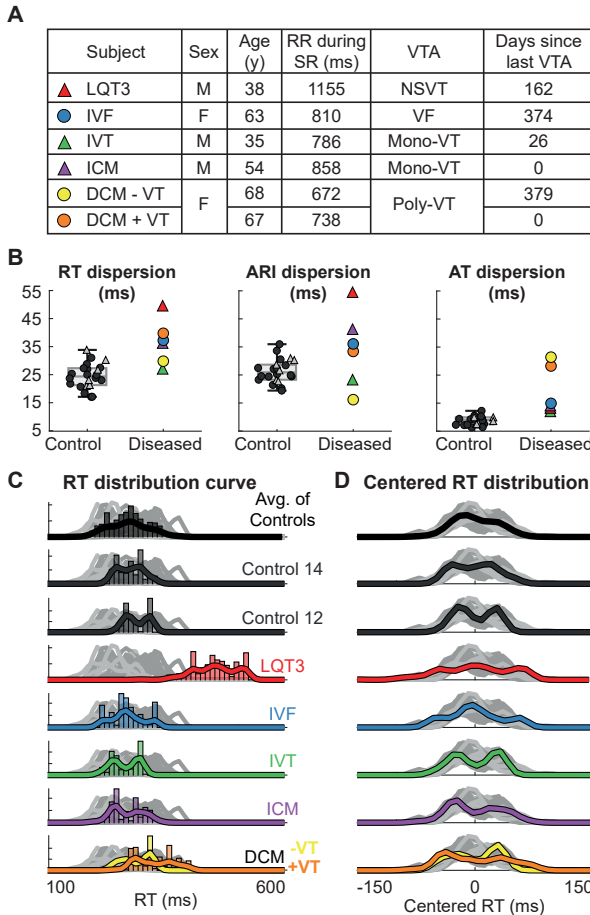


Figure 8.6: Spatial dispersion of electrical recovery during sinus rhythm as measured by ECGI in subjects who experienced VT or VF, compared to controls. SR: sinus rhythm. LQT3: Long-QT syndrome type 3. IVF: idiopathic ventricular fibrillation. IVT: idiopathic ventricular tachycardia. ICM: ischemic cardiomyopathy (see **Chapter 7**). DCM: dilated cardiomyopathy. NSVT: non-sustained VT. Mono-VT/Poly-VT: monomorphic/polymorphic VT. A: subject characteristics. The DCM subject was included twice: once on the day of VT, once a year later in a stable phase. B: Dispersion of RT, ARI and AT, calculated as their standard deviations over the entire epicardium, compared to controls (see **Chapter 5**). C: distribution of absolute RTs in different subjects. D: Distribution of RTs in different subjects, centered at an average value of 0. The average RR interval of all controls was 879 ms. Controls 14 and 12 had RR intervals of 771 ms and 979 ms, respectively. The RT dispersion of controls 14 and 12 closely matched the 33rd and 66th percentile of average RT dispersion of all controls, respectively.

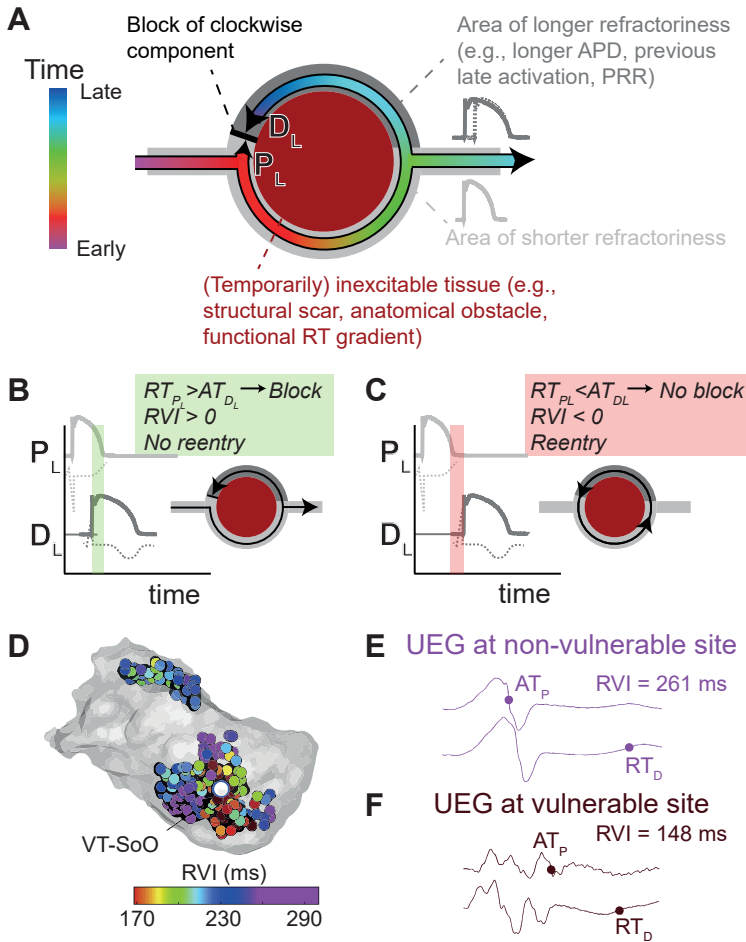


Figure 8.7: Schematic drawing of the reentry vulnerability index (RVI). **A:** An electrical stimulus is given at the left-hand side of the tissue. The dark red area denotes (temporarily) unexcitable tissue. The lower (light grey) part of the tissue has relatively short refractoriness, whereas the upper (dark grey) part has longer refractoriness. When arriving at the bifurcation (right), the clockwise component of the wavefront will block against the area of longer refractoriness in the proximal location (P_L). The counterclockwise component will travel further up to the distal location (D_L). This leads to either bidirectional block (**B**) or reentry (**C**), depending on the time difference between the recovery time (RT) at P_L and the activation time (AT) at D_L (with the assumption that RT resembles recovery from refractoriness). **B:** If ERP at P_L exceeds AT at D_L , RVI is larger than 0, leading to bidirectional block. **C:** If ERP at P_L is exceeded by AT at D_L , RVI will be smaller than one, leading to reentry. A lower RVI indicates a higher local risk of reentry. **D:** Clinical RVI-map adapted from Orini et al. (238) RVI is lowest close to the VT site-of-origin (VT-SoO). **E** and **F** show unipolar electrograms (UEGs) at a non-vulnerable site and a vulnerable site, respectively.

2) Balance between regions of excitability and inexcitability

The initial demonstration of such critical balance facilitating reentry was provided by Cluitmans et al. (72) In a computational model of the ventricular epicardium, they simulated shorter RT in part of the epicardium than the rest of the tissue. This difference was achieved by blocking the rapidly-activating delayed-rectifier potassium channel. Vulnerability to reentry increased if the surface area with early repolarization was close to that with late repolarization. Subsequently, Cluitmans et al. confirmed the importance of this ratio in survivors of idiopathic ventricular fibrillation (74), underscoring that a functional substrate in such patients can have severe arrhythmic consequences.

Based on the results of this thesis work, we pose that the balance between excitable and inexcitable regions can change throughout the recovery of a heart beat, and “early” vs. “late” recovery may occur on a continuous scale rather than a binary one (as in (functional) circle reentry, **Figure 8.2A-B**).

8.1.3.2 Trigger

Both the timing and location of the trigger play crucial roles in initiating reentry. Triggers for reentry can arise from distinct mechanisms of abnormal impulse formation: early and delayed afterdepolarizations (EADs and DADs) leading to triggered activity, abnormal automaticity, and repolarization gradient-induced reexcitation (241), as depicted in **Figure 8.8**. The first three cellular mechanisms are often related to modifications in membrane currents, whereas the last mechanism involves interactions with adjacent tissue. Under the right conditions, any of these mechanisms can lead to the occurrence of an extrasystole.

3) The timing of the trigger relative to the excitability dispersion

EADs typically occur during phase 2 or 3 of the cardiac action potential when the action potential duration is prolonged, e.g., in long-QT syndrome, during severe hypokalemia, or due to repolarization-prolonging drugs (242). These conditions cause an imbalance between depolarizing and repolarizing currents, effectively prolonging repolarization and promoting arrhythmia (243). EADs can also contribute to the dispersion of ventricular repolarization, affecting the substrate (244,245).

DADs are depolarizing afterpotentials that occur after full repolarization. They can arise under various conditions that result in intracellular calcium overload and spontaneous release of calcium from the sarcoplasmic reticulum (14). DADs are notoriously difficult to record in the clinic, but likely underestimated as (contributing) arrhythmogenic triggers in the human heart.

Abnormal automaticity refers to the pathological property of cardiac cells, other than normal pacemaker cells, that leads to spontaneous generation of action potentials via phase-4 depolarization. This can be modulated by an increased extracellular potassium concentration, alterations in the function or expression of I_{K1} channels (246), increased sympathetic activity and hypertrophic remodeling

leading to the expression of the pacemaker current I_f in myocytes. (247)

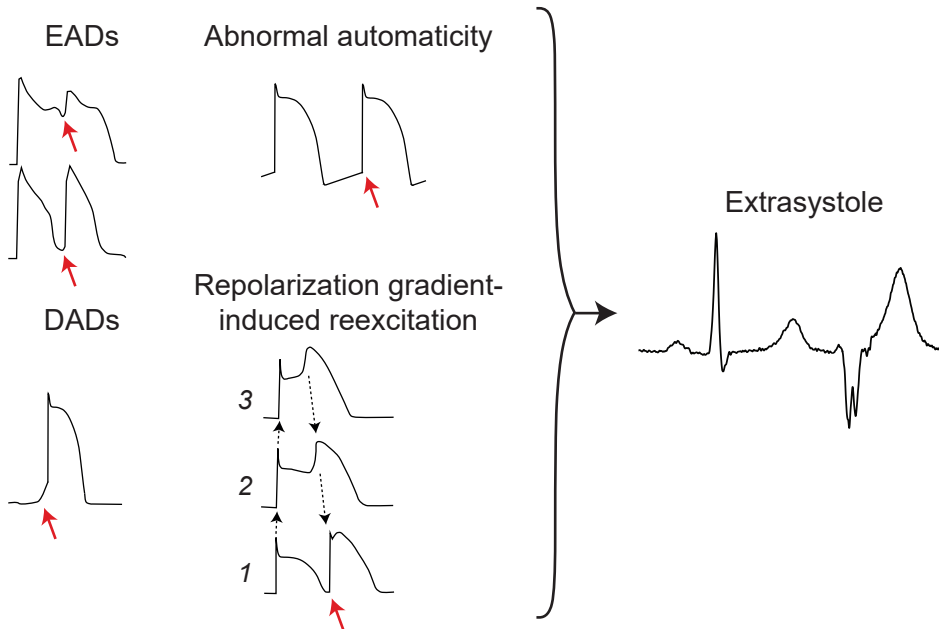


Figure 8.8: Mechanisms of abnormal impulse formation. EAD: early afterdepolarization. DAD: delayed afterdepolarization. Bold arrows indicate abnormal impulse formation. EADs can arise during phase 2 or 3 of the action potential. In repolarization gradient-induced reexcitation, a proximal site of activation (1) is reexcited because of a repolarization gradient opposing the direction of the initial activation wavefront (i.e., repolarization takes longer in location 3 than in location 1, while the initial activation wavefront travelled from location 1 to 3). Strictly spoken, the latter is a reentrant mechanism based on abnormal impulse conduction.

While EADs, DADs, and abnormal automaticity are cellular phenomena, a critical minimal number of myocytes is required to propagate triggered action potentials such that they initiate an arrhythmia. The synchronization of depolarizations in time and space is necessary to reach this critical mass (245). E.g., it has been calculated that approximately 700,000 cells are required for EADs to produce a propagating wavefront in healthy tissue (248). Factors such as reduced gap junction conductance, fibrosis, reduced repolarization reserve, and electrical remodeling of the myocardium can significantly decrease the number of cells needed to produce propagating action potentials. Additionally, the His-fascicular-Purkinje system is more prone to triggered activity due to more “favorable” source-sink mismatches (248).

Furthermore, a significant repolarization gradient between adjacent regions can lead to the reexcitation of early-repolarizing tissue by late-repolarizing tissue, which is known as the “R-from-T” phenomenon (241). Such scenarios can arise during ischemia or possibly Brugada syndrome (phase 2 reentry (249)), long-

QT syndrome, and other conditions that cause significantly heterogeneous repolarization (241). In any scenario, the high-potential area must be sufficiently large to reexcite the adjacent region due to source-sink mismatches. Early triggers such as EADs and reentrant excitation are more likely to elicit reentry than late triggers (29,74), although the initiation of reentry depends on the complex interplay of spatiotemporal characteristics, as captured in the Circle of Reentry.

4) Trigger origin relative to excitability dispersion

Triggers may initiate reentry more easily when they originate from early-excitabile regions (74), because those from late-excitabile regions are less likely to experience unidirectional block. In postinfarct VT, triggers most often arise from within, or in proximity to, structural channels due to more favorable source-sink mismatches (241). These sites are typically associated with an increased dispersion of excitation and generally more prone to reentrant mechanisms. Triggers from the Purkinje system, when located close to early-excitabile myocardium, may also evoke reentrant arrhythmia. Abnormal activation of Purkinje fibers has been frequently observed in patients with idiopathic ventricular fibrillation (250).

8.1.4 The relevance of a personalized multimodal approach

In this thesis, I have demonstrated the importance of multimodal image integration in gaining a comprehensive understanding and assessment of cardiac electrophysiology and arrhythmogenesis.

- In **Chapter 4**, I integrated findings from computational models, historical experimental studies and own investigations using contact mapping and ECGI to gain insights into repolarization in the unipolar contact electrogram. This integration led to a better understanding of the unipolar contact electrogram, and assessment of RT therein.
- **Chapter 5** focused on activation and recovery maps in normal subjects using ECGI, which integrates body-surface potential mapping and imaging of the heart/thorax. This electroanatomical integration enabled to contextualize normal electrophysiology on the ventricular epicardium and identify pathological deviations. I observed typical sites of first and last epicardial activation and repolarization and studied differences between left and right ventricles. I found aberrant and prolonged activation or repolarization in subjects with bundle branch block or long-QT syndrome. Moreover, I demonstrated that high-resolution patterns of activation and repolarization during sinus rhythm are variable between subjects, and that global characteristics are influenced by sex and age. The characteristics of an individual's 3D heart electrophysiology is highly personal and complex, influenced by many anatomical and functional characteristics such as the anatomy and function of the Purkinje network, the conduction system at large, the moderator band(s), papillary muscles, trabecularization and

false tendons, the autonomic nervous system; endocardial, transmural and epicardial differences in activation and recovery; underlying ion-channel expression; and hormone levels (see **Figure 8.9**). Pathological conditions impacting any of these anatomical structures and physiological functions can increase an individual's risk of VT/VF. This emphasizes the importance of complete multimodal phenotyping (preferably also under normal conditions) to determine arrhythmia susceptibility in a personalized manner.

- In **Chapter 6**, we integrated genetic information, patch clamp studies, computational modeling, ECG, and ECGI, to unravel the importance of the I_{Na} - I_{to} balance for ventricular arrhythmogenesis. We demonstrated that variants in the *DPP6* gene can alter I_{Na} and I_{to} , affecting cellular and tissue electrophysiology *in silico* as well as *in vivo*. This translational integration, from cell to bedside, provided novel insights into the mechanisms underlying VT/VF in *DPP6*-variant positive patients.
- In **Chapter 7**, I presented a case study of ischemic VT, where I integrated EAM, ECGI, ECG, CT, and CMR. By doing so, I revealed novel structural-functional relationships, e.g., by showing that concealed areas of slow conduction (in EAM) corresponded to structural heterogeneous tissue corridors (in CMR). Furthermore, the VT-exit site (as assessed from ECG, ECGI and EAM) aligned with the ends of CMR-identified structural corridors.

8.2 Risk stratification for and treatment of individuals at risk for SCD

8.2.1 Current identification of individuals at risk for SCD

Current clinical management aims at preventing any first occurrence of VT/VF (primary prevention) or subsequent episodes after an initial event (secondary prevention). See **Figure 8.10** for a timeline of risk stratification for SCD.

ICDs are commonly implanted for the primary prevention of SCD, but it is challenging to select individuals at an intermediate risk for which the benefit of implantation outweighs short- and long-term complications. In patients with systolic heart failure, primary prevention typically relies on left-ventricular ejection fraction (LVEF) as a population-based clinical determinant. However, only 3-5% of implanted patients with reduced LVEF (<35%) receive appropriate ICD shocks annually, which is about equal to the number of ICD revisions (3%) (5,251). Secondary prevention is installed in case of previous VT/VF occurrence, resulting in varying rates of appropriate ICD therapy (20-58% in 5 years, depending on disease etiology (252,253)). Thus, many patients undergo unnecessary ICD implantations. This aspect, combined with the high costs and the risk of complications (including inappropriate shocks (254)) continuously prompt attempts to improve arrhythmia risk prediction. Single population-based markers (LVEF or previous VT/VF occurrence) fail to accurately assess arrhythmia risk, which is multifactorial, disease-specific and highly individualized (255).

A more effective strategy involves risk stratification based on multiple markers specific to each disease. Risk calculators have been developed for primary prevention of SCD in several arrhythmogenic syndromes, improving accuracy in risk assessment (4,263–266). Some are included in the 2022 ESC Guidelines for the Management of Patients with Ventricular Arrhythmias and the Prevention of Sudden Cardiac Death (4). Risk calculators typically predict a 5-year risk of life-threatening VT/VF, and an arbitrary cutoff (e.g., 5%) is used to advise for or against ICD implantation. At this cutoff (5%), 19 out of 20 ICDs do not provide any therapy. Recent artificial intelligence (AI)-based approaches appear promising in predicting VT/VF recurrence, but they require further validation and incorporation of arrhythmogenic understanding (267).

Just like AI-based approaches, clinical risk-stratification models often lack the mechanistic characteristics of arrhythmias, such as those incorporated in the Circle of Reentry, which considers the three-dimensional structure of the arrhythmogenic substrate and individual patient-specific mechanisms. Factors such as 3D-scar location and density, activation and recovery heterogeneity, and trigger origin and timing play crucial roles (29), as demonstrated in **Chapter 7**, but are typically neglected in population-based statistical models.

Anatomical and functional characteristics of the apparently normal human heart that may influence an individual's risk of VT/VF

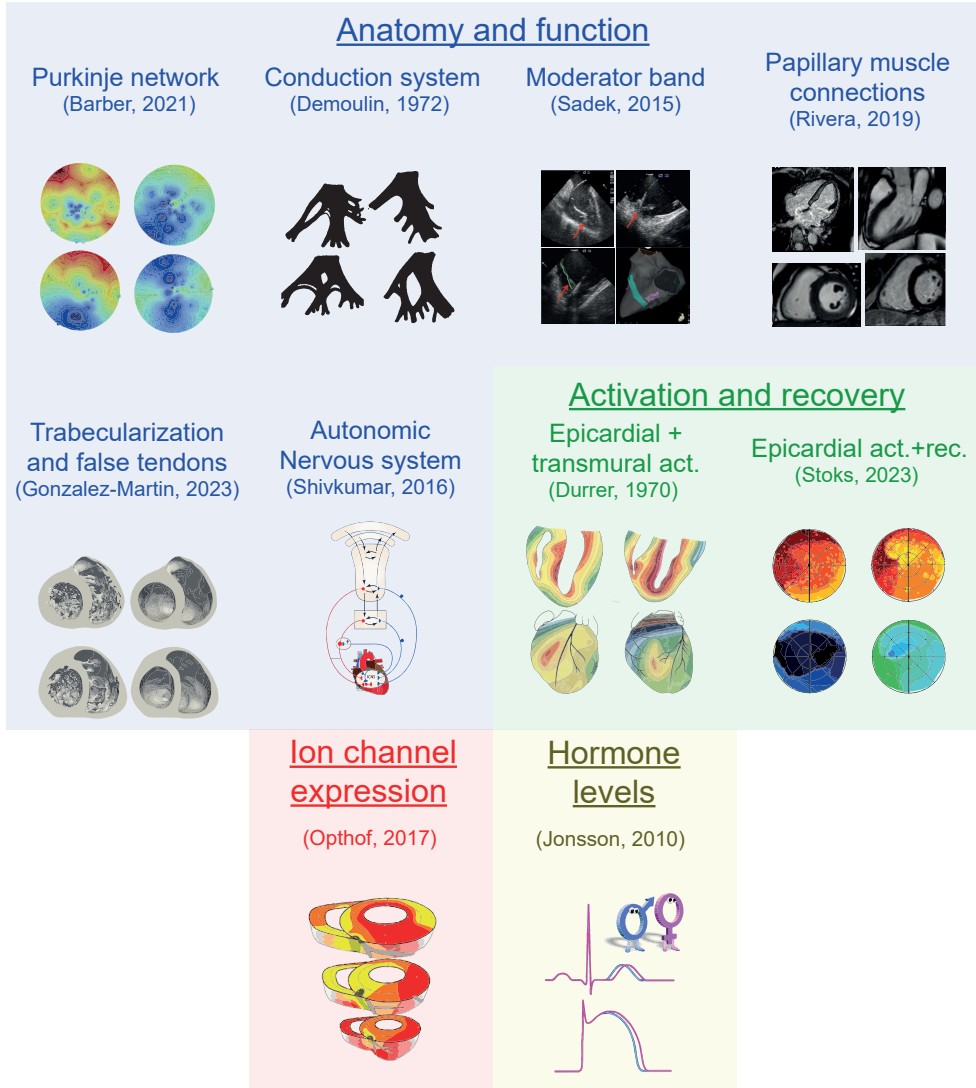


Figure 8.9: Anatomical and functional characteristics of the apparently normal human heart that may influence an individual's risk of VT/VF. Images reproduced from (117,118,256–262) and **Chapter 5**. Potential arrhythmia propensity is multifactorial and highly individual, even in the absence of pathology.

Mechanism-based approaches to predict SCD risk generally enhance risk stratification and improve SCD treatment (208,268–270), but require validation in large patient populations. The results of this thesis (see **Chapter 5-Chapter 7**) highlight the highly individual characteristics of ventricular electrophysiology and propensity to arrhythmias, thereby suggesting that mechanism-based approaches are more accurate for personal risk stratification than population-based methods.

8.2.2 Current treatment of individuals at risk for SCD

Treatment options for (the prevention of) ventricular tachyarrhythmias include ICDs, antiarrhythmic drugs (AADs), ablation of the arrhythmogenic substrate, wearable cardioverter-defibrillators, and in some cases neuroaxial modulation of the heart. Besides, the importance of adequate (upstream) heart-failure treatment should always be emphasized in the right patients.

ICDs are effective in reducing mortality from VT/VF (271,272) but do not prevent arrhythmia onset. Wearable cardioverter-defibrillators offer a temporary solution for patients at risk of SCD who are not currently eligible for an ICD or when the perceived elevated risk is only transient (4,273).

The choice of specific AADs depends on patient characteristics and disease etiology. Amiodarone is generally considered the most effective AAD against VT recurrence (272,274,275), but may increase all-cause mortality in ICD carriers (6) and can have considerable side-effects, including proarrhythmic actions in some patients. Amiodarone has several mechanisms of action. Among those are ERP prolongation and conduction slowing, thereby reducing reentry wavelength.

Although AAD treatment could be personalized, at least partly, by considering the potential arrhythmogenic mechanisms of action in an individual, it is often applied as a “one size fits most approach”, i.e., not tailored to the known/retrievable mechanistic details of the case.

Ablation of the arrhythmogenic substrate is most often based on EAM or the results of programmed electrical stimulation to identify critical areas for VT formation and maintenance. Localized catheter-based treatment, typically through radiofrequency ablation, disrupts the conduction of wavefronts underlying arrhythmia. Despite encompassing empirical 3D information, catheter ablation for VT is still accompanied by relatively high (30-40% within 1-2 years (6,181)) recurrence rates. This relatively modest efficacy may be increased by considering the components of the Circle of Reentry such as local tissue recovery or structural-functional characteristics by multimodal image integration as illustrated in this thesis (**Chapter 7**).

8.2.3 Challenges in SCD risk stratification

8.2.3.1 The variability of arrhythmia propensity over time

Arrhythmia propensity varies over time. Modulators can temporarily or permanently affect the trigger, substrate, or their interactions, see **Figure 8.3**. Modulators include the autonomic nervous system (223) humoral and paracrine factors (262), which may influence the substrate (262,276) and the occurrence of triggers (277). Likewise, changes may occur in myocardial wall thickness and scar architecture, beat-to-beat repolarization (278–280), and circadian activation and repolarization (232).

Monitoring the time-varying influence of trigger and substrate can be achieved through repeated or prolonged recordings of electrocardiographic/-physiological parameters (such as Holter monitoring (223)) conducted under various conditions (such as exercise stress testing or provocation testing with ECG or ECGI). However, repeated recordings only capture snapshots of the dynamic trigger-substrate interactions, and modalities that allow for prolonged recordings often lack spatial resolution. While high-resolution mechanistic methods may offer accurate risk assessment at a specific moment, its variance over time introduces significant uncertainty. To address this, one can introduce small variations in model parameters. This is also illustrated in **Figure 8.10**, in which temporal changes should be considered in future risk stratification models.

8.2.3.2 Updating of risk stratification models

Risk stratification models require to be updated with contemporary data and definitions. Our understanding of measurement techniques and disease mechanisms evolves over time. For example, in **Chapter 4**, we discussed the historical variations in determining local RT, a crucial factor in arrhythmogenesis. Other evolving insights include shifting paradigms on the recognition of distinct electrophysiological properties of the midmyocardial (M-)cell (281,282); the discrepancies between cellular, wedge, and in vivo measurements (95,229); T-wave genesis on the 12-lead ECG being attributed to transmural repolarization gradients (283–285); and the measurement of the monophasic action potential (30,286).

Furthermore, disease progression, treatments, and associated risks for SCD can change over time. For example, improved long-term and short-term prognosis in ST-elevation myocardial infarction reflect advancements in disease management (287). Definitions of arrhythmia syndromes, including idiopathic ventricular fibrillation have also evolved (288). SCD risk-stratification models should also consider technological advancements in imaging modalities, including spatial and temporal resolution, imaging protocols, signal quality, and software updates. Keeping pace with these technical aspects is essential for maintaining the relevance and accuracy of risk stratification models.

Risk stratification for SCD

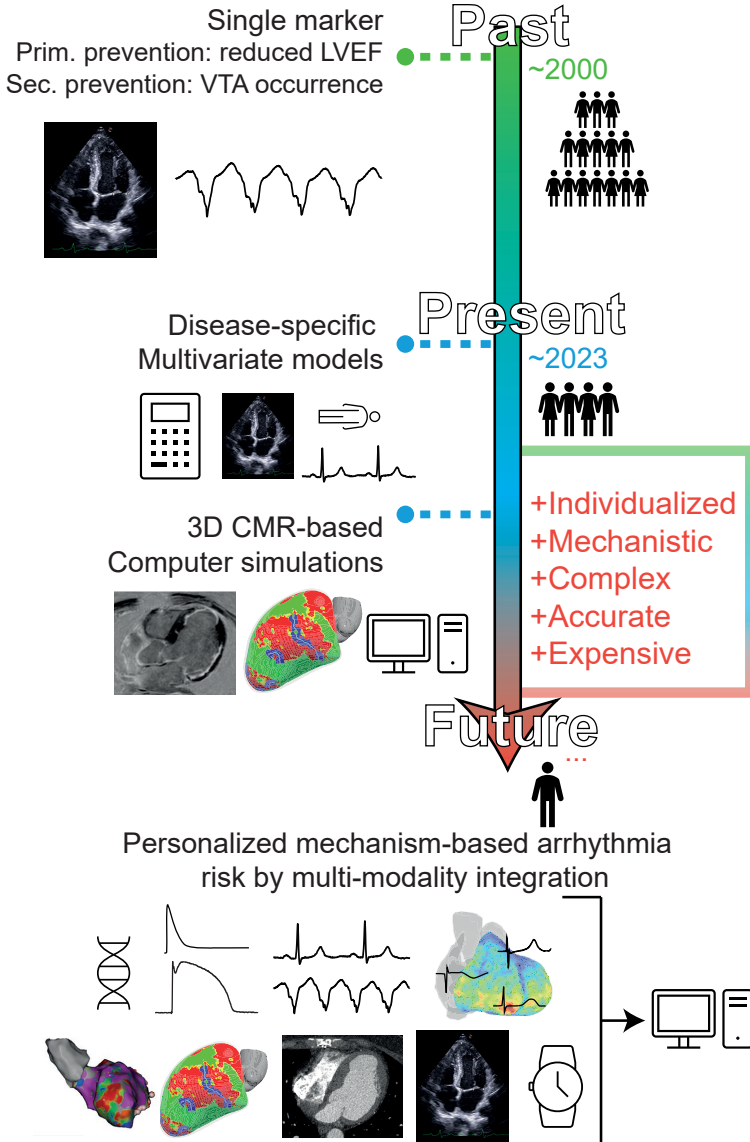


Figure 8.10: Timeline of SCD prevention. In the past, a single marker (e.g., reduced LVEF in (suspected) cardiomyopathy, the occurrence of a major arrhythmic event, or familial SCD in case of (suspected) primary electrical disease) was used to assess SCD risk, based on large cohort studies and with limited specificity (4,5,289,290). At present, risk stratification is becoming more accurate, as disease-specific multivariate models are increasingly being developed and used (4,264–266). Recent developments in computer simulations take the patient-specific 3D scar architecture into account and are promising in small cohorts for

SCD risk stratification and treatment (208,268). In the future, SCD risk stratification will benefit from further personalization by multimodality integration, e.g., functional electrical parameters and possibly mechanics, besides anatomical-structural characteristics. With time, risk stratification methods will progressively gain in mechanistic knowledge and will become more accurate, but may also turn more complex and expensive.

8.2.4 Future outlook: mechanism-based risk stratification and treatment for SCD

8.2.4.1 Personalized 3D computational heart models

In recent years, computational approaches have emerged that utilize 3D information (e.g. from CMR) to simulate VT propensity (208,268). Different from statistical risk calculators, these approaches offer personalized and high-resolution mechanistic insights. Virtual stimuli are provided to a personalized 3D-heart model generated from late gadolinium-enhanced CMR, after which the occurrence of VT in the personalized model is assessed.

In limited populations of patients with old myocardial infarction, these personalized mechanistic approaches showed four times greater success in predicting VT occurrence than when using LVEF (268). Subsequent studies extending these simulations to other arrhythmogenic syndromes have also demonstrated promising results (269,270,291,292). These findings suggest that a personalized and mechanistic approach is more accurate than population-based statistical models for risk stratification in primary prevention of SCD, but obviously this requires confirmation in larger patient numbers.

8.2.4.2 The relevance of a personalized multimodal approach

In **Chapters 5-7** I showed that multimodal image integration of structural and functional imaging can be synergistic and improves mechanistic understanding of 3D individualized electrophysiology and VT arrhythmogenesis. Thus, adding patient-specific electrophysiological parameters (e.g., from EAM, ECGI, or ECG) into 3D heart models can lead to:

- More accurate (personalized) activation and recovery characteristics. For example, see **Chapter 5**, in which activation and repolarization patterns during sinus rhythm are highly variable between subjects.
- The widening of its applicability to non-structural heart disease, as in **Chapter 6**. Various substrate characteristics are not visible on CMR but may be revealed by ECGI (64,73,74), contact electrogram mapping or ECG.
- Accurate pinpointing of the location and timing of arrhythmia triggers, as exemplified in **Chapter 7**.

To enhance the accuracy of personalized models, multimodal assessment could be further expanded. For example, cardiac mechanics, including mechano-electrical reciprocity, could be incorporated as it contributes significantly to

arrhythmogenesis, at least in some arrhythmia syndromes (244). Other examples include DNA diagnostics, cellular current characterization (see **Chapter 6**), CT wall thickness analyses (see **Chapter 7**), and the integration of positron emission tomography (PET) and artificial intelligence into existing CMR-based computer models (270). Ideally, from a patient perspective, noninvasive data from modalities such as ECGI, ECG, CT, and CMR will form the basis of 3D heart models. However, some of these modalities (such as ECGI) may still provide less accurate information compared to invasive counterparts, as discussed in **Chapter 2**.

The addition of any modality into personalized risk assessment may render models more accurate, but also more complex and costly, see **Figure 8.10**. Consequently, for clinical decision-making in which cost-efficiency, time-efficiency and ease-of-use are important, the number of modalities to incorporate in an individual 3D heart model should remain limited to maintain simplicity (293).

8.2.4.3 Mechanism-based and noninvasive therapies

An overview of current and future treatment options for VT/VF is shown in **Figure 8.11**. The development of personalized 3D (multimodal) heart models enables further exploration of mechanism-based localized therapy for VT/VF. Examples of such therapies include catheter ablation of a functional repolarization substrate, regional infusion of repolarization-altering drugs, and gene therapy, which have proven effective in animal models (234,237). While challenges remain for practical and long-term use in humans, these local therapies show promise.

Noninvasive stereotactic arrhythmia radioablation (STAR) has emerged as a promising alternative to conventional catheter ablation for VT/VF (77,294,295). STAR delivers radiotherapy noninvasively to critical sites involved in VT/VF formation and maintenance, similar to treating primary tumors such as lung or prostate cancer. It is particularly beneficial for patients who cannot undergo or have failed catheter ablation due to factors such as age, frailty, advanced heart failure, or comorbidities. Small-scale trials have demonstrated an impressive >85% reduction in VT burden when conventional catheter ablation fails (77,294,295). The MUMC+ is the main regional referral center for STAR in the south of The Netherlands, where the first patient was recently treated. The MUMC+ is part of a larger European consortium known as STOPSTORM (213).

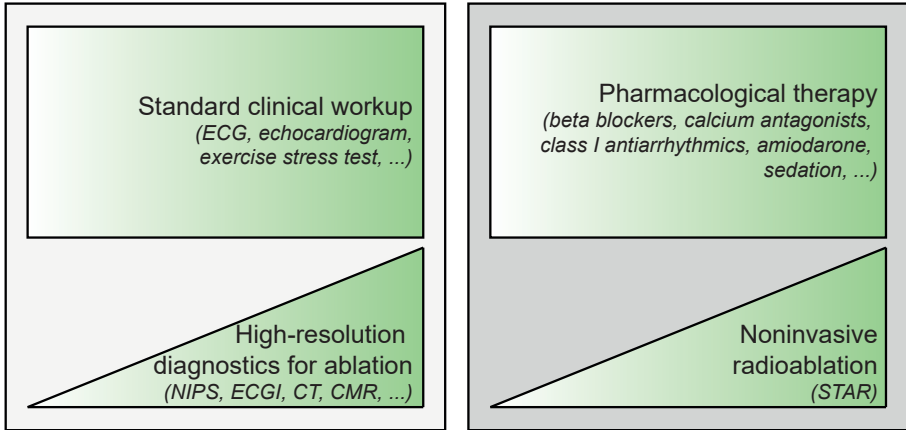
Accurately identifying the critical VT substrate to target is crucial. For STAR, the critical substrate is typically delineated based on information from a previous invasive EAM. However, the EAM is typically obtained before the catheter ablation, which itself alters tissue characteristics. Furthermore, the EAM may not precisely reflect the current state of the substrate on the day of the STAR procedure, due to the effects of modulators and electrical remodeling, see **Figure 8.3** (223,254). Acquiring a novel EAM just prior to the STAR procedure provides current and accurate substrate information, but comes with high costs (182) and complication rates. Finally, such lengthy and invasive procedures are

less appropriate in the targeted (frail) patient population.

Personalized multimodal noninvasive delineation of the critical cardiac substrate using 3D heart modeling can address these challenges. The co-localization of the end of structural heterogeneous tissue corridors by 3D CMR (as in **Chapter 7**) with functional late-activated or early-repolarized areas by ECGI (see **Chapters 3-5**) could denote areas of low RVI which are susceptible to VT/VF formation. This approach has the potential to enhance the accuracy and applicability of STAR, improving its effectiveness as a treatment option.

Diagnostic management Therapeutic management

Noninvasive



Invasive

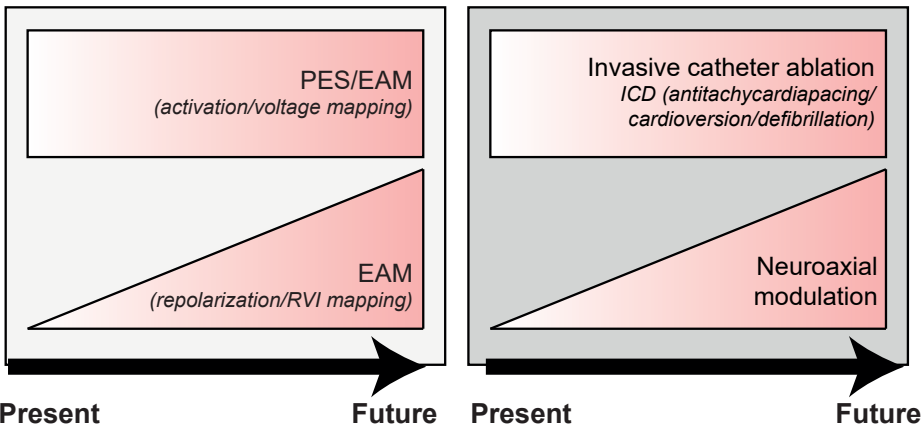


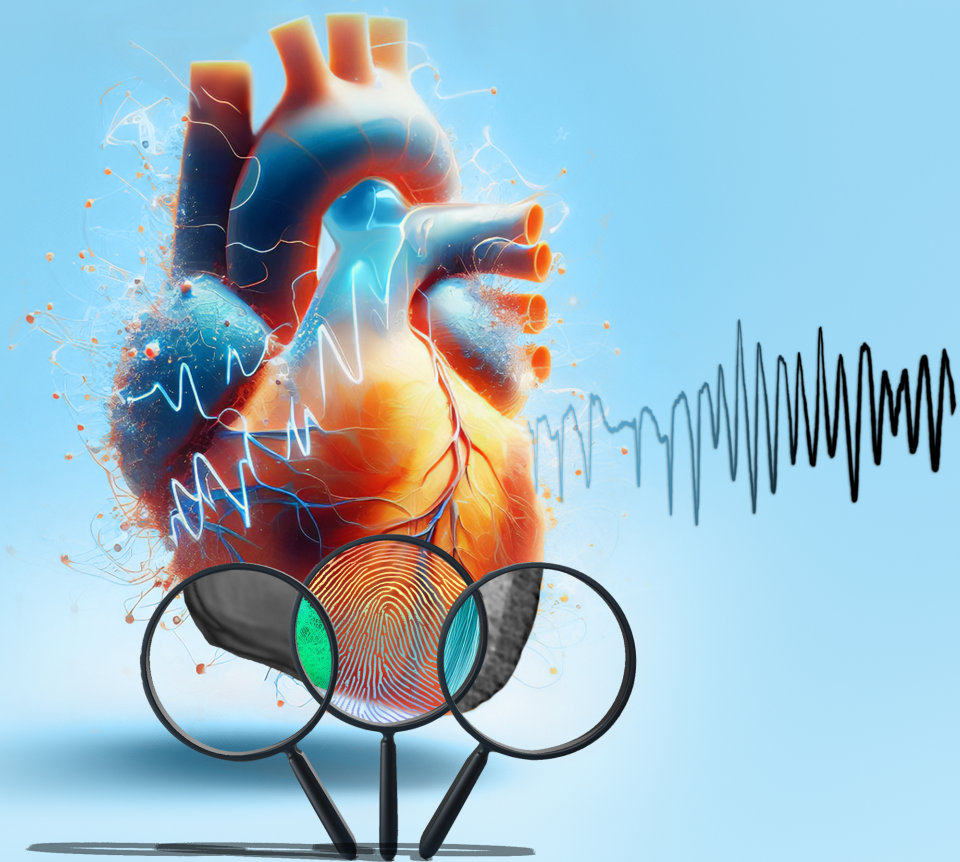
Figure 8.11: Current and future diagnostic (left) and therapeutic (right) management options for VT/VF. Top panels in green indicate noninvasive management options, bottom panels in red indicate invasive ones. Each column contains a time-axis from present to future. The height of each green/red panel indicates the relative importance of that management option. I expect that noninvasive high-resolution diagnostics for ablation, noninvasive radioablation, invasive repolarization/RVI mapping (see Section 8.1.3.1) and neuroaxial modulation will play an increasing role in the future, while conventional diagnostic and therapeutic management will remain as important for treatment of VT/VF. NIPS: noninvasive programmed stimulation (by ICD). STAR: stereotactic arrhythmia radioablation. PES: programmed electrical stimulation. EAM: Electroanatomical mapping.

8.3 Conclusion

Mechanistic understanding of ventricular electrophysiology and tachyarrhythmias can be addressed by multiple theoretical frameworks such as the generalized Coumel's triangle of arrhythmogenesis and the Circle of Reentry. Such understanding forms the basis to improve risk stratification and treatment for ventricular tachyarrhythmias.

Current clinical methods for SCD risk stratification lack accuracy. Recent mechanism-based approaches to risk stratification and treatment of individuals at risk for SCD seem highly promising. However, for clinical implementation, it is important to maintain model simplicity and take inherent uncertainties into account.

In this doctorate thesis, I have shown that multimodality image integration allows to better explain human ventricular tachyarrhythmias, by addressing ventricular pathophysiology and advancing the assessment of cardiac structure and function. This can improve diagnostic and therapeutic management. Multimodal image integration provides a personalized approach to arrhythmia mechanisms and has the potential to enhance the effectiveness and noninvasiveness of current and emerging (noninvasive) therapies.



APPENDIX A

Summary
Samenvatting

Summary

In the studies for this doctorate thesis, I apply multimodal image integration to better explain human ventricular tachyarrhythmias (VT). The findings of this thesis improve mechanistic understanding of the electrophysiology and pathology of the human ventricles and advance the assessment of cardiac structure and function. **Chapter 1** gives a general introduction to the main topics of cardiac arrhythmogenesis and multimodal research to investigate cardiac electrophysiology and electropathology.

In **Chapter 2**, I provide a state-of-the-art review of the history, advantages and challenges, validation studies, applications, and future directions of electrocardiographic imaging (ECGI). ECGI is a noninvasive method that reconstructs electrical activity at the heart level. It provides unique anatomy-related insights into cardiac electrophysiology. Validation studies show moderate-to-good accuracy. ECGI is mainly used in research for studying disease mechanisms, identifying arrhythmogenic substrates, optimizing therapy, and for multimodal image integration, e.g., to improve the outcomes of catheter ablation or cardiac resynchronization therapy. For a more widespread clinical implementation, further maturation is required in terms of standardization, ease of use, and external validation of previous study results. In my view, ECGI's potential lies in personalized insights through integration with other modalities.

In **Chapter 3**, I address standardized visualization of ECGI and quantification of its technological uncertainties. In **Section 3.2**, I present our open-source algorithm Universal Ventricular Bullseye Visualization (UNISYS), which provides a standardized visualization of any kind of single-layer ventricular data. Being aligned with the anatomy of the heart, UNISYS aids in the (clinical) interpretation and standardization of ECGI. Furthermore, in **Section 3.3**, I identify variability in inverse reconstruction between and within systems. Electrical recovery time (RT) estimation is most variable within and between lead sets, which is caused by noisy and low-amplitude signals, as well as regions of a T-wave polarity switch. Finally, in **Section 3.4**, I investigate the impact of using a static diastolic geometry on the inverse solution by comparing epicardial potential maps and isochrones on systolic and diastolic geometries. Inverse solutions of these geometries generally agree, but local differences in recovery can result from low-amplitude epicardial T-waves.

In **Chapter 4**, I address the long-lasting controversy on what is the optimal determination of RT from the intracardiac unipolar electrogram (UEG). I show that the Wyatt method, which defines RT as the moment of steepest UEG T-wave upslope, is the most accurate to determine RT from invasive and noninvasive UEGs, based on novel and historical analyses. This unifies RT measurement (and thereby improves its accuracy) in basic and clinical settings.

In **Chapter 5**, I characterize the natural variation of cardiac electrical activation

and recovery using ECGI in 22 normal subjects. As part of these analyses, I evaluate the influence of sex, age, stability over time, and several pathologic conditions affecting cardiac activation or repolarization. I obtain novel insights in (localized) differences in activation and repolarization between individuals, sexes, and age groups. Although all subjects had a normal 12-lead ECG, their underlying epicardial activation and recovery patterns can be profoundly different. Beat-to-beat epicardial activation and recovery remain stable within a subject over minutes of time. This paves the way for further investigations into the dynamics of cardiac electrophysiology and pathologies.

In the studies for **Chapter 6**, we identify several *DPP6* missense variants associated with long-QT syndrome (LQTS) and J-wave syndrome (JWS). Through a series of translational experiments, we show that *DPP6* regulates I_{Na} and I_{to} in a reciprocal manner, and we investigate its consequences at the tissue and organ level. The variants linked to JWS lead to decreased conduction velocity in the right-ventricular outflow tract, whereas the variants linked to LQTS lead to dispersed and rather prolonged repolarization. This advanced understanding of the genetic basis of proarrhythmia and ventricular fibrillation will improve risk stratification for individuals with *DPP6* variants and potentially aid the development of targeted therapy. *DPP6* genotyping should be considered in case of (suspected) cardiac I_{Na} / I_{to} pathology without apparent other cause.

In **Chapter 7**, I present a personalized noninvasive 3D model that incorporates high-resolution structural and electrical information for the management of VT. The model accurately pinpoints the VT exit site in a patient with ischemic cardiomyopathy and recurrent arrhythmia, collocates areas of structural and functional corridors and provides insights into scar transmural and endocardial voltage characteristics. This proof-of-concept study enhances our mechanistic understanding of scar-related VT and provides an advanced, noninvasive roadmap for catheter ablation.

Chapter 8 contains a broader perspective on the findings of this thesis. Theoretical frameworks such as Coumel's triangle of arrhythmogenesis and the Circle of Reentry aid in our understanding of VT (including ventricular fibrillation) mechanisms, which are personalized and influenced by many anatomical and functional characteristics. Multimodal image integration enhances our understanding of VT, based on the combined personalized assessment of cardiac structure and function. Personalized mechanism-based approaches show promise for identifying and treating subjects at risk for sudden cardiac death (SCD), although any risk stratification model comes with inherent challenges. In the future, personalized noninvasive multimodal assessment of electrical activation/recovery on heart anatomy will likely play a larger role in the diagnostic and therapeutic management of patients with VT.

Samenvatting

In dit proefschrift pas ik multimodale beeldintegratie toe om ventriculaire tachyarritmieën (VT) in mensen beter te verklaren. De bevindingen van dit proefschrift verbeteren het mechanistische begrip van de elektrofysiologie en pathologie van de menselijke hartkamers, evenals de beoordeling van hartstructuur en hartfunctie. **Hoofdstuk 1** geeft een algemene inleiding op de belangrijkste onderwerpen van cardiale aritmogenese en multimodaal onderzoek om de cardiale elektrofysiologie en -pathologie te onderzoeken.

In **Hoofdstuk 2** geef ik een actueel overzicht van de geschiedenis, voordelen en uitdagingen, validatiestudies, toepassingen en toekomstige ontwikkelingsrichtingen van electrocardiografische beeldvorming (*electrocardiographic imaging, ECGI*). ECGI is een techniek om elektrische activiteit op 3D hartniveau te reconstrueren. Het biedt unieke inzichten met betrekking tot de elektrofysiologie van het hart, gerelateerd aan de anatomie. Validatiestudies tonen dat ECGI een redelijke tot goede nauwkeurigheid kent. ECGI wordt voornamelijk gebruikt in onderzoek om ziektemechanismen te bestuderen, aritmogeen substraat te identificeren, therapie te optimaliseren en voor multimodale beeldintegratie, bijvoorbeeld om de uitkomsten van katheterablatie of cardiale resynchronisatietherapie te verbeteren. Voor een bredere klinische implementatie zijn verdere ontwikkelingen in standaardisatie, gebruiksgemak en externe validatie van eerdere onderzoeksresultaten vereist. In mijn optiek ligt het potentieel van ECGI in gepersonaliseerde inzichten door integratie met andere modaliteiten.

In **Hoofdstuk 3** behandel ik gestandaardiseerde visualisatie van ECGI-uitkomsten en de kwantificering van de onzekerheid die gepaard gaat met de ECGI-technologie. In **Sectie 3.2** presenteer ik ons open-source algoritme "Universal Ventricular Bullseye Visualization" (UNISYS), dat een gestandaardiseerde visualisatie biedt voor elk type enkellaagse ventriculaire gegevens. UNISYS helpt bij de (klinische) interpretatie en standaardisatie van ECGI. In **Sectie 3.3** identificeer ik variabiliteit van inverse reconstructie tussen en binnen verschillende elektrodensets. De bepaling van repolarisatietijd (RT) is het meest variabel binnen en tussen elektrodensets, wat wordt veroorzaakt door signalen met lage amplitude en ruis, evenals door regio's met een omschakeling van de T-golf polariteit. Ten slotte, in **Sectie 3.4** onderzoek ik de impact van het gebruik van een statische diastolische geometrie op de inverse reconstructie, door epicardiale potentialen en isochronen op systolische en diastolische geometrieën te vergelijken. Ik toon dat inverse reconstructies van deze geometrieën globaal gezien overeenkomen, maar dat lokale verschillen in RT kunnen voortkomen uit epicardiale T-golven met lage amplitude.

In **Hoofdstuk 4** behandel ik de langdurige controversie over wat de optimale bepaling van de RT is vanuit het intracardiale unipolaire elektrogram (UEG). Ik toon aan dat de Wyatt-methode, die RT definieert als het moment van de

maximale afgeleide van de T-golf, de meest nauwkeurige is om RT te bepalen uit invasieve en niet-invasieve UEG's, gebaseerd op nieuwe en historische analyses. Dit verenigt de meting van RT (en verbetert daarmee de nauwkeurigheid) in onderzoeks- en klinisch verband.

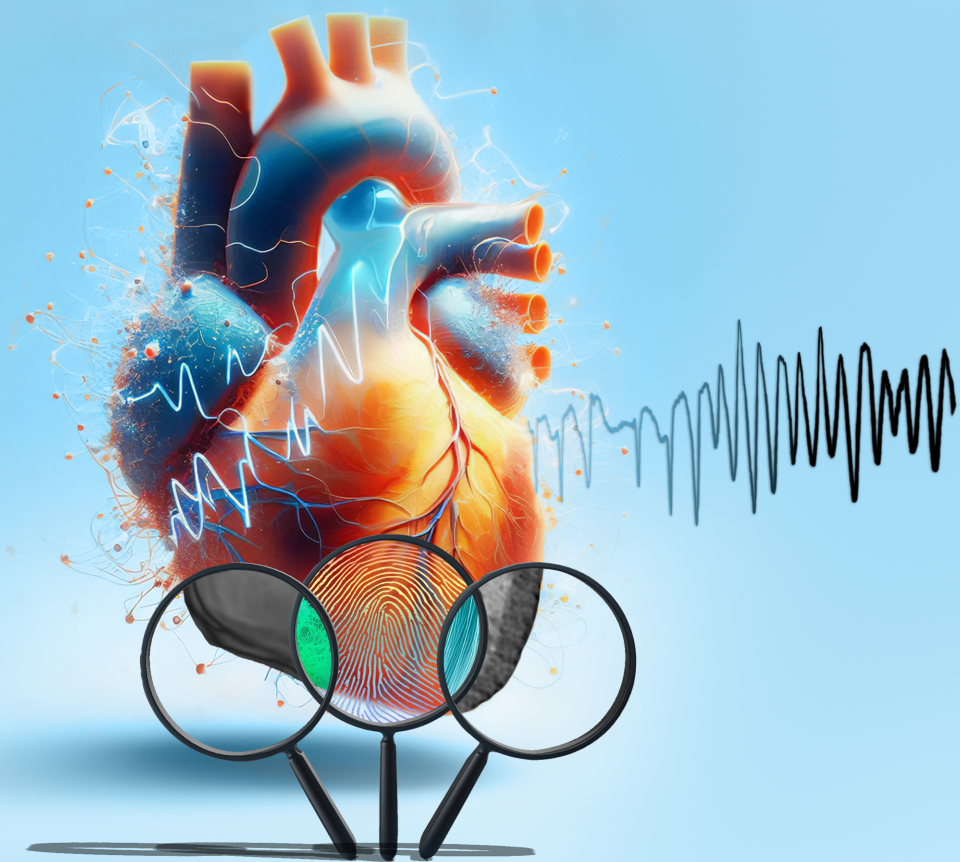
In **Hoofdstuk 5** karakteriseer ik de natuurlijke variatie in elektrische activatie en herstel in het hart met behulp van ECGI bij 22 normale proefpersonen. Als onderdeel van deze analyses evalueer ik de invloed van geslacht, leeftijd, stabiliteit over tijd en verschillende pathologische aandoeningen die van invloed zijn op de epicardiale activatie of het herstel. Ik verkrijg nieuwe inzichten in (gelokaliseerde) verschillen in activatie en herstel tussen individuen, geslachten en leeftijdsgroepen. Hoewel alle proefpersonen een normaal 12-kanaals ECG hebben, ton ik aan dat hun onderliggende epicardiale activatie- en herstelpatronen sterk kunnen verschillen. Epicardiale activatie en herstel bleven stabiel binnen een proefpersoon gedurende enkele minuten. Dit opent de weg voor verder onderzoek naar de dynamiek van de cardiale elektrofysiologie en pathologieën.

In **Hoofdstuk 6** identificeren we verschillende *DPP6* missense varianten die geassocieerd zijn met het lange-QT-syndroom (LQTS) en het J-golf-syndroom (JWS). Door middel van een reeks translationele experimenten tonen we aan dat *DPP6* I_{Na} en I_{to} wederkerig reguleert, en we hebben de gevolgen hiervan op weefsel- en orgaaniveau onderzocht. De varianten die aan JWS zijn gekoppeld, leiden tot een verminderde geleidingssnelheid in de uitstroombaan van het rechterventrikel, terwijl de varianten die aan LQTS zijn gekoppeld, leiden tot verspreide en verlengde repolarisatie. Dit geavanceerde begrip van de genetische basis van pro-aritmie en ventrikelfibrilleren zal de risicostratificatie voor personen met *DPP6*-varianten verbeteren en mogelijk bijdragen aan de ontwikkeling van gerichte therapie. *DPP6*-genotypering moet worden overwogen in geval van (vermoedelijke) cardiale I_{Na}/I_{to} -pathologie zonder duidelijke andere oorzaak.

In **Hoofdstuk 7** presenteer ik een gepersonaliseerd niet-invasief 3D-model dat hoge-resolutie structurele en elektrische informatie samenbrengt voor de behandeling van VT. Het model lokaliseert nauwkeurig de oorsprong van VT in een patiënt met ischemische cardiomyopathie en recidiverende kamerritmestoornissen, identificeert structurele en functionele gebieden waar de VT doorheen kan propageren, en verschaft inzichten in de transmuraliteit van littekenweefsel en endocardiale voltages. Deze proof-of-concept studie verbetert ons mechanistisch begrip van infarctgerelateerde VT en biedt een geavanceerde, noninvasieve routekaart voor katheterablatie.

Hoofdstuk 8 biedt een bredere kijk op de bevindingen van dit proefschrift. Theoretische kaders zoals Coumel's driehoek van aritmogenese en de Cirkel van Re-entry dragen bij aan ons begrip van VT-mechanismen (waaronder ventrikelfibrilleren), die worden beïnvloed door vele anatomische en functionele

kenmerken. Multimodale beeldintegratie versterkt ons begrip van VT, omdat hiermee de gepersonaliseerde beoordeling van de cardiale structuur en functie worden gecombineerd. Gepersonaliseerde mechanisme-gebaseerde benaderingen voor het identificeren en behandelen van personen met een risico op plotselinge hartdood (SCD) zijn beloftevol, hoewel elk risicostratificatiemodel inherente uitdagingen met zich meebrengt. In de toekomst zal gepersonaliseerde noninvasieve multimodale beoordeling van elektrische activatie/elektrisch herstel op de hartanatomie waarschijnlijk een grotere rol spelen in de diagnostiek en therapeutische behandeling van patiënten met VT.



APPENDIX B

Impact

Impact

In this PhD thesis, I apply multimodal image integration to improve the understanding and management of potentially-lethal human ventricular tachyarrhythmias by the combined assessment of cardiac structure and function. The results of my work can aid the indication, timing and focus of ablation for ventricular tachycardia. Being trained in Technical Medicine (MSc), my scientific contributions should be contextualized within the broader framework of global developments in the field of medical technology, specifically cardiac electrophysiology, medical imaging, personalized computational heart modeling and artificial intelligence.

In **Chapter 2**, I provide a state-of-the-art review of the history, applications and future perspectives of electrocardiographic imaging (ECGI). Noninvasive ECGI has significantly advanced our insights of the electrical activity of the heart. However, further development, reproducibility, standardization and user-friendliness are necessary for ECGI's widespread clinical adoption. The contents of this Chapter inform clinicians and engineers about the benefits and pitfalls of ECGI, because only an in-depth understanding of both will allow for reasonable use of ECGI and careful interpretation of the data in clinical context. Moreover, we identify areas where further research is required. This can guide future studies into the technological advancement and standardization of ECGI, by academia and industry. Such advancements can in turn improve ECGI's clinical application, and therefore, personalized medicine and the understanding and treatment of cardiac arrhythmia syndromes. This Chapter is published in an open access book discussing the heritage and promise of electrocardiography and electrophysiology. The book is freely available (ISBN 978 90 67677 82 0).

In **Section 3.2**, I introduce a novel algorithm (UNISYS) that provides a standardized visualization and representation of any kind of single-layer ventricular data, e.g., electrical, mechanical, structural, or a combination of those. This can aid in the interpretation of results obtained by ECGI and other techniques involving ventricular anatomy. For example, regional electrical properties can be compared between subjects in a standardized manner by using UNISYS, such as in **Chapter 5**. Furthermore, UNISYS aids in the integration of multiple modalities, e.g., echocardiographic and ECGI-based measurements of the heart. Thus, UNISYS advances image integration in cardiology and therefore the understanding and management of heart disease. UNISYS can be of use to engineers, scientists and clinicians and is openly available at <http://ecg-imaging.org/software/visualization-tools>. The relevance of this tool is further demonstrated by the fact that world-wide at least five different research groups are currently (October 2023) using the algorithm routinely, helping to achieve standardization in the field. Furthermore, in **Section 3.3**, I identify the influence of using a static diastolic geometry on the inverse solution of ECGI. Although the heart is a contracting and moving organ, it is commonly approximated in a static diastolic state in ECGI. I show that the impact of this approximation is low in

general, but local deviations in electrical recovery time (RT) determination may occur, mainly because of flat or noisy epicardial T-waves. These deviations seem unrelated to the heart's contraction. Consequently, imaging of the heart anatomy for ECGI can be achieved with limited scanning time and radiation exposure, underpinning current practice. In **Section 3.4**, I investigate the variability in inverse reconstruction within one lead set, and between different lead set configurations. I show that in general, between-lead set variability is higher than within-lead set variability, except for RT determination. Variability of RT may be difficult in case of flat or noisy epicardial T-waves. The findings of **Sections 3.3** and **3.4** aid in the interpretation of ECGI by engineers and clinicians, by quantifying the complexities that come with two of its common approximations, and by better identifying the difficulties in RT determination. This further aids in the standardization of ECGI. The technical aspects of these findings may also be of use to other medical inverse problems, such as the reconstruction of electrical activity on the brain or stomach, and therefore also contribute to future research in neuroscience, and gastroenterology. The findings of Chapter 3 were published as 3 papers in *Computing in Cardiology*, thus reaching a broad audience of engineers and scientists in cardiovascular medicine.

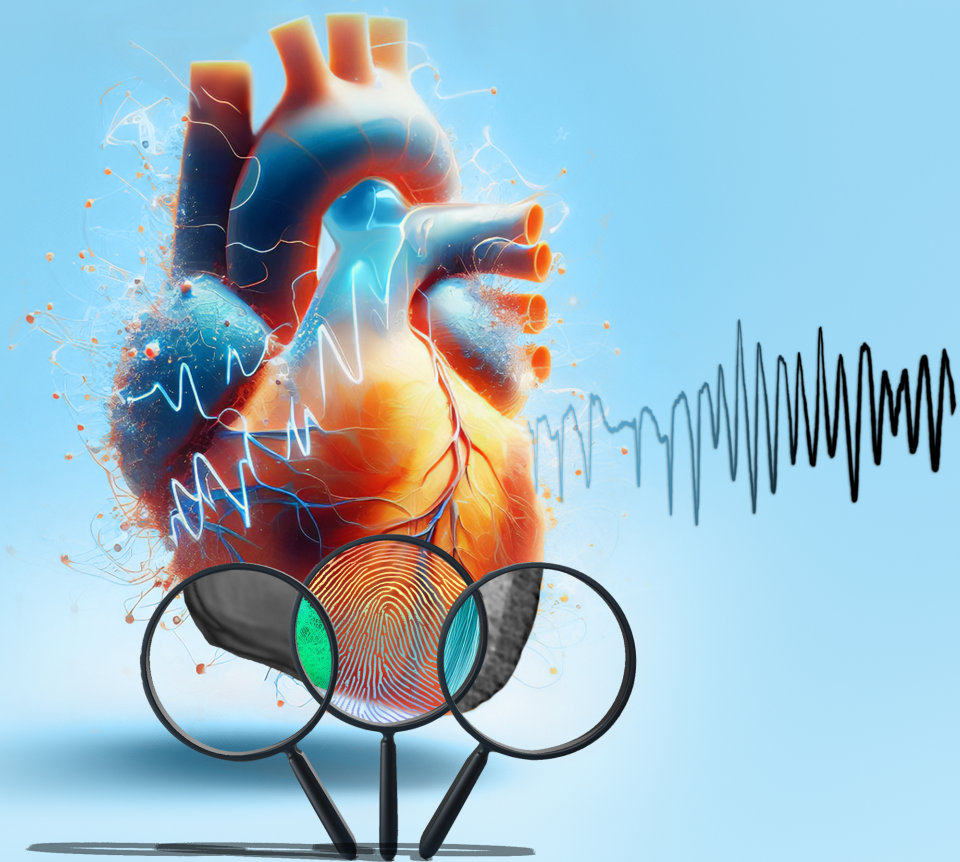
In **Chapter 4**, I address the long-lasting controversy on the determination of RT from the intracardiac unipolar electrogram and ECGI. Accurate assessment of RT is crucial for understanding cardiac conditions related to (regional) abnormal electrical activity. Through novel and historical analyses, I identified the Wyatt method to be the most accurate for determining RT, which unifies RT measurement in experimental and clinical settings and thereby defines a standard for future studies in the field. This will aid basic and clinical scientists, and clinicians, to better examine and understand cardiac electrical recovery in patients. Even though it is known that local RT plays a crucial role in cardiac arrhythmia syndromes, it is often not considered in their clinical treatment, which could in part be caused by the controversy regarding the determination of RT. The unification of RT measurement can thus improve diagnostic assessment, treatment, risk prediction and management of cardiac arrhythmias and other repolarization-dependent conditions of the heart. As the measurement of repolarization in the heart requires clinical protocols and technological aspects that are different from conventional mapping procedures, the findings of this Chapter may also influence the development of mapping protocols and technology by industry. **Chapter 4** was published in *Frontiers in Physiology*, a multidisciplinary open-access journal—and therefore freely available (DOI: 10.3389/fphys.2023.1158003). *Frontiers in Physiology* has a diverse audience, primarily consisting of basic and translational scientists. Thus far (January 2024), it has been viewed and downloaded almost 1800 times. My thread on the social medium X was seen almost 4000 times.

In **Chapter 5**, I report on normal variation of the electrical characteristics of the ventricles of the heart, using ECGI. I evaluate the influence of sex, age, stability over time, and different diseases. I obtain new insights in (localized) differences

in activation and repolarization between individuals, sexes, and age groups. Although all subjects have a normal 12-lead ECG, I show that their underlying epicardial activation and recovery patterns can be profoundly different. My findings provide a reference, based on physiological variation in the human heart, to comprehend and contextualize cardiac electropathologies. Furthermore, these results reveal individual characteristics by ECGI, thus providing a type of cardiac *fingerprinting*. Thus, I contribute to the development of personalized approaches for patients with cardiac electropathologies and arrhythmias. Other functional readouts, such as cardiac mechanics, autonomic or drug responses can be easily added in the future, to provide the next level of understanding of these pathologies. We plan to make all outcome measures of this Chapter publicly available, to support open science. Preliminary results of this work were presented at the *European Society of Cardiology (ESC) Congress (2020)* and the *Computing in Cardiology* conference (2021), thus reaching broad communities of clinicians and engineers.

In the clinical studies for **Chapter 6**, we identify several *DPP6* missense variants associated with long-QT syndrome (LQTS) and J-wave syndrome (JWS) in patients with an increased arrhythmia risk and/or documented ventricular fibrillation (VF). Through a series of translational experiments, we show that *DPP6* reciprocally regulates I_{Na} and I_{to} and demonstrate its consequences at the tissue and heart level. Our integrative findings contribute to the understanding of the genetic basis of VF in the structurally-normal heart. They can aid basic and clinical scientists in the development of targeted therapies for individuals with these genetic variants. Moreover, they lead to better management and the prevention of arrhythmic events, thereby alleviating anxiety and depression in persons at risk. Preliminary results of this work were presented at the *ESC Congress (2022)* and the annual meeting of the *ESC Working Group on Cardiac Cellular Electrophysiology (2022)*, attended by many basic and clinical scientists, and cardiologists.

In **Chapter 7**, I present a personalized 3D model by multimodal image integration that incorporates high-resolution structural and electrical information for the management of ventricular tachycardia (VT). This proof-of-concept study enhances our personalized mechanistic understanding of scar-related VT, and could be further extended to non-structural heart disease. My pioneering study provides an advanced roadmap for catheter ablation in the clinical setting. This may lead to improved success rates of ablation procedures, reduced arrhythmia-recurrence rates, better cost-effectiveness of VT treatment, and enhanced patient safety and quality of life, benefiting patients suffering from VT and clinicians performing these invasive procedures. This Chapter was published in the open-access journal *Frontiers in Cardiovascular Medicine*, and freely available (DOI: 10.3389/fcvm.2023.1112980). Thus far (January 2024), it has been viewed and downloaded almost 1700 times. My post on the social medium X was seen over 1100 times.



APPENDIX C

References

References

1. Hayashi M, Shimizu W, Albert CM. The spectrum of epidemiology underlying sudden cardiac death. *Circ Res* (2015) 116:1887–1906. doi: 10.1161/CIRCRESAHA.116.304521
2. Smith K, Andrew E, Lijovic M, Nehme Z, Bernard S. Quality of life and functional outcomes 12 months after out-of-hospital cardiac arrest. *Circulation* (2015) 131:174–181. doi: 10.1161/CIRCULATIONAHA.114.011200
3. Ilkhanoff L, Goldberger JJ. Out-of-hospital cardiac arrest getting beyond the tip of the iceberg. *Circulation* 2012:793–796. doi: 10.1161/CIRCULATIONAHA.112.123588
4. Zeppenfeld K, Tfelt-Hansen J, de Riva M, Winkel BG, Behr ER, Blom NA, Charron P, Corrado D, Dagues N, de Chillou C, et al. 2022 ESC Guidelines for the management of patients with ventricular arrhythmias and the prevention of sudden cardiac death. *Eur Heart J* (2022) 43:3997–4126. doi: 10.1093/eurheartj/ehac262
5. Bardy GH, Lee KL, Mark DB, Poole JE, Packer DL, Boineau R, Domanski M, Troutman C, Anderson J, Johnson G, et al. Amiodarone or an implantable cardioverter-defibrillator for congestive heart failure. *N Engl J Med* (2005) 352:225–237. doi: 10.1056/NEJMoa043399
6. Santangeli P, Muser D, Maeda S, Filtz A, Zado ES, Frankel DS, Dixit S, Epstein AE, Callans DJ, Marchlinski FE. Comparative effectiveness of antiarrhythmic drugs and catheter ablation for the prevention of recurrent ventricular tachycardia in patients with implantable cardioverter-defibrillators: A systematic review and meta-analysis of randomized controlled trials. *Heart Rhythm* (2016) 13:1552–1559. doi: 10.1016/j.hrthm.2016.03.004
7. Doldi F, Doldi PM, Plagwitz L, Westerwinter M, Wolfes J, Korthals D, Willy K, Wegner FK, Könemann H, Ellermann C, et al. Predictors for major in-hospital complications after catheter ablation of ventricular arrhythmias: validation and modification of the Risk in Ventricular Ablation (RIVA) Score. *Clin Res Cardiol* doi: 10.1007/s00392-023-02223-2
8. Mathew S, Fink T, Feickert S, Osamu Inaba ·, Hashiguchi N, Schlüter · Michael, Wohlmuth P, Wissner · Erik, Tiltz RR, Heeger C-H, et al. Complications and mortality after catheter ablation of ventricular arrhythmias: risk in VT ablation (RIVA) score. *Clin Res Cardiol* (1902) 111:530–540. doi: 10.1007/s00392-021-01902-2
9. Ezzat VA, Lee V, Ahsan S, Chow AW, Segal O, Rowland E, Lowe MD, Lambiase PD. A systematic review of ICD complications in randomised controlled trials

- versus registries: is our “real-world” data an underestimation? *Open Heart* (2015) 2:e000198. doi: 10.1136/openhrt-2014-000198
10. Isbister J, Semsarian C. Sudden cardiac death: an update. *Intern Med J* (2019) 49:826–833. doi: 10.1111/imj.14359
 11. Cerrone M, Remme CA, Tadros R, Bezzina CR, Delmar M. Beyond the one gene-one disease paradigm: complex genetics and pleiotropy in inheritable cardiac disorders. *Circulation* (2019) 140:595–610. doi: 10.1161/CIRCULATIONAHA.118.035954
 12. Neher E, Sakmann B. Single-channel currents recorded from membrane of denervated frog muscle fibres. *Nature* (1976) 260:799–802. doi: 10.1038/260799a0
 13. Sigworth FJ, Neher E. Single Na⁺ channel currents observed in cultured rat muscle cells. *Nature* (1980) 287:447–449. doi: 10.1038/287447a0
 14. Varró A, Tomek J, Nagy N, Virág L, Passini E, Rodriguez B, Baczkó I. Cardiac transmembrane ion channels and action potentials: cellular physiology and arrhythmogenic behavior. *Physiol Rev* (2021) 101:1083–1176. doi: 10.1152/physrev.00024.2019
 15. Franz MR. method and theory of monophasic action potential recording. *Prog Cardiovasc Dis* (1991) 33:347–366.
 16. Franz MR. Long-term recording of monophasic action potentials from human endocardium. *Am J Cardiol* (1983) 51:1629–1634. doi: 10.1016/0002-9149(83)90199-6
 17. O’Shea C, Kabir SN, Holmes AP, Lei M, Fabritz L, Rajpoot K, Pavlovic D. Cardiac optical mapping – state-of-the-art and future challenges. *Int J Biochem Cell Biol* (2020) 126:105804. doi: 10.1016/j.biocel.2020.105804
 18. Gloschat C, Aras K, Gupta S, Faye NR, Zhang H, Syunyaev RA, Pryamonosov RA, Rogers J, Kay MW, Efimov IR. RHYTHM: An open source imaging toolkit for cardiac panoramic optical mapping. *Sci Rep* (2018) 8:2921. doi: 10.1038/s41598-018-21333-w
 19. Kappadan V, Telele S, Uzelac I, Fenton F, Parlitz U, Luther S, Christoph J. High-resolution optical measurement of cardiac restitution, contraction, and fibrillation dynamics in beating vs. blebbistatin-uncoupled isolated rabbit hearts. *Front Physiol* (2020) 11:464. doi: 10.3389/FPHYS.2020.00464/BIBTEX
 20. Christoph J, Luther S. Marker-free tracking for motion artifact compensation and deformation measurements in optical mapping videos of contracting

- hearts. *Front Physiol* (2018) 9:1483. doi: 10.3389/FPHYS.2018.01483/BIBTEX
21. Barkagan M, Sroubek J, Shapira-Daniels A, Yavin H, Jang J, Nezafat R, Anter E. A novel multielectrode catheter for high-density ventricular mapping: electrogram characterization and utility for scar mapping. *Europace* (2020) 22:440–449. doi: 10.1093/EUROPACE/EUZ364
 22. Gepstein L. "Electroanatomical Cardiac Mapping,," In: Cabo C, Rosenbaum DS, editors. *Quantitative cardiac electrophysiology*. New York, New York, USA: Marcel Dekker, Inc. (2002). p. 385–402
 23. Holtackers RJ, Emrich T, Botnar RM, Kooi ME, Wildberger JE, Kreitner KF. Late gadolinium enhancement cardiac magnetic resonance imaging: from basic concepts to emerging methods. *RoFo Fortschritte Auf Dem Geb Rontgenstrahlen Bildgeb Verfahr* (2022) 194:491–504. doi: 10.1055/a-1718-4355
 24. Holtackers RJ, Chiribiri A, Schneider T, Higgins DM, Botnar RM. Dark-blood late gadolinium enhancement without additional magnetization preparation. *J Cardiovasc Magn Reson* (2017) 19:1–10. doi: 10.1186/s12968-017-0372-4
 25. Lin E, Alessio A. What are the basic concepts of temporal, contrast, and spatial resolution in cardiac CT? *J Cardiovasc Comput Tomogr* (2009) 3:403. doi: 10.1016/J.JCCT.2009.07.003
 26. Takigawa M, Duchateau J, Sacher F, Martin R, Vlachos K, Kitamura T, Sermesant M, Cedilnik N, Cheniti G, Frontera A, et al. Are wall thickness channels defined by computed tomography predictive of isthmuses of postinfarction ventricular tachycardia? *Heart Rhythm* (2019) 16:1661–1668. doi: 10.1016/j.hrthm.2019.06.012
 27. Wilkinson MD, Dumontier M, Aalbersberg IJ, Appleton G, Axton M, Baak A, Blomberg N, Boiten J-W, da Silva Santos LB, Bourne PE, et al. The FAIR guiding principles for scientific data management and stewardship. *Sci Data* (2016) 3:160018. doi: 10.1038/sdata.2016.18
 28. Quinn TA, Granite S, Allessie MA, Antzelevitch C, Bollensdorff C, Bub G, Burton RAB, Cerbai E, Chen PS, Delmar M, et al. Minimum information about a cardiac electrophysiology experiment (MICEE): standardised reporting for model reproducibility, interoperability, and data sharing. *Prog Biophys Mol Biol* (2011) 107:4–10. doi: 10.1016/j.pbiomolbio.2011.07.001
 29. Cluitmans MJM, Bayer J, Bear LR, ter Bekke RMA, Heijman J, Coronel R, Volders PGA. The circle of reentry: Characteristics of trigger-substrate interaction leading to sudden cardiac arrest. *Front Cardiovasc Med* (2023) 10:1–10. doi: 10.3389/fcvm.2023.1121517

30. Coronel R, de Bakker JMT, Wilms-Schopman FJG, Opthof T, Linnenbank AC, Belterman CN, Janse MJ. Monophasic action potentials and activation recovery intervals as measures of ventricular action potential duration: Experimental evidence to resolve some controversies. *Heart Rhythm* (2006) 3:1043–1050. doi: 10.1016/j.hrthm.2006.05.027
31. Pullan AJ, Cheng LK, Nash MP, Ghodrati A, MacLeod R, Brooks DH. *Comprehensive electrocardiology*. Macfarlane PW, van Oosterom A, Pahlm O, Kligfield P, Janse M, Camm J, editors. London: Springer London (2010). doi: 10.1007/978-1-84882-046-3
32. Cluitmans MJM, Peeters RLM, Westra RL, Volders PGA. Noninvasive reconstruction of cardiac electrical activity: update on current methods, applications and challenges. *Neth Heart J* (2015) 23:301–311. doi: 10.1007/s12471-015-0690-9
33. Martin RO, Pilkington TC, Morrow MN. Statistically constrained inverse electrocardiography. *IEEE Trans Biomed Eng* (1975) BME-22:487–492. doi: 10.1109/TBME.1975.324470
34. Barr RC, Spach MS. Inverse calculation of QRS-T epicardial potentials from body surface potential distributions for normal and ectopic beats in the intact dog. *Circ Res* (1978) 42:661–675. doi: 10.1161/01.RES.42.5.661
35. Messinger-Rapport BJ, Rudy Y. Noninvasive recovery of epicardial potentials in a realistic heart-torso geometry. Normal sinus rhythm. *Circ Res* (1990) 66:1023–1039. doi: 10.1161/01.RES.66.4.1023
36. Oster HS, Taccardi B, Lux RL, Ershler PR, Rudy Y. Noninvasive electrocardiographic imaging: reconstruction of epicardial potentials, electrograms, and isochrones and localization of single and multiple electrocardiac events. *Circulation* (1997) 96:1012–1024. doi: 10.1161/01.CIR.96.3.1012
37. Colli-Franzone P, Guerri L, Tentoni S, Viganotti C, Baruffi S, Spaggiari S, Taccardi B. A mathematical procedure for solving the inverse potential problem of electrocardiography. analysis of the time-space accuracy from in vitro experimental data. *Math Biosci* (1985) 77:353–396. doi: 10.1016/0025-5564(85)90106-3
38. Ramanathan C, Ghanem RN, Jia P, Ryu K, Rudy Y. Noninvasive electrocardiographic imaging for cardiac electrophysiology and arrhythmia. *Nat Med* (2004) 10:422–428. doi: 10.1038/nm1011
39. Coll-Font J, Dhamala J, Potyagaylo D, Schulze WHW, Tate JD, Guillem MS, Van Dam P, Dossel O, Brooks DH, Macleod RS. The consortium for

- electrocardiographic imaging. *Comput Cardiol* (2016) 43:325–328. doi: 10.22489/cinc.2016.094-431
40. Tikhonov AN, Goncharsky AV, Stepanov VV, Yagola AG. *Numerical methods for the solution of ill-posed problems*. Dordrecht: Springer Netherlands (1995). doi: 10.1007/978-94-015-8480-7
 41. Ramanathan C, Rudy Y. Electrocardiographic imaging: I. Effect of torso inhomogeneities on body surface electrocardiographic potentials. *J Cardiovasc Electrophysiol* (2001) 12:229–240. doi: 10.1046/j.1540-8167.2001.00229.x
 42. Bergquist JA, Coll-Font J, Zenger B, Rupp LC, Good WW, Brooks DH, MacLeod RS. Reconstruction of cardiac position using body surface potentials. *Comput Biol Med* (2022) 142:105174. doi: 10.1016/j.compbiomed.2021.105174
 43. Berruezo A, Mont L, Nava S, Chueca E, Bartholomay E, Brugada J. Electrocardiographic recognition of the epicardial origin of ventricular tachycardias. *Circulation* (2004) 109:1842–1847. doi: 10.1161/01.CIR.0000125525.04081.4B
 44. Tate JD, Zemzemi N, Good WW, Van Dam P, Brooks DH, Macleod RS. Effect of segmentation variation on ECG imaging. *Comput Cardiol* (2018) 2018-Sept:3–6. doi: 10.22489/CinC.2018.374
 45. No FG, Dogrusoz YS, Onak ON, Weber G-W. Reduced leadset selection and performance evaluation in the inverse problem of electrocardiography for reconstructing the ventricularly paced electrograms. *J Electrocardiol* (2020) doi: 10.1016/j.jelectrocard.2020.02.017
 46. Cluitmans M, Brooks DH, MacLeod R, Dössel O, Guillem MS, Van Dam PM, Svehlikova J, He B, Sapp J, Wang L, et al. Validation and opportunities of electrocardiographic imaging: from technical achievements to clinical applications. *Front Physiol* (2018) 9:1–19. doi: 10.3389/fphys.2018.01305
 47. Bear LR, Cluitmans M, Abell E, Rogier J. Electrocardiographic imaging of repolarization abnormalities. *J Am Heart Assoc* (2021) 10: doi: 10.1161/JAHA.120.020153
 48. Duchateau J, Sacher F, Pambrun T, Derval N, Chamorro-Servent J, Denis A, Ploux S, Hocini M, Jaïs P, Bernus O, et al. Performance and limitations of noninvasive cardiac activation mapping. *Heart Rhythm* (2019) 16:435–442. doi: 10.1016/j.hrthm.2018.10.010
 49. Rudy Y. Letter to the Editor—ECG imaging and activation mapping. *Heart Rhythm* (2019) 16:e50–e51. doi: 10.1016/j.hrthm.2019.02.001

50. Cluitmans MJM, Stoks J, Volders PGA. To the Editor— Interpretation of electrograms is key to understand the clinical potential of ECGI. *Heart Rhythm* (2019) 16:e51–e52. doi: 10.1016/j.hrthm.2019.02.030
51. Cluitmans MJM, Bonizzi P, Karel JMH, Das M, Kietselaer BLJH, de Jong MMJ, Prinzen FW, Peeters RLM, Westra RL, Volders PGA. In vivo validation of electrocardiographic imaging. *J Am Coll Cardiol EP* (2017) 3:232–242. doi: 10.1016/j.jacep.2016.11.012
52. Ghanem RN, Jia P, Ramanathan C, Ryu K, Markowitz A, Rudy Y. Noninvasive electrocardiographic imaging (ECGI): comparison to intraoperative mapping in patients. *Heart Rhythm* (2005) 2:339–354. doi: 10.1016/j.hrthm.2004.12.022
53. Sapp JL, Dawoud F, Clements JC, Horáček BM. Inverse solution mapping of epicardial potentials: quantitative comparison with epicardial contact mapping. *Circ Arrhythm Electrophysiol* (2012) 5:1001–1009. doi: 10.1161/CIRCEP.111.970160
54. Revishvili AS, Wissner E, Lebedev DS, Lemes C, Deiss S, Metzner A, Kalinin VV, Sopov OV, Labartkava EZ, Kalinin AV, et al. Validation of the mapping accuracy of a novel non-invasive epicardial and endocardial electrophysiology system. *Europace* (2015) 17:1282–1288. doi: 10.1093/europace/euu339
55. Ghosh S, Rudy Y. Accuracy of quadratic versus linear interpolation in noninvasive electrocardiographic imaging (ECGI). *Ann Biomed Eng* (2005) 33:1187–1201. doi: 10.1007/s10439-005-5537-x
56. Oster HS, Taccardi B, Lux RL, Ershler PR, Rudy Y. Electrocardiographic imaging: noninvasive characterization of intramural myocardial activation from inverse-reconstructed epicardial potentials and electrograms. *Circulation* (1998) 97:1496–1507. doi: 10.1161/01.CIR.97.15.1496
57. Jurak P, Bear LR, Nguyễn UC, Viscor I, Andrla P, Plesinger F, Halamek J, Vondra V, Abell E, Cluitmans MJM, et al. 3-Dimensional ventricular electrical activation pattern assessed from a novel high-frequency electrocardiographic imaging technique: principles and clinical importance. *Sci Rep* (2021) 11:1–11. doi: 10.1038/s41598-021-90963-4
58. Erkapic D, Neumann T. Ablation of premature ventricular complexes exclusively guided by three-dimensional noninvasive mapping. *Card Electrophysiol Clin* (2015) 7:109–115. doi: 10.1016/j.ccep.2014.11.010
59. Salinet J, Molero R, Schindwein FS, Karel J, Rodrigo M, Rojo-Álvarez JL, Berenfeld O, Climent AM, Zenger B, Vanheusden F, et al. Electrocardiographic imaging for atrial fibrillation: a perspective from computer models and animal experiments to clinical value. *Front Physiol* (2021) 12: doi: 10.3389/

fphys.2021.653013

60. Vijayakumar R, Vasireddi SK, Cuculich PS, Faddis MN, Rudy Y. Methodology considerations in phase mapping of human cardiac arrhythmias. *Circ Arrhythm Electrophysiol* (2016) 9: doi: 10.1161/CIRCEP.116.004409
61. Honarbakhsh S, Dhillon G, Abbass H, Waddingham PH, Dennis A, Ahluwalia N, Welch S, Daw H, Sporton S, Chow A, et al. Noninvasive electrocardiographic imaging-guided targeting of drivers of persistent atrial fibrillation: The TARGET-AF1 trial. *Heart Rhythm* (2022)1–10. doi: 10.1016/j.hrthm.2022.01.042
62. Sedova K, Repin K, Donin G, Van Dam P, Kautzner J. Clinical utility of body surface potential mapping in CRT patients. *Arrhythmia Electrophysiol Rev* (2021) 10:113–119. doi: 10.15420/aer.2021.14
63. Ghosh S, Rhee EK, Avari JN, Woordard PK, Rudy Y. Cardiac memory in WPW patients: noninvasive imaging of activation and repolarization before and after catheter ablation. *Circulation* (2008) 118:907–915. doi: 10.1161/CIRCULATIONAHA.108.781658.Cardiac
64. Vijayakumar R, Silva JNA, Desouza KA, Abraham RL, Strom M, Sacher F, Van Hare GF, Haïssaguerre M, Roden DM, Rudy Y. Electrophysiologic substrate in congenital long QT syndrome: noninvasive mapping with electrocardiographic imaging (ECGI). *Circulation* (2014) 130:1936–1943. doi: 10.1161/CIRCULATIONAHA.114.011359
65. Zhang J, Sacher F, Hoffmayer K, O'Hara T, Strom M, Cuculich P, Silva J, Cooper D, Faddis M, Hocini M, et al. Cardiac electrophysiological substrate underlying the ECG phenotype and electrogram abnormalities in Brugada syndrome patients. *Circulation* (2015) 131:1950–1959. doi: 10.1161/CIRCULATIONAHA.114.013698
66. Leong KMW, Ng FS, Yao C, Roney C, Taraborrelli P, Linton NWF, Whinnett ZI, Lefroy DC, Davies DW, Boon Lim P, et al. ST-elevation magnitude correlates with right ventricular outflow tract conduction delay in type I Brugada ECG. *Circ Arrhythm Electrophysiol* (2017) 10:1–12. doi: 10.1161/CIRCEP.117.005107
67. Pannone L, Monaco C, Sorgente A, Vergara P, Gauthey A, Calborean PA, Bisignani A, Paparella G, Ramak R, Overeinder I, et al. SCN5A mutation in Brugada syndrome is associated with substrate severity detected by electrocardiographic imaging and high-density electroanatomic mapping. *Heart Rhythm* (2022)1–7. doi: 10.1016/j.hrthm.2022.01.034
68. Zhang J, Hocini M, Strom M, Cuculich PS, Cooper DH, Sacher F, Haïssaguerre M, Rudy Y. The Electrophysiological substrate of early repolarization syndrome: noninvasive mapping in patients. *JACC Clin Electrophysiol* (2017)

3:894–904. doi: 10.1016/j.jacep.2016.12.017

69. Andrews CM, Srinivasan NT, Rosmini S, Bulluck H, Orini M, Jenkins S, Pantazis A, McKenna WJ, Moon JC, Lambiase PD, et al. Electrical and structural substrate of arrhythmogenic right ventricular cardiomyopathy determined using noninvasive electrocardiographic imaging and late gadolinium magnetic resonance imaging. *Circ Arrhythm Electrophysiol* (2017) 10:1–12. doi: 10.1161/CIRCEP.116.005105
70. Perez-Alday EA, Haq KT, German DM, Hamilton C, Johnson K, Phan F, Rogovoy NM, Yang K, Wirth A, Thomas JA, et al. Mechanisms of arrhythmogenicity in hypertrophic cardiomyopathy: insight from non-invasive electrocardiographic imaging. *Front Physiol* (2020) 11:1–13. doi: 10.3389/fphys.2020.00344
71. Priori SG, Blomstrom-Lundqvist C, Mazzanti A, Bloma N, Borggrefe M, Camm J, Elliott PM, Fitzsimons D, Hatala R, Hindricks G, et al. 2015 ESC Guidelines for the management of patients with ventricular arrhythmias and the prevention of sudden cardiac death :the task force for the management of patients with ventricular arrhythmias and the prevention of sudden cardiac death of the european society of cardiology (ESC). Endorsed by: association for european paediatric and congenital cardiology (AEPC). *Eur Heart J* (2015) 36:2793–2867. doi: 10.1093/eurheartj/ehv316
72. Leong KMW, Ng FS, Roney C, Cantwell C, Shun-Shin MJ, Linton NWF, Whinnett ZI, Lefroy DC, Davies DW, Harding SE, et al. Repolarization abnormalities unmasked with exercise in sudden cardiac death survivors with structurally normal hearts. *J Cardiovasc Electrophysiol* (2018) 29:115–126. doi: 10.1111/jce.13375
73. Leong KMW, Ng FS, Shun-Shin MJ, Koa-Wing M, Qureshi N, Whinnett ZI, Linton NF, Lefroy D, Francis DP, Harding SE, et al. Non-invasive detection of exercise-induced cardiac conduction abnormalities in sudden cardiac death survivors in the inherited cardiac conditions. *Europace* (2021) 23:305–312. doi: 10.1093/europace/euaa248
74. Cluitmans MJM, Bear LR, Nguyễn UC, van Rees B, Stoks J, ter Bekke RMA, Muhl C, Heijman J, Lau KD, Vigmond E, et al. Noninvasive detection of spatiotemporal activation-repolarization interactions that prime idiopathic ventricular fibrillation. *Sci Transl Med* (2021) 13:1–11. doi: 10.1126/scitranslmed.abi9317
75. Nguyễn UC, Cluitmans MJM, Strik M, Luermans JG, Gommers S, Wildberger JE, Bekkers SCAM, Volders PGA, Muhl C, Prinzen FW, et al. Integration of cardiac magnetic resonance imaging, electrocardiographic imaging, and coronary venous computed tomography angiography for guidance of left

- ventricular lead positioning. *Europace* (2019) 21:626–635. doi: 10.1093/europace/euy292
76. Nguyen D, Jeudy J, Restrepo AJ, Dickfeld TM. A novel use of noninvasive registered electrocardiographic imaging map for localization of VT and PVC. *JACC Case Rep* (2021) 3:591–593. doi: 10.1016/j.jaccas.2021.01.031
77. Cuculich PS, Schill MR, Kashani R, Mutic S, Lang A, Cooper D, Faddis M, Gleva M, Noheria A, Smith TW, et al. Noninvasive cardiac radiation for ablation of ventricular tachycardia. *N Engl J Med* (2017) 377:2325–2336. doi: 10.1056/nejmoa1613773
78. Trayanova NA, Popescu DM, Shade JK. Machine learning in arrhythmia and electrophysiology. *Circ Res* (2021) 128:544–566. doi: 10.1161/CIRCRESAHA.120.317872
79. Einthoven W. Le télécardiogramme. *Archives Internationales de Physiologie* (1906) 4 (sept./a2):132–164.
80. De Craene M, Tobon-Gomez C, Butakoff C, Duchateau N, Piella G, Rhode KS, Frangi AF. Temporal diffeomorphic free form deformation (TDDFD) applied to motion and deformation quantification of tagged MRI sequences. Camara, O., Konukoglu, E., Pop, M., Rhode, K., Sermesant, M., Young, A. (editors) *In: Statistical Atlases and Computational Models of the Heart. Imaging and Modelling Challenges. STACOM 2011. Lecture Notes in Computer Science, vol 7085. Springer, Berlin, Heidelberg.* doi: 10.1007/978-3-642-28326-0_7
81. Paun B, Bijmens B, Iles T, Iazzo PA, Butakoff C. Patient independent representation of the detailed cardiac ventricular anatomy. *Med Image Anal* (2017) 35:270–287. doi: 10.1016/j.media.2016.07.006
82. Bayer J, Prassl AJ, Pashaei A, Gomez JF, Frontera A, Neic A, Plank G, Vigmond EJ. Universal ventricular coordinates: a generic framework for describing position within the heart and transferring data. *Med Image Anal* (2018) 45:83–93. doi: 10.1016/j.media.2018.01.005
83. Stoks J, van Rees B, Groeneveld S, Schipaanboord D, Blom L, Hassink R, Cluitmans M, Peeters R, Volders P. Variability of electrocardiographic imaging within and between leadsets. *Comput Cardiol* (2020) doi: 10.22489/CinC.2020.097
84. Cluitmans MJM, Karel J, Bonizzi P, De Jong MMJ, Volders PGA, Peeters RLM, Westra RL. In-vivo evaluation of reduced-lead-systems in noninvasive reconstruction and localization of cardiac electrical activity. *Comput Cardiol* (2015) 42:221–224. doi: 10.1109/CIC.2015.7408626

85. Stoks J, Cluitmans MJM, Peeters R, Volders PGA. The influence of using a static diastolic geometry in ECG imaging. *Comput Cardiol* (2019) 2019-Sept:2–5. doi: 10.23919/CinC49843.2019.9005847
86. Haws CW, Lux RL. Correlation between in vivo transmembrane action potential durations and activation-recovery intervals from electrograms. Effects of interventions that alter repolarization time. *Circulation* (1990) 81:281–288. doi: 10.1161/01.CIR.81.1.281
87. Srinivasan NT, Garcia J, Schilling RJ, Ahsan S, Hunter RJ, Lowe M, Chow AW, Lambiase PD. Dynamic spatial dispersion of repolarization is present in regions critical for ischemic ventricular tachycardia ablation. *Heart Rhythm* O2 (2021) 2:280–289. doi: 10.1016/j.hroo.2021.05.003
88. Wyatt RF, Burgess MJ, Evans AK, Lux RL, Abildskov JA, Tsutsumi T. Estimation of ventricular transmembrane action potential durations and repolarization times from unipolar electrograms. *Am J Cardiol* (1981) 47:488. doi: 10.1016/0002-9149(81)91028-6
89. Millar CK, Kralios FA, Lux RL. Correlation between refractory periods and activation-recovery intervals from electrograms: effects of rate and adrenergic interventions. *Circulation* (1985) 72:1372–1379. doi: 10.1161/01.CIR.72.6.1372
90. Chen PS, Moser KM, Dembitsky WP, Auger WR, Daily PO, Calisi CM, Jamieson SW, Feld GK. Epicardial activation and repolarization patterns in patients with right ventricular hypertrophy. *Circulation* (1991) 83:104–118. doi: 10.1161/01.CIR.83.1.104
91. Gepstein L, Hayam G, Ben-Haim SA. Activation-repolarization coupling in the normal swine endocardium. *Circulation* (1997) 96:4036–4043. doi: 10.1161/01.CIR.96.11.4036
92. Yue AM, Paisey JR, Robinson S, Betts TR, Roberts PR, Morgan JM. Determination of human ventricular repolarization by noncontact mapping: validation with monophasic action potential recordings. *Circulation* (2004) 110:1343–1350. doi: 10.1161/01.CIR.0000141734.43393.BE
93. Franzone PC, Pavarino LF, Scacchi S, Taccardi B. Monophasic action potentials generated by bidomain modeling as a tool for detecting cardiac repolarization times. *Am J Physiol - Heart Circ Physiol* (2007) 293:2771–2785. doi: 10.1152/ajpheart.00651.2007
94. Potse M, Coronel R, Opthof T, Vinet A. The positive T wave. *Anadolu Kardiyol Derg* (2007) 7 suppl 1:164–167.

95. Boukens BJ, Meijborg VMF, Belterman CN, Opthof T, Janse MJ, Schuessler RB, Coronel R, Efimov IR. Local transmural action potential gradients are absent in the isolated, intact dog heart but present in the corresponding coronary-perfused wedge. *Physiol Rep* (2017) 5:e13251. doi: 10.14814/phy2.13251
96. Wijers SC, Sprenkeler DJ, Bossu A, Dunnink A, Beekman JDM, Varkevisser R, Hernández AA, Meine M, Vos MA. Beat-to-beat variations in activation-recovery interval derived from the right ventricular electrogram can monitor arrhythmic risk under anesthetic and awake conditions in the canine chronic atrioventricular block model. *Heart Rhythm* (2018) 15:442–448. doi: 10.1016/j.hrthm.2017.11.011
97. Durrer D, Van der Tweel H. Spread of activation in the left ventricular wall of the dog. II. *Am Heart J* (1954) 47:192–203.
98. Punske BB, Ni Q, Lux RL, MacLeod RS, Ershler PR, Dustman TJ, Allison MJ, Taccardi B. Spatial methods of epicardial activation time determination in normal hearts. *Ann Biomed Eng* (2003) 31:781–792. doi: 10.1114/1.1581877
99. Steinhaus BM. Estimating cardiac transmembrane activation and recovery times from unipolar and bipolar extracellular electrograms: a simulation study. *Circ Res* (1989) 64:449–462. doi: 10.1161/01.RES.64.3.449
100. Arora R, Kadish A. “Fundamentals of intracardiac mapping,,” In: Huang SKS, Wood MA, editors. *Catheter Ablation of Cardiac Arrhythmias*. Philadelphia: Elsevier Saunders (2010). p. 103–126
101. Potse M, Vinet A, Opthof T, Coronel R. Validation of a simple model for the morphology of the T wave in unipolar electrograms. *Am J Physiol-Heart Circ Physiol* (2009) 297:H792–H801. doi: 10.1152/ajpheart.00064.2009
102. Van Duijvenboden S, Orini M, Taggart P, Hanson B. Accuracy of measurements derived from intracardiac unipolar electrograms: a simulation study. *Proc Annu Int Conf IEEE Eng Med Biol Soc EMBS* (2015) 2015-Novem:76–79. doi: 10.1109/EMBC.2015.7318304
103. Western D, Hanson B, Taggart P. Measurement bias in activation-recovery intervals from unipolar electrograms. *Am J Physiol - Heart Circ Physiol* (2015) 308:H331–H338. doi: 10.1152/ajpheart.00478.2014
104. Bear LR, Walton RD, Abell E, Coudière Y, Haissaguerre M, Bernus O, Dubois R, Myles RC, Bear LR. Optical imaging of ventricular action potentials in a torso tank : a new platform for non-invasive electrocardiographic imaging validation. *Front Physiol* (2019) 10:1–11. doi: 10.3389/fphys.2019.00146
105. Bear LR, Bouhamama O, Cluitmans M, Duchateau J, Walton RD, Abell E,

- Belterman C, Haissaguerre M, Bernus O, Coronel R, et al. Advantages and pitfalls of noninvasive electrocardiographic imaging. *J Electrocardiol* (2019) 57:S15–S20. doi: 10.1016/j.jelectrocard.2019.08.007
106. Chinushi M, Tagawa M, Kasai H, Washizuka T, Abe A, Furushima H, Aizawa Y. Correlation between the effective refractory period and activation-recovery interval calculated from the intracardiac unipolar electrogram of humans with and without dl-sotalol treatment. *Jpn Circ J* (2001) 65:702–706. doi: 10.1253/jcj.65.702
107. Orini M, Srinivasan N, Graham AJ, Taggart P, Lambiase PD. Further evidence on how to measure local repolarization time using intracardiac unipolar electrograms in the intact human heart. *Circ Arrhythm Electrophysiol* (2019) 12:1–3. doi: 10.1161/CIRCEP.119.007733
108. Schilling RJ, Peters NS, Davies DW. Simultaneous endocardial mapping in the human left ventricle using a noncontact catheter: comparison of contact and reconstructed electrograms during sinus rhythm. *Circulation* (1998) 98:887–898. doi: 10.1161/01.CIR.98.9.887
109. Coronel R, de Bakker JM, Janse MJ, Opthof T. To the editor—response. *Heart Rhythm* (2007) 4:121. doi: 10.1016/j.hrthm.2006.10.007
110. Orini M, Taggart P, Lambiase PD. In vivo human sock-mapping validation of a simple model that explains unipolar electrogram morphology in relation to conduction-repolarization dynamics. *J Cardiovasc Electrophysiol* (2018) 29:990–997. doi: 10.1111/jce.13606
111. Langfield P, Feng Y, Bear LR, Duchateau J, Sebastian R, Abell E, Dubois R, Labrousse L, Rogier J, Hocini M, et al. A novel method to correct repolarization time estimation from unipolar electrograms distorted by standard filtering. *Med Image Anal* (2021) 72:102075. doi: 10.1016/j.media.2021.102075
112. Cluitmans M, Coll-Font J, Erem B, Bear L, Nguyễn UC, ter Bekke R, Volders PGA, Brooks D. Spatiotemporal approximation of cardiac activation and recovery isochrones. *J Electrocardiol* (2022) 71:1–9. doi: 10.1016/j.jelectrocard.2021.12.007
113. Coronel R, Janse MJ, Opthof T, Wilde AA, Taggart P. Postrepolarization refractoriness in acute ischemia and after antiarrhythmic drug administration: action potential duration is not always an index of the refractory period. *Heart Rhythm* (2012) 9:977–982. doi: 10.1016/j.hrthm.2012.01.021
114. Cowan JC, Hiltón CJ, Griffiths CJ, Tansuphaswadikul S, Bourke JP, Murray A, Campbell RWF. Sequence of epicardial repolarisation and configuration of the T wave. *Heart* (1988) 60:424–433. doi: 10.1136/hrt.60.5.424

115. Franz MR, Bargheer K, Rafflenbeul W, Haverich A, Lichtlen PR. Monophasic action potential mapping in human subjects with normal electrocardiograms: Direct evidence for the genesis of the T wave. *Circulation* (1987) 75:379–386. doi: 10.1161/01.CIR.75.2.379
116. Opthof T, Janse MJ, Meijborg VMF, Cinca J, Rosen MR, Coronel R. Dispersion in ventricular repolarization in the human, canine and porcine heart. *Prog Biophys Mol Biol* (2016) 120:222–235. doi: 10.1016/j.pbiomolbio.2016.01.007
117. Opthof T, Remme CA, Jorge E, Noriega F, Wiegerinck RF, Tasiyam A, Beekman L, Alvarez-Garcia J, Munoz-Guijosa C, Coronel R, et al. Cardiac activation–repolarization patterns and ion channel expression mapping in intact isolated normal human hearts. *Heart Rhythm* (2017) 14:265–272. doi: 10.1016/j.hrthm.2016.10.010
118. Durrer D, van Dam RT, Freud GE, Janse MJ, Meijler FL, Arzbaecher RC. Total excitation of the isolated human heart. *Circulation* (1970) 41:899–912. doi: 10.1161/01.CIR.41.6.899
119. Andrews C, Cupps BP, Pasque MK, Rudy Y. Electromechanics of the normal human heart in situ. *Circ Arrhythm Electrophysiol* (2019) 12:1–3. doi: 10.1161/CIRCEP.119.007484
120. Ramanathan C, Jia P, Ghanem R, Ryu K, Rudy Y. Activation and repolarization of the normal human heart under complete physiological conditions. *Proc Natl Acad Sci* (2006) 103:6309–6314. doi: 10.1073/pnas.0601533103
121. Waddingham PH, Mangual JO, Orini M, Badie N, Muthumala A, Sporton S, McSpadden LC, Lambiase PD, Chow AWC. Electrocardiographic imaging demonstrates electrical synchrony improvement by dynamic atrioventricular delays in patients with left bundle branch block and preserved atrioventricular conduction. *Europace* (2023) 25:536–545. doi: 10.1093/europace/euac224
122. Jackson T, Claridge S, Behar J, Sieniewicz B, Gould J, Porter B, Sidhu B, Yao C, Lee A, Niederer S, et al. Differential effect with septal and apical RV pacing on ventricular activation in patients with left bundle branch block assessed by non-invasive electrical imaging and in silico modelling. *J Interv Card Electrophysiol Int J Arrhythm Pacing* (2020) 57:115–123. doi: 10.1007/s10840-019-00567-2
123. Nguyen UC, Stoks J, Cluitmans MJ, Strik M, van Rees B, Meiburg R, Mihil C, Volders PG, Vernooij K, Prinzen FW. Delayed ventricular conduction alters ventricular repolarization in patients with heart failure: an electrocardiographic imaging study. *Heart Rhythm* (2023) 20:S156–S157. doi: 10.1016/j.hrthm.2023.03.519

124. Alhede C, Higuchi S, Hadjis A, Bibby D, Abraham T, Schiller NB, Gerstenfeld EP. Premature ventricular contractions are presaged by a mechanically abnormal sinus beat. *JACC Clin Electrophysiol* (2022) 8:943–953. doi: 10.1016/j.jacep.2022.05.005
125. Wyndham CR, Meeran MK, Smith T, Saxena A, Engelman RM, Levitsky S, Rosen KM. Epicardial activation of the intact human heart without conduction defect. *Circulation* (1979) 59:161–168. doi: 10.1161/01.CIR.59.1.161
126. Maffessanti F, Wanten J, Potse M, Regoli F, Caputo ML, Conte G, Sürder D, Illner A, Krause R, Moccetti T, et al. The relation between local repolarization and T-wave morphology in heart failure patients. *Int J Cardiol* (2017) 241:270–276. doi: 10.1016/j.ijcard.2017.02.056
127. Bear LR, Huntjens PR, Walton RD, Bernus O, Coronel R, Dubois R. Cardiac electrical dyssynchrony is accurately detected by noninvasive electrocardiographic imaging. *Heart Rhythm* (2018) 15:1058–1069. doi: 10.1016/j.hrthm.2018.02.024
128. CIBC. Seg3D: Volumetric image segmentation and visualization. Scientific Computing and Imaging Institute (SCI). (2016) <http://www.seg3d.org>
129. Maas SA, Ellis BJ, Ateshian GA, Weiss JA. FEBio: finite elements for biomechanics. *J Biomech Eng* (2012) 134:011005. doi: 10.1115/1.4005694
130. Ricciardi D, Cavallari I, Creta A, Di Giovanni G, Calabrese V, Di Belardino N, and others. Impact of the high-frequency cutoff of bandpass filtering on ECG quality and clinical interpretation: a comparison between 40 Hz and 150 Hz cutoff in a surgical preoperative adult outpatient population. *J Electrocardiol* (2016) 49:691–695. doi: 10.1016/j.jelectrocard.2016.07.002
131. Barr RC, Ramsey M, Spach MS. Relating epicardial to body surface potential distributions by means of transfer coefficients based on geometry measurements. *IEEE Trans Biomed Eng* (1977) BME-24:1–11. doi: 10.1109/TBME.1977.326201
132. Burton BM, Tate JD, Erem B, Swenson DJ, Wang DF, Steffen M, Brooks DH, van Dam PM, Macleod RS. A toolkit for forward/inverse problems in electrocardiography within the SCIRun problem solving environment. *Annu Int Conf IEEE Eng Med Biol Soc* (2011) 2011:267–270. doi: 10.1109/IEMBS.2011.6090052
133. Ramanathan C, Rudy Y. Electrocardiographic imaging: II. Effect of torso inhomogeneities on noninvasive reconstruction of epicardial potentials, electrograms, and isochrones. *J Cardiovasc Electrophysiol* (2001) 12:241–252. doi: 10.1046/j.1540-8167.2001.00241.x

134. Hansen PC, O'Leary DP. The use of the L-curve in the regularization of discrete ill-posed problems. *SIAM J Sci Comput* (1993) 14:1487–1503. doi: 10.1137/0914086
135. Duchateau J, Potse M, Dubois R. Spatially coherent activation maps for electrocardiographic imaging. *IEEE Trans Biomed Eng* (2017) 64:1149–1156. doi: 10.1109/TBME.2016.2593003
136. Conte G, Giudicessi JR, Ackerman MJ. Idiopathic ventricular fibrillation: the ongoing quest for diagnostic refinement. *Europace* (2021) 23:4–10. doi: 10.1093/europace/euaa211
137. Alders M, Koopmann TT, Christiaans I, Postema PG, Beekman L, Tanck MWT, Zeppenfeld K, Loh P, Koch KT, Demolombe S, et al. Haplotype-sharing analysis implicates chromosome 7q36 harboring DPP6 in familial idiopathic ventricular fibrillation. *Am J Hum Genet* (2009) 84:468–476. doi: 10.1016/j.ajhg.2009.02.009
138. Radicke S, Cotella D, Graf EM, Ravens U, Wettwer E. Expression and function of dipeptidyl-aminopeptidase-like protein 6 as a putative beta-subunit of human cardiac transient outward current encoded by Kv4.3. *J Physiol* (2005) 565:751–756. doi: 10.1113/jphysiol.2005.087312
139. Xiao L, Koopmann TT, Ördög B, Postema PG, Verkerk AO, Iyer V, Sampson KJ, Boink GJJ, Mamarbachi MA, Varro A, et al. Unique cardiac Purkinje fiber transient outward current β -subunit composition: a potential molecular link to idiopathic ventricular fibrillation. *Circ Res* (2013) 112:1310–1322. doi: 10.1161/CIRCRESAHA.112.300227
140. Ding D-B, Fan L-L, Xiao Z, Huang H, Chen Y-Q, Guo S, Liu Z-H, Xiang R. A novel mutation of dipeptidyl aminopeptidase-like protein-6 in a family with suspicious idiopathic ventricular fibrillation. *QJM Mon J Assoc Physicians* (2018) 111:373–377. doi: 10.1093/qjmed/hcy033
141. Ji C-C, Yao F-J, Cheng Y-J, Yao H, Fan J, Chen X-M, Zheng Z-H, Dong Y-G, Wu S-H. A novel DPP6 variant in Chinese families causes early repolarization syndrome. *Exp Cell Res* (2019) 384:111561. doi: 10.1016/j.yexcr.2019.111561
142. Sturm AC, Kline CF, Glynn P, Johnson BL, Curran J, Kilic A, Higgins RSD, Binkley PF, Janssen PML, Weiss R, et al. Use of whole exome sequencing for the identification of Ito-based arrhythmia mechanism and therapy. *J Am Heart Assoc* (2015) 4: doi: 10.1161/JAHA.114.001762
143. Clatot J, Neyroud N, Cox R, Souil C, Huang J, Guicheney P, Antzelevitch C. Inter-regulation of K(v)4.3 and voltage-gated sodium channels underlies predisposition to cardiac and neuronal channelopathies. *Int J Mol Sci* (2020)

21: doi: 10.3390/ijms21145057

144. Belau F, Metzner K, Christ T, Ravens U, Schaefer M, Künzel S, Li W, Wettwer E, Dobrev D, El-Armouche A, et al. DPP10 is a new regulator of Nav1.5 channels in human heart. *Int J Cardiol* (2019) 284:68–73. doi: 10.1016/j.ijcard.2018.12.072
145. Qi SY, Riviere PJ, Trojnar J, Junien J-L, Akinsanya KO. Cloning and characterization of dipeptidyl peptidase 10, a new member of an emerging subgroup of serine proteases. *Biochem J* (2003) 373:179–189. doi: 10.1042/BJ20021914
146. Giudicessi JR, Ye D, Tester DJ, Crotti L, Mugione A, Nesterenko VV, Albertson RM, Antzelevitch C, Schwartz PJ, Ackerman MJ. Transient outward current (I_{to}) gain-of-function mutations in the KCND3-encoded Kv4.3 potassium channel and Brugada syndrome. *Heart Rhythm* (2011) 8:1024–1032. doi: 10.1016/j.hrthm.2011.02.021
147. Wilde AAM, Amin AS. Clinical Spectrum of SCN5A Mutations: Long QT syndrome, Brugada syndrome, and cardiomyopathy. *J Am Coll Cardiol EP* (2018) 4:569–579. doi: 10.1016/j.jacep.2018.03.006
148. Richards S, Aziz N, Bale S, Bick D, Das S, Gastier-Foster J, Grody WW, Hegde M, Lyon E, Spector E, et al. Standards and guidelines for the interpretation of sequence variants: a joint consensus recommendation of the American College of Medical Genetics and Genomics and the Association for Molecular Pathology. *Genet Med* (2015) 17:405–424. doi: 10.1038/gim.2015.30
149. Al'Aref SJ, Ip JE, Markowitz SM, Liu CF, Thomas G, Frenkel D, Panda NC, Weinsaft JW, Lerman BB, Cheung JW. Differentiation of papillary muscle from fascicular and mitral annular ventricular arrhythmias in patients with and without structural heart disease. *Circ Arrhythm Electrophysiol* (2015) 8:616–624. doi: 10.1161/CIRCEP.114.002619
150. GNOMAD database. *GNOMAD database* <https://gnomad.broadinstitute.org/> [Accessed September 27, 2023]
151. Lin L, Long LK, Hatch MM, Hoffman DA. DPP6 domains responsible for its localization and function. *J Biol Chem* (2014) 289:32153–32165. doi: 10.1074/jbc.M114.578070
152. Chiamvimonvat N, Chen-Izu Y, Clancy CE, Deschenes I, Dobrev D, Heijman J, Izu L, Qu Z, Ripplinger CM, Vandenberg JL, et al. Potassium currents in the heart: functional roles in repolarization, arrhythmia and therapeutics. *J Physiol* (2017) 595:2229–2252. doi: 10.1113/JP272883

153. Lainez S, Doray A, Hancox JC, Cannell MB. Regulation of Kv4.3 and hERG potassium channels by KChIP2 isoforms and DPP6 and response to the dual K(+) channel activator NS3623. *Biochem Pharmacol* (2018) 150:120–130. doi: 10.1016/j.bcp.2018.01.036
154. Lord SJ, Velle KB, Mullins RD, Fritz-Laylin LK. Superplots: communicating reproducibility and variability in cell biology. *J Cell Biol* (2020) 219: doi: 10.1083/jcb.202001064
155. Cacace R, Heeman B, Van Mossevelde S, De Roeck A, Hoogmartens J, De Rijk P, Gossye H, De Vos K, De Coster W, Strazisar M, et al. Loss of DPP6 in neurodegenerative dementia: a genetic player in the dysfunction of neuronal excitability. *Acta Neuropathol (Berl)* (2019) 137:901–918. doi: 10.1007/s00401-019-01976-3
156. Gaborit N, Le Bouter S, Szuts V, Varro A, Escande D, Nattel S, Demolombe S. Regional and tissue specific transcript signatures of ion channel genes in the non-diseased human heart. *J Physiol* (2007) 582:675–693. doi: 10.1113/jphysiol.2006.126714
157. Soltysinska E, Olesen S-P, Christ T, Wettwer E, Varró A, Grunnet M, Jespersen T. Transmural expression of ion channels and transporters in human nondiseased and end-stage failing hearts. *Pflugers Arch* (2009) 459:11–23. doi: 10.1007/s00424-009-0718-3
158. Lundby A, Jespersen T, Schmitt N, Grunnet M, Olesen S-P, Cordeiro JM, Calloe K. Effect of the I(to) activator NS5806 on cloned K(V)4 channels depends on the accessory protein KChIP2. *Br J Pharmacol* (2010) 160:2028–2044. doi: 10.1111/j.1476-5381.2010.00859.x
159. Huelsing DJ, Spitzer KW, Cordeiro JM, Pollard AE. Conduction between isolated rabbit Purkinje and ventricular myocytes coupled by a variable resistance. *Am J Physiol* (1998) 274:H1163–1173. doi: 10.1152/ajpheart.1998.274.4.H1163
160. Brackenbury WJ, Isom LL. Na Channel β Subunits: Overachievers of the ion channel family. *Front Pharmacol* (2011) 2:53. doi: 10.3389/fphar.2011.00053
161. Remme CA, Verkerk AO, Hoogaars WMH, Aanhaanen WTJ, Scicluna BP, Annink C, van den Hoff MJB, Wilde AAM, van Veen TAB, Veldkamp MW, et al. The cardiac sodium channel displays differential distribution in the conduction system and transmural heterogeneity in the murine ventricular myocardium. *Basic Res Cardiol* (2009) 104:511–522. doi: 10.1007/s00395-009-0012-8
162. Watanabe Y. Purkinje repolarization as a possible cause of the U wave in the electrocardiogram. *Circulation* (1975) 51:1030–1037. doi: 10.1161/01.

cir.51.6.1030

163. Bufalari A, Furbetta D, Santucci F, Solinas P. Abnormality of the U wave and of the T-U segment of the electrocardiogram; the syndrome of the papillary muscles. *Circulation* (1956) 14:1129–1137. doi: 10.1161/01.cir.14.6.1129
164. El-Sherif N. Early afterdepolarizations and arrhythmogenesis. Experimental and clinical aspects. *Arch Mal Coeur Vaiss* (1991) 84:227–234.
165. El-Sherif N, Caref EB, Chinushi M, Restivo M. Mechanism of arrhythmogenicity of the short-long cardiac sequence that precedes ventricular tachyarrhythmias in the long QT syndrome. *J Am Coll Cardiol* (1999) 33:1415–1423. doi: 10.1016/s0735-1097(98)00700-1
166. Lehmann MH, Denker S, Mahmud R, Akhtar M. Postextrasystolic alterations in refractoriness of the His-Purkinje system and ventricular myocardium in man. *Circulation* (1984) 69:1096–1102. doi: 10.1161/01.cir.69.6.1096
167. Wilde AAM, Postema PG, Di Diego JM, Viskin S, Morita H, Fish JM, Antzelevitch C. The pathophysiological mechanism underlying Brugada syndrome. Depolarization versus repolarization. *J Mol Cell Cardiol* (2010) 49:543–553. doi: 10.1016/j.yjmcc.2010.07.012
168. Zhao Z, Xie Y, Wen H, Xiao D, Allen C, Fefelova N, Dun W, Boyden PA, Qu Z, Xie L-H. Role of the transient outward potassium current in the genesis of early afterdepolarizations in cardiac cells. *Cardiovasc Res* (2012) 95:308–316. doi: 10.1093/cvr/cvs183
169. Koponen M, Marjamaa A, Väänänen H, Tuiskula AM, Kontula K, Swan H, Viitasalo M. Effects of β -blockers on ventricular repolarization documented by 24-hour electrocardiography in long QT syndrome type 2. *Heart Rhythm* (2022) 19:1491–1498. doi: 10.1016/j.hrthm.2022.04.028
170. Rasche U, Reijerkerk, Arie. Controlled manufacturing of hiPSC-derived cardiomyocytes in stirred-tank bioreactors enabling high-throughput phenotypic screening. (2019) <https://www.ncardia.com/insights/resources/controlled-large-scale-manufacturing-of-ipsc-derived-cardiomyocytes> [Accessed June 30, 2023]
171. Sirover MA. Subcellular dynamics of multifunctional protein regulation: Mechanisms of GAPDH intracellular translocation. *J Cell Biochem* (2012) 113:2193–2200. doi: 10.1002/jcb.24113
172. Trovato C, Passini E, Nagy N, Varró A, Abi-Gerges N, Severi S, Rodriguez B. Human Purkinje in silico model enables mechanistic investigations into automaticity and pro-arrhythmic abnormalities. *J Mol Cell Cardiol* (2020)

- 142:24–38. doi: 10.1016/j.yjmcc.2020.04.001
173. Passini E, Mincholé A, Coppini R, Cerbai E, Rodriguez B, Severi S, Bueno-Orovio A. Mechanisms of pro-arrhythmic abnormalities in ventricular repolarisation and anti-arrhythmic therapies in human hypertrophic cardiomyopathy. *J Mol Cell Cardiol* (2016) 96:72–81. doi: 10.1016/j.yjmcc.2015.09.003
 174. O'Hara T, Virág L, Varró A, Rudy Y. Simulation of the undiseased human cardiac ventricular action potential: model formulation and experimental validation. *PLoS Comput Biol* (2011) 7:e1002061. doi: 10.1371/journal.pcbi.1002061
 175. Clerx M, Collins P, de Lange E, Volders PGA. Myokit: A simple interface to cardiac cellular electrophysiology. *Prog Biophys Mol Biol* (2016) 120:100–114. doi: 10.1016/j.pbiomolbio.2015.12.008
 176. Glukhov AV, Fedorov VV, Kalish PW, Ravikumar VK, Lou Q, Janks D, Schuessler RB, Moazami N, Efimov IR. Conduction remodeling in human end-stage nonischemic left ventricular cardiomyopathy. *Circulation* (2012) 125:1835–1847. doi: 10.1161/CIRCULATIONAHA.111.047274
 177. Kupersmith J, Krongrad E, Waldo AL. Conduction intervals and conduction velocity in the human cardiac conduction system. Studies during open-heart surgery. *Circulation* (1973) 47:776–785. doi: 10.1161/01.cir.47.4.776
 178. Boukens BJ, Sylva M, de Gier-de Vries C, Remme CA, Bezzina CR, Christoffels VM, Coronel R. Reduced sodium channel function unmasks residual embryonic slow conduction in the adult right ventricular outflow tract. *Circ Res* (2013) 113:137–141. doi: 10.1161/CIRCRESAHA.113.301565
 179. Reddy VY, Reynolds MR, Neuzil P, Richardson AW, Taborsky M, Jongnarangsin K, Kralovec S, Sediva L, Ruskin JN, Josephson ME. Prophylactic Catheter Ablation for the Prevention of Defibrillator Therapy. *N Engl J Med* (2007) 357:2657–2665. doi: 10.1056/NEJMoa065457
 180. Kuck K-H, Schaumann A, Eckardt L, Willems S, Ventura R, Delacrétaz E, Pitschner H-F, Kautzner J, Schumacher B, Hansen PS. Catheter ablation of stable ventricular tachycardia before defibrillator implantation in patients with coronary heart disease (VTACH): a multicentre randomised controlled trial. *The Lancet* (2010) 375:31–40. doi: 10.1016/S0140-6736(09)61755-4
 181. Briceño DF, Romero J, Villablanca PA, Londoño A, Diaz JC, Maraj I, Batul SA, Madan N, Patel J, Jagannath A, et al. Long-term outcomes of different ablation strategies for ventricular tachycardia in patients with structural heart disease: systematic review and meta-analysis. *Europace* (2018) 20:104–115. doi: 10.1093/europace/eux109

182. Coyle K, Coyle D, Nault I, Parkash R, Healey JS, Gray CJ, Gardner MJ, Sterns LD, Essebag V, Hruczkowski T, et al. Cost effectiveness of ventricular tachycardia ablation versus escalation of antiarrhythmic drug therapy. *J Am Coll Cardiol EP* (2018) 4:660–668. doi: 10.1016/j.jacep.2018.01.007
183. Calkins H, Epstein A, Packer D, Arria AM, Hummel J, Gilligan DM, Trusso J, Carlson M, Luceri R, Kopelman H, et al. Catheter ablation of ventricular tachycardia in patients with structural heart disease using cooled radiofrequency energy. *J Am Coll Cardiol* (2000) 35:1905–1914. doi: 10.1016/S0735-1097(00)00615-X
184. Soto-Iglesias D, Penela D, Jáuregui B, Acosta J, Fernández-Armenta J, Linhart M, Zucchelli G, Syrovnev V, Zaraket F, Terés C, et al. Cardiac magnetic resonance-guided ventricular tachycardia substrate ablation. *J Am Coll Cardiol EP* (2020) 6:436–447. doi: 10.1016/j.jacep.2019.11.004
185. Hendriks AA, Kis Z, Glisic M, Bramer WM, Szili-Torok T. Pre-procedural image-guided versus non-image-guided ventricular tachycardia ablation—a review. *Neth Heart J* (2020) 28:573–583. doi: 10.1007/s12471-020-01485-z
186. Cronin EM, Bogun FM, Maury P, Peichl P, Chen M, Namboodiri N, Aguinaga L, Leite LR, Al-Khatib SM, Anter E, et al. 2019 HRS/EHRA/APHRS/LAHRs expert consensus statement on catheter ablation of ventricular arrhythmias. *Europace* (2019) 21:1143–1144. doi: 10.1093/europace/euz132
187. Wang Y, Cuculich PS, Zhang J, Desouza KA, Vijayakumar R, Chen J, Faddis MN, Lindsay BD, Smith TW, Rudy Y. Noninvasive electroanatomic mapping of human ventricular arrhythmias with electrocardiographic imaging. *Sci Transl Med* (2011) 3:1–7. doi: 10.1126/scitranslmed.3002152
188. Andreu D, Fernández-Armenta J, Acosta J, Penela D, Jáuregui B, Soto-Iglesias D, Syrovnev V, Arbelo E, Tolosana JM, Berruezo A. A QRS axis-based algorithm to identify the origin of scar-related ventricular tachycardia in the 17-segment American Heart Association model. *Heart Rhythm* (2018) 15:1491–1497. doi: 10.1016/j.hrthm.2018.06.013
189. Segal OR, Chow AWC, Wong T, Trevisi N, Lowe MD, Davies DW, Della Bella P, Packer DL, Peters NS. A novel algorithm for determining endocardial VT exit site from 12-lead surface ECG characteristics in human, infarct-related ventricular tachycardia. *J Cardiovasc Electrophysiol* (2007) 18:161–168. doi: 10.1111/j.1540-8167.2007.00721.x
190. Holtackers RJ, Gommers S, Van De Heyning CM, Muhl C, Smink J, Higgins DM, Wildberger JE, ter Bekke RMA. Steadily increasing inversion time improves blood suppression for free-breathing 3D late gadolinium enhancement MRI with optimized dark-blood contrast. *Invest Radiol* (2021) 56:335–340. doi:

10.1097/RLI.0000000000000747

191. Holtackers RJ, Gommers S, Heckman LIB, Van De Heyning CM, Chiribiri A, Prinzen FW. Histopathological validation of dark-blood late gadolinium enhancement mri without additional magnetization preparation. *J Magn Reson Imaging* (2022) 55:190–197. doi: 10.1002/jmri.27805
192. Andreu D, Ortiz-Pérez JT, Fernández-Armenta J, Guiu E, Acosta J, Prat-González S, De Caralt TM, Perea RJ, Garrido C, Mont L, et al. 3D delayed-enhanced magnetic resonance sequences improve conducting channel delineation prior to ventricular tachycardia ablation. *Europace* (2015) 17:938–945. doi: 10.1093/europace/euu310
193. Andreu D, Berruezo A, Ortiz-Pérez JT, Silva E, Mont L, Borràs R, de Caralt TM, Perea RJ, Fernández-Armenta J, Zeljko H, et al. Integration of 3D electroanatomic maps and magnetic resonance scar characterization into the navigation system to guide ventricular tachycardia ablation. *Circ Arrhythm Electrophysiol* (2011) 4:674–683. doi: 10.1161/CIRCEP.111.961946
194. Ecabert O, Peters J, Walker MJ, Ivanc T, Lorenz C, von Berg J, Lessick J, Vembar M, Weese J. Segmentation of the heart and great vessels in CT images using a model-based adaptation framework. *Med Image Anal* (2011) 15:863–876. doi: 10.1016/j.media.2011.06.004
195. Jackson N, Gizurarson S, Viswanathan K, King B, Massé S, Kusha M, Porta-Sanchez A, Jacob JR, Khan F, Das M, et al. Decrement evoked potential mapping. *Circ Arrhythm Electrophysiol* (2015) 8:1433–1442. doi: 10.1161/CIRCEP.115.003083
196. de Riva M, Naruse Y, Ebert M, Androulakis AFA, Tao Q, Watanabe M, Wijnmaalen AP, Venlet J, Brouwer C, Trines SA, et al. Targeting the hidden substrate unmasked by right ventricular extrastimulation improves ventricular tachycardia ablation outcome after myocardial infarction. *J Am Coll Cardiol EP* (2018) 4:316–327. doi: 10.1016/j.jacep.2018.01.013
197. de Chillou C, Groben L, Magnin-Poull I, Andronache M, Abbas MM, Zhang N, Abdelaal A, Ammar S, Sellal J-M, Schwartz J, et al. Localizing the critical isthmus of postinfarct ventricular tachycardia: the value of pace-mapping during sinus rhythm. *Heart Rhythm* (2014) 11:175–181. doi: 10.1016/j.hrthm.2013.10.042
198. Fedorov A, Beichel R, Kalpathy-Cramer J, Finet J, Fillion-Robin J-C, Pujol S, Bauer C, Jennings D, Fennessy F, Sonka M, et al. 3D Slicer as an image computing platform for the quantitative imaging network. *Magn Reson Imaging* (2012) 30:1323–1341. doi: 10.1016/j.mri.2012.05.001

199. Orini M, Seraphim A, Graham A, Bhuva A, Zacur E, Kellman P, Schilling R, Hunter R, Dhinoja M, Finlay MC, et al. Detailed assessment of low-voltage zones localization by cardiac mri in patients with implantable devices. *JACC Clin Electrophysiol* (2022) 8:225–235. doi: 10.1016/j.jacep.2021.10.002
200. Graham AJ, Orini M, Zacur E, Dhillon G, Daw H, Srinivasan NT, Martin C, Lane J, Mansell JS, Cambridge A, et al. Evaluation of ECG imaging to map hemodynamically stable and unstable ventricular arrhythmias. *Circ Arrhythm Electrophysiol* (2020)155–165. doi: 10.1161/CIRCEP.119.007377
201. Wellens HJ, Schuilenburg RM, Durrer D. Electrical stimulation of the heart in patients with ventricular tachycardia. *Circulation* (1972) 46:216–226. doi: 10.1161/01.CIR.46.2.216
202. Josephson ME, Horowitz LN, Waxman HL, Cain ME, Spielman SR, Greenspan AM, Marchlinski FE, Ezri MD. Sustained ventricular tachycardia: role of the 12-lead electrocardiogram in localizing site of origin. *Circulation* (1981) 64:257–272. doi: 10.1161/01.CIR.64.2.257
203. Wittkamp FHM, Wever EFD, Derksen R, Wilde AAM, Ramanna H, Hauer RNW, Robles de Medina EO. Localisa. *Circulation* (1999) 99:1312–1317. doi: 10.1161/01.CIR.99.10.1312
204. De Groot NMS, Bootsma M, Van Der Velde ET, Schalij MJ. Three-dimensional catheter positioning during radiofrequency ablation in patients: first application of a real-time position management system. *J Cardiovasc Electrophysiol* (2000) 11:1183–1192. doi: 10.1046/j.1540-8167.2000.01183.x
205. Marchlinski FE, Callans DJ, Gottlieb CD, Zado E. Linear ablation lesions for control of unmappable ventricular tachycardia in patients with ischemic and nonischemic cardiomyopathy. *Circulation* (2000) 101:1288–1296. doi: 10.1161/01.CIR.101.11.1288
206. Dickfeld T, Calkins H, Bradley D, Solomon SB. Stereotactic catheter navigation using magnetic resonance image integration in the human heart. *Heart Rhythm* (2005) 2:413–415. doi: 10.1016/j.hrthm.2004.11.023
207. Tian J, Jeudy J, Smith MF, Jimenez A, Yin X, Bruce PA, Lei P, Turgeman A, Abbo A, Shekhar R, et al. Three-dimensional contrast-enhanced multidetector CT for anatomic, dynamic, and perfusion characterization of abnormal myocardium to guide ventricular tachycardia ablations. *Circ Arrhythm Electrophysiol* (2010) 3:496–504. doi: 10.1161/CIRCEP.109.889311
208. Prakosa A, Arevalo HJ, Deng D, Boyle PM, Nikolov PP, Ashikaga H, Blauer JJE, Ghafoori E, Park CJ, Blake RC, et al. Personalized virtual-heart technology for guiding the ablation of infarct-related ventricular tachycardia. *Nat Biomed*

- Eng* (2018) 2:732–740. doi: 10.1038/s41551-018-0282-2
209. Lozoya RC, Berte B, Cochet H, Jaïs P, Ayache N, Sermesant M. Model-based feature augmentation for cardiac ablation target learning from images. *IEEE Trans Biomed Eng* (2019) 66:30–40. doi: 10.1109/TBME.2018.2818300
 210. Codreanu A, Odille F, Aliot E, Marie P-Y, Magnin-Poull I, Andronache M, Mandry D, Djaballah W, Régent D, Felblinger J, et al. Electroanatomic characterization of post-infarct scars. *J Am Coll Cardiol* (2008) 52:839–842. doi: 10.1016/j.jacc.2008.05.038
 211. Wijnmaalen AP, Van Der Geest RJ, Van Huls Van Taxis CFB, Siebelink HMJ, Kroft LJM, Bax JJ, Reiber JHC, Schalij MJ, Zeppenfeld K. Head-to-head comparison of contrast-enhanced magnetic resonance imaging and electroanatomical voltage mapping to assess post-infarct scar characteristics in patients with ventricular tachycardias: Real-time image integration and reversed registration. *Eur Heart J* (2011) 32:104–114. doi: 10.1093/eurheartj/ehq345
 212. Cochet H, Komatsu Y, Sacher F, Jadidi AS, Scherr D, Riffaud M, Derval N, Shah A, Roten L, PASCALÉ P, et al. Integration of merged delayed-enhanced magnetic resonance imaging and multidetector computed tomography for the guidance of ventricular tachycardia ablation: a pilot study. *J Cardiovasc Electrophysiol* (2013) 24:419–426. doi: 10.1111/jce.12052
 213. Grehn M, Mandija S, Andratschke N, Zeppenfeld K, Blamek S, Fast M, Botrugno C, Blanck O, Verhoeff J, Pruvot E. Survey results of the STOPSTORM consortium about stereotactic arrhythmia radioablation in Europe. *Europace* (2022) 24:40849. doi: 10.1093/europace/euac053.376
 214. Mayer AG. "Rhythmical Pulsation in Scyphomedusæ. II.," *Papers from the Tortugas Laboratory*. Carnegie Institution of Washington (1908). p. 113–131
 215. Mines GR. On dynamic equilibrium in the heart. *J Physiol* (1913) 46:349–383. doi: 10.1113/jphysiol.1913.sp001596
 216. Garrey WE. The nature of fibrillary contraction of the heart.—Its relation to tissue mass and form. *Am J Physiol* (1914) 33:397–414.
 217. Wiener N, Rosenblueth A. The mathematical formulation of the problem of conduction of impulses in a network of connected excitable elements, specifically in cardiac muscle. *Arch Inst Cardiol Mex* (1946) 16:205–265.
 218. Allesie MA, Bonke FIM, Schopman FJG. Circus movement in rabbit atrial muscle as a mechanism of tachycardia. *Circ Res* (1973) 33:54–62. doi: 10.1161/01.RES.33.1.54

219. Allesie MA, Bonke FI, Schopman FJ. Circus movement in rabbit atrial muscle as a mechanism of tachycardia. III. The "leading circle" concept: a new model of circus movement in cardiac tissue without the involvement of an anatomical obstacle. *Circ Res* (1977) 41:9–18. doi: 10.1161/01.res.41.1.9
220. Kléber AG, Rudy Y. Basic mechanisms of cardiac impulse propagation and associated arrhythmias. *Physiol Rev* (2004) 84:431–488. doi: 10.1152/physrev.00025.2003
221. Martin R, Maury P, Bisceglia C, Wong T, Estner H, Meyer C, Dallet C, Martin CA, Shi R, Takigawa M, et al. Characteristics of scar-related ventricular tachycardia circuits using ultra-high-density mapping: a multi-center study. *Circ Arrhythm Electrophysiol* (2018) 11:e006569. doi: 10.1161/CIRCEP.118.006569
222. Coumel P. [From provocation tests to clinical practice: invasive and non-invasive electrophysiology]. *Arch Mal Coeur Vaiss* (2003) 96 Spec No 4:48–53.
223. Coumel P. The management of clinical arrhythmias. An overview on invasive versus non-invasive electrophysiology. *Eur Heart J* (1987) 8:92–99. doi: 10.1093/oxfordjournals.eurheartj.a062259
224. FARRE J. Obituary to: Philippe Coumel? A founding father of modern arrhythmology. *Eur Heart J* (2004) 25:1083–1084. doi: 10.1016/j.ehj.2004.04.032
225. Tabereaux PB, Dossdall DJ, Ideker RE. Mechanisms of VF maintenance: Wandering wavelets, mother rotors, or foci. *Heart Rhythm* (2009) 6:405–415. doi: 10.1016/j.hrthm.2008.11.005
226. Smoczynska A, Aarnink EW, Dunnink A, Bossu A, Van Weperen VYH, Meijborg VMF, Beekman HDM, Coronel R, Vos MA. Interplay between temporal and spatial dispersion of repolarization in the initiation and perpetuation of torsades de pointes in the chronic atrioventricular block dog. *Am J Physiol - Heart Circ Physiol* (2021) 321: doi: 10.1152/AJPHEART.00945.2020/ASSET/IMAGES/LARGE/AJPHEART.00945.2020_F004.JPEG
227. Rivaud MR, Bayer JD, Cluitmans M, van der Waal J, Bear LR, Boukens BJ, Belterman C, Gottlieb L, Vaillant F, Abell E, et al. Critical repolarization gradients determine the induction of reentry-based torsades de pointes arrhythmia in models of long QT syndrome. *Heart Rhythm* (2021) 18:278–287. doi: 10.1016/j.hrthm.2020.09.020
228. Chauhan VS, Downar E, Nanthakumar K, Parker JD, Ross HJ, Chan W, Picton P. Increased ventricular repolarization heterogeneity in patients with ventricular arrhythmia vulnerability and cardiomyopathy: A human in vivo study. *Am J Physiol - Heart Circ Physiol* (2006) 290:79–86. doi: 10.1152/

- ajpheart.00648.2005
229. Kelemen K, Greener ID, Wan X, Parajuli S, Donahue JK. Heterogeneous repolarization creates ventricular tachycardia circuits in healed myocardial infarction scar. *Nat Commun* (2022) 13:830. doi: 10.1038/s41467-022-28418-1
 230. Amoni M, Vermoortele D, Ekhteraei-Tousi S, Doñate Puertas R, Gilbert G, Youness M, Thienpont B, Willems R, Roderick HL, Claus P, et al. Heterogeneity of repolarization and cell-cell variability of cardiomyocyte remodeling within the myocardial infarction border zone contribute to arrhythmia susceptibility. *Circ Arrhythm Electrophysiol* (2023) doi: 10.1161/CIRCEP.122.011677
 231. Meijborg VMF, Boukens BJD, Janse MJ, Salavatian S, Dacey MJ, Yoshie K, Opthof T, Swid MA, Hoang JD, Hanna P, et al. Stellate ganglion stimulation causes spatiotemporal changes in ventricular repolarization in pig. *Heart Rhythm* (2020) 17:795–803. doi: 10.1016/j.hrthm.2019.12.022
 232. Black N, D'Souza A, Wang Y, Piggins H, Dobrzynski H, Morris G, Boyett MR. Circadian rhythm of cardiac electrophysiology, arrhythmogenesis, and the underlying mechanisms. *Heart Rhythm* (2019) 16:298–307. doi: 10.1016/j.hrthm.2018.08.026
 233. Severs NJ, Bruce AF, Dupont E, Rothery S. Remodelling of gap junctions and connexin expression in diseased myocardium. *Cardiovasc Res* (2008) 80:9–19. doi: 10.1093/cvr/cvn133
 234. Greener ID, Sasano T, Wan X, Igarashi T, Strom M, Rosenbaum DS, Donahue JK. Connexin43 gene transfer reduces ventricular tachycardia susceptibility after myocardial infarction. *J Am Coll Cardiol* (2012) 60:1103–1110. doi: 10.1016/j.jacc.2012.04.042
 235. Weiss JN, Karma A, Shiferaw Y, Chen PS, Garfinkel A, Qu Z. From pulsus to pulseless: The saga of cardiac alternans. *Circ Res* (2006) 98:1244–1253. doi: 10.1161/01.RES.0000224540.97431.f0
 236. Coronel R, Wilms-schopman FJG, Opthof T, Janse MJ. Dispersion of repolarization and arrhythmogenesis. *Heart Rhythm* (2020) 6:537–543. doi: 10.1016/j.hrthm.2009.01.013
 237. Child N, Bishop MJ, Hanson B, Coronel R, Opthof T, Boukens BJ, Walton RD, Efimov IR, Bostock J, Hill Y, et al. An activation-repolarization time metric to predict localized regions of high susceptibility to reentry. *Heart Rhythm* (2015) 12:1644–1653. doi: 10.1016/j.hrthm.2015.04.013
 238. Orini M, Graham AJ, Srinivasan NT, Campos FO, Hanson BM, Chow A,

- Hunter RJ, Schilling RJ, Finlay M, Earley MJ, et al. Evaluation of the reentry vulnerability index to predict ventricular tachycardia circuits using high-density contact mapping. *Heart Rhythm* (2020) 17:576–583. doi: 10.1016/j.hrthm.2019.11.013
239. Sasano T, Kelemen K, Greener ID, Donahue JK. Ventricular tachycardia from the healed myocardial infarction scar: Validation of an animal model and utility of gene therapy. *Heart Rhythm* (2009) 6:S91–S97. doi: 10.1016/j.hrthm.2009.03.048
240. Sasano T, McDonald AD, Kikuchi K, Donahue JK. Molecular ablation of ventricular tachycardia after myocardial infarction. *Nat Med* (2006) 12:1256–1258. doi: 10.1038/nm1503
241. Qu Z, Liu MB, Olcese R, Karagueuzian H, Garfinkel A, Chen P-S, Weiss JN. R-on-T and the initiation of reentry revisited: Integrating old and new concepts. *Heart Rhythm* (2022) 19:1369–1383. doi: 10.1016/j.hrthm.2022.03.1224
242. El-Sherif N. Mechanism of ventricular arrhythmias in the long QT syndrome: on hermeneutics. *J Cardiovasc Electrophysiol* (2001) 12:973–976. doi: 10.1046/j.1540-8167.2001.00973.x
243. Zhang Z, Qu Z. Mechanisms of phase-3 early afterdepolarizations and triggered activities in ventricular myocyte models. *Physiol Rep* (2021) 9:e14883. doi: 10.14814/phy2.14883
244. Odening KE, Van Der Linde HJ, Ackerman MJ, Volders PGA, Ter Bekke RMA. Electromechanical reciprocity and arrhythmogenesis in long-QT syndrome and beyond: state of the art review. *Eur Heart J* (2022) 43:3018–3028. doi: 10.1093/eurheartj/ehac135
245. Sato D, Xie LH, Sovari AA, Tran DX, Morita N, Xie F, Karagueuzian H, Garfinkel A, Weiss JN, Qu Z. Synchronization of chaotic early afterdepolarizations in the genesis of cardiac arrhythmias. *Proc Natl Acad Sci U S A* (2009) 106:2983–2988. doi: 10.1073/pnas.0809148106
246. Antzelevitch C, Burashnikov A. Overview of basic mechanisms of cardiac arrhythmia. *Card Electrophysiol Clin* (2011) 3:23–45. doi: 10.1016/j.ccep.2010.10.012
247. Cerbai E, Pino R, Porciatti F, Sani G, Toscano M, Maccherini M, Giunti G, Mugelli A. Characterization of the hyperpolarization-activated current, *if*, in ventricular myocytes from human failing heart. *Circulation* (1997) 95:568–571. doi: 10.1161/01.CIR.95.3.568
248. Xie Y, Sato D, Garfinkel A, Qu Z, Weiss JN. So little source, so much sink:

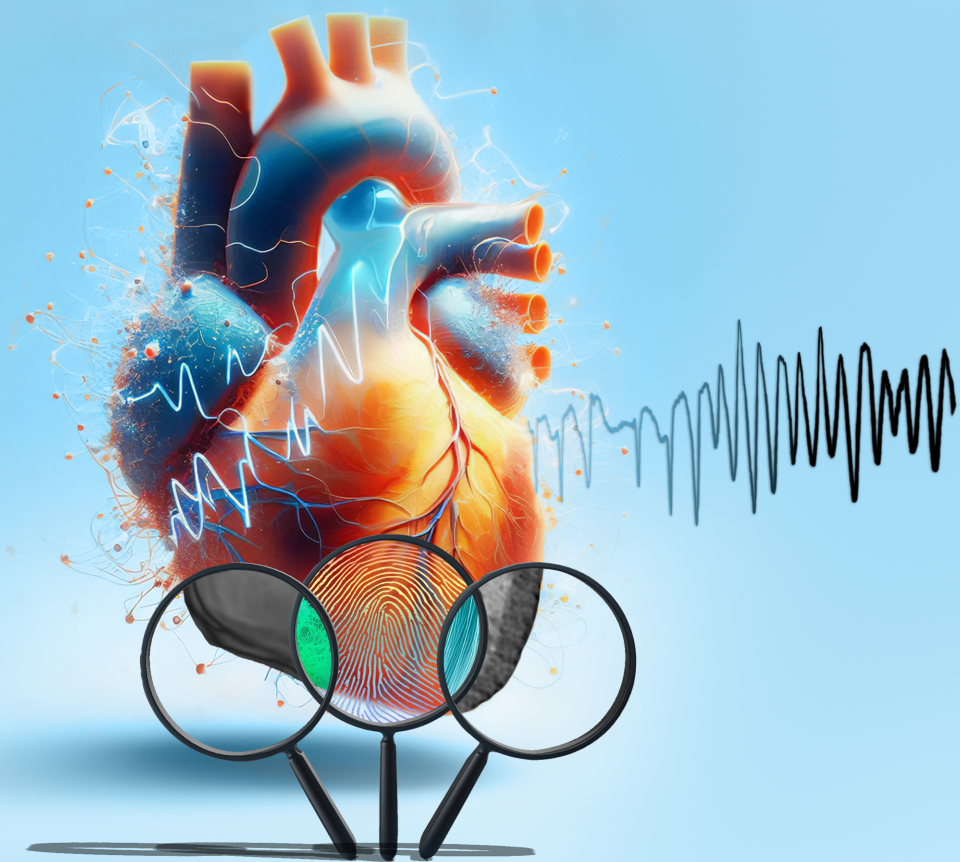
- requirements for afterdepolarizations to propagate in tissue. *Biophys J* (2010) 99:1408–1415. doi: 10.1016/j.bpj.2010.06.042
249. Lukas A, Antzelevitch C. Phase 2 reentry as a mechanism of initiation of circus movement reentry in canine epicardium exposed to simulated ischemia. *Cardiovasc Res* (1996) 32:593–603.
250. Haissaguerre M, Vigmond E, Stuyvers B, Hocini M, Bernus O. Ventricular arrhythmias and the His-Purkinje system. *Nat Rev Cardiol* (2016) 13:155–166. doi: 10.1038/nrcardio.2015.193
251. Zabel M, Willems R, Lubinski A, Bauer A, Brugada J, Conen D, Flevari P, Hasenfuß G, Svetlosak M, Huikuri HV, et al. Clinical effectiveness of primary prevention implantable cardioverter-defibrillators: results of the EU-CERT-ICD controlled multicentre cohort study. *Eur Heart J* (2020) 41:3437–3447. doi: 10.1093/eurheartj/ehaa226
252. Ruwald MH, Ruwald A-C, Johansen JB, Gislason G, Lindhardt TB, Nielsen JC, Torp-Pedersen C, Riahi S, Vinther M, Philbert BT. Temporal incidence of appropriate and inappropriate therapy and mortality in secondary prevention ICD patients by cardiac diagnosis. *J Am Coll Cardiol EP* (2021) 7:781–792. doi: 10.1016/j.jacep.2020.11.005
253. Groeneveld SA, Verheul LM, van der Ree MH, Mulder BA, Scholten MF, Alings M, van der Voort P, Bootsma M, Evertz R, Balt JC, et al. Importance of systematic diagnostic testing in idiopathic ventricular fibrillation: results from the Dutch iVF registry. *J Am Coll Cardiol EP* (2023) 9: doi: 10.1016/j.JACEP.2022.10.003
254. Poole JE, Johnson GW, Hellkamp AS, Anderson J, Callans DJ, Raitt MH, Reddy RK, Marchlinski FE, Yee R, Guarnieri T, et al. Prognostic importance of defibrillator shocks in patients with heart failure. *N Engl J Med* (2008) 359:1009–1017. doi: 10.1056/NEJMoa071098
255. Buxton AE. Should everyone with an ejection fraction less than or equal to 30% receive an implantable cardioverter-defibrillator? Not everyone with an ejection fraction $<$ or $=$ 30% should receive an implantable cardioverter-defibrillator. *Circulation* (2005) 111:2537–49; discussion 2537–49. doi: 10.1161/01.CIR.0000165057.88551.2C
256. Barber F, Langfield P, Lozano M, Garcia-Fernandez I, Duchateau J, Hocini M, Haissaguerre M, Vigmond E, Sebastian R. Estimation of personalized minimal Purkinje systems from human electro-anatomical maps. *IEEE Trans Med Imaging* (2021) 40:2182–2194. doi: 10.1109/TMI.2021.3073499
257. Demoulin JC, Kulbertus HE. Histopathological examination of concept of left

- hemiblock. *Heart* (1972) 34:807–814. doi: 10.1136/hrt.34.8.807
258. Sadek MM, Benhayon D, Sureddi R, Chik W, Santangeli P, Supple GE, Hutchinson MD, Bala R, Carballeira L, Zado ES, et al. Idiopathic ventricular arrhythmias originating from the moderator band: electrocardiographic characteristics and treatment by catheter ablation. *Heart Rhythm* (2015) 12:67–75. doi: 10.1016/j.hrthm.2014.08.029
259. Rivera S, Vecchio N, Ricapito P. Anatomical connections between the papillary muscles and the ventricular myocardium: correlation with QRS variability of ventricular arrhythmias. *Circ Arrhythm Electrophysiol* (2019) 12:e007004. doi: 10.1161/CIRCEP.118.007004
260. Gonzalez-Martin P, Sacco F, Butakoff C, Doste R, Bederian C, Gutierrez Espinosa de Los Monteros LK, Houzeaux G, Iazzo PA, Iles TL, Vazquez M, et al. Ventricular anatomical complexity and sex differences impact predictions from electrophysiological computational models. *PLoS One* (2023) 18:e0263639. doi: 10.1371/journal.pone.0263639
261. Shivkumar K, Ajjjola OA, Anand I, Armour JA, Chen P-S, Esler M, De Ferrari GM, Fishbein MC, Goldberger JJ, Harper RM, et al. Clinical neurocardiology defining the value of neuroscience-based cardiovascular therapeutics. *J Physiol* (2016) 594:3911–3954. doi: 10.1113/JP271870
262. Jonsson MKB, Vos MA, Duker G, Demolombe S, van Veen TAB. Gender disparity in cardiac electrophysiology: Implications for cardiac safety pharmacology. *Pharmacol Ther* (2010) 127:9–18. doi: 10.1016/j.pharmthera.2010.04.002
263. Narayan SM, Wang PJ, Daubert JP. New concepts in sudden cardiac arrest to address an intractable epidemic: JACC State-of-the-Art Review. *J Am Coll Cardiol* (2019) 73:70–88. doi: 10.1016/j.jacc.2018.09.083
264. Mazzanti A, Trancuccio A, Kukavica D, Pagan E, Wang M, Mohsin M, Peterson D, Bagnardi V, Zareba W, Priori SG. Independent validation and clinical implications of the risk prediction model for long QT syndrome (1-2-3-LQTS-Risk). *EP Eur* (2022) 24:614–619. doi: 10.1093/EUROPACE/EUAB238
265. Wahbi K, Ben Yaou R, Gandjbakhch E, Anselme F, Gossios T, Lakdawala NK, Stalens C, Sacher F, Babuty D, Trochu JN, et al. Development and validation of a new risk prediction score for life-threatening ventricular tachyarrhythmias in laminopathies. *Circulation* (2019) 140:293–302. doi: 10.1161/CIRCULATIONAHA.118.039410
266. Kaski JP, Norrish G, Ding T, Field E, Ziólkowska L, Olivotto I, Limongelli G, Anastasakis A, Weintraub R, Biagini E, et al. Development of a novel risk prediction model for sudden cardiac death in childhood hypertrophic

- cardiomyopathy (HCM risk-kids). *JAMA Cardiol* (2019) 4:918–927. doi: 10.1001/JAMACARDIO.2019.2861
267. Holmström L, Zhang FZ, Ouyang D, Dey D, Slomka PJ, Chugh SS. Artificial intelligence in ventricular arrhythmias and sudden death. *Arrhythmia Electrophysiol Rev* 2023;12:e17 (2023) doi: 10.15420/aer.2022.42
268. Arevalo HJ, Vadakkumpadan F, Guallar E, Jebb A, Malamas P, Wu KC, Trayanova NA. Arrhythmia risk stratification of patients after myocardial infarction using personalized heart models. *Nat Commun* (2016) 7:1–8. doi: 10.1038/ncomms11437
269. Nikolov P, Prakosa A, Arevalo HJ, Wu KC, Trayanova N. Abstract 20903: A novel approach to arrhythmia risk stratification in patients with non-ischemic cardiomyopathy. *Circulation* (2016) 134:A20903–A20903. doi: 10.1161/circ.134.suppl_1.20903
270. Shade JK, Prakosa A, Okada DR, Chrispin J, Trayanova N. Abstract 15069: novel approach to arrhythmia risk stratification in patients with cardiac sarcoidosis incorporating machine learning and a MRI-PET-fusion computational model. *Circulation* (2018) 138:A15069–A15069. doi: 10.1161/circ.138.suppl_1.15069
271. Connolly SJ, Hallstrom AP, Cappato R, Schron EB, Kuck K-H, Zipes DP, Greene HL, Boczor S, Domanski M, Follmann D, et al. Meta-analysis of the implantable cardioverter defibrillator secondary prevention trials. *Eur Heart J* (2000) 21:2071–2078. doi: 10.1053/euhj.2000.2476
272. Medeiros P, Santos M, Arantes C, Pereira VH, Rocha S. Implantable cardioverter-defibrillator in patients with inherited arrhythmia syndromes: a systematic review. *Heart Lung* (2023) 60:1–7. doi: 10.1016/j.hrtlng.2023.02.012
273. Garcia R, Combes N, Defaye P, Narayanan K, Guedon-Moreau L, Boveda S, Blangy H, Bouet J, Briand F, Chevalier P, et al. Wearable cardioverter-defibrillator in patients with a transient risk of sudden cardiac death: the WEARIT-France cohort study. *Europace* (2021) 23:73–81. doi: 10.1093/europace/euaa268
274. Larson J, Rich L, Deshmukh A, Judge EC, Liang JJ. Pharmacologic management for ventricular arrhythmias: overview of anti-arrhythmic drugs. *J Clin Med* (2022) 11: doi: 10.3390/jcm11113233
275. AlTurki A, Proietti R, Russo V, Dhanjal T, Banerjee P, Essebag V. Anti-arrhythmic drug therapy in implantable cardioverter-defibrillator recipients. *Pharmacol Res* (2019) 143:133–142. doi: 10.1016/j.phrs.2019.03.020
276. Valensi PE, Johnson NB, Maison-Blanche P, Extramania F, Motte G, Coumel

- P. Influence of cardiac autonomic neuropathy on heart rate dependence of ventricular repolarization in diabetic patients. *Diabetes Care* (2002) 25:918–923. doi: 10.2337/diacare.25.5.918
277. Jhuo S-J, Lo L-W, Chang S-L, Lin Y-J, Chung F-P, Hu Y-F, Chao T-F, Tuan T-C, Liao J-N, Lin C-Y, et al. Characteristics of diurnal ventricular premature complex variation in right ventricular outflow tract arrhythmias after catheter ablation. *Medicine (Baltimore)* (2017) 96:e6516. doi: 10.1097/MD.00000000000006516
278. Karagueuzian HS, Stepanyan H, Mandel WJ. Bifurcation theory and cardiac arrhythmias. *Am J Cardiovasc Dis* (2013) 3:1–16.
279. Smoczynska A, Beekman HD, Vos MA. The increment of short-term variability of repolarisation determines the severity of the imminent arrhythmic outcome. *Arrhythmia Electrophysiol Rev* (2019) 8:166–172. doi: 10.15420/aer.2019.16.2
280. Smoczyńska A, Loen V, Sprenkeler DJ, Tuinenburg AE, Ritsema van Eck HJ, Malik M, Schmidt G, Meine M, Vos MA. Short-Term Variability of the QT interval can be used for the prediction of imminent ventricular arrhythmias in patients with primary prophylactic implantable cardioverter defibrillators. *J Am Heart Assoc* (2020) 9:18133. doi: 10.1161/JAHA.120.018133
281. Wilson LD, Jennings MM, Rosenbaum DS. Point: M cells are present in the ventricular myocardium. *Heart Rhythm* (2011) 8:930–933. doi: 10.1016/j.hrthm.2011.01.026
282. Janse MJ, Coronel R, Opthof T. Counterpoint: M cells do not have a functional role in the ventricular myocardium of the intact heart. *Heart Rhythm* (2011) 8:934–937. doi: 10.1016/j.hrthm.2010.10.048
283. Boukens BJ, Sulkin MS, Gloschat CR, Ng FS, Vigmond EJ, Efimov IR. Transmural APD gradient synchronizes repolarization in the human left ventricular wall. *Cardiovasc Res* (2015) 108:188–196. doi: 10.1093/cvr/cvv202
284. Janse MJ, Coronel R, Opthof T, Sosunov EA, Anyukhovskiy EP, Rosen MR. Repolarization gradients in the intact heart: Transmural or apico-basal? *Prog Biophys Mol Biol* (2012) 109:6–15. doi: 10.1016/j.pbiomolbio.2012.03.001
285. Opthof T, Coronel R, Janse MJ. Is there a significant transmural gradient in repolarization time in the intact heart?: Repolarization gradients in the intact heart. *Circ Arrhythm Electrophysiol* (2009) 2:89–96. doi: 10.1161/CIRCEP.108.825356
286. Kondo M, Nesterenko V, Antzelevitch C. Cellular basis for the monophasic action potential. Which electrode is the recording electrode? *Cardiovasc Res*

- (2004) 63:635–644. doi: 10.1016/j.cardiores.2004.05.003
287. García-García C, Oliveras T, Serra J, Vila J, Rueda F, Cediel G, Labata C, Ferrer M, Carrillo X, Dégano IR, et al. Trends in short-and long-term st-segment-elevation myocardial infarction prognosis over 3 decades: a mediterranean population-based ST-segment-elevation myocardial infarction registry. *J Am Heart Assoc* (2020) 9:17159. doi: 10.1161/JAHA.120.017159
288. Visser M, Van Der Heijden JF, Doevendans PA, Loh P, Wilde AA, Hassink RJ. Idiopathic ventricular fibrillation: the struggle for definition, diagnosis, and follow-up. *Circ Arrhythm Electrophysiol* (2016) 9: doi: 10.1161/CIRCEP.115.003817
289. Risk stratification and survival after myocardial infarction. *N Engl J Med* (1983) 309:331–336. doi: 10.1056/NEJM198308113090602
290. Wellens HJJ, Schwartz PJ, Lindemans FW, Buxton AE, Goldberger JJ, Hohnloser SH, Huikuri HV, Kääb S, La Rovere MT, Malik M, et al. Risk stratification for sudden cardiac death: current status and challenges for the future†. *Eur Heart J* (2014) 35:1642–1651. doi: 10.1093/eurheartj/ehu176
291. Prakosa A, Cartoski MJ, Boyle PM, O’Hara RP, Pashakhanloo F, Coppini R, Pradella S, Zimmerman S, Abraham MR, Maurizi N, et al. Abstract 16889: Ventricular Arrhythmia (VA) in Hypertrophic Cardiomyopathy (HCM): Novel Arrhythmia Risk Stratification using T1 Mapping, late gadolinium enhancement MRI (LGE-MRI), and computational modeling. *Circulation* (2017) 136:A16889–A16889. doi: 10.1161/circ.136.suppl_1.16889
292. Cartoski MJ, Nikolov P, Boyle PM, Spevak PJ, Trayanova NA. Abstract 15442: Personalized risk stratification for ventricular arrhythmia in pediatric patients with myocarditis via image-based computational simulations. *Circulation* (2017) 136:A15442–A15442. doi: 10.1161/circ.136.suppl_1.15442
293. Holmes JW, Lumens J. Clinical applications of patient-specific models: the case for a simple approach. *J Cardiovasc Transl Res* (2018) 11:71–79. doi: 10.1007/s12265-018-9787-z
294. Neuwirth R, Cvek J, Knybel L, Jiravsky O, Molenda L, Kodaj M, Fiala M, Peichl P, Feltl D, Januška J, et al. Stereotactic radiosurgery for ablation of ventricular tachycardia. *Europace* (2019) 21:1088–1095. doi: 10.1093/europace/euz133
295. Lloyd MS, Wight J, Schneider F, Hoskins M, Attia T, Escott C, Lerakis S, Higgins KA. Clinical experience of stereotactic body radiation for refractory ventricular tachycardia in advanced heart failure patients. *Heart Rhythm* (2020) 17:415–422. doi: 10.1016/j.hrthm.2019.09.028



APPENDIX D

Acknowledgements

Acknowledgements

Met veel plezier kan ik terugkijken op de afgelopen jaren waarin ik mijn promotieonderzoek mogen doen. Bij dezen wil ik graag mijn oprechte waardering uitspreken aan alle personen die direct of indirect een bijdrage hebben geleverd aan het tot stand komen van dit proefschrift. In het bijzonder wil ik bedanken:

Mijn promotor **Paul Volders**: bedankt voor de altijd motiverende en stimulerende gesprekken. Jouw uitspraak "the sky is the limit", wat je vroeg in het eerste jaar aan Bianca en mij introduceerde, heeft me geïnspireerd om altijd naar het hoogst mogelijke niveau te streven. Je oog voor detail is bewonderenswaardig, zelfs als het soms frustrerend kan zijn. Ik heb dankzij jouw begeleiding veel kunnen leren van de uitgestrekte wereld van cardiale elektrofysiologie, vanuit verschillende historische perspectieven. Het was een voorrecht om door jouw brede blik vele experts te ontmoeten en het internationale veld te verkennen. Ik ben dankbaar voor je onnoemelijke bijdrage en kijk uit naar de komende jaren van samenwerking.

Mijn promotor **Ralf Peeters**: bedankt voor je nuchtere blik en je grote bereidheid om altijd te helpen, zelfs met een overvolle agenda. Een bevestiging of een geruststelling van jouw kant - te danken aan je bescheiden houding en relativerend vermogen - kwam vaak als geroepen. Je benadert uitdagingen op een hele praktische manier, en bouwt bruggen met andere afdelingen en centra. Ook hier heb ik veel van geleerd.

Mijn promotor **Paul Dendale**: bedankt voor je altijd behulpzame houding en pragmatische kijk op zaken. Jij was, vooral in de vroegere fases van mijn promotieonderzoek, vaak degene die in complexe academische discussies altijd met beide benen op de grond bleef staan en dit voor mij vertaalde naar concrete actiepunten of wensen. Dankzij jouw toegankelijkheid kon ik altijd rekenen op hulp wanneer nodig.

Mijn copromotor **Matthijs Cluitmans**: dank voor je directe supervisie en open blik op de academische wereld. Je hebt me blootgesteld aan diverse disciplines, centra en mensen, wat mijn persoonlijke en professionele leerervaring enorm heeft verrijkt. Je coöperatieve instelling doorbreekt bestaande structuren en politiek, iets waar ik veel waardering voor heb. Ik ben dankbaar voor jouw inhoudelijke (en vaak ook financiële) bijdragen die je uit eigen initiatief aanbood, aan congresbezoeken en publicaties. Ook op persoonlijk vlak heb ik ook erg veel geleerd van jouw oprechte optimisme; ik vraag me nog dagelijks af hoe je dat nu doet. Bedankt voor je luisterend oor in werk- en privésituaties, en je inhoudelijke expertise op het gebied van dit onderzoek. Ondanks dat onze wegen zich nu langzamerhand steeds iets meer lijken te scheiden, hoop ik nog vele jaren met jou te mogen samenwerken.

I would also like to thank the members of the Assessment Committee **Prof. Tammo Delhaas, Dr. Virginie Bito, Prof. Eline Kooi, Prof. Pier Lambiase, Prof. Dominik Linz, and Prof. Yoram Rudy** for taking the time to review this thesis.

Alle artsen en laboranten die me wegwijs hebben gemaakt in het MUMC+ en Jessa ziekenhuis, en die hebben geholpen in het verkrijgen en interpreteren en publiceren van klinische data. **Rachel**, jouw no-nonsense blik op zaken is erg stimulerend en verhelderend. Als de vraag is wanneer een onderzoeksmeting uitgevoerd moet zijn of wanneer een artikel gepubliceerd moet kunnen worden, is jouw antwoord vaak: het liefst gisteren. In de wereld van onderzoek die soms erg log kan zijn was dat soms even wennen, maar dit leidt tot hele effectieve resultaten. Jouw aanpak heeft geleid tot enkele mooie gezamenlijke publicaties, en ik hoop dat we deze lijn de komende jaren nog kunnen voortzetten. **Johan**, bedankt voor je grote expertise en inhoudelijke begeleiding op het gebied van elektrofysiologie. Ook wil ik **Kevin Vernooy, Justin Luermans, Jos Habets, Hilco Snippe, Tim Jacobs, Pieter Koopman, Dagmara Dilling-Boer, Thomas Philips** en **Philippe Timmermans** bedanken voor hun hulp bij het opnemen of interpreteren van onze vele ECGI-metingen en klinische data.

Langs diezelfde weg wil ik graag alle collega's van de radiologie bedanken voor hun onuitputbare hulp in het mogelijk maken, plannen en uitvoeren van ECGI-metingen, waaronder **Joachim Wildberger, Casper Muhl, Suzanne Gommers, Rob Holtackers, Ankie Hersbach** en **Serena Kruchten**. Dit geldt ook voor de collega's in het Jessa ziekenhuis, waaronder **Geert Souverijns, Olivier Ghekiere, Eric Bijmens** en **Dominic Moermans**.

Paranimfen **Daan** en **Roel**, ook jullie hebben, soms direct en soms indirect, een grote bijdrage geleverd aan dit proefschrift en mijn promotie. **Daan**, bedankt voor het luisterend oor op welk vlak dan ook, het relativerende vermogen, de vakanties, maar ook de bodemloze put aan droge humor, al vanaf de tijd van meneer Van Empel. **Roel**, jij ook bedankt voor het luisterend oor op werk en je adviezen, op inhoudelijk maar ook op persoonlijk vlak. Je staat altijd voor mensen klaar, en ik sta nog steeds achter het "secret santa" gedicht van twee(?) jaar geleden. Daarnaast kijk ik nu al uit naar onze volgende fietsrit (dit geldt voor jullie beide trouwens)!

All of the colleagues that I shared an office with throughout the years. **Henry**, I am thankful for our time in F3.106 together, and I was honored to be your paranymp. I have always admired your unstoppable drive, not only back when we were office mates, but still in your current position. I was often pleasantly surprised by your friendly attitude below the surface. Most of all, this was demonstrated by your absolutely selfless decision to turn your PhD gift into a donation for charity. I wish you all the best in your current and future (clinical) positions in Indonesia. **Stefan**, jouw aanwezigheid, gezelligheid en wilde verhalen zorgen zelfs op de drukste dagen voor een welkome afleiding. **Minsi**, "Dr. M.", your kind presence and free coffees have always been welcome and will

remain that way, hopefully we get to share many more. **Xi**, I always appreciate the stories about your travelling stories and PhD during lunch times, and our shared coffee/vlaai moments. I am also happy that I got to share an office with all interns who managed to improve the (sometimes boring) PhD experience by a lot: **Christian, Lian, Sam, Annick, Adele, Fateme, Paula and Fransesco**.

Of course, these thanks extend to the colleagues from experimental cardiology (or related departments) I did not directly share an office with. **Bianca**, jouw complementaire (klinische) blik bood vaak een waardevol nieuw perspectief. Het feit dat we in 2018 tegelijkertijd begonnen zijn aan ons promotietraject is van grote waarde geweest op niet alleen onze ECGI-metingen en de onderzoeken van dit proefschrift, maar ook op mijn eigen ontwikkeling. Ik wens je het beste toe in je opleiding tot huisarts. **Alberto**, ik hoop dat ik nog niet het laatste gezien heb van onze gezamenlijke fietsritten, fietsreizen, fietsreparatiesessies, en etentjes. Ondanks dat je als ANIOS begonnen bent in het Zuyderland is het altijd leuk om je regelmatig nog te spreken over onze gezamenlijke interesses, je onderzoek en je werk. Je kunt trots zijn op je promotieonderzoek (waaronder het DPP6-werk), wat je zonder twijfel binnenkort succesvol zult gaan verdedigen. **Sandrine**, bedankt voor alle gezellige momenten op werk en daaraan gerelateerd, zoals tijdens de lunch en de CARIM borrels en feestjes, en de 20K in Brussel! **Jordi**, bedankt voor je hulp en supervisie op het computationele en mechanistische vlak; ik blijf overweldigd door jouw kennis als “lopende encyclopedie” en je passie voor je werk. Heel veel succes gewenst in Graz. **Kelly** en **Simone**, ontzettend bedankt voor jullie sterke support in het plannen, bespreken, inventariseren, en noem maar op. Zonder jullie was het niet mogelijk dit onderzoek (of gerelateerd; VIGILANCE, BREACH-ECGI, ELSTAR-VT) te doen of voort te zetten. **Yesim**, bedankt voor je eerlijke, coöperatieve en bescheiden houding, en natuurlijk je hulp bij ECGI-metingen en ADAS-analyses. Ik hoop dat je nog lang in Maastricht onderzoek kunt blijven doen. **Cristina** and **Joyce**, even though you have left Maastricht quite a while ago, I can still look back at a fun time together where I was taught the do's and don'ts of the Italian cuisine, but also joining you to the PhD boat party and meeting up with Joyce on the other side of the world in Kuala Lumpur. **Anna**, talking to you in the hallway or sharing vlaai moments is always a welcome distraction. **Peter**, thank you for the inspiring collaborations and discussions; these really bring my work to the next level. I also appreciate our lunch and beer-drinking moments, which I hope to extend in Berlin later this year. **Monique**, ondanks dat de frequentie hiervan is afgenomen sinds covid, is het bijpraten met jou altijd een welkome afleiding. **Lilian**, bedankt voor al je hulp in het plannen, organiseren, en beantwoorden van vragen.

De “buren” van fysiologie. **Ben**, al vanaf de start van mijn afstudeerstage bij BME heb ik erg veel gehad aan je inhoudelijke kennis van signaalanalyse en (voornamelijk invasieve) elektrofysiologie. Je bent altijd behulpzaam en beschikbaar voor een praatje. Veel succes in je klinische baan als TG'er. **Uyen**, bedankt voor je waardevolle inhoudelijke en persoonlijke inzichten als voorbeeld van een TG'er om naar op te kijken. Ik blijf erg positief verrast door

jouw bewonderenswaardige drive en de manier waarop je allerlei verschillende rollen, zowel persoonlijk als professioneel, combineert. Mocht je hier een geheim recept voor hebben, dan hoor ik het graag! **Bas**, net als bij Matthijs ben ik vaak onder de indruk van je open houding richting de wetenschap, hier kan ik nog veel van leren. Ook heeft je pragmatische blik al enkele analyses en plannen op een daadkrachtige manier vooruitgeholpen, en ik kijk ernaar uit om deze samenwerking voort te zetten. **Zarina** en **Arne**, de momenten waarop we even konden bijpraten over onderzoek, het doen van een PhD of de volgende fietstrip, waren (en zijn) altijd erg welkom. **Karin**, het is altijd gezellig even bij te praten over je laatste sportieve ontwikkelingen of je vooruitgang op het gebied van je promotie of ECGI-analyses, laten we dat blijven doen.

Our colleagues from DACS. **Pietro**, thank you for the hospitality in the first couple of years of my PhD, in which we sometimes worked in the same office. I have always appreciated your insights in our fruitful discussions, and enjoyed the lunches with you and sometimes **Rachel**. **Joël**, bedankt voor je technische inzichten in ECGI, maar ook de gezellige gezamenlijke congresbezoeken. **Tiantian**, I always enjoyed the dinners together, amongst which the famous hotpot, and our technical discussions on ECGI and the dog data. I wish you all the best back in China.

My colleagues from the Liryc institute in Bordeaux, in particular **Jason Bayer**, **Ed Vigmond**, **Vladimir Sobota**, **Laura Bear**, **Yingjing Feng**, and **Peter Langfield**. Thank you not only for the excellent supervision on the use of OpenCARP and computational modelling, which was challenging for me, but also for the openness with which I was welcomed into your institute. Although my time in Bordeaux was relatively short, I felt genuinely welcome and I enjoyed it, mostly because of all of you.

My national and international colleagues from the ECG Imaging community, amongst which the Consortium for ECG Imaging (CEI). Thank you for all of the interesting and inspiring discussions, which taught me a lot on not only ECGI, but also organisational aspects and how to have a fun time when you visit a congress! Particular thanks go to **Jake** and **Machteld**; thank you for being co-chairs during the executive board meetings, and also the fun times during congresses and thereafter.

Het VIGILANCE consortium, onder wie **Arthur Wilde**, **Pieter Postema**, en **Rutger Hassink**, **Lennart Blom**, **Sanne Groeneveld**, **Martijn van der Ree**, **Lisa Verheul**, en **Wiert Hoeksema**. Bedankt voor jullie waardevolle inzichten in lopende onderzoeken en de fijne samenwerking. Ik kijk uit naar het vervolg hiervan. **Lennart** was een zeer gewaardeerde collega die zijn werk met veel toewijding deed. Hij was altijd geïnteresseerd en prettig om mee samen te werken, waar ik hem altijd dankbaar voor zal blijven. **Sanne** en **Martijn**, bedankt voor de gezellige momenten tijdens het onderzoek en borrels, en jullie uitgebreide hulp in het doen van ECGI-metingen en analyses. Ook jullie complementaire medische

kennis was, en blijft, zeer welkom. **Lisa**, dat geldt ook voor jou! Altijd gezellig om weer even bij te praten als je weer voor een (lange) dag naar Maastricht komt, en ook om iemand te hebben voor “strategisch beraad” als mede-onderzoeker.

De (fietsende) collega’s van (het vroegere) BM2Wielers en BME, waaronder **Frank van Rosmalen, Ben Hermans, Joost Lumens, Tammo Delhaas, Frank Bennis, Maarten Heusinkveld, Tijmen Koopsen, Aurore Lyon, Letty van Vliet, Erik Willemen, Alberto Rossetti, Sjeng Quicken, Peter Huntjens, Koen Reesink, Wouter Huberts, Nick van Osta, Raoul Stevens, Sabine Daemen, Lauren Dupuis, Myrthe van der Bruggen** en **Bart Pasman**. Mijn stage bij BME heeft de basis gelegd om hier in Maastricht te blijven, mede dankzij jullie. Ondanks dat de frequentie van onze fietsritten exponentieel is afgenomen, was dit aan het begin van mijn promotie altijd een gezellig wekelijks moment om naar uit te kijken. **Frank, Maarten, Tijmen** en **Alberto**: dit geldt nog meer voor onze fietsvakanties naar Tenerife en de Vogezen; ik kijk nog altijd met veel plezier terug op de vakantiefoto’s, die af en toe nog op mijn bureaublad voorbijkomen. **Aurore**, bedankt voor de Franse les om me voor te bereiden op de grote reis naar Bordeaux, en voor de gezellige wandelingen tijdens de lange thuiswerkperiodes.

Het TG-studiegroepje, **Sjors, Niels, Dieuwke, Han, Karlijn**, en **Ruben**, ondanks dat onze etentjes of feestjes inmiddels (mede door geografische redenen) steeds iets zeldzamer worden, keek ik hier altijd erg naar uit en waren deze erg gezellig.

Thijs en **Maxi**: ik kijk nog altijd met veel plezier terug op onze studententijd in Enschede, waarin niets te gek was. Ik kan het nog altijd goed met jullie beide vinden, van “the Human Embodiment of Switzerland” tot “de Koning”. Onze regelmatige gesprekken en iets-minder-regelmatige bezoekjes zijn altijd een welkome afleiding van het werk als onderzoeker.

Mannen uit Blitterswijck, waaronder “De Buizers” (**Tom, Wouter, Rik, Max, Kenny, Job, Nick, Dennis, Roel, Harm, Dirk, Thom** en **Sjimmie**), maar ook “TWC de Verloren Spaak” (waaronder **Pieter, Geert, Dennis, Bart, Frank, Toon, Ward, Yoeri, Jelle** en **Jens**). Met de ene groep is het vooral belangrijk feest te vieren en mentaal af te schakelen voor al meer dan de helft van mijn leven, met de andere om dat fysiek te doen. Ondanks dat mijn bezoekjes aan Blitterswijck het afgelopen jaar wat af zijn genomen in frequentie, blijf ik hier altijd nog evenveel naar uitkijken. Van carnaval vieren tot samen op vriendenweekend, en van een rondje Venlo tot aan de Marmotte: mooi dat dit al een hele lange tijd kan, en ik hoop dat dit nog lang zo kan blijven.

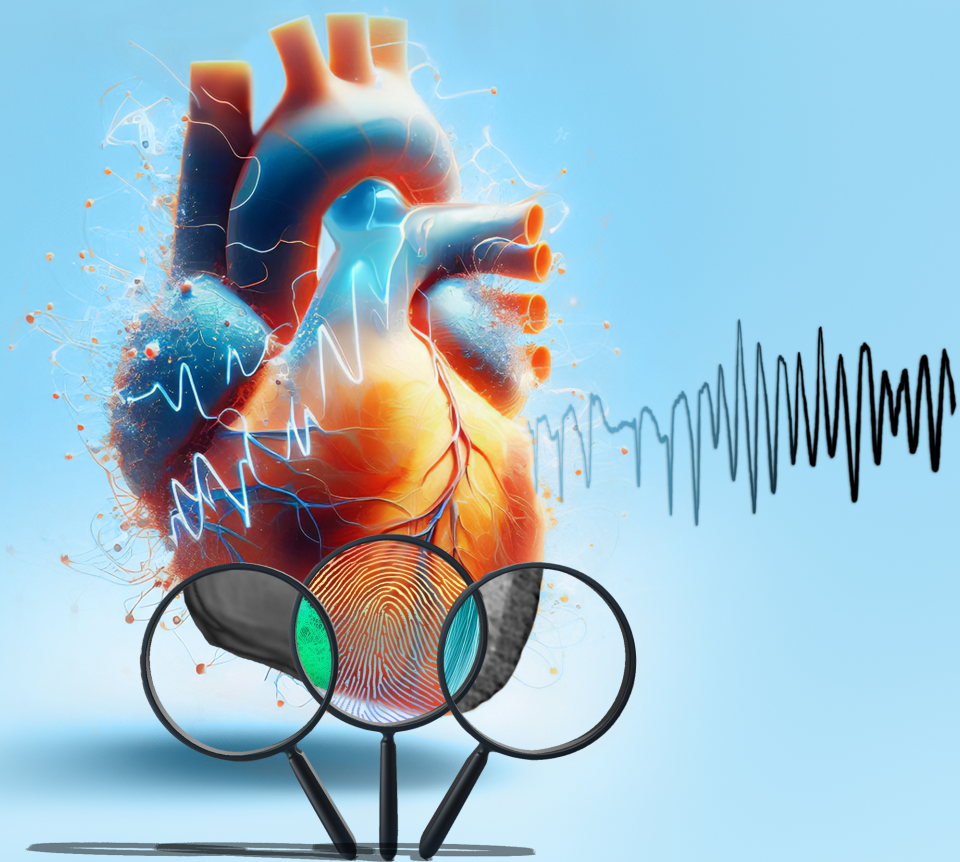
Daan, Teun en **Wouter**: misschien een beetje onorigineel, maar voor jullie geldt hetzelfde. Herinneringen zoals de viskraam in Maastricht en het pak yoghurt op het Raayland zorgen ervoor dat ik permanent uitkijk naar de volgende vriendendag.

De “schoonfamilie”: **Huub** en **Marie José, Jean Paul** en **Vicky, Anne, Roos, Manon**

en **Marino, Cyriel, en Yannick**. Erg bedankt voor jullie hulp en steun wanneer nodig, en voor alle gezellige momenten die soms hard nodig waren. Dat geldt ook voor **Manouk en Bas en Eveline en Maikel**: de verhuishulp, morele support, etentjes, barbecues, het casinobezoek en het suppen waren een welkome verlichting van de promotiestress, hopelijk kunnen we dit blijven doen.

Pap en mam, heel erg bedankt voor de onvoorwaardelijke steun en vertrouwen door alle jaren heen, waardoor ik mijn interesses altijd heb kunnen najagen en hobby's altijd heb kunnen beoefenen. Of het nu om een korte vraag, een diepe zorg of een kapotte fiets ging, ik kon (en kan) altijd bij jullie terecht. Bedankt dat de deur altijd open staat en ik weet dat ik altijd op jullie hulp en advies kan rekenen. Al zijn er inmiddels wat dingen veranderd en verbouwd aan het huis, nog steeds voel ik me in Blitterswijck heel erg thuis, en ik weet dat dat altijd zo zal blijven. **Roy en Sylvana**, heel leuk om te zien hoe jullie samen een toekomst op aan het bouwen zijn, en ik vind het heel leuk dat ik hier ook een klein deel van mag uitmaken. Jullie ook bedankt voor alle gezelligheid die vaak als geroepen kwam. **Oma**, bedankt voor alle goede zorgen, alle gezellige momenten en etentjes, de interesse en het vertrouwen. Dit geldt ook voor de rest van de familie.

Lieve **Aline**, jouw onvoorwaardelijke steun de afgelopen jaren is een belangrijke reden dat ik dit dankwoord mag schrijven. Al ben ik soms moeilijk te overtuigen of heb ik het niet altijd direct door, jouw hulp voor welk probleem dan ook is vaak een schot in de roos. Daarom is het soms alsof jij mij beter kent dan ikzelf. Door jou heb ik geleerd dat het belangrijk is om de rem even aan te trekken en te ontspannen. Hoewel deze door "uiteenlopende omstandigheden" soms moeilijk te plannen zijn, kijk ik altijd uit naar de volgende vakanties met jou, en ik hoop dat we nog vele avonturen mogen beleven samen. We groeien steeds meer naar elkaar toe, en ik kijk uit naar onze toekomst samen.



APPENDIX E

Curriculum Vitae

Curriculum Vitae

Job Stoks was born on November 21, 1992 in Venray, the Netherlands. He grew up in Blitterwijck, and graduated from secondary education (“atheneum”) in Venray in 2011. He then studied Technical Medicine at the University of Twente in Enschede. He obtained his Bachelor’s degree in 2015. During his Technical Medicine Master track “Medical Sensing and Stimulation”, he did clinical internships at the Orthopedics and Cardiology Departments of the Radboud UMC (Nijmegen), the Pediatrics Department of the Ziekenhuis Groep Twente (Enschede) and the Biomedical Engineering/Cardiology Departments at the Maastricht UMC+ (Maastricht). He obtained his Master’s degree and his BIG (“Beroepen in de Individuele Gezondheidszorg”)-registration as a Clinical Technologist in 2018.



Shortly thereafter, Job started a dual PhD program at Maastricht University and Hasselt University, under the supervision of Prof. Paul Volders (Department of Cardiology, Maastricht UMC+), Prof. Ralf Peeters (Department of Advanced Computing Sciences, Maastricht University), Prof. Paul Dendale (Department of Cardiology, Jessa Hospital) and Dr. Matthijs Cluitmans (Department of Cardiology, Maastricht UMC+). During his PhD trajectory, Job focused on multimodal image integration to better explain human ventricular tachyarrhythmias. With his hybrid background in Technical Medicine, he collaborated with colleagues from different departments, universities, and specialties, as evidenced by his doctoral thesis.



List of publications

Journal articles

1. **Understanding repolarization in the intracardiac unipolar electrogram: a long-lasting controversy revisited.**

Stoks J, Bear LR, Vijgen J, Dendale P, Peeters R, Volders PGA*, Cluitmans MJM*

*Shared last author

Frontiers in Physiology. 2023; 14. DOI: 10.3389/fphys.2023.1158003

2. **High-resolution structural-functional substrate-trigger characterization: future roadmap for catheter ablation of ventricular tachycardia.**

Stoks J, Hermans BJM, Boukens BJD, Holtackers RJ, Gommers S, Kaya YS, Vernooij K, Cluitmans MJM, Volders PGA, Ter Bekke RMA

Frontiers in Cardiovascular Medicine. 2023; 10. DOI: 10.3389/fcvm.2023.1112980

3. **Noninvasive detection of spatiotemporal activation-repolarization interactions that prime idiopathic ventricular fibrillation.**

Cluitmans MJM, Bear LR, Nguyen UC, Van Rees BD, Stoks J, Ter Bekke RMA, Muhl C, Heijman J, Lau K, Vigmond E, Bayer J, Belterman C, Abell E, Labrousse L, Rogier J, Bernus O, Haïssaguerre M, Hassink R, Dubois R, Coronel R, Volders PGA

Science Translational Medicine. 2021;13(620). DOI: 10.1126/scitranslmed.abi9317

4. **The effect of interpolating low amplitude leads on the inverse reconstruction of cardiac electrical activity.**

Rababah AS, Bear LR, Dogrusoz YS, Good W, Bergquist J, Stoks J, MacLeod R, Rjoob K, Jennings M, Mclaughlin J, Finlay DD

Computers in Biology and Medicine. 2021;136. DOI: 10.1016/j.compbiomed.2021.104666

5. Support vector machine-based assessment of the T-wave morphology improves long QT syndrome diagnosis.

Hermans BJM*, Stoks J*, Bennis FC, Vink AS, Garde A, Wilde AAM, Pison LAFG, Postema PG, Delhaas T
*Shared first author

Europace. 2018;20:iii113-iii119. DOI: 10.1093/europace/euy243

Book Chapters

1. Electrocardiographic imaging: history, applications and future perspectives.

Stoks J, Cluitmans MJM

In: "IEEE Milestone Award 'String Galvanometer - The heritage and the promise of electrocardiography and electrophysiology" (2022). ISBN 978 90 67677 82 0

Letters to the Editor

1. Methodological and mechanistic considerations in local repolarization mapping.

Stoks J, Langfield P, Cluitmans MJM

JACC: Clinical Electrophysiology (in press). DOI: 10.1016/j.jacep.2023.12.018.

2. Interpretation of electrograms is key to understand the clinical potential of ECGI.

Cluitmans MJM, Stoks J, Volders PGA

Heart rhythm. 2019;16:435-442. DOI: 10.1016/j.hrthm.2019.02.030

Presentations

Oral presentations

1. **High-resolution repolarization changes preceding short-coupled ectopy in idiopathic ventricular fibrillation, and effects of quinidine (accepted)**, to be presented at the European Heart Rhythm Association Congress, 2024 (Berlin, Germany). *Doi: N/A*
2. **Hartstilstand door onbegrepen kamerfibrilleren**, presented at the "Loop met je dokter Kick-off Meeting", 2023 (Maastricht, The Netherlands). *Doi: N/A*
3. **Dynamics of ventricular electrophysiology are unmasked through noninvasive electrocardiographic imaging**, presented at Computing in Cardiology, 2021 (Brno, Czech Republic). *Doi: 10.23919/CinC53138.2021.9662863*
4. **Noninvasive unipolar electrogram T-wave upslope is an accurate marker of local refractoriness in explanted hearts with drug-induced repolarization dispersion**, presented at the European Heart Rhythm Association Congress, 2021 (Virtual). *Doi: 10.1093/europace/euab116.036*
5. **An open-source algorithm for standardized bullseye visualization of high-resolution cardiac ventricular data: UNISYS**, presented at Computing in Cardiology, 2020 (Virtual). *Doi: 10.22489/CinC.2020.160*
6. **Variability of electrocardiographic imaging within and between leadsets**, presented at Computing in Cardiology, 2020 (Virtual). *Doi: 10.22489/CinC.2020.097*
7. **The influence of using a static diastolic geometry in ECG imaging**, presented at Computing in Cardiology, 2019 (Singapore, Singapore). *Doi: 10.22489/CinC.2019.266*

Poster presentations

1. **Multimodal image integration improves management of ventricular tachycardia**, presented at the Cardiovascular Research Institute Symposium, 2023 (Maastricht, The Netherlands). *Doi: N/A*
2. **The consequences of the DPP6 p.(R274H) variant on the purkinje and ventricular action potential: an in-silico study**, presented at the European Working Group for Cardiac Cellular Electrophysiology Meeting 2022 (Toledo, Spain). *Doi: N/A*

3. **Noninvasive assessment of dynamic cardiac electrophysiology in normal human subjects**, presented at the European Society of Cardiology Congress 2020 (Virtual). *Doi: 10.1093/ehjci/ehaa946.3596*

Awards and grants

1. **CVON PREDICT2 young talent fellowship**, 2023, Amsterdam, The Netherlands (€18,500).
2. **Cardiovascular research institute Maastricht symposium - Division heart poster prize**, 2023, Maastricht, The Netherlands.
3. **CVON VIGILANCE young talent grant**, 2023, Utrecht, The Netherlands (€11,000).
4. **Scientific exchange grant of the ESC working group on cardiac cellular electrophysiology**, 2021, Biot, France (€2,500).
5. **Cardiovascular research institute Maastricht (CARIM) HS-BAFTA fellowship for talented PhD candidates**, 2021, Maastricht, The Netherlands (€4,500).